

Dynamics and Control of Flexible Manipulators

A Thesis Submitted to
the College of Graduate Studies and Research
in Partial Fulfillment of Requirements
for the Degree of Doctor of Philosophy
in the Department of Mechanical Engineering,
University of Saskatchewan, Saskatoon
Canada

By:

Mohammad Vakil

© Copyright Mohammad Vakil, July 2008. All rights reserved.

Permission to use

In presenting this thesis in partial fulfillment of the requirement for a postgraduate degree from the University of Saskatchewan, I agree that the Libraries of this University may make it freely available for inspection. I further agree that the permission for copying this thesis in any manner, in whole or in part for scholarly purposes, may be granted by the professors who supervised my thesis work or, in their absence, by the Head of the Department or Dean of the college in which my thesis work was conducted. It is understood that any copying or publication or use of this thesis or parts therefore for financial gain shall not be allowed without my written permission. It is also understood that due recognition shall be given to me and to the University of Saskatchewan in any scholarly use which may be made of any material in my thesis.

Request for permission to copy or to make other use of material in this thesis, in whole or part, should be addressed to:

Head of the Department of Mechanical Engineering

University of Saskatchewan

College of Engineering

57 Campus Drive

Saskatoon, Saskatchewan, S7N 5A9

Canada

Abstract

Flexible link manipulators (FLM) are well-known for their light mass and small energy consumption compared to rigid link manipulators (RLM). These advantages of FLM are even of greater importance in applications where energy efficiency is crucial, such as in space applications. However, RLM are still preferred over FLM for industrial applications. This is due to the fact that the reliability and predictability of the performance of FLM are not yet as good as those of RLM. The major cause for these drawbacks is link flexibility, which not only makes the dynamic modeling¹ of FLM very challenging, but also turns its end-effector² trajectory tracking (EETT) into a complicated control problem.

The major objectives of the research undertaken in this project were to develop a dynamic model for a FLM and model-based controllers for the EETT. Therefore, the dynamic model of FLM was first derived. This dynamic model was then used to develop the EETT controllers.

A dynamic model of a FLM was derived by means of a novel method using the dynamic model of a single flexible link manipulator on a moving base (SFLMB). The computational efficiency of this method is among its novelties. To obtain the dynamic model, the Lagrange method³ was adopted. Derivation of the kinetic energy and the calculation of the corresponding derivatives, which are required in the Lagrange method, are complex for the FLM. The new method introduced in this thesis alleviated these complexities by calculating the kinetic energy and the required derivatives only for a SFLMB, which were much simpler than those of the FLM. To verify the derived dynamic model the simulation results for a two-link manipulator, with both links being flexible, were compared with those of full nonlinear finite element analysis. These comparisons showed sound agreement.

A new controller for EETT of FLM, which used the singularly perturbed form⁴ of the dynamic model and the integral manifold concept, was developed. By using the

¹ The term “dynamic model” refers to the differential equations which relate the time derivatives of the degrees-of-freedom of FLM to the input torques.

² The tip of the end-link of the manipulator is called “end-effector”.

³ Lagrange method is an approach for the derivation of the dynamic model.

⁴ Dynamic model of FLM can be expressed in the singularly perturbed form which is composed of slow and fast subsystems. This can be achieved since the response of FLM consists of the rotations of the links (slow subsystem) and the links’ lateral deflections, links’ vibration (fast subsystem).

integral manifold concept the links' lateral deflections were approximately represented in terms of the rotations of the links and input torques. Therefore the end-effector displacement, which was composed of the rotations of the links and links' lateral deflections, was expressed in terms of the rotations of the links and input torques. The input torques were then selected to reduce the EETT error. The originalities of this controller, which was based on the singularly perturbed form of the dynamic model of FLM, are: (1) it is easy and computationally efficient to implement, and (2) it does not require the time derivative of links' lateral deflections, which are impractical to measure. The ease and computational efficiency of the new controller were due to the use of the several properties of the dynamic model of the FLM. This controller was first employed for the EETT of a single flexible link manipulator (SFLM) with a linear model. The novel controller was then extended for the EETT of a class of flexible link manipulators, which were composed of a chain of rigid links with only a flexible end-link (CRFE). Finally it was used for the EETT of a FLM with all links being flexible. The simulation results showed the effectiveness of the new controller. These simulations were conducted on a SFLM, a CRFE (with the first link being rigid and second link being flexible) and finally a two-link manipulator, with both links being flexible. Moreover, the feasibility of the new controller proposed in this thesis was verified by experimental studies carried out using the equipment available in the newly established Robotic Laboratory at the University of Saskatchewan. The experimental verifications were performed on a SFLM and a two-link manipulator, with first link being rigid and second link being flexible.

Another new controller was also introduced in this thesis for the EETT of single flexible link manipulators with the linear dynamic model. This controller combined the feedforward torque, which was required to move the end-effector along the desired path, with a feedback controller. The novelty of this EETT controller was in developing a new method for the derivation of the feedforward torque. The feedforward torque was obtained by redefining the desired end-effector trajectory. For the end-effector trajectory redefinition, the summation of the stable exponential functions was used. Simulation studies showed the effectiveness of this new controller. Its feasibility was also proven by experimental verification carried out in the Robotic Laboratory at the University of Saskatchewan.

Acknowledgment

I would like to express my earnest and heartfelt gratitude and appreciation to my supervisors Professors Reza Fotouhi and Peter N. Nikiforuk. Without their invaluable guidance, support and encouragement through my PhD program, this work would not have been possible. I also would like to extend my acknowledgment to my advisory committee members Professors Walerian Szyszkowski, Greg J. Schoenau, and Bruce F. Sparling. Mr. Hamid Salmasi was also of great help in completing this work.

Financial support of this work provided by the University of Saskatchewan Graduate Scholarship and NSERC discovery grant and is gratefully acknowledged.

Dedication



This thesis is dedicated to my mother Safieh Kossari and my brother Dr. Ali Vakil, and is in memory of my father, Farhad Vakil.

List of acronyms

FLM: Flexible link manipulator
SFLMB: Single flexible link manipulator with a moving base
SFLM: Single flexible link manipulator
NOC: Natural orthogonal complement
LNOC: Combination of the Lagrange method and NOC
ODE: Ordinary differential equation
PDE: Partial differential equation
AMM: Assumed mode shape method
FEA: Finite element analysis
FE: Finite element
DOF: Degrees-of-freedom
EETT: end-effector trajectory tracking
CTC: computed torque command
SSEF: Summation of Stable Exponential Functions
PWC: Pulse width control
RLM: Rigid link manipulator
IMC: Integral manifold controller
CRFE: A class of planar flexible link manipulators which consists of a chain of rigid links with the flexible end-link
EE: End-effector
DP: Desired path

Copy right permission of the papers

At the time of the publication of this thesis the paper “*A constrained Lagrange formulation of multi-link planar flexible manipulator*” (chapter 2) was only accepted. Therefore the contents of the other chapters (papers) might change according to the reviewers’ comments and will not necessarily be as they appeared here. The permission to include the accepted paper in chapter 2 has been sought from the publisher through email. The correspondence between the author and publisher is as follows:

Date: Tue, 22 Apr 2008 13:42:21 -0400
From: Beth Darchi <DarchiB@asme.org>
To: mov955@mail.usask.ca
Subject: Re: ASME PUBLICATIONS PERMISSION REQUEST FORM SUBMISSION
Part(s):  2 Error! Hyperlink reference not valid. text/html 10.39 KB 

*This message was written in a character set other than your own. If it is not displayed correctly, **Error! Hyperlink reference not valid.** to open it in a new window.*

Dear Mr. Vakil:

It is our pleasure to grant you permission to use ASME paper *A Constrained Lagrange Formulation of Multilink Planar Flexible Manipulator,* by M. Vakil, R. Fotouhi, P. N. Nikiforuk, H. Salmasi, Journal of Vibration and Acoustics, Vol. 130, 2008, cited in your letter for inclusion in your Doctorual Thesis entitled Dynamics and Control of Flexible manipulators to be published by University of Saskatchewan.

As is customary, we ask that you ensure full acknowledgment of this material, the author(s), and ASME as original publisher on all printed copies being distributed.

Many thanks for your interest in ASME publications.

Sincerely,

Beth Darchi
Permissions & Copyrights
ASME, 3 Park Avenue
New York, NY 10016
T: 212-591-7700
F: 212-591-7841
E: darchib@asme.org

Table of Content

Chapter 1. Introduction.....	1
1.1. Background.....	2
1.2. Problem statement.....	5
1.2.1. Under-actuation.....	6
1.2.2. Nonminimum phase feature.....	6
1.3. Research objectives.....	8
1.4. Synopsis of thesis.....	9
1.5. References:.....	16
Chapter 2. A constrained Lagrange formulation of multi-link planar flexible manipulator	19
2.1. Introduction.....	20
2.1.1. Literature review	20
2.1.2. FEA for dynamics, AMM for control	21
2.1.3. The proposed approach	22
2.1.4. Outline of the chapter.....	24
2.2. Dynamic equations of a single flexible link manipulator with a moving base (SFLMB).....	24
2.2.1. Derivation of the kinetic energy of a SFLMB	26
2.2.2. Potential energy of a SFLMB	31
2.3. Dynamics of a FLM using dynamics of a SFLMB and Lagrange multipliers..	33
2.4. Eliminating Lagrange multipliers from the dynamic equations	38
2.5. Simulation Results	40
2.5.1. Example one: One element per link, Bang-bang torque	42
2.5.2. Example two: 10 elements per link, Bang-bang torque.....	45
2.5.3. Example three: 10 elements per link, Rigid torque.....	49
2.6. Conclusions.....	53
2.7. Acknowledgment	54

2.8.	Nomenclature	54
2.9.	Appendices.....	58
2.10.	References.....	64
Chapter 3. Piece-wise causal inversion by output redefinition for a flexible link manipulator 69		
3.1.	Introduction.....	70
3.2.	Dynamic modeling of a SFLM	73
3.3.	End-effector inversion procedure	75
3.4.	Causal inversion by output redefinition.....	78
3.5.	Piece-wise trajectory inversion by output redefinition	82
3.6.	Selection of variables (m_{jk}, r) of the redefined output.....	85
3.7.	Simulation results.....	88
3.7.1.	Example 1: A SFLM with non-hyperbolic internal dynamics.....	88
3.7.2.	Example 2: A SFLM with near non-hyperbolic internal dynamics	93
3.7.3.	Example 3: A SFLM with hyperbolic internal dynamics	97
3.8.	Experimental results.....	102
3.8.1.	Example 4: End-effector trajectory tracking of an experimental SFLM	102
3.9.	Conclusions.....	108
3.10.	Nomenclature	109
3.11.	Appendices.....	113
3.12.	References.....	120
Chapter 4. End-effector trajectory tracking of a flexible link manipulator using integral manifold concept..... 125		
4.1.	Introduction.....	126
4.2.	Dynamic model derivation.....	128
4.3.	Singularly perturbed form and integral manifold concept.....	129

4.4.	Controller design.....	131
4.5.	Stability analysis	136
4.6.	Simulation results.....	139
4.7.	Experimental results.....	144
4.8.	Conclusions.....	148
4.9.	Nomenclature	149
4.10.	Appendix.....	151
4.11.	Reference	152
Chapter 5. End-effector trajectory tracking for a class of flexible link manipulators		155
5.1.	Introduction.....	157
5.2.	A class of FLM with a chain of rigid links and the flexible end-link.....	159
5.2.1.	Dynamic model of the CRFE.....	160
5.2.2.	Properties of the matrices in the dynamic model of the CRFE.....	162
5.2.3.	The control variable of the CRFE.....	164
5.3.	Singularly perturbed model of the CRFE and the integral manifold concept.	166
5.4.	Controller design.....	170
5.5.	Simulation results.....	177
5.6.	Experimental results.....	183
5.7.	Conclusions.....	191
5.8.	Nomenclature	192
5.9.	Appendix.....	196
5.10.	Reference	201
Chapter 6. Maneuver control of the multilink flexible manipulators.....		205
6.1.	Introduction.....	206

6.2.	Dynamic model of MLFM and the integral manifold concept	209
6.2.1.	Dynamic model of MLFM.....	209
6.2.2.	Singularly perturbed form and the integral manifold concept	210
6.3.	End-effector trajectory tracking.....	214
6.4.	Simulation Studies	222
6.5.	Conclusions.....	231
6.6.	Nomenclature	232
6.7.	Appendices.....	234
6.8.	References	241
Chapter 7.	Closing.....	244
7.1.	Summary and Conclusion	245
7.2.	Contributions of the research:	246
7.3.	Potential Future research.....	248

Chapter 1. Introduction

1.1. Background

Industrial robots are mechanical devices which can be programmed to perform different tasks [1]. The ease with which they can be programmed and the accuracy with which they can carry out repetitive tasks leads to their wide spread use in industry. Moreover, increasing labor costs, as well as the capability of executing tasks which are impossible, difficult, or dangerous to humans are other motives for the increased use of robots in manufacturing lines. The average yearly installation of robots in the United States between the years 2002 to 2004 was 10,000 units [2], which showed their great industrial application. One of the most important classes of industrial robots is that of manipulators. A manipulator is a robot that can accomplish different tasks. An example of an industrial manipulator which is available in the robotic laboratory of the University of Saskatchewan is shown in Fig. 1-1.

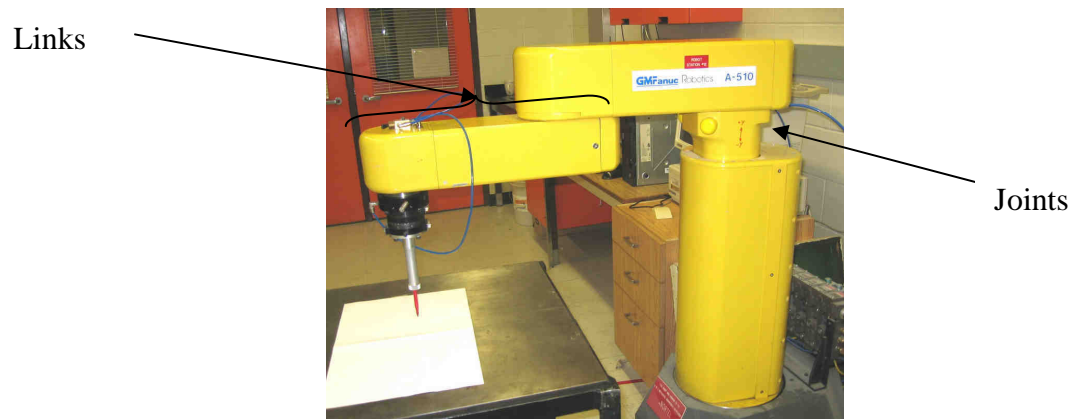


Fig. 1-1: Three-rigid-link manipulator in the robotic laboratory of the University of Saskatchewan

The point where two parts of a manipulator are connected is called a joint, while the part by itself is referred to as a link. As an example, in Fig. 1-1 a joint and a link of the manipulator are shown. The links of the manipulators can be manufactured from different types of materials and designed in various forms. However, based on the flexibility of the links of the manipulators, they fall into two main categories: rigid link manipulators and light weight, flexible, link manipulators.

If the links of a manipulator are designed so as to remain almost stiff during maneuvers, the manipulator is called a rigid link manipulator (RLM). Almost all the manipulators which are currently used in the manufacturing lines are RLM; that is, their flexibility can be neglected. Perhaps the simple dynamic modeling of the RLM which eases their controller design is one of the main reasons for their large industrial applications. However, RLM are heavy and massive, and their load-carrying capacity is limited to 5-10% of their weight [3]. Therefore, they are not easily transportable nor are they energy efficient. The considerable mass of RLMs, and consequently their energy consumption are of even more concern when RLMs are used in space applications. To reduce the mass of RLMs, the length of their links can be shortened or the cross section area of their links can be reduced. Shortening the length of the links results in a smaller workspace for the manipulator and is not practical. However, reducing the cross section area of links is feasible and does not reduce the workspace. The remedy of reducing the cross section area of links to decrease the mass of the RLM creates a new class of manipulators, usually referred to as light weight manipulators.

The links of light weight manipulators are slender since, at least one dimension of their cross section is relatively small compared to their length. Therefore, the links of light weight manipulators will vibrate and bend during and after a maneuver. The faster the maneuver, the greater will be their deflection and the more severe will be their vibration. It is because of this vibrating behavior that light weight flexible manipulators are usually referred to as flexible link manipulators (FLM). Moreover, these vibrations limit the performance of FLM compared to that of RLM. A flexible two-link manipulator, which is available at the robotic laboratory of the University of Saskatchewan, is shown in Fig. 1-2.

Provided that the performance of FLMs is predictable and reliable, they can be promising substitutes for RLMs since they are compact, light and energy efficient. The performance of FLMs can be improved through the design of proper controllers. Although many controllers have been developed for the RLM and have been experimentally verified, the application of these controllers to FLM does not lead to satisfactory performance. This is due to flexibility of the links of FLM which do not exist for RLM, thus, in their controller design, this flexibility is not considered. For example,

vibration suppression is not of a concern in the controller design of RLMs whereas it is one of the main concerns that should be addressed in the controller design of FLMs. The link flexibility makes the dynamic model of a FLM much more complicated than that of a RLM and increases the numbers of the degrees-of-freedom of the FLM. This complicated dynamic model thus creates several challenges in the design and implementation of model-based controllers for FLM.

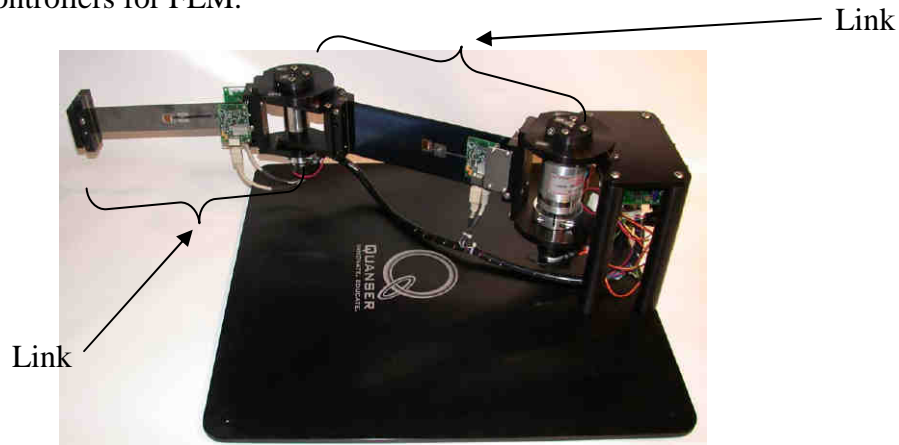


Fig. 1-2: Flexible two-link manipulator at the robotic laboratory of the University of Saskatchewan

While researchers have done much during the past few decades [4,5], much more has to be done before FLM can be widely used. Because of link flexibility, the governing dynamic equations for multilink flexible manipulators are nonlinear partial differential equations (PDE) [6]. Therefore, theoretically, the numbers of the degrees-of-freedom for a FLM is infinite, whereas the numbers of the degrees-of-freedom for a RLM is finite. Finding an exact solution for the governing PDE of a FLM for a given input torque is very difficult, if not impossible. Thus, to solve these nonlinear PDE, approximate methods like the finite element method [7] have to be adopted to change the PDE into ordinary differential equations (ODE). The resulting ODE can then be solved using the strategies like Newark Newton-Raphson technique. The transformation of the PDE of flexible link manipulators into ODE is also critical from the controller design view point, since almost all the developed controllers in the published works are studies for the ODE and not PDE [4]. The complex nature of the governing ODE of FLM still requires considerable effort for the controller design and increases the computational cost of the controller. Finally, since the numbers of the degrees-of-freedom for the FLM are much

larger than that for their rigid link counterparts, the required numbers of sensors for the implementation of controllers are considerably larger.

1.2. Problem statement

In most industrial applications, such as painting or welding, the end-effector of a robot has to move along a desired path with a specified speed, which is referred to as end-effector trajectory tracking (EETT). In this type of application, for example, for the flexible two-link manipulator shown in Fig. 1-3, with the desired path (DP) and a given velocity profile, the end-effector (EE) has to move along the DP with the assigned velocity to accomplish the EETT. For the EETT, the actuators apply the control torque (or force) according to the end-effector feedback of position and velocity, so that the tracking error becomes as close as possible to zero. From Fig. 1-3, it is clear that the control of the links' rotation angles, θ_1 and θ_2 , does not lead to the EETT. This is due to the fact that not only θ_1 and θ_2 , but also the links' deflections, ξ_1 and ξ_2 , contribute to the exact location of the end-effector.

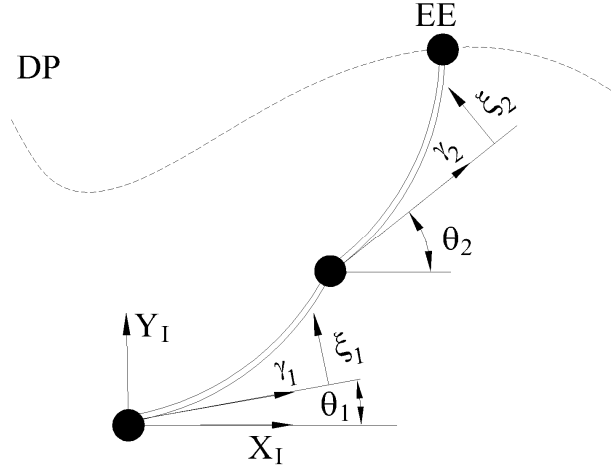


Fig. 1-3: Schematic of a flexible two-link manipulator

The links' flexibility of the FLM creates difficulties for the EETT, which are the under-actuation feature and nonminimum phase characteristics that are discussed in detail below.

1.2.1. Under-actuation

The under-actuation feature is due to the fewer number of actuators for FLM compared to their numbers of degrees-of-freedom [8]. As already explained, theoretically FLM have infinite numbers of the degrees-of-freedom, while the number of actuators is finite. Even after changing the governing PDE into ODE by using an approximate method, such as finite element method, the under-actuation feature still exists. As an example, the flexible two-link manipulator shown in Fig. 1-3 has two actuators to move the first and second links. However, the degrees-of-freedom are the links' rotation angles, θ_1 and θ_2 , and the degrees-of-freedom to describe the lateral deflection of the flexible links, ξ_1 and ξ_2 . Therefore, the numbers of the degrees-of-freedom will be more than two, which is the number of actuators. It is worth recalling that the governing equations of the FLM are dynamically coupled. That is, there are constraints which relate the degrees-of-freedom. These constraints are non-holonomic; which means they are differential equations that can not be transferred into a complete differential form. In other words, these constraints can not be obtained by differentiation from an algebraic equation.

1.2.2. Nonminimum phase feature

The nonminimum phase feature can be considered as the side effect of the under-actuation of the FLM. In fact, the non-holonomic constraints that exist due the underaction of the FLM have an unbounded response during the causal end-effector dynamic inversion and, thus, the calculated torque is not acceptable. From the mathematical point of view, the unbounded torque which is obtained in the end-effector inversion of FLM is due to the unstable internal dynamics⁵ of the FLM. Therefore, the nonminimum phase feature of FLM is equal to the instability of their internal dynamic. The flexibility of the links and noncollocation of the sensor and actuators are the reasons for the nonminimum phase characteristic of FLM [10, 11]. The noncollocation of the sensor and actuators means that the actuators, which apply the torques, are located on the

⁵ The part of the system which is rendered unobservable during the input-output linearization is called internal dynamics [9]. For FLM internal dynamic can be considered as a representation of the non-holonomic constraints.

joints, while the measurement of the end-effector displacement occurs at the end of the last link, which is not the same as the location of the actuators. For example, for the single flexible link manipulator (SFLM) shown in Fig. 1-4, the torque τ is applied at the base while the measurement of the end-effector displacement is on the other end of the link.

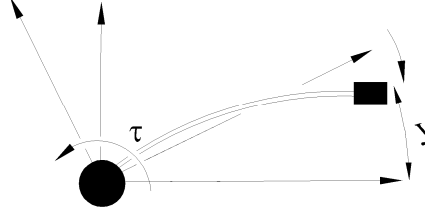


Fig. 1-4: Schematic of the movement of the end-effector of a SFLM upon applying a torque

The initial movement of the end-effector in the opposite direction of the applied base torque, as shown in Fig. 1-4 for a SFLM, is the consequence of the nonminimum phase characteristic. For a stable linear system, the nonminimum property means that the corresponding transfer function in the S-plane has right-hand-side zeros. For example, for a SFLM which is modeled linearly, let the transfer function $F(s)$ between the end-effector displacement, y , and applied torque, τ , be:

$$F(s) = \frac{y(s)}{\tau(s)} = \frac{p(s)}{q(s)} \quad (1-1)$$

Then, some roots of numerator $p(s) = 0$ are located on the right-hand-side of the S-plane. In Fig. 1-5, the schematic of the locations of the two sets of zeros for a SFLM, namely $(-s_1, s_1)$ and $(-s_2, s_2)$, are shown. The right-hand-side zeros in Fig. 1-5 are s_1 and s_2 . The zeros of a SFLM are always conjugate as is clear from Fig. 1-5, which is also proven in [10, 11, 12].

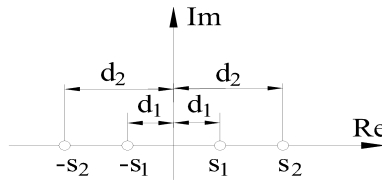


Fig. 1-5: Schematic of the two sets of zeros for a SFLM

1.3. Research objectives

The research that is described in this thesis was undertaken to further pave the ground of industrial implementation of the FLM. Due to the importance of the EETT, as explained in Section 1.2, developing a controller to reduce the EETT error, as small as possible, is of vital importance if the FLM is to be used in manufacturing. Thus, in this research, model-based controllers for the EETT of FLM have been developed. Because of the model-based nature of the study, deriving the dynamic model of the FLM was the first step that had to be taken; then, based on the derived dynamic model, the EETT controllers were developed. Finally, the effectiveness of the proposed controllers was verified by experimental studies. Therefore, the objectives of this research fell into the two main categories:

1- *Developing the dynamic model of FLM; and*

2- *Developing controllers for the EETT of FLM and their experimental verifications.*

To accomplish objective 2, the following sub-objectives were defined and achieved:

2-1- Approximate end-effector inversion of a SFLM and experimental verification;

2-2-Model-based EETT of a SFLM using the integral manifold concept and experimental verification;

2-3- Model-based EETT of a class of FLM which is composed of a chain of rigid links with the flexible end-link and experimental verification by using the integral manifold concept; and

2-4- Model-based EETT of the multilink flexible manipulator using the integral manifold concept. .

Remark: Because of the manuscript nature of this thesis, figures as well as references might be repeated several times in the thesis.

1.4. Synopsis of thesis

The chapters of this thesis have been arranged in order to cover the objectives explained above. That is, the dynamic model of the FLM is first derived and then it is used to develop different controllers. Therefore, in Chapter 2 the dynamic model of FLM is obtained and verified. In Chapter 3 a new controller for the EETT of a single flexible link manipulator (SFLM) is introduced which combines the joint proportional-derivative (PD) controller with the approximate end-effector inverse dynamic torque. The feasibility of the introduced controller in Chapter 3 was shown by experimental study. In Chapter 4 a new controller for the EETT of a SFLM based on the concept of the integral manifold of the singularly perturbed differential equations [13] was proposed and experimentally verified. In Chapter 5, the developed EETT controller of Chapter 4, which was for a SFLM with linear dynamics, was extended to a class of nonlinear FLM. This class of FLM was composed of a chain of rigid links with a flexible end-link. The introduced controller in Chapter 5 was experimentally verified. Finally, in Chapter 6, the EETT controller proposed earlier in Chapter 5, which was based on the concept of the integral manifold of the singularly perturbed differential equations, was extended to the multi-link flexible manipulators. The summaries of each chapter are as follows.

Chapter 2:

The content of chapter 2 was published in the ASME Journal of Vibration and Acoustics under the title of “A constrained Lagrange formulation of multi-link planar flexible manipulator” [14]. In this chapter, the closed form dynamic equation of a FLM which can be used in the design of a model-based EETT controller was developed. The proposed approach in this chapter combined the assumed mode (shape) method, to model flexibility of the links, with Lagrange equations. In the assumed mode method the lateral deflections of the links were represented by the summation of a number of predefined spatial functions which were multiplied by time varying weight functions [15]. That is $\xi_i, i = 1, 2$ in Fig. 1-3, were:

$$\xi_i = \sum_{j=1}^n \phi_{ij}(\gamma_i) \lambda_{ij}(t) \quad (1-2)$$

where $\phi_{ij}(x)$ was the assumed j th mode shape for the i th link's lateral deflection, $\lambda_{ij}(t)$ was its time varying weight function, called flexible variables, and n was the number of assumed modes used to model the flexibility. However, combining the assumed mode method with the Lagrange equations had the drawbacks of complicated and lengthy Lagrangian function calculations and derivative evaluations. To alleviate this drawback, in Chapter 2 a new method was introduced that evaluated the Lagrangian function and the required derivatives only once for a single flexible link manipulator on a moving base, which were not lengthy or complex. Then, using the dynamic model of a single flexible link manipulator on a moving base, the dynamic equation of a FLM was obtained without any further derivative calculations or Lagrangian function evaluations. It is worth emphasizing that the proposed method here was computationally cost effective and less prone to error compared to the available methods which combined the assumed mode method with the Lagrange equations.

The method was employed to derive a dynamic model of the flexible two-link manipulator which is schematically shown in Fig. 1-3. For verification, the results of the dynamic analysis from the dynamic model, obtained after adopting the method proposed in Chapter 2, were compared with those found using full nonlinear finite element analysis. In the verification examples, a bang-bang torque and the torque from the rigid manipulator were applied to a flexible two-link manipulator. For these examples, the joint rotations, end-effector path, components of the end-effector velocity, and deviation index from the model and the full nonlinear finite element analysis were compared so as to check the accuracy of the developed model. These comparisons showed sound agreement.

The dynamic model derived in Chapter 2, was used in Chapters 3, 4, 5 and 6 to develop EETT controllers.

Chapter 3:

The content of this chapter has been submitted for possible publication in the CSME transactions under the title of "Piece-wise causal inversion by output redefinition for a flexible link manipulator" [16]. In this chapter, a new EETT controller for a SFLM

was introduced and its effectiveness and feasibility investigated through the simulation and experimental studies. The new controller in [16] added the off-line torque obtained from the end-effector inversion to the on-line state feedback controller which was a joint PD controller, as shown in the figure below.

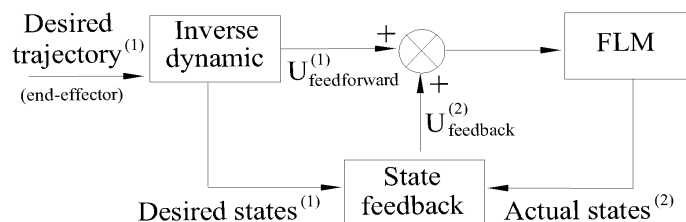


Fig. 1-6: Schematic of the end-effector trajectory tracking method, 1: off-line signal, 2: on-line signal

The novelty of this method was in introducing a new technique for the end-effector inversion. The new end-effector inversion method redefined the end-effector trajectory so that causal stable end-effector inversion could be achieved. For this purpose, the internal dynamics of a SFLM was first obtained. It was shown that the states of the internal dynamics were the variables used to describe the lateral deflection of the link, $\lambda_{1j}, j = 1 \dots n$ in Eq. (1-2), and their time derivatives, $\dot{\lambda}_{1j}, j = 1 \dots n$. Then the desired end-effector trajectory was redefined so that the bounded values for the states of the internal dynamic could be obtained. For the redefinition of the end-effector trajectory, the summations of stable exponential functions were used, that is:

$$\tilde{y}_d(t) = \sum_{j=0}^r c_j e^{m_j t}, \quad m_j < 0 \quad (1-3)$$

where $\tilde{y}_d(t)$ is the redefined end-effector trajectory (the desired end-effector trajectory was $y_d(t)$) and c_j are constants which were calculated, after the selection of the r and m_j , so that a bounded continuous torque could be obtained. An example which was provided in Chapter 3 clarified the main concept of the approach.

To achieve the EETT, the torque derived based on the new end-effector inversion method had to be combined with a state-feedback controller, as shown in Fig. 1-6. It is worth mentioning that the addition of the inverse dynamic torque to the state feedback

controller made the proposed method a closed-loop controller. For this purpose, the joint proportional-derivative (PD) controller, a state feedback, was added to the inverse dynamic torque. The stability of the proposed end-effector controller was proven using the Lyapunov criterion. Simulation studies carried on SFLMs showed the effectiveness of the new method. The experimental verification conducted on the SFLM, available at the robotic laboratory of the University of Saskatchewan, proved the feasibility of this approach.

Although new end-effector inversion was studied in Chapter 3 for a SFLM, it can be easily extended for the output inversion and thus for the output tracking of any linear single-input single-output nonminimum phase system. Moreover, this method can be used for the end-effector inversion of a single flexible link manipulator with nonzero initial conditions [17].

The main limitation of the proposed method was its applicability to a linear dynamic model. Thus it could only be used for the EETT of a SFLM and could not be extended to the EETT of multilink FLM with a nonlinear dynamic model. Since EETT for multilink FLM, with nonlinear model, was the goal of the candidate's research, another controller, which work even for nonlinear systems, had to be developed. This new controller was introduced in Chapter 4, 5 and 6.

Chapter 4:

The content of this chapter has been submitted for the possible publication in the International Journal of Robotics and Automation under the title of "End-effector trajectory tracking of a flexible link manipulator using integral manifold concept" [18]. In this chapter a new end-effector controller for a linear model of a SFLM was introduced and experimentally verified. The new method was based on the singularly perturbed model of the manipulator.

A singularly perturbed system is a system in which derivatives of some states are multiplied by a small parameter, ε . The following is an example of a singularly perturbed system in which the derivative of state z is multiplied by the small parameter ε :

$$\begin{cases} \dot{x} = f(x, z, u, \varepsilon) & (1-4a) \\ \varepsilon \dot{z} = g(x, z, u, \varepsilon) & (1-4b) \end{cases}$$

In Eqs. (1-4), x and z are the states of the system and u is the input. One of the main features of the system in Eq. (1-4) is that the dynamic of the state z is relatively faster than that of the state x . That is why z in Eq. (1-4) is called the state of the fast subsystem, while x is the state of the slow subsystem. The dynamic response of FLM, in general, has slow rigid body link rotations (slow subsystem) and relatively fast links' vibration (fast subsystem). Therefore, the dynamic model of FLM can be expressed in the singularly perturbed form, as in Eq. (1-4). Consequently, the possibility of using the concepts and control strategies developed for the singularly perturbed systems can be explored for the EETT of the FLM [13].

In Chapter 4, the concept of the integral manifold of the singularly perturbed differential equations was used to develop a new EETT controller for a SFLM with a linear model. Based on this concept it was possible to find an approximate solution for z from Eq. (1-4b) in terms of x and u . For a SFLM it meant that the lateral deflection of the link could be expressed in terms of the link's rotation and input torque, details of which are available in Chapter 4. Therefore, the end-effector displacement that was described by the link's rotation and lateral deflection could be described only in terms of the link's rotation and input torque. Finally, since the number of link's rotation and input torque were the same, the under-actuated SFLM appeared to change to an approximate fully-actuated system and its EETT could be accomplished.

Almost always the implementation of the controller developed for the FLM required the links' lateral deflections and their time derivative. Although measuring the links' lateral deflections was possible, for example by strain gauges, the measurements of the time derivatives of the links' lateral deflections were hardly practical. One of the valuable features of the controller introduced in Chapter 4 was that its implementation did not require the measurement of the time derivative of the single link's lateral deflection. This was achieved by an observer designed to estimate the time derivative of the link's lateral deflection.

The stability of the new proposed controller was proven using the Lyapunov criterion. Simulation studies showed the superiority of this new controller in the reduction of the EETT error. The experimental verification of the new controller which was conducted on a SFLM available at the robotic laboratory of the University of Saskatchewan showed the feasibility of the method. The limitation of the proposed method is its applicability to only linear systems.

Chapter 5:

The content of chapter 5 has been submitted for possible publication in Journal of Vibration and Control under the title of “End-effector trajectory tracking for a class of flexible link manipulator” [19]. In this chapter the EETT controller developed in Chapter 4, which was based on a linear dynamic model of a SFLM, was successfully extended to a class of flexible link manipulator. This class was composed of a chain of rigid links with the flexible end-link (CRFE), which had nonlinear dynamic model. A schematic of a member of a CRFE with the first link rigid and second link flexible is shown in Fig. 1-7. Therefore, the concept of the integral manifold of the singularly perturbed differential equations was successfully used to reduce the EETT error of the CRFE.

To investigate the possibility of implementing the controller introduced in [18], which was for a SFLM with linear dynamics, for the EETT of the multilink FLM with nonlinear dynamic model, first its extension to the CRFE was studied in Chapter 5. This was due to the fact that the CRFE had a simpler dynamic model than the multilink flexible manipulator. The successful extension of the method developed in [18] for the EETT of the partially flexible nonlinear system, CREF, increased the possibility of its application to a full flexible nonlinear multilink manipulator. The implementation of the introduced controller, similar to that developed in Chapter 4, did not require the measurement of the time derivative of the link’s lateral deflection. This feature made the implementation of the controller feasible. The time derivative of the link’s lateral deflection was estimated by using an observer which was designed based on the gain-scheduling technique, detail of gain-scheduling can be found in [20].

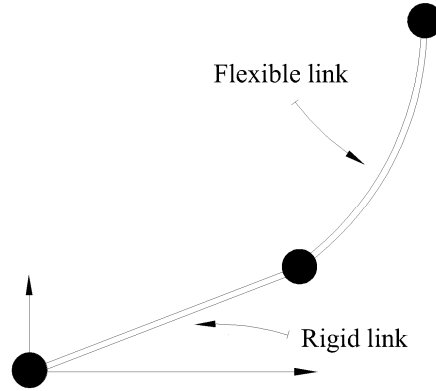


Fig. 1-7: Schematic of a two link manipulator with first link rigid and second link flexible

The stability of the proposed controller was proven using the Lyapunov criterion. Simulation studies were performed on the manipulator shown in Fig. 1-7. Experimental verification was conducted on the manipulator, shown in Fig. 1-8, with the first link rigid and second link flexible, a configuration called rigid shoulder-link flexible elbow-link manipulator. The limitation of the proposed method in chapter 5 was that it could only be used for the EETT of CREF, and could not be used for the EETT of multilink flexible manipulators.



Fig. 1-8: Rigid shoulder-link flexible elbow-link manipulator available at the robotic laboratory of the University of the Saskatchewan

Chapter 6:

The content of chapter 6 has been submitted for possible publication in the International Journal of Non-linear Mechanics under the title of “End-effector maneuver control of the multilink flexible manipulators” [21]. In this chapter, the EETT controller which was studied, developed and experimentally verified in Chapters 4 and 5 for SFLM

and CREF, respectively, was successfully extended to the EETT of multilink flexible manipulators with full nonlinear dynamic models. That is, the concept of the integral manifold of the singularly perturbed differential equations was successfully employed to reduce the EETT error of the multilink flexible manipulators.

Similar to Chapters 4 and 5, the implementation of the controller did not require the measurement of the time derivatives of the links' lateral deflections, making this feature practical. The stability of the new controller was proven using the Lyapunov criterion. The simulation results for the EETT of a two-link flexible manipulator, shown in Fig. 1-3, proved the effectiveness of the new controller in reducing the EETT error.

Chapter 7:

In this chapter the summary and conclusionsof the thesis are presented. The contributions of the research are discussed. The directions for the future research study are also provided in this chapter.

1.5. References:

1. J. J. Craig, "Introduction to Robotics; Mechanics and Control", Pearson Education, NJ, USA, 2005.
2. The International Federation of Robotics, and the United Nations, "World Robotics 2001," Statistics, Market Analysis, Forecasts, Case Studies and Profitability of Robot Investment, 2001.
3. A. R. Fraser and R. W. Daniel, "Perturbation Techniques for Flexible Manipulators", Kluwer Academic Publishers, Boston, USA, 1991.
4. F. Y. Wang and Y. Gao, "Advanced Studies of Flexible Robotic Manipulators: Modeling, Design, Control and Application: Series in Intelligent Control and Intelligent Automation", Word Scientific, New York, USA, 2003.
5. M. Moallem, R.V. Patel and K. Khorasani, "Flexible-Link Robot Manipulators: Control Techniques and Structural Design", Springer-Verlag, London, 2000.

6. X. Zhang, W. Xu, S. S. Nair and V. Cellabonia, “ PDE Modeling and Control of a Flexible Two-link Manipulator”, IEEE Transactions on Control System Technology, 13 (2), pp. 301-312.
7. K. J. Bathe, “Finite Element Procedures”, Prentice Hall, New Jersey, USA, 1996.
8. A. De Luca, S. Iannitti, R. Mattone and G. Oriolo, “ Control Problems in Underactuated manipulators”, IEEE/ASME International Conference on Advanced Intelligent Mechatronics, 2, 855-861, 2001.
9. J. J. Slotine and W. Li, “Applied Nonlinear Control”, Prentice Hall, NJ, USA, 1991.
10. J. H. Park and H. Asada, “Dynamic Analysis of Noncollocated Flexible Arms and Design of Torque Transmission Mechanisms”, Journal of Dynamic Systems, Measurement and Control, 116(2), 201-207, 1994 .
11. V. A. Spector and H. Flashner, “Modeling and Design Implications of Noncollocated Control in Flexible Systems”, Journal of Dynamic Systems, Measurement and Control, 112(2), 186-193, 1990.
12. M. Vakil, R. Fotouhi and P. N. Nikiforuk , “On the Zeros of the Transfer Function of a Single Flexible Link Manipulator”, 17th IASTED International Conference on Modeling and Simulation, Montreal, Quebec, Canada, 20-25, 2006.
13. P. V. Kokotovic, H. K. Khalil, and J. O'Reilly, “Singular Perturbation Methods in Control: Analysis and Design”, Academic, New York, 1999.
14. M. Vakil, R. Fotouhi, P. N. Nikiforuk and H. Salmasi, “A Constrained Lagrange Formulation of Multi-link Planar Flexible Manipulator”, ASME Journal of Vibration and Acoustics, 130 (3), 031007 (1-16), 2008.
15. W. J. Book, “Recursive Lagrangian Dynamics of Flexible Manipulator Arms”, International Journal of Robotics Research, 3(3), 1984.
16. M. Vakil , Fotouhi R., Nikiforuk P. N., “Piece-Wise Causal Inversion by Output Redefinition for a Flexible Link Manipulator”, CSME Transactions, submitted, 2008.
17. M. Vakil , R. Fotouhi and P. N. Nikiforuk, “End-effector Trajectory Inversion of a Single Flexible Link Manipulator with Non-zero Initial States”, 16th IASTED

International Conference on Applied Simulation and Modeling, Palma de Mallorca, Spain, 485-490, 2007.

18. M. Vakil, Fotouhi R., Nikiforuk P. N., “End-effector trajectory tracking of a flexible link manipulator using integral manifold concept”, International Journal of Robotics and Automation, submitted, 2008.

19. M. Vakil, Fotouhi R., Nikiforuk P. N., “End-effector trajectory tracking for a class of flexible link manipulators”, Journal of Vibration and Control, submitted, 2008.

20. S. M. Shahruz and B. Behtash, “Design of Controller for Linear Parameter-Varying System by Gain Scheduling Technique”, Journal of Mathematical Analysis and Application, 168, 195-217, 1992.

21. M. Vakil , Fotouhi R., Nikiforuk P. N., “End-effector maneuver control of the multilink flexible manipulators”, International Journal of Non-linear mechanics, submitted, 2008.

Chapter 2. A constrained Lagrange formulation of multi-link planar flexible manipulator

Abstract:

In this chapter, the closed form dynamic equations of planar flexible link manipulators (FLM), with revolute joints and constant cross sections, are derived combining the Lagrange's equations and the assumed mode shape method. To overcome the lengthy and complicated derivative calculation of the Lagrangian function of a FLM, these computations are done only once for a single flexible link manipulator with a moving base (SFLMB). Employing the Lagrange multipliers and the dynamic equations of the SFLMB, the equations of motion of the FLM are derived in terms of the dependent generalized coordinates. To obtain the closed form dynamic equations of the FLM in terms of the independent generalized coordinates, the natural orthogonal complement of the Jacobian constraint matrix, which is associated with the velocity constraints in the linear homogeneous form, is used. To verify the proposed closed form dynamic model, the simulation results obtained from the model were compared with the results of the full nonlinear finite element analysis. These comparisons showed sound agreement. One of the main advantages of this approach is that the derived dynamic model can be used for the model based end-effector control and the vibration suppression of planar flexible link manipulators.

Keywords: Flexible link manipulators, dynamics, Lagrange multipliers

2.1. Introduction

The derivation of a dynamic model for a flexible link manipulator (FLM) which captures the effects of the link's flexibility is the first step in model based research. To apply the control strategies developed for a finite order system to a FLM [1], the partial integro-differential equations (PDE) of a FLM [2,3] have to be changed into ordinary differential equations (ODE).

2.1.1. Literature review

An effective technique for converting the governing PDE of a FLM [2,3] into an ODE is to employ finite element analysis (FEA) [4] as was done in [5-10,46]. In [5] the dynamic equations, as well as the natural frequencies of a single flexible link manipulator

(SFLM) rotating with a constant angular velocity were discussed. It was shown in [5] that by increasing the angular velocity, the natural frequencies of the rotating SFLM increase due to the centrifugal force and consequently stress stiffening effect. In [6] a linear shape function was employed to derive the dynamic model of a planar FLM. In [7] using cubic or Hermitian shape functions, the dynamic model of a planar FLM was derived. In [8,9] the dynamic equations of a rotating SFLM were first obtained and then a piezoelectric actuator was used to suppress the vibration. In [10] the dynamic equations of several flexible link mechanisms considering complete geometrical nonlinearity [11 p. 338] were derived.

Another method of changing the PDE of a FLM into an ODE is to use the assumed mode shape method (AMM) [12 Section 7.6]. This approach was used in [13-17]. The concept of using the AMM to derive the dynamic model of a FLM was explored in [13]. In [14] the details of the dynamic equations of a planar flexible two-link manipulator using the first two mode shapes of a clamped-free beam per link were given. In [15], the dynamic equations of a planar FLM were obtained and the results were compared with the results of experimental studies. In [16] the linearization technique and the dynamics of rigid link manipulators were combined to model the dynamics of a planar FLM. In [17] the model of a SFLM was derived and used to experimentally suppress the vibration employing piezoelectric actuators.

2.1.2. FEA for dynamics, AMM for control

FEA is usually used to obtain the static and dynamic response of a system to known forces. However, the AMM is used not only to obtain the dynamic response of the system, but also to control unwanted vibration and end-effector. Compared to FEA, the drawbacks of the AMM are (1) - the mode shapes employed in the AMM are an approximation of the real mode shapes of the system (2) - the nonlinear terms in the strain energy which lead to effects such as stress stiffening can not be addressed properly and (3) - the AMM does not lead to realistic approximation for the dynamic model of a FLM with a varying cross section such as a tapered beam. These drawbacks are the source of errors in the use of the AMM for modeling a FLM. Therefore, the FEA provides a more precise dynamic model for a FLM than the AMM [18]. However, the

FEA not only requires more complicated modeling and calculation but it also needs considerable more computational time than the AMM. It is to be noted that among the main motivations for using the AMM over FEA, is to have a closed form dynamics of a FLM to design computationally fast controllers. This is a critical requirement, to have states of the system available with essentially small delay [19]. As a comparison the simulation of example 2 given in Section 2.5 took 7 (sec) using the AMM but 170 (sec) employing the FEA⁶. Moreover, fewer degrees of freedom, which means fewer sensors and measurements, is another motivation for utilizing the AMM instead of FEA for controller development and experimental verification. Many controllers which have used dynamics based on the AMM for the FLM with constant cross sections were experimentally verified [20-23]. Moreover, for a practical difference between AMM modeling and the use of real apparatus, robust control techniques [24,25] can compensate for drawbacks (1) and (2) above. Thus, for preliminary studies on the design of a controller, it is reasonable to start with AMM which is a model that is less complicated than the one obtained using FEA.

2.1.3. The proposed approach

In this chapter a combination of the AMM and the Lagrange's equations is used to derive the dynamic model of a FLM with revolute joints and constant cross sections. However, in adopting the Lagrangian approach for the dynamic model derivation, after the evaluation of the Lagrangian function, $\mathcal{L} = T_{FM} - U_{FM}$, a set of derivative calculations have to be carried out [26, 27]. For a FLM considering the AMM for the modeling of the flexibility, as the number of links increases, the calculation of the Lagrangian function and evaluation of the derivatives becomes more lengthy and complicated and thus more prone to error [14,16]. Previous attempts to alleviate this problem employed computer programming for symbolic simplification [28] or reduced computation [29], but the evaluation of the Lagrangian and/or calculation of the derivatives still required considerable effort. In this chapter the problem is overcome as follows.

⁶ To solve the governing equations in the AMM model, the fourth-order Runge-Kutta with a sampling time of 0.0008 (sec) was used. The solver of the FEA was the Newmark method with the full Newton-Raphson technique for updating matrices with the same sampling time of 0.0008 (sec).

The Lagrangian function calculation and derivative evaluation are computed just once for a single flexible link manipulator with a moving base (SFLMB) and with a constant cross section. Then, using the dynamic equations of a SFLMB, and defining a set of dependent generalized coordinates, the dynamic equations of the FLM are derived. In this approach there is no need to calculate the lengthy derivatives of the Lagrangian function of the FLM. However, since the manipulator kinematics are based on the dependent coordinates⁷, the forces associated with the constraint conditions will enter the Lagrange's equations; that is, the constraint forces are considered as a part of the generalized forces. This issue is addressed by the use of the Lagrange multipliers ([26] Section 7.1, [27] Section 6.7). To express the dynamic equations in terms of the independent coordinates and also to eliminate the Lagrange multipliers, the orthogonal complement of the Jacobian constraint matrix, the matrix associated with the velocity constraints in the linear homogeneous form, is used. Since the orthogonal complement of the Jacobian constraint matrix is obtained naturally from the velocity constraint equations, without any complex computations, it is referred to as a natural orthogonal complement (NOC) [30, 31]. Therefore the closed-form dynamic model of the planar FLM with revolute joints and constant cross section is derived in terms of the independent coordinates. The validity of the proposed approach was checked by a fully nonlinear finite element analysis (FEA) [32]. It is essential that the results of the full nonlinear FEA must be reliable; that is they must be close to the experimental results. Therefore, the verification of the derived dynamic model with the full nonlinear FEA implies close agreement between the results of the model introduced here with the experiment. It is worth noting that the dynamic model derived here was used in the design of our proposed model based controllers for the end-effector trajectory tracking and vibration suppression and was experimentally verified for a SFLM [33, 34].

⁷ For simplicity in the rest of this chapter, the term “coordinate” refers to the “generalized coordinate”. (The generalized coordinates of a system are the geometrical quantities that by knowing them it is possible to draw a diagram of the system. The minimum number of generalized coordinates required to specify the position of a system is *the number of degree of freedom* (DOF) of that system [26].)

2.1.4. Outline of the chapter

In Section 2.2, the mass and stiffness matrices, the matrix representing the Coriolis and centrifugal forces and the gravity matrix for a SFLMB are presented. In Section 2.3, introducing the Lagrange multipliers, the dynamic equations of a FLM are derived. In Section 2.4, using the NOC method, the Lagrange multipliers are eliminated from the dynamic equations of a FLM and the closed form dynamic equations in terms of the independent coordinates are proposed. In Section 2.5 the simulation results for a flexible two-link manipulator are presented. For verification purposes, the results explained in detail in Section 2.5 obtained from the simulation of the proposed dynamic model, are compared with those obtained employing full nonlinear FEA. Finally, in Section 2.6 conclusions of the research are presented.

2.2. Dynamic equations of a single flexible link manipulator with a moving base (SFLMB)

A SFLMB with a constant cross section, as shown in Fig. 2-1, is considered for the dynamic model derivation. The flexible link is modeled as an Euler-Bernouli beam. Therefore, deformations due to shear and rotary inertia are neglected [35]. The (X_I, Y_I) and (x, ξ) , shown in Fig. 2-1, are the inertial and moving coordinate frames, respectively. The (x, ξ) coordinate frame, attached to the link, has base translation (X_o, Y_o) and rotation (θ) . The mass and the mass moment of inertia at the tip of this link represent the motor which moves the next link. For the last link, the mass and the mass moment of inertia at the tip represent the end-effector. To consider the hub of the first link, an additional mass moment of inertia is added to the base of the SFLMB shown in Fig. 2-1. A schematic of the first link is shown in Fig. 2-2. In this way all the links, mass and mass moment of inertia of the motors and end-effector are taken into consideration. Since the first link of a FLM is attached to the ground, the (x, ξ) coordinate frame attached to the first link can only rotate.

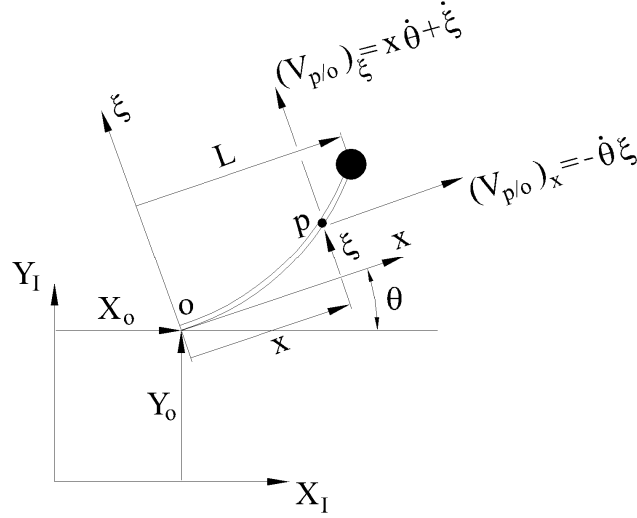


Fig. 2-1: Schematic of a SFLMB with a moving base

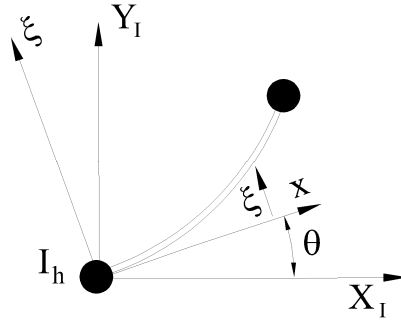


Fig. 2-2: Schematic of the first link of a FLM

According to the AMM the lateral deflection of the link, $\xi(x, t)$ in Fig. 2-1 (or Fig. 2-2), is

$$\xi(x, t) = \sum_{i=1}^n \lambda_i(t) \phi_i(x) \quad (2-1)$$

where $\phi_i(x)$ is the i th spatial assumed mode shape, out of n mode shapes and $\lambda_i(t)$ is its time varying weight function. The closer the selected mode shapes, $\phi_i(x)$, are to the exact real mode shapes of the system, the more accurate will be the approximation proposed in Eq. (2-1). The approximation of the mode shapes is a source of error for AMM. The other source of error is the truncation on the number of mode shapes, n . Increasing this number usually improves the approximation given in Eq. (2-1) at the expense of computational time. However, in the case of a real system and in the presence of the internal material

damping, which is usually modeled proportional to the stiffness matrix [36], the higher modes of vibration will be damped out more quickly than the first few modes. Therefore, only the first few modes of vibration mainly contribute to the dynamic response. It is clear then, that since the method introduced in this chapter is based on the AMM, it has the same source of error as the AMM, as explained above, and will not introduce extra error to the system.

To derive the dynamic equations of a SFLMB, a combination of the Hamiltonian principle and the AMM is used. Since the number of required independent coordinates to define kinematically the SFLMB shown in Fig. 2-1, $q = [X_o, Y_o, \theta, \lambda_1, \dots, \lambda_n]$, is finite, it has been proven ([26] Section 6.5) that to satisfy the Hamiltonian principle, each independent generalized coordinate has to satisfy the following Lagrange's equation⁸

$$\frac{d}{dt} \left(\frac{\partial T_{SM}}{\partial \dot{q}} \right) - \frac{\partial T_{SM}}{\partial q} + \frac{\partial U_{SM}}{\partial q} = Q_{SM} \quad (2-2)$$

where, T_{SM} is the kinetic energy of the SFLMB, U_{SM} is the potential energy of the SFLMB and Q_{SM} is the generalized force vector corresponding to q .

2.2.1. Derivation of the kinetic energy of a SFLMB

The kinetic energy of the SFLMB shown in Fig. 2-1, T_{SM} , is composed of the kinetic energy of the flexible link, T_l , and the kinetic energy of the tip mass, T_{tip} . The kinetic energy of the link and the corresponding terms after its differentiation are first derived. Then, the effect of the tip mass is added.

The kinetic energy of the link of a SFLMB

The kinetic energy of the link, T_l , ignoring the rotational kinetic energy (based on the Euler- Bernoulli beam assumption) is

$$T_l = \frac{1}{2} \int (V_p \cdot V_p) dm \quad (2-3)$$

⁸ The Lagrange's equation, Eq. (2), must be satisfied for every single component of the vector q .

where V_p is the velocity of an arbitrary point p on the link as shown in Fig. 2-1 and “ \cdot ” is the dot product. V_p can be expressed as $V_p = V_o + V_{p/o}$, where V_o is the velocity of point o , the origin of the (x, ξ) coordinate frame, and $V_{p/o}$ is the relative velocity of point p with respect to point o . Hence

$$V_p = V_o + V_{(p/o)_x} + V_{(p/o)_\xi} \quad (2-4)$$

where $V_{(p/o)_x}$ and $V_{(p/o)_\xi}$ are the components of $V_{p/o}$ in the x and ξ directions, respectively, as illustrated in Fig. 2-1. Substituting Eq. (2-4) into Eq. (2-3) and using $dm = \rho dx$, where ρ is the mass per unit length, leads to

$$T_l = (T_l)_1 + (T_l)_2 + (T_l)_3 + (T_l)_4 + (T_l)_5 \quad (2-5)$$

where

$$\begin{aligned} (T_l)_1 &= \frac{1}{2} \int_0^L \rho V_o \cdot V_o dx & (T_l)_2 &= \frac{1}{2} \int_0^L \rho V_{(p/o)_\xi} \cdot V_{(p/o)_\xi} dx & (T_l)_3 &= \frac{1}{2} \int_0^L \rho V_{(p/o)_x} \cdot V_{(p/o)_x} dx \\ (T_l)_4 &= \int_0^L \rho V_o \cdot V_{(p/o)_x} dx & (T_l)_5 &= \int_0^L \rho V_o \cdot V_{(p/o)_\xi} dx \end{aligned} \quad (2-6)$$

and $\int_0^L \rho V_{(p/o)_x} \cdot V_{(p/o)_\xi} dx = 0$. The term $(T_l)_1$ is the kinetic energy due to the translation of the (x, ξ) coordinate frame, $(T_l)_2$ and $(T_l)_3$ are the kinetic energies due to the relative velocities of the point p with respect to the point o and $(T_l)_4$ and $(T_l)_5$ are the kinetic energies due to the interaction of the (x, ξ) coordinate frame's translations and the relative velocity of the point p with respect to the point o . Based on the AMM, Eq. (2-1), $V_{(p/o)_x}$ and $V_{(p/o)_\xi}$ are

$$V_{(p/o)_x} = -\dot{\theta}\xi = -\dot{\theta}\left(\sum_{i=1}^n \lambda_i(t)\phi_i(x)\right) \quad , \quad V_{(p/o)_\xi} = x\dot{\theta} + \dot{\xi} = x\dot{\theta} + \sum_{i=1}^n \dot{\lambda}_i(t)\phi_i(x) \quad (2-7)$$

Moreover, V_o in the (X_l, Y_l) coordinate frame is

$$(V_o)_{x_I y_I} = \begin{bmatrix} \dot{X}_o & \dot{Y}_o \end{bmatrix}^T \quad (2-8)$$

For the calculations of $(T_l)_4$ and $(T_l)_5$, the velocities $V_{(p/o)_x}$, $V_{(p/o)_\xi}$ and V_o should be defined in the same coordinate frame. Thus, V_o is expressed in the (x, ξ) coordinate frame

$$(V_o)_{x\xi} = R_\theta^T (V_o)_{x_I y_I} \quad (2-9)$$

where

$$R_\theta^T = \begin{bmatrix} \cos(\theta) & \sin(\theta) \\ -\sin(\theta) & \cos(\theta) \end{bmatrix} \quad (2-10)$$

Substituting Eqs. (2-7), (2-8) and (2-9) into Eqs. (2-5) and (2-6), the first two terms of Eq. (2-2) become

$$\begin{aligned} \frac{d}{dt} \left(\frac{\partial T_l}{\partial \dot{q}} \right) - \frac{\partial T_l}{\partial q} &= \sum_{i=1}^5 \frac{d}{dt} \left(\frac{\partial (T_l)_i}{\partial \dot{q}} \right) - \frac{\partial (T_l)_i}{\partial q} = \left(\sum_{i=1}^5 (M_l)_i \right) \ddot{q} + \left(\sum_{i=1}^5 (C_l)_i \right) \dot{q} \\ &= M_l \ddot{q} + C_l \dot{q} \end{aligned} \quad (2-11)$$

where $(M_l)_i$ and $(C_l)_i$ are the mass matrix and the matrix representing the Coriolis and centrifugal forces obtained after the differentiation of $(T_l)_i$, $i = 1..5$, respectively⁹. Moreover, $M_l = \sum_{i=1}^5 (M_l)_i$ and $C_l = \sum_{i=1}^5 (C_l)_i$. The elements of $(M_l)_i$ and $(C_l)_i$ modeling the flexibility of the link with two assumed mode shapes, $n=2$ in Eq. (2-1), are given in Appendix 2.I.

Remark 2.1: Alternatively, after obtaining the kinetic energy of the system and writing it in the form $T = (1/2) \dot{q}^T M \dot{q}$, the mass matrix, M , can be obtained. Moreover, the elements of the matrix C can be obtained from the mass matrix using the Christoffel symbol. That is

$$C(i, j) = \sum_{k=1}^p c_{i,jk} \dot{q}_k$$

⁹ Hereafter, the terms “mass matrix” and “matrix representing the Coriolis and centrifugal forces” refer to the coefficients of the multiplier of the second and first derivative of the generalized coordinate with respect to time which is obtained after the differentiation of the kinetic energy, respectively.

$$c_{i,jk} = (1/2)(\partial M(i,j)/\partial q_k + \partial M(i,k)/\partial q_j - \partial M(j,k)/\partial q_i)$$

where p is number of the element in the vector q and $c_{i,jk}$ is the Christoffel symbol. The elements of the mass matrix, and the matrix representing the Coriolis and centrifugal forces, given in Appendices I and II, were checked using the above method.

The kinetic energy of the tip mass of a SFLMB

The tip mass has both linear and angular velocities. Thus, its kinetic energy is

$$T_{tip} = (T_{tip})_{linear} + (T_{tip})_{angular} \quad (2-12)$$

where $(T_{tip})_{linear}$ and $(T_{tip})_{angular}$ are the translational and rotational kinetic energies of the tip mass, respectively. The translational kinetic energy, $(T_{tip})_{linear}$, can be derived from T_l as follows. Assume that the tip mass, m_{tip} , is a virtual link with length L_v and mass per unit length ρ_v attached to the flexible link such that $m_{tip} = L_v \rho_v$. Therefore

$$\rho_v = \frac{m_{tip}}{L_v} \quad (2-13)$$

Shrinking the length of the virtual link to the zero and knowing that $m_{tip} = L_v \rho_v$ is constant turns ρ_v into the Dirac delta function, that is

$$\rho_v = m_{tip} \delta_d(x - L) \quad (2-14)$$

where L is the length of the flexible link with m_{tip} at its tip and x is as shown in Fig. 2-

1. For an arbitrary function $f(x)$ it is known that

$$\int_0^L m_{tip} \delta_d(x - L) f(x) dx = m_{tip} f(L) \quad (2-15)$$

Using Eqs. (2-14) and (2-15), the translational kinetic energy and the corresponding terms (mass matrix, $(M_{tip})_{linear}$, and the matrix representing the Coriolis and centrifugal forces, $(C_{tip})_{linear}$) are obtained from the relations given in Eqs. (2-6) and (2-5) and the expressions given in Appendix 2.I. Thus,

$$\frac{d}{dt} \left(\frac{\partial (T_{tip})_{linear}}{\partial \dot{q}} \right) - \frac{\partial (T_{tip})_{linear}}{\partial q} = (M_{tip})_{linear} \ddot{q} + (C_{tip})_{linear} \dot{q} \quad (2-16)$$

The rotational kinetic energy of the tip mass is

$$(T_{tip})_{angular} = \frac{1}{2} I_{tip} (\dot{\theta} + \dot{\xi}'(L, t))^2 = \frac{1}{2} I_{tip} (\dot{\theta} + (\sum_{i=1}^n \phi'_i(L) \dot{\lambda}_i))^2 \quad (2-17)$$

$$\xi'(L, t) = \left. \frac{\partial \xi(x, t)}{\partial x} \right|_{x=L} \quad \phi'_i(L) = \left. \frac{d\phi_i(x)}{dx} \right|_{x=L} \quad (2-18)$$

where I_{tip} is the mass moment of inertia of the tip mass, θ is as shown in Fig. 2-1, and ξ is given in Eq. (2-1). Therefore

$$\frac{d}{dt} \left(\frac{\partial (T_{tip})_{angular}}{\partial \dot{q}} \right) - \frac{\partial (T_{tip})_{angular}}{\partial q} = (M_{tip})_{angular} \ddot{q} + (C_{tip})_{angular} \dot{q} \quad (2-19)$$

The elements of $(M_{tip})_{angular}$ and $(C_{tip})_{angular}$ modeling the flexibility of the link with two assumed mode shapes, $n=2$ in Eq. (2-1), are given in Appendix 2.II. Combining Eqs. (2-16) and (2-19)

$$\frac{d}{dt} \left(\frac{\partial T_{tip}}{\partial \dot{q}} \right) - \frac{\partial T_{tip}}{\partial q} = M_{tip} \ddot{q} + C_{tip} \dot{q} \quad (2-20)$$

where $M_{tip} = (M_{tip})_{linear} + (M_{tip})_{angular}$ and $C_{tip} = (C_{tip})_{linear} + (C_{tip})_{angular}$.

Kinetic energy of a SFLMB

The (total) kinetic energy of a SFLMB, T_{SM} , is composed of the link and tip mass kinetic energies, T_l and T_{tip} respectively. Thus,

$$\frac{d}{dt} \left(\frac{\partial T_{SM}}{\partial \dot{q}} \right) - \frac{\partial T_{SM}}{\partial q} = \frac{d}{dt} \left(\frac{\partial T_l}{\partial \dot{q}} + \frac{\partial T_{tip}}{\partial \dot{q}} \right) - \left(\frac{\partial T_l}{\partial q} + \frac{\partial T_{tip}}{\partial q} \right) = M_{SM} \ddot{q} + C_{SM} \dot{q} \quad (2-21)$$

where

$$\begin{cases} M_{SM} = M_l + M_{tip} \\ C_{SM} = C_l + C_{tip} \end{cases} \quad (2-22)$$

M_{SM} is the mass matrix, and C_{SM} is the matrix representing the Coriolis and centrifugal forces for a SFLMB.

Remark 2.2: To have a linear model for a single flexible link manipulator with a fixed base, which is usually used in the design of the linear controllers [1, 37], the lateral deflection of the link with respect to the shadow link, ξ , is considered to be very small. Then, $(T_l)_3$ as defined in Eq. (2-6), can be neglected from the kinetic energy's expression. As well, for a single flexible link manipulator with a fixed base $(T_l)_1, (T_l)_4$ and $(T_l)_5$ are zero.

2.2.2. Potential energy of a SFLMB

To derive the last term on the left hand side of Eq. (2-2), $\partial U / \partial q_i$ is required. The term U , called U_{SM} for a SFLMB, is composed of the potential energy due to the gravitational force if the manipulator moves in the vertical plane, and the potential energy (strain energy) due to the link's flexibility. Assuming that the SFLMB is utilized in the vertical plane, the potential energy of the link due to gravity, for X_l as the datum, is

$$(U_l)_{potential} = \int_0^L \rho g (Y_0 + x \sin(\theta) + \xi \cos(\theta)) dx \quad (2-23)$$

where g is the gravitational acceleration, ρ is the mass per unit length and Y_0, x, ξ and θ are shown in Fig. 2-1. The potential energy (strain energy) due to the link's flexibility, neglecting the geometric effect for a beam in bending ([11] p. 388) and the shear and axial deformations, and assuming linear elastic material, is:

$$(U_l)_{strain} = \frac{1}{2} \int_0^L EI \left(\frac{\partial^2 \xi}{\partial x^2} \right)^2 dx \quad (2-24)$$

where E and I are respectively the Young's modules and the second moment of area for a SFLMB. It is to be noted that addressing all neglected terms in the strain energy requires use of full nonlinear FEA [32, 38] at the expense of high computational time. In the three examples presented in Section 2.5, the section dealing with the simulation, the results of the full nonlinear FEA are compared with the AMM without these nonlinear terms. The

close agreement of the FEA and AMM indicates that neglecting these nonlinear terms in the AMM modeling of those examples are reasonably justifiable. These nonlinear terms may have some effects, which are not captured by AMM, on the dynamic motion for special circumstances, such as a very flexible beam or high speed maneuvers [10, 32, 38].

The potential energy of the link of a SFLMB, U_l , is the summation of $(U_l)_{potential}$ and $(U_l)_{strain}$, that is

$$U_l = (U_l)_{potential} + (U_l)_{strain} \quad (2-25)$$

By substituting Eq. (2-1) into Eq. (2-25), $\partial U / \partial q$ is

$$\frac{\partial U_l}{\partial q} = G_l + (K_l)_B q \quad (2-26)$$

where G_l represents the gravity matrix and $(K_l)_B$ is the stiffness matrix of the (flexible) link. The elements of G_l and $(K_l)_B$ modeling the flexibility of the link with two mode shapes, $n=2$ in Eq. (2-1), are given in Appendix 2.III.

To consider the potential energy due to the gravitational force for the tip mass, the strategy of deriving T_{tip} , M_{tip} and C_{tip} is adopted. That is, the mass per unit length given in Eq. (2-14) is substituted in the expression of $(U_l)_{potential}$ and G_l given in Eq. (2-25) and Appendix 2.III, respectively and are called U_{tip} and G_{tip} . Thus,

$$\frac{\partial U_{SM}}{\partial q} = G_{SM} + (K_l)_B q \quad (2-27)$$

and

$$G_{SM} = G_l + G_{tip} \quad (2-28)$$

where $U_{SM} = U_l + U_{tip}$ is the potential energy of a SFLMB, shown in Fig. 2-1, including the link's flexibility and the gravity of the link and tip mass.

2.3. Dynamics of a FLM using dynamics of a SFLMB and Lagrange multipliers

To derive the dynamic equations of a flexible link manipulator (FLM) with revolute joints and constant cross sections, which is composed of several links, the dynamic equations of a SFLMB can be used. Fig. 2-3 illustrates a FLM composed of three links. For each link a set of coordinates, equivalent to the ones adopted for the SFLMB in Section 2. 2, is used. Therefore, for the FLM the coordinates are

$$Z = [q_1 \quad q_2 \quad \dots \quad q_r]^T \quad (2-29)$$

where $q_i = [X_{oi} \quad Y_{oi} \quad \theta_i \quad \lambda_{1i} \quad \dots \quad \lambda_{ni}]^T$ is the coordinates of the i th SFLMB. The kinetic and potential energies of the FLM are

$$T_{FM} = \sum_{i=1}^r (T_{SM})_i \quad (2-30)$$

$$U_{FM} = \sum_{i=1}^r (U_{SM})_i \quad (2-31)$$

where sets of $(T_{FM}$ and $(T_{SM})_i$) and $(U_{FM}$ and $(U_{SM})_i$) are the kinetic and potential energies of the FLM and the i th SFLMB, respectively, and r is the number of the links. Substituting Eqs. (2-30) and (2-31) in the Lagrange's equations

$$\begin{aligned} \frac{d}{dt} \left(\frac{\partial T_{FM}}{\partial \dot{Z}} \right) - \frac{\partial T_{FM}}{\partial Z} + \frac{\partial U_{FM}}{\partial Z} &= \sum_{i=1}^r \left(\frac{d}{dt} \left(\frac{\partial (T_{SM})_i}{\partial \dot{q}_i} \right) - \frac{\partial (T_{SM})_i}{\partial q_i} + \frac{\partial (U_{SM})_i}{\partial q_i} \right) = \\ M_{FM} \ddot{Z} + C_{FM} \dot{Z} + G_{FM} + (K_{FM})_B Z &= Q \end{aligned} \quad (2-32)$$

where

$$M_{FM} = \begin{bmatrix} (M_{SM})_1 & 0 & 0 & 0 \\ 0 & (M_{SM})_2 & 0 & 0 \\ 0 & 0 & \dots & 0 \\ 0 & 0 & 0 & (M_{SM})_r \end{bmatrix} \quad C_{FM} = \begin{bmatrix} (C_{SM})_1 & 0 & 0 & 0 \\ 0 & (C_{SM})_2 & 0 & 0 \\ 0 & 0 & \dots & 0 \\ 0 & 0 & 0 & (C_{SM})_r \end{bmatrix} \quad (2-33)$$

$$G_{FM} = \begin{bmatrix} (G_{SM})_1 \\ (G_{SM})_2 \\ \dots \\ (G_{SM})_r \end{bmatrix} \quad (K_{FM})_B = \begin{bmatrix} ((K_l)_B)_1 & 0 & 0 & 0 \\ 0 & ((K_l)_B)_2 & 0 & 0 \\ 0 & 0 & \dots & 0 \\ 0 & 0 & 0 & ((K_l)_B)_r \end{bmatrix} \quad (2-34)$$

and $(M_{SM})_i, (C_{SM})_i, (G_{SM})_i$ and $((K_l)_B)_i$ are the mass matrix, matrix representing the Coriolis and centrifugal forces, gravity matrix, and stiffness matrix for the i th SFLMB, respectively. These matrices are obtained in Section 2.2. The right hand side of Eq. (2-32), Q , is addressed later in this section, Eqs. (2-36) to (2-44).

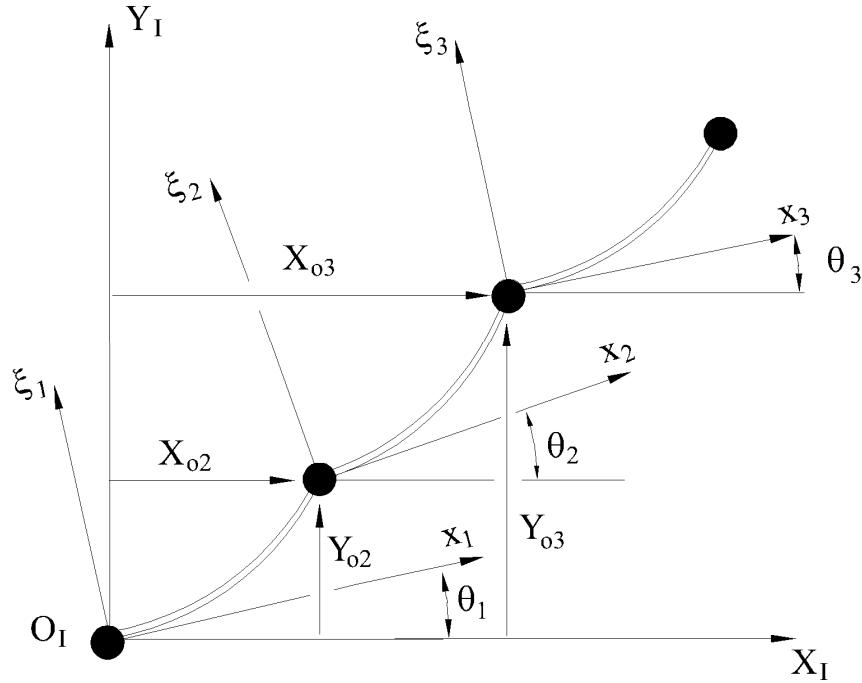


Fig. 2-3: Schematic of a FLM

Remark 2.3: The elements of the mass matrix in Eq. (2-32), $(M_{SM})_i$ $i=1..r$, are for the SFLMB shown in Fig. 2-1, which does not take into account the first SFLMB's hub, I_h . This difference can be observed by comparing Figs. 2-1 and 2-2. To consider the mass moment of inertia of the hub, I_h has to be added to the element of the third row and third column of $(M_{SM})_1$, the mass matrix of the first SFLMB.

Remark 2.4: Since the first two rows and columns of M_{SM} and C_{SM} , and the first two rows of G_{SM} are related to the displacement at the origin of the attached coordinate frame to each link, and due to the fact that for the first SFLMB the origin is fixed, the first two rows and corresponding columns have to be omitted from $(M_{SM})_1$ and $(C_{SM})_1$. Moreover, for the same reason, the first two rows of $(G_{SM})_1$ are omitted. This is similar to modifying the matrices in FEA when applying boundary conditions. The changes that have to be applied to the stiffness matrix $(K_{FM})_B$ are discussed in Section 2.4.

Lagrange's equation for the FLM is

$$\frac{d}{dt}\left(\frac{\partial T_{FM}}{\partial \dot{Z}}\right) - \frac{\partial T_{FM}}{\partial Z} + \frac{\partial U_{FM}}{\partial Z} = Q \quad (2-35)$$

To complete the derivation of the dynamic model, the generalized forces Q corresponding to generalized coordinates have to be calculated. Since there are more generalized coordinates than the DOF of the system, the coordinates are not independent; that is, there are constraint equations. These constraint equations create constraint forces which must be considered in the generalized forces expressions ([26] Chapter 7.1, [27] Chapter 6.7). In other words, when the generalized coordinates form a constrained set, the reactions associated with the constraint conditions enter into the Lagrange's equations ([26] p.324). Thus, the generalized forces at the right-hand side of Eq. (2-35) consist of the actuator's forces Q_a and constraint force Q_{CF}

$$Q = Q_a + Q_{CF} \quad (2-36)$$

Recalling the fact that the lateral displacement of the i th link is $\xi_i = \sum_{j=1}^n \lambda_{ij}(t)\phi_{ij}(x)$, where ϕ_{ij} is the j th mode shape of the i th flexible link, assuming that ϕ_{ij} satisfies the clamped boundary condition, and considering the i th link, shown in Fig. 2-4, the virtual work (δw) due to the virtual displacement of the coordinates is

$$\delta w_i = (\tau_i - \tau_{i+1})\delta\theta_i - \tau_{i+1} \sum_{j=1}^r \phi'_{ij}(L_i)\delta\lambda_{ij} \quad i \neq r, \quad \delta w_i = \tau_i\delta\theta_i \quad i = r \quad (2-37)$$

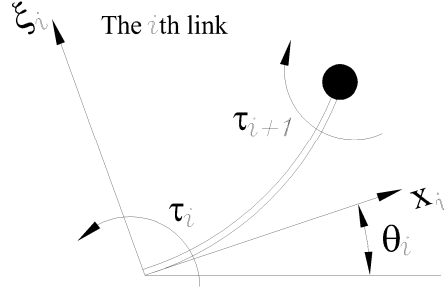


Fig. 2-4: The i th link of a FLM with the applied actuator torques

The virtual work due to the constraint forces will be addressed later. Therefore, the generalized forces for the i th flexible link due to the actuators' forces (torques), using Eq. (2-37), are

$$Q_{ai} = B_i \begin{bmatrix} \tau_i \\ \tau_{i+1} \end{bmatrix} \quad (2-38)$$

$$B_i = \begin{bmatrix} 1 & -1 \\ 0 & -\phi'_{il}(L_i) \\ \dots & \dots \\ 0 & -\phi'_{in}(L_i) \end{bmatrix}_{(1+n) \times 2} \quad i=1, B_i = \begin{bmatrix} 0 & 0 \\ 0 & 0 \\ 1 & -1 \\ 0 & -\phi'_{il}(L_i) \\ \dots & \dots \\ 0 & -\phi'_{in}(L_i) \end{bmatrix}_{(3+n) \times 2} \quad i=2,3,\dots,r-1, B_i = \begin{bmatrix} 0 \\ 0 \\ 1 \\ 0 \\ \dots \\ 0 \end{bmatrix}_{(3+n) \times 1}$$

$$i=r \quad (39)$$

Thus

$$Q_a = \bar{B} \bar{\tau} \quad (2-40)$$

where

$$\bar{B} = \begin{bmatrix} B_1(:,1) & B_1(:,2) & 0 & 0 & 0 & 0 \\ 0 & B_2(:,1) & B_2(:,2) & 0 & 0 & 0 \\ 0 & 0 & B_3(:,1) & B_3(:,2) & \dots & \dots \\ \dots & 0 & 0 & 0 & \dots & \dots \\ \dots & \dots & 0 & 0 & 0 & 0 \\ \dots & \dots & \dots & \dots & B_{r-1}(:,1) & B_{r-1}(:,2) \\ 0 & 0 & 0 & 0 & 0 & B_r(:,1) \end{bmatrix}, \quad \bar{\tau} = \begin{bmatrix} \tau_1 \\ \tau_2 \\ \tau_3 \\ \dots \\ \dots \\ \tau_{r-1} \\ \tau_r \end{bmatrix} \quad (2-41)$$

and $B_i(:,1)$ and $B_i(:,2)$ represent the first and second columns of B_i in Eq. (2-39). The consideration of the constraint forces in the Lagrange's equations is addressed by employing the Lagrange multipliers γ . The constraint forces are due to the holonomic constraints¹⁰ on the coordinates: The displacement of the tip of the i th link is the same as the displacement at the base of the $i+1$ th link, which is

$$\begin{bmatrix} X_{oi} \\ Y_{oi} \end{bmatrix} + R_{\theta} \left[\sum_{j=1}^n \lambda_{ij} \phi_{ij}(L_i) \right] = \begin{bmatrix} X_{oi+1} \\ Y_{oi+1} \end{bmatrix} \quad (2-42)$$

where R_{θ} is the rotation matrix for the i th SFLMB, as defined in Eq. (2-10). Taking the derivative of Eq. (2-42) with respect to time, the velocity constraints are obtained, that is the velocity of the tip of the i th link has to be the same as the velocity of the base of the $i+1$ th link. The velocity constraint can be rewritten as

$$A_j \dot{Z} = 0 \quad (2-43)$$

Details of matrix A_j , called the Jacobian constraint matrix, for a flexible two link manipulator modeling the flexibility of each link with two assumed mode shapes are given in Appendix 2.IV. Using the Lagrange multipliers, γ , the constraint forces are [26, 27]

$$Q_{CF} = A_j^T \gamma \quad (2-44)$$

Combining Equations (2-35), (2-36), (2-40) and (2-44), the dynamic equation of the FLM is

$$M_{FM} \ddot{Z} + C_{FM} \dot{Z} + G_{FM} + (K_{FM})_B Z = \bar{B} \bar{\tau} + A_j^T \gamma \quad (2-45)$$

To solve the dynamic equation of the FLM for a given input torque, τ , the equations of motion, Eq. (2-45), and the constraint equations, Eq. (2-42), have to be solved simultaneously. Thus, the values of the time varying Lagrange multipliers and constrained coordinates are obtained.

¹⁰ If a velocity constraint is holonomic, then there exists an integration factor for which the Pfaffian form of the constraint equation becomes a perfect differential [16].

2.4. Eliminating Lagrange multipliers from the dynamic equations

In this section, the Lagrange multipliers are eliminated from Eq. (2-45) and the dynamic equation of the FLM is obtained in terms of the independent coordinates. To eliminate the Lagrange multipliers from Eq. (2-45), the orthogonal complement matrix, T , of the Jacobian constraint matrix, A_j in Eq. (2-43), is obtained. This matrix, T , is called the natural orthogonal complement (NOC) [30], because it is obtained naturally from the velocity constraint equations without any complex computation. Therefore, to derive the closed form dynamic equation in terms of the independent generalized coordinates, the NOC of matrix A_j in Eq. (2-43), is combined with Eq. (2-45). It should be mentioned that NOC is a projection method of the dynamic equations into the tangent space of the constraint manifold. The concept of this projection technique is discussed in [39 Sections 6.5 and 6.7]. More details of the NOC can be found in [31, 40, 41]. A brief description of this method is as follows. The independent coordinates for the FLM are [13-17]

$$Z_{ID} = [\theta_1 \ \lambda_{11} \ \dots \ \lambda_{1n} \ \theta_2 \ \lambda_{21} \ \dots \ \lambda_{2n} \ \dots \ \theta_r \ \lambda_{r1} \ \dots \ \lambda_{rn}]^T \quad (2-46)$$

where r is the number of the link and n is the number of the assumed mode shapes per link. The relation between the velocity of the dependent coordinates, \dot{Z} , and the velocity of the independent coordinates, \dot{Z}_{ID} , is

$$\dot{Z} = T\dot{Z}_{ID} \quad (2-47)$$

Details of the transformation matrix T , for a flexible two-link manipulator using two assumed mode shapes per link are given in Appendix 2.IV. Substituting Eq. (2-47) into Eq. (2-43) leads to

$$A_j T = T^T A_j^T = 0 \quad (2-48)$$

Eq. (2-48) shows that T is an orthogonal complement of A_j and is referred to as the natural orthogonal complement (NOC) since it is obtained from the velocity constraint, Eq. (2-47), without complex calculations. Taking the derivative of Eq. (2-47) one obtains

$$\ddot{Z} = T\ddot{Z}_{ID} + \dot{T}\dot{Z}_{ID} \quad (2-49)$$

Substituting Eqs. (2-47) and (2-49) into Eq. (2-45) results in

$$(M_{FM}T)\ddot{Z}_{ID} + (M_{FM}\dot{T} + C_{FM}T)\dot{Z}_{ID} + G_{FM} + (K_{FM})_B Z = \bar{B}\bar{\tau} + A_J^T \gamma \quad (2-50)$$

Pre-multiplying both sides of Eq. (2-50) with T^T and considering Eq. (2-48), Eq. (2-50) is changed to:

$$\tilde{M}\ddot{Z}_{ID} + \tilde{C}\dot{Z}_{ID} + \tilde{G} + T^T(K_{FM})_B Z = \tilde{B}\bar{\tau} \quad (2-51)$$

where

$$\begin{aligned} (T^T M_{FM} T) &= \tilde{M} & T^T (M_{FM}\dot{T} + C_{FM}T) &= \tilde{C} \\ T^T G_{FM} &= \tilde{G} & T^T \bar{B} &= \tilde{B} \end{aligned} \quad (2-52)$$

are the dynamic equations without Lagrange multipliers. However, the stiffness matrix is multiplied by Z and not by Z_{ID} . The stiffness matrix of the FLM can be expressed in terms of Z_{ID} as follows. The stiffness matrix of the dynamic model is derived by differentiating Eq. (2-24). Since Eq. (2-24) is independent of θ_i , X_{oi} and Y_{oi} , the elements of the stiffness matrix corresponding to θ_i , X_{oi} and Y_{oi} are zero and the only non-zero elements are those corresponding to λ_{ij} , see matrix $(K_l)_B$ in Appendix 2.III. Given that the transformation between Z_{ID} and Z does not affect λ_{ij} , the non-zero elements of the stiffness matrix related to the λ_{ij} will not change. Thus, $T^T K^{FM} Z$ can be replaced by $\tilde{K}Z_{ID}$ where

$$\tilde{K} = \begin{bmatrix} ((K'_l)_B)_1 & 0 & 0 & 0 \\ 0 & ((K'_l)_B)_2 & 0 & 0 \\ 0 & 0 & \dots & 0 \\ 0 & 0 & 0 & ((K'_l)_B)_r \end{bmatrix} \quad (2-53)$$

and $((K'_l)_B)_p$ ($p=1,2,\dots,r$) is obtained by omitting the first two rows and corresponding columns of $((K_l)_B)_p$. Therefore, the closed form dynamic equations for the FLM in terms of the independent coordinates are

$$\tilde{M}\ddot{Z}_{ID} + \tilde{C}\dot{Z}_{ID} + \tilde{G} + \tilde{K}Z_{ID} = \tilde{B}\bar{\tau} \quad (2-54)$$

To summarize the steps taken to obtain the closed form dynamic Eq. (2-54) a flowchart is given in Appendix 2.V.

2.5. Simulation Results

In the simulation study, the joints' rotations, end-effector path, components of the end-effector velocity in the X_I and Y_I directions and the absolute value of the end-effector deviation with respect to the shadow manipulator for a flexible two-link manipulator were considered. In Fig. 2-5, the flexible two-link manipulator and the end-effector deviation with respect to the shadow manipulator¹¹, called “D”, are shown. The physical properties of the flexible two-link manipulator are provided in Table 2-1. To verify the proposed dynamic model, the simulation results from Eq. (2-54), referred to here as the LNOC (Lagrange and Natural Orthogonal Complement), were compared with the results of the full nonlinear dynamics employing finite element analysis (FEA) [32].

Table 2-1: Physical properties of the flexible two-link manipulator

Physical properties	Value(s)
L_1, L_2 (Length of the links)	0.5000 (<i>m</i>)
E_1, E_2 (Young's modulus)	20.00 (<i>GPa</i>)
ρ_1, ρ_2 (Mass per unit length)	0.7800 (<i>kg / m</i>)
A_1, A_2 (area cross section)	0.0001 (<i>m</i> ²)
I_1, I_2 (second moment of area)	833.3×10^{-12} (<i>m</i> ⁴)
I_{h1}, I_{h2} (mass moment of inertia of hubs)	1.200×10^{-4} (<i>kg.m</i> ²)
m_{h2} (mass of the motor at the elbow joint)	0.0100 (<i>kg</i>)
m_{tip}, I_{tip} (mass and mass moment of inertia at the tip of the manipulator) 2.000 (<i>kg</i>), 0.0100 (<i>kg.m</i> ²)	

¹¹ The difference between the end-effector location of a FLM and the end-effector location of a rigid, shadow, link manipulator with the same lengths and joint rotation is called end-effector deviation of a FLM with respect to the shadow manipulator (See Fig. 2-5)

In the LNOC simulation, the flexibility of each link was modeled using two assumed mode shapes per link; that is, $n=2$ in Eq. (2-1). The mode shape of each link, ϕ_{ij} which was the i th mode shape of the j th link, was selected based on the mode shapes introduced in [42]. Although increasing the number of mode shapes per link may improve the accuracy of the approximation of the AMM to some extent, it also increases the computational time. However, for a physical system, FLM, there is internal material damping, which is usually modeled proportional to stiffness [36]. Due to this material damping, the high frequency vibration is damped out more quickly than the low frequency vibration. Hence, even if the higher modes are excited, the first few modes of vibration are dominant in the dynamic response. In the simulations reported here, the damping was not modeled so that the effect of the high frequency vibration, if any, would be captured in the FEA. Moreover, the applied torques in example one and two were of the bang-bang type which can excite high frequency vibration. The good agreement of the AMM results, based on only $n=2$, with the FEA results justified the use of two mode shapes per links. Having said that, the use of only two modes per link in this approach may be seen as a limitation, but also is an advantage of being fast and reasonably accurate. Furthermore, the results can easily be used by a model based controller for the end-effector control and suppression of unwanted vibration of the manipulator during and at the end of its motion.

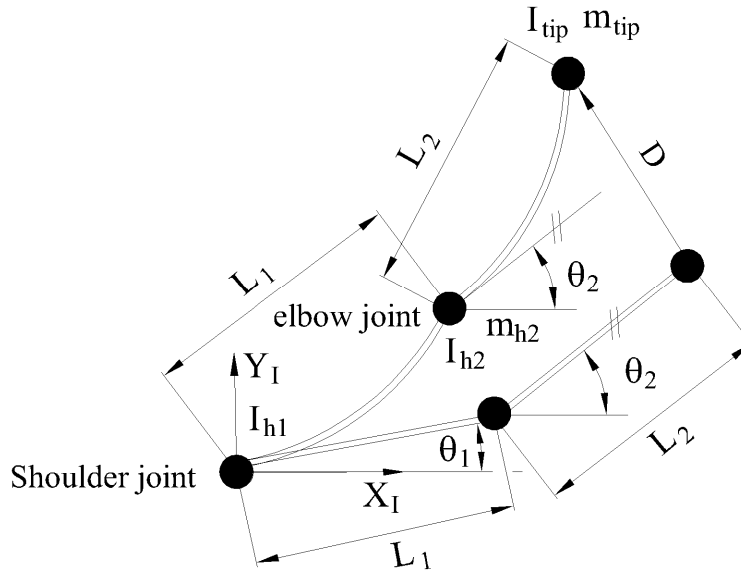


Fig. 2-5: Schematic of a flexible two-link manipulator

For the FEA, the links were modeled by the BEAM3 element and the hubs and end-effector mass were modeled by MASS21 from the ANSYS library [43]. The BEAM3 element is a two-dimensional uniaxial element with three DOF at each node, two translations and one rotation. It has the ability to model tension, compression and bending. The MASS21 is a point element with three DOF, two translations and one rotation. Details of a similar FEA and simulation to the ones presented here can be found in [32] and Appendix B of [44].

2.5.1. Example one: One element per link, Bang-bang torque

For the first example, each link in the FEA was modeled with one BEAM3 element. Thus, the LNOG model, assuming two mode shapes per link, and the finite element (FE) model had approximately the same DOF; that is six and eight, respectively. To generate relatively severe vibrations, the applied torques to the shoulder and elbow joints were chosen as bang-bang with switches at 0.6 and 0.4 seconds, respectively, as shown in Fig. 2-6.

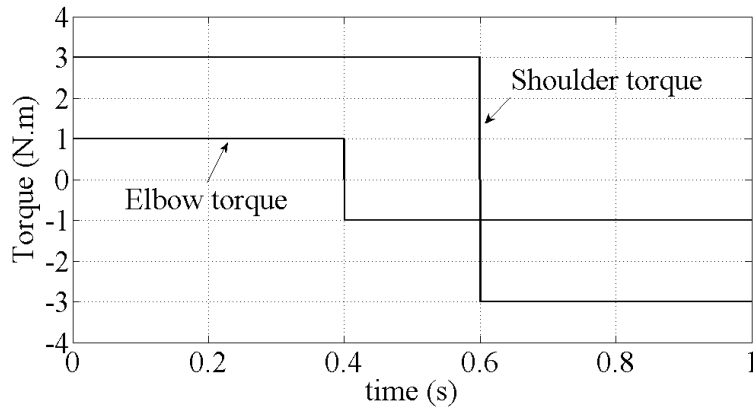


Fig. 2-6: Example one, applied bang-bang torque to the shoulder and elbow joints

The joints' rotations, end-effector path, components of the end-effector velocity in the X_f and Y_f directions and the absolute value of the end-effector deviation with respect to shadow manipulator are shown in Figs. 2-7, 2-8, 2-9, 2-10, 2-11, and 2-12, respectively.

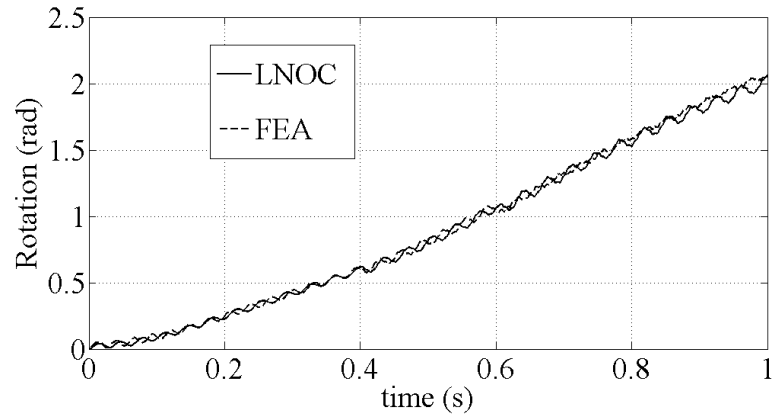


Fig. 2-7: Example one, rotation of the shoulder joint, one element per link in FEA

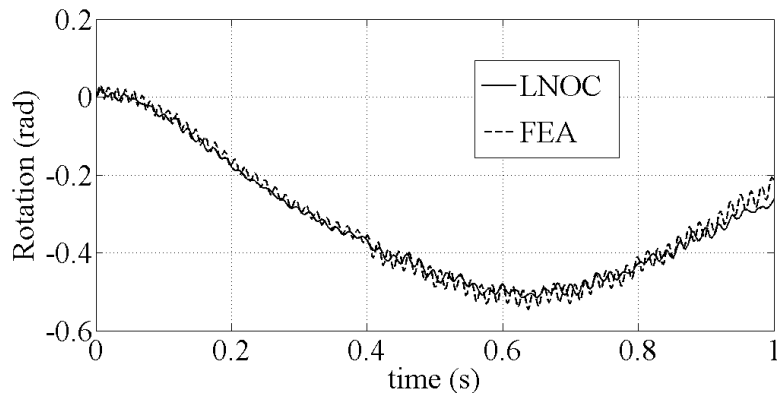


Fig. 2-8: Example one, rotation of the elbow joint, one element per link in FEA

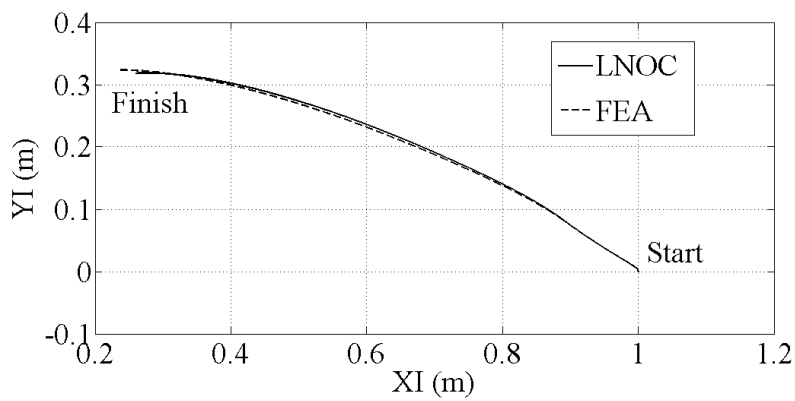


Fig. 2-9: Example one, end-effector paths, one element per link in FEA

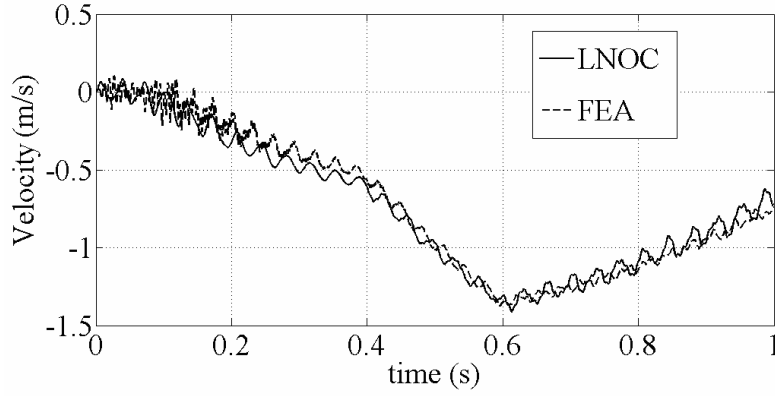


Fig. 2-10: Example one, end-effector velocity, X_I direction, one element per link in FEA

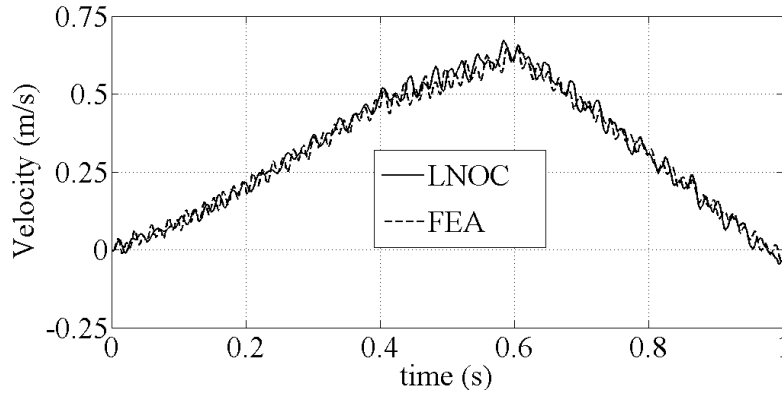


Fig. 2-11: Example one, end-effector velocity, Y_I direction, one element per link in FEA

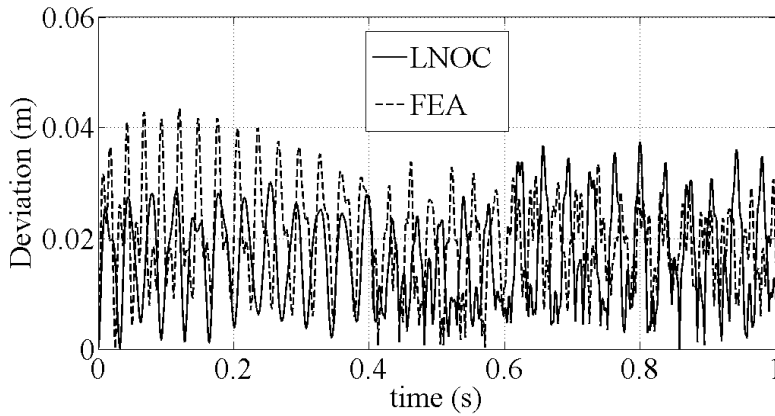


Fig. 2-12: Example one, absolute value of D shown in Fig. 5, one element per link in FEA

From Figs. (2-7 to 2-9), the maximum difference between the results of the FEA, with one element per link, and the LNOC, with two mode shapes per link, for the shoulder joint rotation, elbow joint rotation and end-effector position were 0.1278 (rad),

0.0676 (rad), and 0.0268 (m), respectively. It is worth noting that, like the examples in [44], the end-effector vibration was not obvious from Fig. 2-9. However, the components of the end-effector velocity in the X_I and Y_I directions, shown in Figs. 2-10 and 2-11, clearly showed the existence of the links' vibrations. The maximum difference between the result of the FEA, with one element per link, and the LNOC, with two mode shapes per link, for the end-effector velocities in the X_I and Y_I directions were 0.2994 (m/s), and 0.0968 (m/s), respectively. To determine the average normalized deviation of the end-effector of the FLM with respect to the (rigid) shadow link manipulator over the manoeuvre time, t_f , the following deviation index was defined

$$\|D\| = \frac{\int_0^{t_f} |D| dt}{t_f \times \max(|D|)} \quad (2-55)$$

where “ D ”, the end-effector deviation with respect to shadow manipulator, is as shown in Fig. 2-5. From Fig. 2-12, the deviation index for the LNOC and the FE models were 0.4270 and 0.4470, respectively.

2.5.2. Example two: 10 elements per link, Bang-bang torque

For the second example, the physical properties and the applied torques were the same as in example one (See Table 2-1 and Fig. 2-6, respectively). However, in the FEA the number of the elements per link was increased from 1 to 10 since it was expected that by increasing the number of the elements per link, the accuracy of the FEA result would improve. The number of elements, 10, was chosen for the following two reasons, (1) - to comply with the Euler-Bernoulli (thin) beam theory, theoretically the length-to-height ratio of the elements has to be about five or larger and (2) - to capture the effect of the higher modes (perhaps up to fifth¹²). In this particular example, about 10 elements per link satisfied the above two requirements. Moreover this number, 10 elements per link, made the FEA computationally efficient.

¹² From a simple analysis for a rotating single flexible link manipulator, the first five nonzero natural frequencies were compared against the analytical values when increasing the number of elements from 2 to 10. The finding indicated that 10 elements is reasonably capable of capturing up to five natural frequencies. Details can be found in appendix 2-VI.

The joints' rotations, end-effector path, components of the end-effector velocity in the X_I and Y_I directions and the deviation index, given in Eq. (2-55), were obtained from the LNOC, with two mode shapes per link, and compared with the FEA, with 10 elements per link. These results are given in Figs. 2-13, 2-14, 2-15, 2-16, 2-17, and 2-18, respectively.

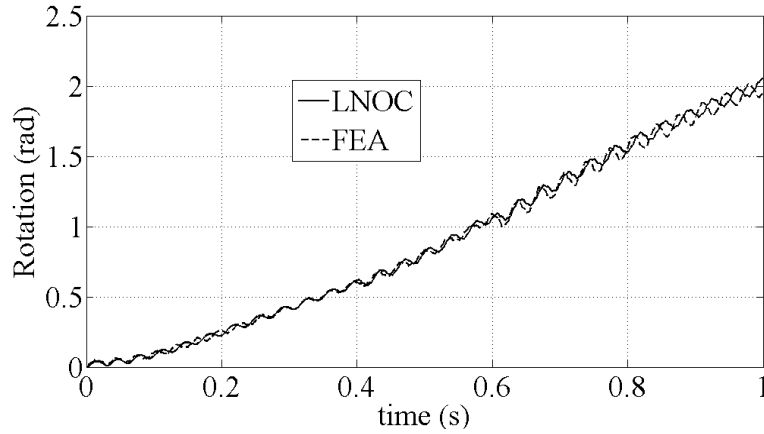


Fig. 2-13: Example two, rotation of the shoulder joint, 10 elements per link in FEA

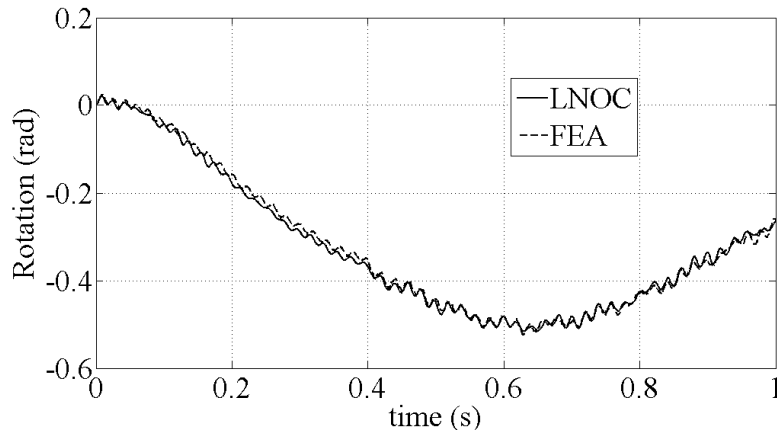


Fig. 2-14: Example two, rotation of the elbow joint, 10 elements per link in FEA

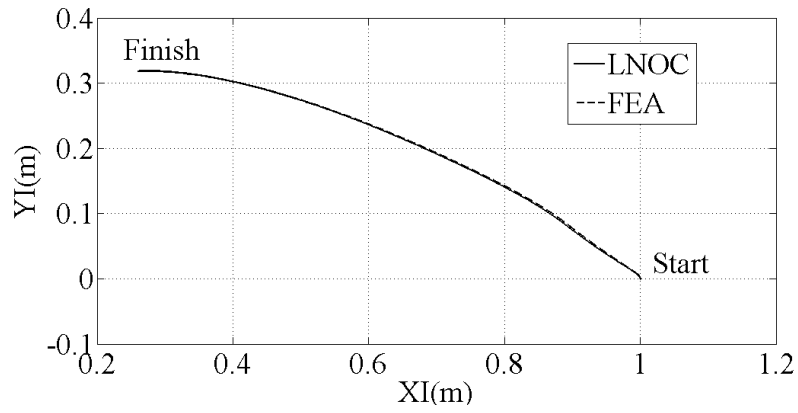


Fig. 2-15: Example two, end-effector paths, 10 elements per link in FEA

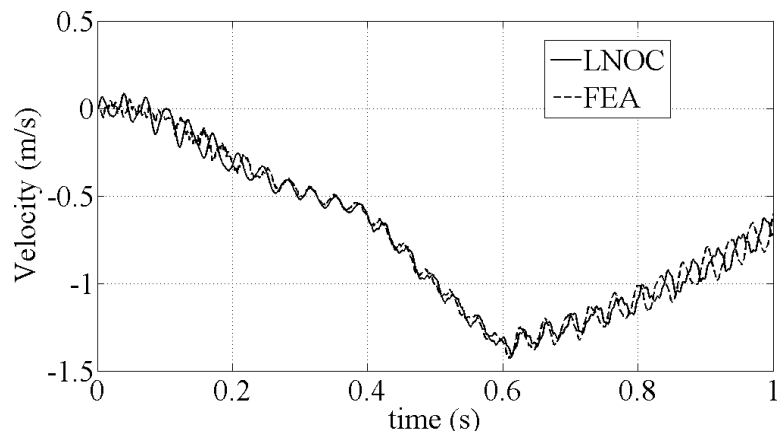


Fig. 2-16: Example two, end-effector velocity, X_I direction, 10 elements per link in FEA

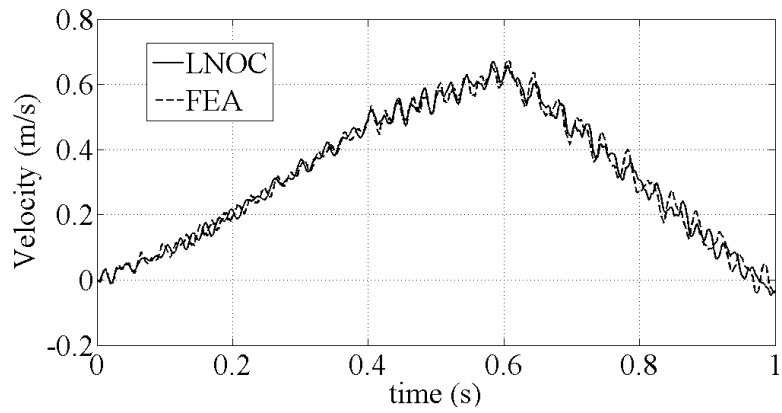


Fig. 2-17: Example two, end-effector velocity, Y_I direction, 10 elements per link in FEA

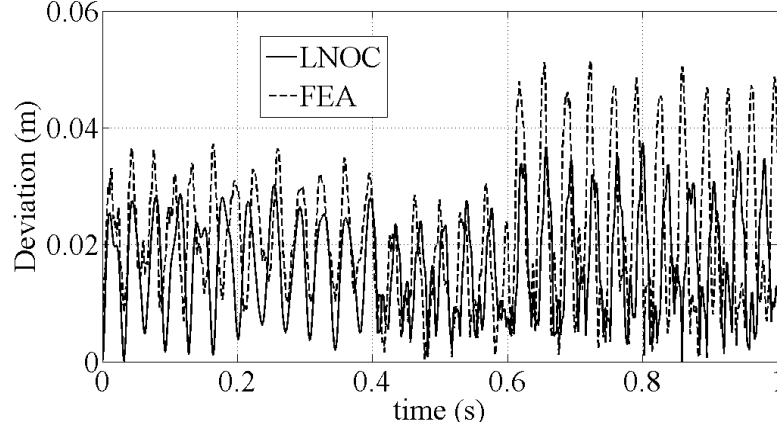


Fig. 2-18: Example two, absolute value of D shown in Fig. 5, 10 elements per link in FEA

From Figs. (2-13 to 2-15), the maximum difference between the results of the FEA, with 10 elements per link, and the LNOC, with two mode shapes per link, for the shoulder joint rotation, elbow joint rotation and end-effector position were 0.1241 (rad), 0.0311 (rad) and 0.0051 (m), respectively. These differences were small compared to those given in the example 1, when only one element per link was used for the FEA. Moreover, the maximum difference between the end-effector velocities in the X_f and Y_f directions obtained from the FEA, with 10 elements per link, and the LNOC, with two mode shapes per link, were 0.2003 (m/s) and 0.0705 (m/s) which were smaller than their counterparts in example 1. Finally, the deviation index for the FEA, with 10 elements per link, was 0.4040. It is to be noted that the deviation index for the FE model, with 10 element per link, ($\|D\|=0.4040$) was closer to this index for the LNOC model ($\|D\|=0.4270$) than its one element per link counterpart, ($\|D\|=0.4470$) (compare the difference of $0.4270-0.4040=0.0230$ with $0.4470-0.4040=0.043$). Thus, although, in the first example the DOF of the LNOC with two assumed mode shapes per link was almost the same as in the FE model with one element per link, differences existed between the results. In the second example, for the FEA each link was modeled with 10 elements and the difference between the results were smaller compared to the first example. Therefore, it is seen that the LNOC with many fewer DOF produced similar results to the FEA with many DOF.

2.5.3. Example three: 10 elements per link, Rigid torque

For this example, the same manipulator was used as in the previous examples. In the FE model, as in the second example, each link was composed of 10 BEAM3 elements. The torques, shown in Fig. 2-19, were calculated from the inverse dynamic of the rigid link counterpart [45] of the FLM to follow a given trajectory and were referred to as rigid torques.

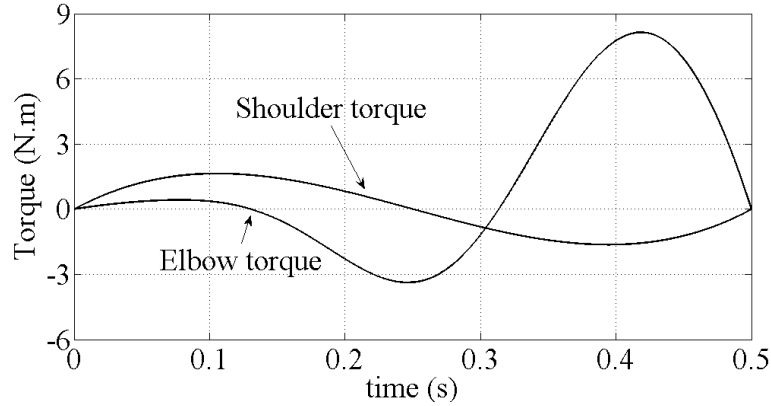


Fig. 2-19: Example three, applied rigid torque to the shoulder motor and elbow joints

The reference trajectories, rigid trajectories, were quintic trajectories for 0.5 seconds, and are shown in Figs. 2-20 and 2-21. The final values for the rigid trajectories of the shoulder and elbow joints, as shown in Figs. 2-20 and 2-21, were 0.7850 (rad) and -0.7850 (rad).

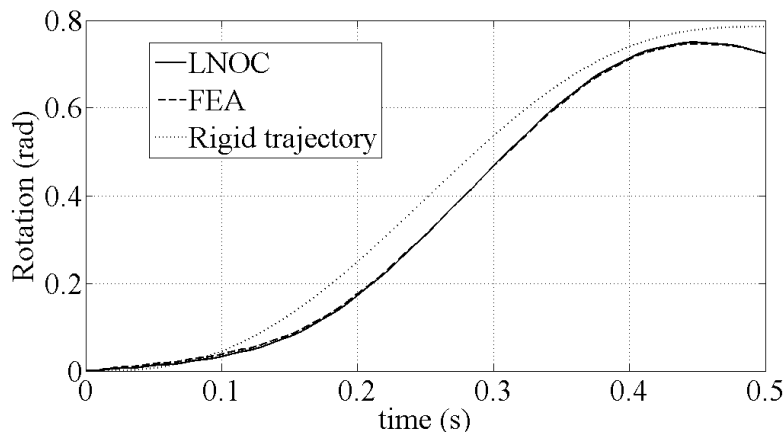


Fig. 2-20: Example three, rotation of the shoulder joint, 10 elements per link in FEA

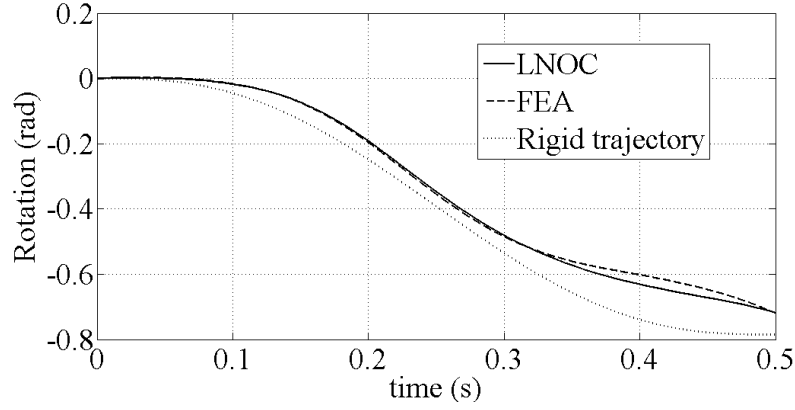


Fig. 2-21: Example three, rotation of the elbow joint, 10 elements per link in FEA

The joints' rotations, end-effector path, components of the end-effector velocity in the X_I and Y_I directions and the absolute value of the end-effector deviation with respect to shadow manipulator are shown in Figs. 2-20, 2-21, 2-22, 2-23, 2-24, and 2-25, respectively.

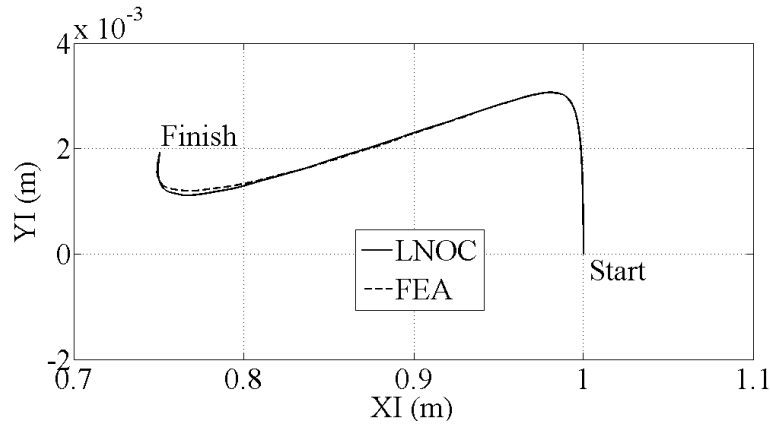


Fig. 2-22: Example three, end-effector paths, 10 elements per link in FEA

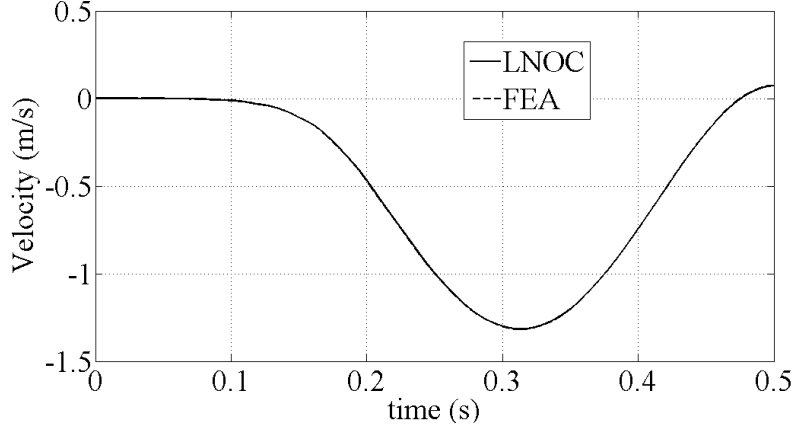


Fig. 2-23: Example three, end-effector velocity, X , direction, 10 elements per link in FEA

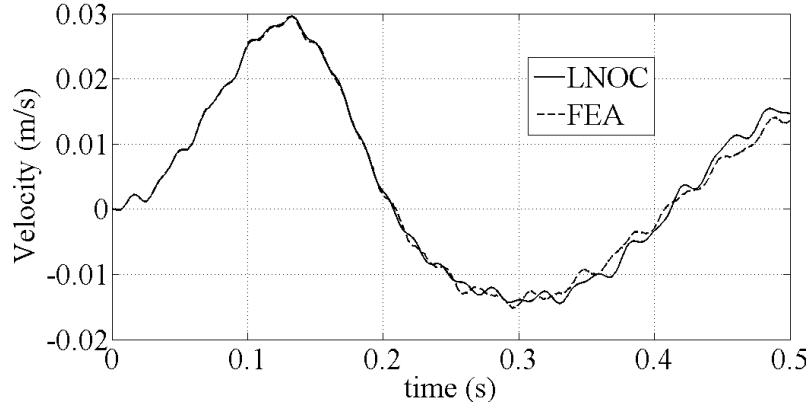


Fig. 2-24: Example three, end-effector velocity, Y , direction, 10 elements per link in FEA

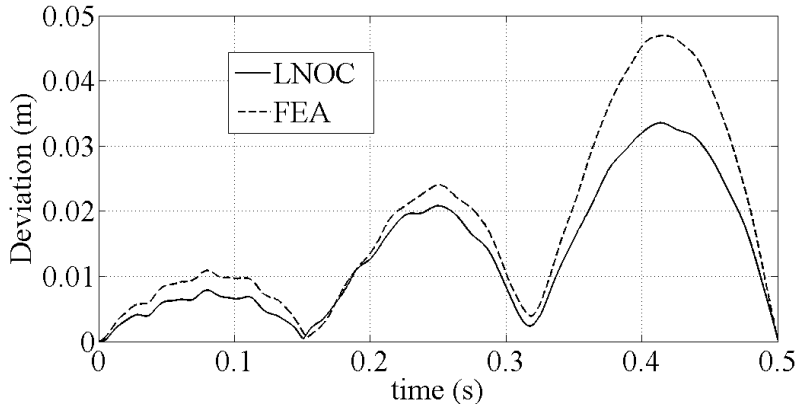


Fig. 2-25: Example three, absolute value of D shown in Fig. 5, 10 elements per link in FEA

The differences between the rotations of the elbow and shoulder joints of the flexible two-link manipulator compared to its rigid link counterpart, rigid trajectory, as shown in Figs. 2-20 and 2-21 were due primarily to the flexibility of the links. From Figs.

(2-20 to 2-24) the maximum differences between the shoulder joint rotation, elbow joint rotation, end-effector position, and the end-effector velocities in the X_f and Y_f directions from the LNOC, with two mode shapes per link, and the FEA, with 10 elements per link, were 0.0054 (rad), 0.0308 (rad), 6.311×10^{-4} (m), 0.0059 (m/s), and 0.0031 (m/s) respectively. The differences between the LNOC and the FEA results in the third example were considerably smaller than in the second example. This was due to the fact that torque in the third example was much more smooth than the bang-bang torque in the second example. In addition, the deviation indices from Eq. (2-55) for the LNOC and the FE model were 0.4060 and 0.3830, respectively. Again the closeness of these values indicated the validity of the proposed approach.

Comparison of the results based on the dynamic model derived here with those of the full nonlinear dynamic simulation using the FE with 10 elements per link justified the proposed LNOC method which used only two mode shapes per link. In the FEA, the axial deformation, shear deformation, and the nonlinear terms in strain energy which lead to effects such as stress stiffening [10, 32, 38, 43] were also considered, while they were neglected in the LNOC model. Thus, differences between the simulation results must exist. Nevertheless, the results of the LNOC model, as shown in the examples for a bang-bang and rigid torques, were reasonably accurate and were comparable with the FEA.

It is worth noting that in examples 2 and 3, the results of a full nonlinear, FEA were used as the basis for the comparison and verification of the dynamic equations presented in Eq. (2-54). In this context, full nonlinear FEA here is taken to mean that a sufficient number of elements were used, all the nonlinearities were considered, and the time integration and iterative solver (the Newmark and full Newton/Raphson) provided accurate results. Obviously, comparing the numerical simulation with the experimental results is the best way to validate an approach; which we have done in our published and in progress papers [33,34], which examine the use of AMM for design of othe proposed controller for a SFLM. In the absence of the experimental results for a two-link flexible manipulator, comparison with full nonlinear FEA is the second best choice. It is believed that the results of such a full nonlinear FEA will be quite reliable and close to the

experimental results. Thus, verification of the AMM with the full nonlinear FEA implied the sound agreement of the AMM results to the experimental results.

2.6. Conclusions

The derivation of the dynamic models of flexible link manipulators (FLM) based on the combination of the Lagrange's equations and the assumed mode shape method requires evaluation and differentiation of the Lagrangian function. A new method was introduced in this chapter to alleviate the lengthy evaluation and complicated derivative calculation of the Lagrangian function of a FLM. All the computations, evaluation and derivative calculations of the Lagrangian function were carried out only once and for a single flexible link manipulator with a moving base (SFLMB). Details of the dynamic equations of a SFLMB when the flexibility of the link is modelled with two mode shapes were presented.

Based on the dynamic model of a SFLMB and by employing the Lagrange multipliers, the dynamic equations of a FLM in terms of the dependent generalized coordinates were obtained. To have the closed form dynamic equations without Lagrange multipliers, the natural orthogonal complement of the Jacobian constraint matrix was combined with the dynamic equation of a FLM obtained in terms of the dependent generalized coordinates. Thus, the closed form dynamic equations of a FLM in terms of the independent generalized coordinates and without the Lagrange multipliers were achieved. Details of the matrices to obtain the dynamic model of a flexible two-link manipulator were given. To verify the derived dynamic equations, the results of simulation from the introduced model were compared with the ones obtained from the full nonlinear finite element analysis and were found to be in very good agreement. In the three examples in the simulation study a bang-bang torque, and the torque from the rigid manipulator, were applied to a flexible two-link manipulator. For these examples, joints' rotations, end-effector path, components of the end-effector velocity and deviation index, from the model and the full nonlinear finite element analysis were compared as checks for the accuracy of the developed model.

It is to be noted that the sources of the errors of the introduced approach are only those typical of the AMM, which are approximations of the mode shapes and the number

of the mode shapes used. Thus, the proposed method detailed here will not introduce extra error to the system other than the AMM above mentioned errors.

2.7. Acknowledgment

Financial support for this study was provided by a NSERC Discovery Grant. Fruitful discussions with Professor W. Szyszkowski are gratefully acknowledged. The authors would also like to express their gratitude toward the referees for their valuable comments.

2.8. Nomenclature

A_J : Jacobian constraint matrix.

\bar{B} : Torque mapping matrix for a FLM derived based on the dependent generalized coordinates.

\tilde{B} : Torque mapping matrix for a FLM derived based on the independent generalized coordinates.

$(C_l)_i$: Matrix representing the Coriolis and centrifugal forces obtained after the differentiation of $(T_l)_i$.

C_l : Matrix representing the Coriolis and centrifugal forces for the link of a SFLMB,

$$C_l = \sum_{i=1}^5 (C_l)_i.$$

$(C_{tip})_{linear}, (C_{tip})_{angular}$: Matrices representing the Coriolis and centrifugal forces obtained after the differentiation of $(T_{tip})_{linear}$ and $(T_{tip})_{angular}$, respectively.

C_{tip} : Matrix representing the Coriolis and centrifugal forces for the tip mass of a SFLMB, $C_{tip} = (C_{tip})_{linear} + (C_{tip})_{angular}$.

C_{SM} : Matrix representing the Coriolis and centrifugal forces for SFLMB,

$$C_{SM} = C_{tip} + C_l.$$

C_{FM} : Matrix representing the Coriolis and centrifugal forces for a FLM derived based on the dependent generalized coordinates.

\tilde{C} : Matrix representing the Coriolis and centrifugal forces for a FLM derived based on the independent generalized coordinates.

D : End-effector deviation with respect to the shadow manipulator.

E : Young's modules.

EI : Rigidity of the link.

G_l : Gravity matrix of the link of a SFLMB.

G_{tip} : Gravity matrix of the tip mass of a SFLMB.

G_{SM} : Gravity matrix of a SFLMB, $G_{SM} = G_{tip} + G_l$.

G_{FM} : Gravity matrix of a FLM derived based on the dependent generalized coordinates.

\tilde{G} : Gravity matrix of a FLM derived based on the independent generalized coordinates.

I : Second moment of area.

I_{tip} : Mass moment of inertia at the tip of a SFLMB (or Mass moment of inertia of the end-effector of a FLM).

I_h : Mass moment of inertia of the hub.

$(K_l)_B$: Stiffness matrix of the link of a SFLMB.

$(K'_l)_B$: Stiffness matrix obtained by omitting the first two rows and corresponding columns of $(K_l)_B$.

$(K_{FM})_B$: Stiffness matrix of a FLM derived based on the dependent generalized coordinates.

\tilde{K} : Stiffness matrix of a FLM derived based on the independent generalized coordinates.

L : Length of a SFLMB.

\mathcal{L} : Lagrangian function, $\mathcal{L} = T_{FM} - U_{FM}$.

$(M_l)_i$: Mass matrix obtained after the differentiation of $(T_l)_i$.

M_l : Mass matrix of the link of a SFLMB, $M_l = \sum_{i=1}^5 (M_l)_i$.

$(M_{tip})_{linear}$, $(M_{tip})_{angular}$: Mass matrix obtained after the differentiation of $(T_{tip})_{linear}$ and $(T_{tip})_{angular}$, respectively.

M_{tip} : Mass matrix of the tip mass of a SFLMB, $M_{tip} = (M_{tip})_{linear} + (M_{tip})_{angular}$.

M_{SM} : Mass matrix of a SFLMB, $M_{SM} = M_{tip} + M_l$.

M_{FM} : Mass matrix of a FLM derived based on the dependent generalized coordinates.

\tilde{M} : Mass matrix of a FLM derived based on the independent generalized coordinates.

m_{tip} : Mass at the tip of a SFLMB (or Mass of the end-effector for FLM).

Q_a : Generalized force for a FLM due to the actuator forces derived based on the dependent generalized coordinates.

Q_{CF} : Generalized force for a FLM due to the constraint forces derived based on the dependent generalized coordinates.

Q : Generalized force for a FLM derived based on the dependent generalized coordinates,

$$Q = Q_a + Q_{CF}.$$

q_i : Generalized coordinates for the i th SFLMB

r : number of the flexible links of a FLM

R_θ : Rotation matrix

T : Transformation matrix

$(T_l)_i$: The i th component of the T_l

T_l : Kinetic energy of the link of a SFLMB, $T_l = \sum_{i=1}^5 (T_l)_i$.

$(T_{tip})_{linear}$, $(T_{tip})_{angular}$: Translational and rotational kinetic energies of the mass at the tip of a SFLMB, respectively.

T_{tip} : Kinetic energy of the mass at the tip of a SFLMB, $T_{tip} = (T_{tip})_{linear} + (T_{tip})_{angular}$.

T_{SM} : Kinetic energy of a SFLMB, $T_{SM} = T_{tip} + T_l$.

T_{FM} : Kinetic energy of a FLM, $T_{FM} = \sum_{i=1}^r (T_{SM})_i$.

$(U_l)_{potential}$: Potential energy of the link of a SFLMB due to gravity.

U_{tip} : Potential energy of the tip mass of a SFLMB due to gravity.

$(U_l)_{strain}$: Potential energy (strain energy) of the link of a SFLMB due to flexibility.

U_l : Potential energy of the link of a SFLMB, $U_l = (U_l)_{potential} + (U_l)_{strain}$.

U_{SM} : Potential energy of a SFLMB, $U_{SM} = U_l + U_{tip}$.

U_{FM} : Potential energy of a FLM, $U_{FM} = \sum_{i=1}^r (U_{SM})_i$.

V_p : Velocity of point “p” on the link.

V_o : Velocity of point “o”, origin of (x, ξ) coordinate frame.

$V_{p/o}$: Relative velocity of point “p” with respect to point “o”.

$V_{(p/o)_x}$, $V_{(p/o)_\xi}$: Components of $V_{p/o}$ in the x and ξ directions, respectively.

(X_l, Y_l) : Inertial coordinate frames.

(x, ξ) : Moving coordinate frame attached to a SFLMB.

X_o, Y_o : Base translation of the (x, ξ) coordinate frame attached to a SFLMB.

\dot{X}_o, \dot{Y}_o : Derivatives of X_o, Y_o with respect to time, respectively.

Z : Dependent generalized coordinates for a FLM.

Z_{ID} : Independent generalized coordinates for a FLM.

θ : Rotation of the (x, ξ) coordinate frame.

ξ : Spatial, lateral, deformation of the flexible link.

ϕ_j : The j th assumed mode shape.

ϕ_{ij} : The j th mode shape of the i th link.

λ_j : Time varying weight function of the j th mode shape.

λ : Vector composed of the time varying weights of the mode shape.

ρ : Mass per unit length.

τ_i : The input actuator torque for the i th SFLMB.

$\bar{\tau}$: A vector composed of τ_i .

$\delta_d(x)$: Dirac delta function.

γ : Lagrange multipliers.

2.9. Appendices

Appendix 2.I: Elements of $(M_l)_i$ and $(C_l)_i$

$$\begin{aligned}
 m_L &= \int_0^L \rho dx & I_{o1} &= \int_0^L \rho x dx & I_o &= \int_0^L \rho x^2 dx & \Phi_{1x} &= \int_0^L \rho x \phi_1 dx \\
 \Phi_{2x} &= \int_0^L \rho x \phi_2 dx & \Phi_{11} &= \int_0^L \rho \phi_1^2 dx & \Phi_{12} &= \int_0^L \rho \phi_1 \phi_2 dx & \Phi_{22} &= \int_0^L \rho \phi_2^2 dx \\
 \Phi_{10} &= \int_0^L \rho \phi_1 dx & \Phi_{20} &= \int_0^L \rho \phi_2 dx & \Phi_{11xx} &= \int_0^L \left(\frac{d^2 \phi_1}{dx^2} \right)^2 dx & \Phi_{22xx} &= \int_0^L \left(\frac{d^2 \phi_2}{dx^2} \right)^2 dx
 \end{aligned}$$

$$\Phi_{12xx} = \int_0^L \frac{d^2\phi_1}{dx^2} \frac{d^2\phi_2}{dx^2} dx \quad \phi'_i(L_i) = \frac{d\phi_i}{dx} \Big|_{L_i}$$

The elements of $(M_l)_i$ and $(C_l)_i$, modeling the flexibility by two mode shapes, $\xi = \lambda_1\phi_1 + \lambda_2\phi_2$ are as follows:

$$(M_l)_1 = \begin{bmatrix} m_L & 0 & 0 & 0 & 0 \\ 0 & m_L & 0 & 0 & 0 \\ 0 & 0 & 0 & 0 & 0 \\ 0 & 0 & 0 & 0 & 0 \\ 0 & 0 & 0 & 0 & 0 \end{bmatrix}$$

$$(C_l)_1 = 0$$

$$(M_l)_2 = \begin{bmatrix} 0 & 0 & 0 & 0 & 0 \\ 0 & 0 & 0 & 0 & 0 \\ 0 & 0 & I_o & \Phi_{1x} & \Phi_{2x} \\ 0 & 0 & \Phi_{1x} & \Phi_{11} & \Phi_{12} \\ 0 & 0 & \Phi_{2x} & \Phi_{12} & \Phi_{22} \end{bmatrix}$$

$$(C_l)_2 = 0$$

$$(M_l)_3 = \begin{bmatrix} 0 & 0 & 0 & 0 & 0 \\ 0 & 0 & 0 & 0 & 0 \\ 0 & 0 & (\lambda_1^2\Phi_{11} + \lambda_2^2\Phi_{22} + 2\lambda_1\lambda_2\Phi_{12}) & 0 & 0 \\ 0 & 0 & 0 & 0 & 0 \\ 0 & 0 & 0 & 0 & 0 \end{bmatrix}$$

$$(C_l)_3 = \begin{bmatrix} 0 & 0 & 0 & 0 & 0 \\ 0 & 0 & 0 & 0 & 0 \\ 0 & 0 & \dot{\lambda}_1(\lambda_1\Phi_{11} + \lambda_2\Phi_{12}) + \dot{\lambda}_2(\lambda_2\Phi_{22} + \lambda_1\Phi_{12}) & \dot{\theta}(\lambda_1\Phi_{11} + \lambda_2\Phi_{12}) & \dot{\theta}(\lambda_2\Phi_{22} + \lambda_1\Phi_{12}) \\ 0 & 0 & -\dot{\theta}(\lambda_1\Phi_{11} + \lambda_2\Phi_{12}) & 0 & 0 \\ 0 & 0 & -\dot{\theta}(\lambda_2\Phi_{22} + \lambda_1\Phi_{12}) & 0 & 0 \end{bmatrix}$$

$$(M_1)_4 = \begin{bmatrix} 0 & 0 & -(\lambda_1 \Phi_{10} + \lambda_2 \Phi_{20}) \cos(\theta) & 0 & 0 \\ 0 & 0 & -(\lambda_1 \Phi_{10} + \lambda_2 \Phi_{20}) \sin(\theta) & 0 & 0 \\ -(\lambda_1 \Phi_{10} + \lambda_2 \Phi_{20}) \cos(\theta) & -(\lambda_1 \Phi_{10} + \lambda_2 \Phi_{20}) \sin(\theta) & 0 & 0 & 0 \\ 0 & 0 & 0 & 0 & 0 \\ 0 & 0 & 0 & 0 & 0 \end{bmatrix}$$

$$(C_1)_4 = \begin{bmatrix} 0 & 0 & \dot{\theta}(\lambda_1 \Phi_{10} + \lambda_2 \Phi_{20}) \sin(\theta) & -\dot{\theta} \cos(\theta) \Phi_{10} & -\dot{\theta} \cos(\theta) \Phi_{20} \\ 0 & 0 & -\dot{\theta}(\lambda_1 \Phi_{10} + \lambda_2 \Phi_{20}) \cos(\theta) & -\dot{\theta} \sin(\theta) \Phi_{10} & -\dot{\theta} \sin(\theta) \Phi_{20} \\ -(\dot{\lambda}_1 \Phi_{10} + \dot{\lambda}_2 \Phi_{20}) \cos(\theta) & -(\dot{\lambda}_1 \Phi_{10} + \dot{\lambda}_2 \Phi_{20}) \sin(\theta) & 0 & 0 & 0 \\ \dot{\theta} \cos(\theta) \Phi_{10} & \dot{\theta} \sin(\theta) \Phi_{10} & 0 & 0 & 0 \\ \dot{\theta} \cos(\theta) \Phi_{20} & \dot{\theta} \sin(\theta) \Phi_{20} & 0 & 0 & 0 \end{bmatrix}$$

$$(M_1)_5 = \begin{bmatrix} 0 & 0 & -I_{o1} \sin(\theta) & -\Phi_{10} \sin(\theta) & -\Phi_{20} \sin(\theta) \\ 0 & 0 & I_{o1} \cos(\theta) & \Phi_{10} \cos(\theta) & \Phi_{20} \cos(\theta) \\ -I_{o1} \sin(\theta) & I_{o1} \cos(\theta) & 0 & 0 & 0 \\ -\Phi_{10} \sin(\theta) & \Phi_{10} \cos(\theta) & 0 & 0 & 0 \\ -\Phi_{20} \sin(\theta) & \Phi_{20} \cos(\theta) & 0 & 0 & 0 \end{bmatrix}$$

$$(C_l)_5 = \begin{bmatrix} 0 & 0 & -(\dot{\theta}_{o1} + \dot{\lambda}_1 \Phi_{10} + \dot{\lambda}_2 \Phi_{20}) \cos(\theta) & 0 & 0 \\ 0 & 0 & -(\dot{\theta}_{o1} + \dot{\lambda}_1 \Phi_{10} + \dot{\lambda}_2 \Phi_{20}) \sin(\theta) & 0 & 0 \\ (\dot{\lambda}_1 \Phi_{10} + \dot{\lambda}_2 \Phi_{20}) \cos(\theta) & (\dot{\lambda}_1 \Phi_{10} + \dot{\lambda}_2 \Phi_{20}) \sin(\theta) & 0 & 0 & 0 \\ -\dot{\theta} \Phi_{10} \cos(\theta) & -\dot{\theta} \Phi_{10} \sin(\theta) & 0 & 0 & 0 \\ -\dot{\theta} \Phi_{20} \cos(\theta) & -\dot{\theta} \Phi_{20} \sin(\theta) & 0 & 0 & 0 \end{bmatrix}$$

Appendix 2.II: Elements of $(M_{tip})_{angular}$ and $(C_{tip})_{angular}$

$$(M_{tip})_{angular} = \begin{bmatrix} 0 & 0 & 0 & 0 & 0 \\ 0 & 0 & 0 & 0 & 0 \\ 0 & 0 & I_{tip} & I_{tip} \phi'_1(L) & I_{tip} \phi'_2(L) \\ 0 & 0 & I_{tip} \phi'_1(L) & I_{tip} (\phi'_1(L))^2 & I_{tip} \phi'_1(L) \phi'_2(L) \\ 0 & 0 & I_{tip} \phi'_2(L) & I_{tip} \phi'_1(L) \phi'_2(L) & I_{tip} (\phi'_2(L))^2 \end{bmatrix}$$

$$(C_{tip})_{angular} = 0$$

Appendix 2.III: Elements of G_l and $(K_l)_B$

$$G_l = \begin{bmatrix} 0 \\ m_L g \\ gI_{o1} \cos(\theta) - g(\lambda_1 \Phi_{10} + \lambda_2 \Phi_{20}) \sin(\theta) \\ g\Phi_{10} \cos(\theta) \\ g\Phi_{20} \cos(\theta) \end{bmatrix} \quad (K_l)_B = \begin{bmatrix} 0 & 0 & 0 & 0 & 0 \\ 0 & 0 & 0 & 0 & 0 \\ 0 & 0 & 0 & 0 & 0 \\ 0 & 0 & 0 & EI\Phi_{11xx} & EI\Phi_{12xx} \\ 0 & 0 & 0 & EI\Phi_{12xx} & EI\Phi_{22xx} \end{bmatrix}$$

Appendix 2.IV: Elements of matrix A and T for a flexible two-link manipulator

For the flexible two link manipulator shown in Fig.2-5, assuming that the flexibility of each link is modeled with two mode shapes, the dependent generalized coordinates are

$$Z = [\theta_1 \quad \lambda_{11} \quad \lambda_{12} \quad X_{o2} \quad Y_{o2} \quad \theta_2 \quad \lambda_{21} \quad \lambda_{22}]$$

and the matrices A and T are

$$A_J = \begin{bmatrix} -\phi_{11}(L_1)\lambda_{11} - \phi_{12}(L_1)\lambda_{12} & 0 & 0 & -R_{\theta 1}^T & 0_{2 \times 3} \\ L_1 & \phi_{11}(L_1) & \phi_{12}(L_1) & & \end{bmatrix}$$

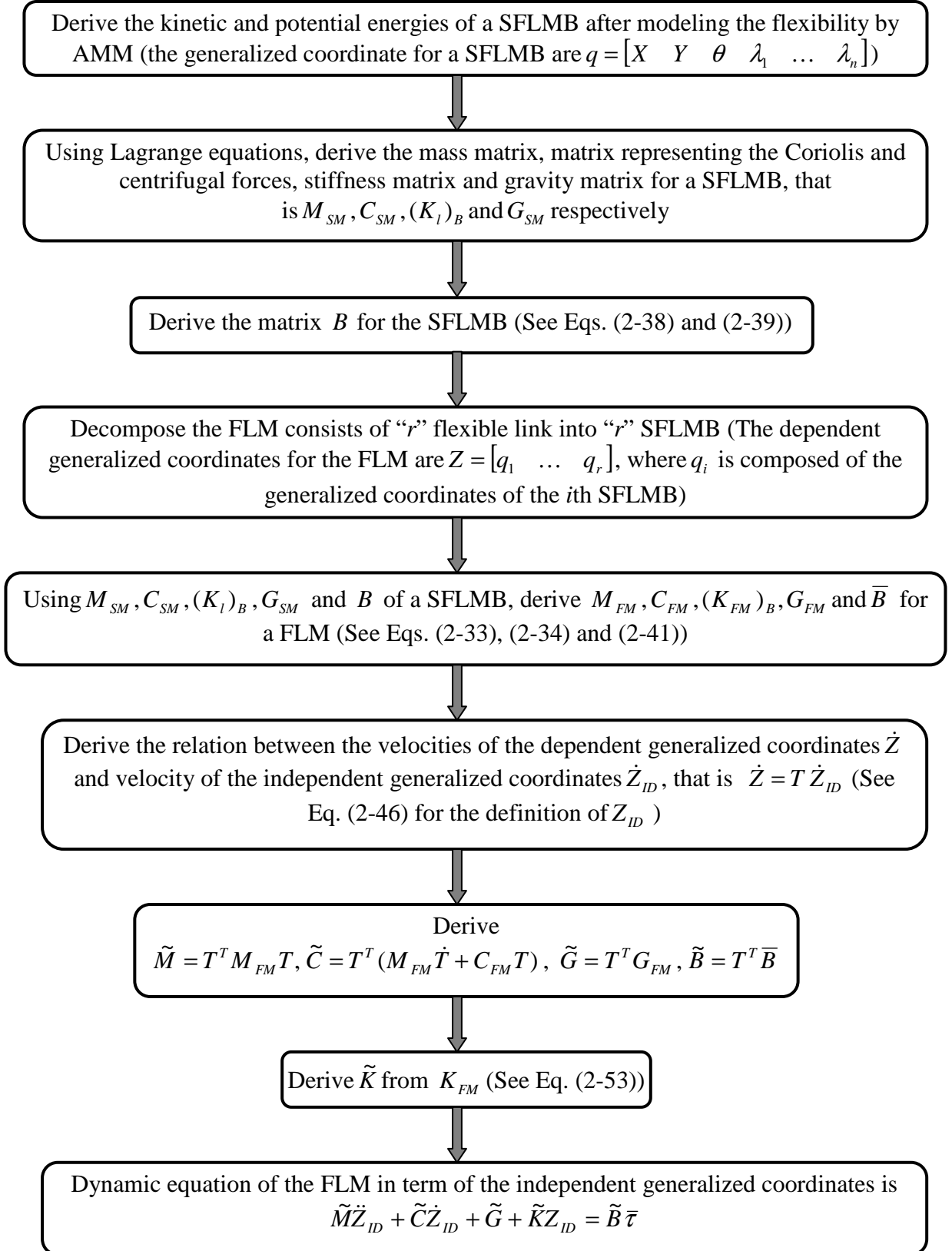
$$T = \begin{bmatrix} I_{3 \times 3} & 0_{3 \times 3} \\ R_{\theta 1} \begin{bmatrix} -\phi_{11}(L_1)\lambda_{11} - \phi_{12}(L_1)\lambda_{12} & 0 & 0 \\ L_1 & \phi_{11}(L_1) & \phi_{12}(L_1) \end{bmatrix} & 0_{2 \times 3} \\ 0_{3 \times 3} & I_{3 \times 3} \end{bmatrix}$$

where

$$R_{\theta 1}^T = \begin{bmatrix} \cos(\theta_1) & \sin(\theta_1) \\ -\sin(\theta_1) & \cos(\theta_1) \end{bmatrix}$$

and $0_{n \times m}$ and $I_{n \times n}$ are the zero matrix and the unity matrix of order $n \times m$ and $n \times n$, respectively.

Appendix 2.V: Flowchart of the steps for the dynamic model derivation



Appendix 2.VI: Natural frequencies versus number of elements

A single flexible link manipulator rotating in the horizontal plane, as shown in Fig. 2-26, was considered.

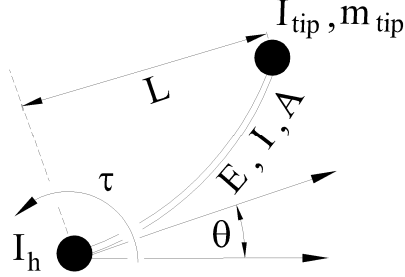


Fig. 2-26: Schematic of a rotating single flexible link manipulator

The length, L , second moment of area, I , cross section area, A , young modules, E , mass moment of inertia of the hub, I_h , mass moment of inertia of the payload, I_{tip} , the beam's mass per unit length, ρ , and mass of the payload, m_{tip} , of this manipulator were:

$$L = 0.5000 \text{ (m)} \quad I_h = 1.200 \times 10^{-4} \text{ (kg.m}^2\text{)}$$

$$I = 833.3 \times 10^{-12} \text{ (m}^4\text{)} \quad E = 20.00 \text{ (GPa)}$$

$$I_{tip} = 0.0100 \text{ (kg.m}^2\text{)} \quad m_{tip} = 2.000 \text{ (kg)}$$

$$A = 0.0001 \text{ (m}^2\text{)} \quad \rho = 0.7800 \text{ (kg / m)}$$

These physical parameters were the same as those of the second link of the manipulator used in Section 2.5.

The analytical natural frequencies of the manipulator were calculated [042] and compared against the natural frequencies obtained by ANSYS-FEA for different number of elements. In Fig. 2-27, the percentages of the frequency error for the first five nonzero natural frequencies versus number of elements are shown. The frequency error for the i th mode is defined as:

$$(\text{Frequency error})_i = \frac{(nf)_i - (nf_{FEA})_i}{(nf)_i}$$

where $(nf)_i$ and $(nf_{FEA})_i$ are the analytical and FEA natural frequencies for the i th mode shape, respectively. From Fig. 2-27, it can be seen that 10 elements per link can capture up to fifth nonzero natural frequencies accurately.

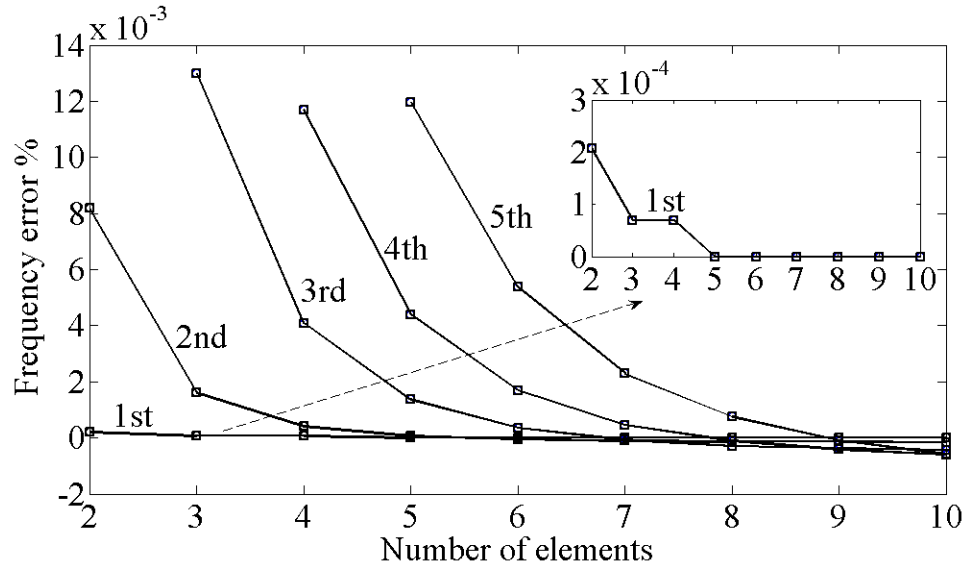


Fig. 2-27: Comparison of FEA and analytical natural frequency errors as a function of number of elements for the first five modes of a rotating single flexible manipulator

2.10. References

1. Wang, F. Y., and Gao, Y., 2003, *Advanced Studies Of Flexible Robotic Manipulators: Modeling, Design, Control And Applications: Series In Intelligent Control And Intelligent Automation*, Word Scientific, New Jersey, USA.
2. Low, K. H., and Vidyasagar, M., 1988, "A Lagrangian Formulation Of the Dynamic Model For Flexible Manipulator Systems," *Journal of Dynamic Systems, Measurement and Control*, **110** (2), pp. 175-181.
3. Zhang, X., Xu, W., Nair, S. S., and Cellabonia, V., 2005, "PDE Modeling And Control Of A Flexible Two-Link Manipulator," *IEEE Transactions on Control System Technology*, **13** (2), pp. 301- 312.
4. Bathe, K. J., 1996, *Finite Element Procedures*, Prentice Hall, New Jersey, USA.
5. Hoa, S. V., 1979, "Vibration Of A Rotating Beam With Tip Mass," *Journal of Sound and Vibration*, **67** (3), pp. 369-381.

6. Naganathan, G., and Soni, A. H., 1987, "Coupling Effects Of Kinematics And Flexibility In Manipulators," *International Journal of Robotics Research*, **6** (1), pp. 75-84.
7. Khulief, Y. A., 1992, "On The Finite Element Dynamic Response Of Flexible Mechanism," *Computer Methods in Applied Mechanics and Engineering*, **97** (1), pp. 23-32.
8. Khulief, Y. A., 2001, "Vibration Suppression In Rotating Beams Using Active Modal Control," *Journal of Sound and Vibration*, **242** (4), pp. 681-699.
9. Yang, J. B., Jiang, L. J., and D. Ch., Chen, 2004, "Dynamic Modeling And Control Of A Rotating Euler-Bernoulli Beam," *Journal of Sound and Vibration*, **274** (3), pp. 863-875.
10. Mayo, J., Dominguez, J., 1997, "Finite Element Geometrically Nonlinear Dynamic Formulation Of Flexible Multibody System Using A New Displacement Representation," *Journal of Vibration and Acoustics*, **119** (4), pp. 573-581.
11. Prezemieniecki, J. S., 1967, *Theory Of Matrix Structural Analysis*, McGraw Hill, New York, USA.
12. Meirovitch, L., 1986, *Elements Of Vibration Analysis*, McGraw Hill, New York, USA.
13. Book, W. J., 1984, "Recursive Lagrangian Dynamics Of Flexible Manipulator Arms," *International Journal of Robotics Research*, **3** (3), pp. 87-101.
14. De Luca, A., and Siciliano, B., 1991, "Closed-Form Dynamic Model Of Planar Multilink Lightweight Robots," *IEEE Transactions on Systems, Man and Cybernetics*, **21** (4), pp. 826-839.
15. Yuan, B. S., Book, W. J., and Huggins, J. D., 1993, "Dynamics Of Flexible Manipulator Arms: Alternative Derivation, Verification, And Characteristics For Control," *Journal of Dynamic Systems, Measurement and Control*, **115** (3), pp. 394-404.
16. Chen, W., 2001, "Dynamic Modeling Of Multi-Link Flexible Robotic Manipulators," *Computers and Structures*, **79** (2), pp. 183-195.

17. Gosavi, S. V., and Kelkar, A. G., 2004, "Modelling, Identification And Passivity-Based Robust Control Of Piezo-Actuated Flexible Beam," *Journal of Vibration and Acoustics*, **126** (2), pp. 260-271.
18. Theodore, R. J., and Ghosal, A., 1995, "Comparison Of The Assumed Modes and Finite Element Models For Flexible Multilink Manipulators," *International Journal of Robotics Research*, **14** (2), pp. 91-111.
19. Hale, J. K., and Verduyn Lunel, S. M., 2001, "Effects Of Small Delays On Stability And Control", *Operator theory: Advances and Applications*, **122**, pp. 275-301.
20. Benosman, M., Le Vey, G., Lanari, L., and De Luca, A., 2004, "Rest-to-Rest Motion For Planar Multi-Link Flexible Manipulator Through Backward Recursion", *Journal of Dynamic Systems, Measurement and Control*, **126** (1), pp. 115-123.
21. Cheong, J., Chung, W. K., and Youm, Y., 2004, "Inverse Kinematic Of Multilink Flexible Robotics For High-Speed Application", *IEEE Transactions on Robotics and Automation*, **20** (2), pp. 269-282.
22. Moallem, M., Patel, R. V., and Khorasani, K., 2001, "Nonlinear Tip-Position Control Of A Flexible-Link Manipulator: Theory And Experiments", *Automatica*, **37** (11), pp. 1825-1834.
23. Shan, J., Hong, T. L., and Sun, D., 2005, "Slewing and Vibration Control Of A Single-Link Flexible Manipulator By Positive Position Feedback (PPF)", *Mechatronics*, **15** (4), pp. 487-503.
24. Morita, Y., Ukia, H., and Kando, H., 1997, "Robust Trajectory Tracking Control Of Elastic Robot Manipulators", *ASME Journal of Dynamic Systems, Measurements and Control*, **119** (4), pp. 727-735.
25. Moallem, M., Khorasani, K., and Patel, R. V., 1998, "Inversion – Based Sliding Control Of A Flexible-Link Manipulator", *International Journal of Control*, **71** (3), pp. 477-490.
26. Ginsberg, J. H., 1995, *Advanced Engineering Dynamics*, Cambridge University Press, New York, USA.

27. Greenwood, D. T., 1965, *Principles Of Dynamics*, Prentice Hall, New York, USA.
28. Centinkunt, S., and Ittoop, B., "Computer-Automated Symbolic Modeling Of Dynamics Of Robotic Manipulators With Flexible Link," *IEEE Transactions on Robotics and Automation*, **8** (1), pp. 94-105.
29. Li, C. J., and Sankar, T. S., 1993, "Systematic Methods For Efficient Modeling And Dynamics Of Flexible Robot Manipulators," *IEEE Transactions on Systems, Man, and Cybernetics*, **23** (1), pp. 77-95.
30. Angeles, J., and Lee, S., 1988, "The Formulation Of Dynamical Equations Of Holonomic Mechanical Systems Using A Natural Orthogonal Complement," *Journal of Applied Mechanics*, **55** (1), pp. 243-244.
31. Saha, S. K., and Angeles, J., 1991, "Dynamics Of Nonholonomic Mechanical Systems Using A Natural Orthogonal Complement," *Journal of Applied Mechanics*, **58** (1), pp. 238-243.
32. Fotouhi, R., 2007, "Dynamic Analysis Of A Very Flexible Beam", *Journal of Sound and Vibration*, **305** (3), pp. 521-533.
33. Vakil, M., Fotouhi, R., and Nikiforuk, P. N., 2007 "Application Of The Integral Manifold Concept For The End-Effector Trajectory Tracking Of A Flexible Link Manipulator", *American Control Conference*, July 11-13, New York, USA, pp. 741-747.
34. Vakil, M., Fotouhi, R., and Nikiforuk, P. N., 2007 "End-Effector Trajectory Tracking Of A Flexible Link Manipulator Using Integral Manifold Concept", *Journal of Sound and Vibration*, Submitted.
35. Oguamanam, D. C. D., Heppler, G. R., and Hansen, J. S., 1998, "Modelling Of A Flexible Slewing Link," *Journal of Vibration and Acoustics*, **120** (4), pp. 994-996.
36. Alberts, T. A., Xia, H., and Chen, Y., 1990, "Dynamic Analysis To Evaluate Viscoelastic Passive Damping Augmentation For The Space Shuttle Remote Manipulator System" *Advances In Dynamic and Control of Flexible Spacecraft and Spaced-based Manipulators*, **20**, pp. 35-41.

37. Fraser, R., and Daniel, R. W., 1991, *Perturbation Techniques For Flexible Manipulators*, Kulwer Academic Publishers, Boston, USA.
38. Trindade, M. A., and Sampaio, R., 2002, "Dynamics Of Beams Undergoing Large Rotations Accounting For Arbitrary Axial Deformation", *Journal of Guidance, Control and Dynamics*, **25** (4), pp. 634-643.
39. Shabana, A. A., 2001, *Computational Dynamics*, John Wiley & Sons, New York, USA.
40. Saha, S. K., 1999, "Dynamics Of Serial Multibody Systems Using The Decoupled Natural Orthogonal Complement Matrices," *Journal of Applied Mechanics*, **66** (4), pp. 986-996.
41. Khan, A. W., Krovi, V. N., Saha, S. K., and Angeles, J. , 2005, " Recursive Kinematics And Inverse Dynamics For A Planar 3R Parallel Manipulator", *ASME Journal of Dynamic Systems, Measurement, and Control*, **127** (4), pp. 529-536.
42. Bellezza, F., Lanari L., and Ulivi, G., 1990, "Exact Modeling Of Flexible Slewing Link," *Proceedings of IEEE International Conference on Robotics and Automation*, Los Angeles, USA, pp. 734-739.
43. ANSYS, Release 10, "Release 10 Documentation For ANSYS", element reference. (www.ansys.com)
45. Fotouhi, R., 1996, "Time Optimal Control Of 2-Link Manipulators," Ph.D. thesis, University of Saskatchewan.
46. Fotouhi, R., Szyszkowski, W., Nikiforuk, P. N., and Gupta, M. M., 1999, "Parameter Identification and Trajectory Following Of A Two-Link Rigid Manipulator," *Journal of Systems and Control Engineering, Proceedings Institution of Mechanical Engineering, Part I*, **213** (6), pp. 455-466.
47. Zhang, X., and Erdman, A. G., 2006, "Optimal Placement Of Piezoelectric Sensors And Actuators For Controlled Flexible Linkage Mechanisms," *Journal of Vibration and Acoustics*, **128** (2), pp. 256-260.

Chapter 3. Piece-wise causal inversion by output redefinition for a flexible link manipulator

Abstract:

A new causal dynamic end-effector inversion method for a single flexible link manipulator is introduced. Contrary to the available non-causal inversion technique, this method does not lead to pre-actuation and works even in the presence of the purely imaginary zeros for the transfer function. Based on this approach, the desired end-effector trajectory is divided into a finite number of segments. In each segment, the desired trajectory is redefined so that a bounded continuous torque through causal dynamic inversion is obtained. The redefinition of the desired trajectory at each segment employs summation of stable exponential functions, which leads to a family of answers for the redefined trajectory which is an advantage for control engineers. The included results of the simulation and experimental studies show the feasibility and effectiveness of this new technique.

Key words: Flexible link Manipulator, Causal dynamic inversion, Dynamic modeling, Non-minimum phase system

3.1. Introduction

Smaller mass, lower peak power and less energy consumption are among the main potential advantages of Flexible Link Manipulators (FLM) over rigid link manipulators [1]. Because of these potential advantages, their application in industry is expected to increase provided their performance becomes more predictable and reliable. To improve the general performance of FLM, much research has been carried out during the past decade; in particular, because of the importance of End-Effector Trajectory Tracking (EETT), many of them have been focused on the EETT of FLM. The challenging aspect of the research, the EETT of FLM, is due to the fact that the system is non-minimum phase [2]. The non-minimum phase property is the consequence of the flexibility of the link and the non-collocation of the actuator, which is the input, at the base and sensor, which is the output, at the end-effector of the manipulator [3,4,5].

A possible approach for the EETT of FLM is the use of the output regulation technique introduced in [6]. The feasibility of applying this method to FLM was studied in [7]. To apply this method, the nontrivial solution for a set of first order partial

differential equations is required. Moreover, for the EETT of a FLM which has non-minimum phase characteristics, the application of the method introduced in [6] leads to transient errors at the initial and final portions of the manoeuvre [8]. Another alternative for the EETT of a FLM is the use of stabilizing feedback (on-line signal indicated by 2 in Fig. 3-1) with the feedforward command (off-line signal indicated by 1 in Fig. 3-1) created by the inversion of the system dynamic. Due to the non-minimum phase property of the system, bounded causal inversion of the dynamic equation for a desired end-effector trajectory is not achievable [9 Ch. 6]. However, for a linear model of a Single Flexible Link Manipulator (SFLM), the non-causal inversion of the dynamic equations for a desired end-effector trajectory was introduced in [10,11] and the extension of the method to the general nonlinear systems was studied in [8]. Rather than the non-causal¹³ input torque, in [12] a method was proposed that creates a causal end-effector inversion for a SFLM through rest-to-rest and point-to-point motion planning. In general, however, it is more desirable to invert the dynamic equations for the desired end-effector trajectory rather than planning a point-to-point and rest-to-rest motion.

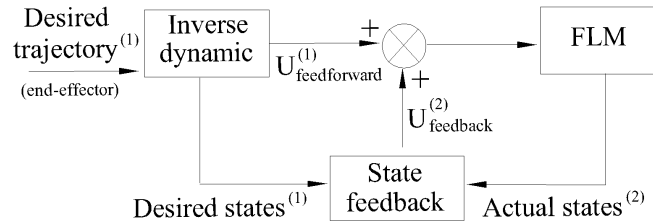


Fig. 3-1: Schematic of the end-effector trajectory tracking method, 1: off-line signal, 2: on-line signal

In this chapter a causal end-effector trajectory inversion by the output redefinition for a SFLM is introduced. This new causal method, unlike the available non-causal inversion technique [10,11] which does not tolerate the existence of purely imaginary zeros [13], works even if the transfer function of the system has purely imaginary zeros. To utilize this new technique, the desired end-effector trajectory is divided into several segments and is redefined in each segment by the Summation of Stable Exponential Functions (SSEF) [14], that is:

¹³ The causal signal at any time depends on the values of the states up to that time, while the non-causal signal depends on the values of states before and after that time.

$$\tilde{y}_d(t) = \sum_{j=0}^r c_j e^{m_j t}, \quad m_j < 0 \quad (3-1)$$

Here $\tilde{y}_d(t)$ is the redefined end-effector trajectory and c_j are constants which are calculated, after the selection of r and m_j , so that a bounded continuous torque through causal inversion is possible. To clarify the concept an example is provided in Section 3.4. There are four steps to this approach which are explained in Section 3.5. Also a method for the selection of r and m_j is introduced in Section 3.6. Comparing the SSEF with a polynomial function having r terms, which has the same number of terms as the SSEF, that is:

$$y_p(t) = \sum_{j=0}^r p_j t^j \quad (3-2)$$

it can be seen that the number of the choices available using SSEF, c_j and m_j in Eq. (3-1), is twice the number of choices available in the polynomial, p_j in Eq. (3-2). Therefore, while for a predefined set of conditions equal to the number of coefficients in $y_p(t)$ there is only one solution set for the polynomial function, for the same conditions there is a family of possible solution for $\tilde{y}_d(t)$ in SSEF. Hence, by minimizing the error between the desired trajectory and the redefined trajectory, it is possible to find the best member of the family of the solutions. Finally, although, this method has been developed for the end-effector trajectory inversion of a SFLM, it can easily be extended to any linear single-input single-output nonminimum phase system with or without purely imaginary zeros. It is worth noting that as a limitation, this approach can not be applied to any nonlinear system.

In the following sections, first the dynamic equation of a SFLM is derived. The piece-wise stable inversion is then introduced. After presenting the simulation and experimental results, the conclusions drawn from the research are provided.

3.2. Dynamic modeling of a SFLM

Due to the link flexibility, FLM have an infinite number of degrees of freedom and their dynamic equations have infinite dimensions characteristics [15,16]. Not only is working with infinite dimensional dynamic equations troublesome, but also controllers are generally designed for finite dimensional systems [17, p. 194]. Therefore, the infinite dimensional dynamic equations should be changed into finite dimensional, truncated ones. In this chapter, to change the infinite dimensional dynamic equations of a SFLM into a finite dimensional one, a combination of the Lagrange equations and the Assumed Mode shape Method (AMM) approximation [18,19] is used. Also, the flexible link is modeled as an Euler-Bernoulli beam. Therefore, the rotary inertia and deformation due to shear are neglected.

In the AMM the spatial deflection of the flexible link, $\xi(\gamma, t)$ in Fig. 3-2, is described by a finite series composed of spatial pre-defined shape functions, $\phi_j(\gamma)$, multiplied by the time varying weight functions, $\lambda_j(t)$. Therefore:

$$\xi(\gamma, t) = \sum_{j=1}^n \phi_j(\gamma) \lambda_j(t) \quad (3-3)$$

where n is the number of the assumed mode shapes and the $\phi_j(\gamma)$ which were adopted from [20], are the exact mode shape of a slewing SFLM. To employ the Lagrange equation, the kinetic and potential energies of the SFLM are required and will be obtained in the following.

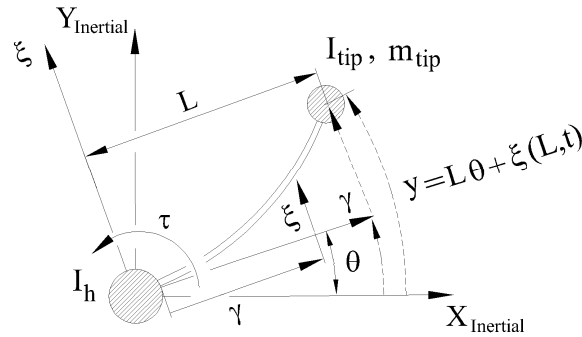


Fig. 3-2: Schematic of a SFLM

The kinetic energy of the SFLM, shown in Fig. 3-1, is:

$$T_M = T_l + T_h + T_{tip} \quad (3-4)$$

where

$$T_l = (1/2) \int_0^L \rho ((\dot{\gamma}\theta + \dot{\xi})^2 + (\dot{\theta}\xi)^2) d\gamma \quad (3-4a)$$

$$T_h = (1/2) I_h \dot{\theta}^2 \quad (3-4b)$$

$$T_{tip} = (1/2) m_{tip} ((L\dot{\theta} + \dot{\xi}(L,t))^2 + (\dot{\theta}\xi(L,t))^2) + (1/2) I_{tip} (\dot{\theta} + (\partial\dot{\xi}(L,t)/\partial\gamma))^2 \quad (3-4c)$$

and T_M is the total kinetic energy of the manipulator, T_l is the kinetic energy of the flexible link, T_h is the kinetic energy of the hub, T_{tip} is the kinetic energy of the end-effector, ρ is the mass per unit length of the flexible link, $\dot{\theta}$, $\dot{\xi}$ and $\partial\dot{\xi}/\partial\gamma$ represent, respectively, the time derivatives of θ , ξ and $\partial\xi/\partial\gamma$, I_h is the mass moment of inertia of the hub, m_{tip} and I_{tip} are the mass and mass moment of inertia of the end-effector, and L is the length of the link.

Since the manipulator motion is in the horizontal plane, there is no potential energy due to gravity. However, there is a strain energy due to the link's flexibility. This strain energy, neglecting the geometric effect for a beam in bending ([21], p. 388) and neglecting the portion of the strain energy due to the shearing and axial strains, for a linear elastic material is:

$$U_M = (1/2) \int_0^L EI (\partial^2 \xi / \partial \gamma^2)^2 d\gamma \quad (3-5)$$

where E is Young's modulus and I is the second moment of area. Substituting Eq. (3-3) into Eqs. (3-4) and (3-5), and using the Lagrange equations¹⁴ with the consideration that θ and λ_i $i = 1 \dots n$ are the generalized coordinates, the dynamic equations of a SFLM are:

$$\mathbf{M}(\lambda) \ddot{\mathbf{q}} + \mathbf{C}_{cc}(\dot{\theta}, \lambda, \dot{\lambda}) \dot{\mathbf{q}} + \mathbf{K}_B \mathbf{q} = \mathbf{F} \quad (3-6)$$

¹⁴ $d(\partial T_M / \partial \dot{q}_i) / dt - \partial T_M / \partial q_i + \partial U_M / \partial q_i = f_i$ where q_i is the i th generalized coordinate and f_i is the corresponding generalized force.

where $\mathbf{q} = [\theta \quad \lambda^T]^T$, $\lambda = [\lambda_1 \quad \lambda_2 \quad \dots \quad \lambda_n]^T$, λ_n is the weighting parameter for the n th mode shape, $\mathbf{M}(\lambda)$ is the mass matrix, $\mathbf{C}_{cc}(\dot{\theta}, \lambda, \dot{\lambda})$ is the matrix representing the Coriolis force and the component of the centrifugal force in the lateral direction, \mathbf{K}_B is the stiffness matrix and \mathbf{F} is the force vector. Since $\phi_j(x)$ is selected to satisfy the clamped boundary condition [19,20], \mathbf{F} is:

$$\mathbf{F} = \mathbf{H} \tau \quad (3-7)$$

where τ is the actuator torque and $\mathbf{H} = [1 \quad \mathbf{0}_{1 \times n}]^T$. Details of Eq. (3-6) are given in Appendix 3.I.

It is clear that the dynamic equation of a SFLM, Eq. (3-6), is nonlinear. The nonlinearity is the result of the $(\dot{\theta}^\xi)^2$ in the kinetic energy expressions of T_l and T_{Tip} in Eqs. (3-4a) and (3-4c), respectively. Neglecting the nonlinearities in the kinetic energy expressions by assuming small lateral deflection, the linear time invariant dynamic equation of a SFLM is:

$$\mathbf{M}\ddot{\mathbf{q}} + \mathbf{K}_B \mathbf{q} = \mathbf{H} \tau \quad (3-8)$$

where \mathbf{M} is constant contrary to $\mathbf{M}(\lambda)$ in Eq. (3-6). Details of Eq. (3-8) are available in the Appendix 3.I.

Finally, considering the material damping due to the internal friction and using the Rayleigh damping model, the damping matrix \mathbf{C}_D , is:

$$\mathbf{C}_D = (2\eta / \omega) \mathbf{K}_B \quad (3-9)$$

where η and ω are the damping ratio and natural frequency of the fundamental vibration mode shape, respectively. Thus, the linear time invariant dynamic model of a SFLM is:

$$\mathbf{M}\ddot{\mathbf{q}} + \mathbf{C}_D \dot{\mathbf{q}} + \mathbf{K}_B \mathbf{q} = \mathbf{H} \tau \quad (3-10)$$

3.3. End-effector inversion procedure

Definition 1: Consider the linear single-input single-output system of the form:

$$\begin{cases} \dot{X} = \mathbf{A}X + \mathbf{B}\tau & (3-11a) \\ y = \mathbf{C}X & (3-11b) \end{cases}$$

where \mathbf{A} , \mathbf{B} and \mathbf{C} are called state, input and output matrices respectively, and τ is the input and y is the output. This system has a well-defined relative degree r_w if and only if $\mathbf{C}\mathbf{A}^{(r_w-1)}\mathbf{B} \neq 0$. In other words, in the r_w th time differentiation of Eq. (3-11b), the input τ appears explicitly; that is, $y^{(r_w)} = \mathbf{C}\mathbf{A}^{r_w}X + \mathbf{C}\mathbf{A}^{(r_w-1)}\mathbf{B}\tau$.

The linear time invariant dynamic model of a SFLM, Eq. (3-10), considering the base torque as the input and the end-effector displacement as the output can be written as Eqs. (3-11a) and (3-11b), where: (y is shown in Fig. 3-2)

$$X = \begin{bmatrix} q \\ \dot{q} \end{bmatrix}, \mathbf{A} = \begin{bmatrix} \mathbf{0}_{n+1 \times n+1} & \mathbf{I}_{n+1 \times n+1} \\ -\mathbf{M}^{-1}\mathbf{K}_B & -\mathbf{M}^{-1}\mathbf{C}_D \end{bmatrix}, \mathbf{B} = \begin{bmatrix} \mathbf{0}_{n+1 \times 1} \\ \mathbf{M}^{-1}\mathbf{H} \end{bmatrix}, \mathbf{C} = [\mathbf{D} \quad \mathbf{0}_{1 \times n+1}],$$

$$\mathbf{D} = [L \quad \phi_1(L) \quad \dots \quad \phi_n(L)] \quad (3-12)$$

For the purpose of inversion the output y has to be differentiated $r_w = 2$ times [10,11] so that the input τ appears explicitly. That is, for a SFLM considering the end-effector displacement as the output, the relative degree is two and $\mathbf{C}\mathbf{A}\mathbf{B} \neq 0$. Thus, differentiating y in Eq. (3-11b) twice and noting that $\mathbf{C}\mathbf{B} = 0$ leads to:

$$\ddot{y} = \mathbf{C}\mathbf{A}^2X + \mathbf{C}\mathbf{A}\mathbf{B}\tau \quad (3-13)$$

Using the input-output linearization technique ([9] Ch. 6.1.3 and 6.4), the base torque has to be:

$$\tau_l = (1/\mathbf{C}\mathbf{A}\mathbf{B})(\ddot{y}_d - \mathbf{C}\mathbf{A}^2X) \quad (3-14)$$

where y_d is the desired end-effector trajectory and, for a SFLM, the scalar value $\mathbf{C}\mathbf{A}\mathbf{B} \neq 0$. Thus, replacing τ in Eq. (3-13) with the torque τ_l given in Eq. (3-14), results in:

$$\ddot{y} = \ddot{y}_d \quad (3-15)$$

However, since the order of this inversed system, Eq. (3-15), is two and the order of the original system, Eq. (3-11a) with \mathbf{A} and \mathbf{B} defined in Eq. (3-12), is $2(n+1)$ there is an internal dynamics¹⁵ of order $2(n+1)-2$ as pointed out in [9] which is discussed in the following. To obtain the associated internal dynamics, the transformation:

$$\boldsymbol{\psi} = \mathbf{T}\mathbf{X} \quad (3-16)$$

is considered where:

$$\boldsymbol{\psi} = [y \quad \dot{y} \quad \lambda_1 \quad \dots \quad \lambda_n \quad \dot{\lambda}_1 \quad \dots \quad \dot{\lambda}_n]^T, \mathbf{T} = \begin{bmatrix} \mathbf{D}_{1 \times n+1} & \mathbf{0}_{1 \times n+1} \\ \mathbf{0}_{1 \times n+1} & \mathbf{D}_{1 \times n+1} \\ \mathbf{0}_{2n \times 1} & (\mathbf{I}_o)_{2n \times 2n+1} \end{bmatrix}, \mathbf{I}_o = \begin{bmatrix} \mathbf{I}_{n \times n} & \mathbf{0}_{n \times n+1} \\ \mathbf{0}_{n \times n+1} & \mathbf{I}_{n \times n} \end{bmatrix}$$

The transformation given in Eq. (3-16), changes the dynamic model of a SFLM, given in Eq. (3-11a) considering \mathbf{X} , \mathbf{A} , \mathbf{B} and \mathbf{C} as given in Eq. (3-12), into:

$$\dot{\boldsymbol{\psi}} = \mathbf{T}\mathbf{A}\mathbf{T}^{-1}\boldsymbol{\psi} + \mathbf{T}\mathbf{B}\tau \quad (3-17)$$

Replacing τ in Eq. (3-17) with the torque τ_l given in Eq. (3-14) results in:

$$\dot{\boldsymbol{\psi}} = \mathbf{A}_\psi \boldsymbol{\psi} + \mathbf{B}_\psi \ddot{y}_d \quad (3-18)$$

where \mathbf{A}_ψ and \mathbf{B}_ψ are:

$$\mathbf{A}_\psi = \mathbf{T}\mathbf{A}\mathbf{T}^{-1} - (\mathbf{T}\mathbf{B}\mathbf{C}\mathbf{A}^2\mathbf{T}^{-1})/(\mathbf{C}\mathbf{A}\mathbf{B}) \quad \mathbf{B}_\psi = (\mathbf{T}\mathbf{B})/(\mathbf{C}\mathbf{A}\mathbf{B}) \quad (3-19)$$

and as mentioned earlier the scalar $\mathbf{C}\mathbf{A}\mathbf{B}$ is not zero. According to the definition of $\boldsymbol{\psi}$, and using the torque given in Eq. (3-14), for a SFLM the matrices \mathbf{A}_ψ and \mathbf{B}_ψ are:

$$\mathbf{A}_\psi = \begin{bmatrix} 0 & 1 & \mathbf{0}_{1 \times 2n} \\ 0 & 0 & \mathbf{0}_{1 \times 2n} \\ \mathbf{0}_{2n \times 1} & \mathbf{0}_{2n \times 1} & (\mathbf{A}_I)_{2n \times 2n} \end{bmatrix} \quad \mathbf{B}_\psi = \begin{bmatrix} 0 \\ 1 \\ (\mathbf{B}_I)_{2n \times 1} \end{bmatrix} \quad (3-20)$$

and the internal dynamics is:

$$\dot{\mathbf{X}}_I = \mathbf{A}_I \mathbf{X}_I + \mathbf{B}_I \ddot{y}_d \quad (3-21)$$

¹⁵ The part of the system dynamic which has been rendered “unobservable” in the input-output linearization is called the internal dynamics (See [9 Ch. 6] for more detail)

where $\mathbf{X}_I = [\lambda_1 \dots \lambda_n \dot{\lambda}_1 \dots \dot{\lambda}_n]^T$.

After the inversion procedure, since $\mathbf{X} = \mathbf{T}^{-1} [y_d \dot{y}_d \mathbf{X}_I^T]^T$, if \mathbf{X}_I is bounded for a bounded \ddot{y}_d , \mathbf{X} is also bounded. Thus, the inversion torque from Eq. (3-14) is bounded. However, because SFLM is a non-minimum phase system, some of the eigenvalues of \mathbf{A}_I in Eq. (3-21) have positive real parts ([9] Ch. 6.1.3, [10], [11]) and thus the internal dynamics is unstable. This means that the feedforward integration of Eq. (3-21), even for a bounded \ddot{y}_d , generally leads to an unbounded¹⁶ response for \mathbf{X}_I . For stable inversion if there are no purely imaginary eigenvalues for \mathbf{A}_I , the non-causal integration explained in [8,10,11] can be adopted. However, in this chapter, to have a bounded response for \mathbf{X}_I , y_d is redefined so that the causal integration of Eq. (3-21) assures a bounded \mathbf{X}_I . It should be noted that existence of the purely imaginary eigenvalues for \mathbf{A}_I is not a restriction for implementing this method.

3.4. Causal inversion by output redefinition

By using the transformation $\mathbf{X}_I = \mathbf{G}[(\mathbf{X}_I^s)^T (\mathbf{X}_I^u)^T]^T$, where the columns of the matrix \mathbf{G} are the eigenvectors of the matrix \mathbf{A}_I , $\mathbf{G}^{-1}\mathbf{A}_I\mathbf{G}$ is a diagonal matrix in Jordan canonical form. Eq. (3-21) can then be written as:

$$\begin{bmatrix} \dot{\mathbf{X}}_I^s \\ \dot{\mathbf{X}}_I^u \end{bmatrix} = \begin{bmatrix} \mathbf{A}_I^- & \mathbf{0} \\ \mathbf{0} & \mathbf{A}_I^+ \end{bmatrix} \begin{bmatrix} \mathbf{X}_I^s \\ \mathbf{X}_I^u \end{bmatrix} + \begin{bmatrix} \mathbf{B}_I^s \\ \mathbf{B}_I^u \end{bmatrix} \ddot{y}_d \quad (3-22)$$

where \mathbf{A}_I^- is a diagonal matrix with the diagonal elements that are the eigenvalues of \mathbf{A}_I with negative real parts, and \mathbf{A}_I^+ is a diagonal matrix with the diagonal elements that are the eigenvalues of \mathbf{A}_I with positive real parts. Also, if \mathbf{A}_I has purely imaginary eigenvalues, the corresponding diagonal matrix, also known as the Jordan block, will be included in \mathbf{A}_I^+ . Due to the existence of \mathbf{A}_I^+ , the causal integration of Eq. (3-22) for a

¹⁶ The unbounded signal grows to infinity as time goes to infinity. Also, a signal which has an ever-oscillating behavior is classified here as an unbounded signal.

bounded desired acceleration \ddot{y}_d , generally results in an unbounded response for \dot{X}_I'' and thus X_I will be unbounded.

For a given set of initial condition(s), to have a bounded causal \dot{X}_I'' , the desired acceleration \ddot{y}_d , is replaced by its redefinition, $\tilde{\ddot{y}}_d$, so that the causal solution for:

$$\dot{X}_I'' = \mathbf{A}_I^+ \dot{X}_I'' + \mathbf{B}_I'' \tilde{\ddot{y}}_d \quad (3-23)$$

is bounded. After finding the bounded \dot{X}_I'' from Eq. (3-23), the bounded \dot{X}_I^s can be calculated by the feedforward integration of:

$$\dot{X}_I^s = \mathbf{A}_I^- \dot{X}_I^s + \mathbf{B}_I^s \tilde{\ddot{y}}_d \quad (3-24)$$

Having \dot{X}_I'' and \dot{X}_I^s for the redefined acceleration $\tilde{\ddot{y}}_d$, the bounded \dot{X}_I , $\psi = [\tilde{y}_d \quad \dot{\tilde{y}}_d \quad \dot{X}_I^T]^T$, and \dot{X} (from Eq. (3-16)) can be calculated. Thus, by substituting $\tilde{\ddot{y}}_d$ and \dot{X} in Eq. (3-14), the required causal torque for the inversion of $\tilde{\ddot{y}}_d$ is obtained.

To clarify the basic concept of calculating a bounded \dot{X}_I'' by output redefinition, the following example is provided.

Example: Find the bounded \dot{X}_I'' by the output redefinition for $\dot{X}_I'' - a\dot{X}_I'' = b\ddot{y}_d$ $a > 0$

Without loss of generality, it is assumed that the following differential equation has to be solved for \dot{X}_I'' :

$$\dot{X}_I'' - a\dot{X}_I'' = b\ddot{y}_d \quad a > 0 \quad (3-25)$$

where $a > 0$ and b are arbitrary constants and \ddot{y}_d is the acceleration of the desired trajectory. Also it is assumed that the initial condition on \dot{X}_I'' is:

$$\dot{X}_I''(0) = \dot{X}_0 \quad (3-26)$$

The complete answer of \dot{X}_I'' from Eq. (3-25) is composed of two parts, the particular part $(\dot{X}_I'')_p$, and complementary part $(\dot{X}_I'')_c$, that is:

$$X_I'' = (X_I'')_c + (X_I'')_p \quad (3-27)$$

The particular part $(X_I'')_p$, depends on \ddot{y}_d and can be found by the convolution integral.

The complementary part $(X_I'')_c$, is:

$$(X_I'')_c = se^{at} \quad (3-28)$$

where s is constant and will be found from the initial condition and excitation function \ddot{y}_d . Since $a > 0$ if $s \neq 0$, $(X_I'')_c$ is unbounded; thus, generally an unbounded X_I'' will exist. To have a bounded X_I'' the desired acceleration \ddot{y}_d , is replaced by its redefinition $\tilde{\tilde{y}}_d$, in Eq. (3-25) so that:

1- The constant s in Eq. (3-28) is zero

2- The particular solution $(X_I'')_p$, corresponding to $\tilde{\tilde{y}}_d$, is bounded and satisfies the initial condition $X_I''(0) = X_0$, as given in Eq. (3-26).

For this purpose, \ddot{y}_d is redefined by:

$$\tilde{\tilde{y}}_d = \sum_{j=1}^r c_j e^{m_j t} \quad m_j < 0 \quad (3-29)$$

By replacing \ddot{y}_d in Eq. (3-25) with $\tilde{\tilde{y}}_d$:

$$\dot{X}_I'' - aX_I'' = b\tilde{\tilde{y}}_d \quad (3-30)$$

Moreover, in order for the redefined acceleration $\tilde{\tilde{y}}_d$, to have the same values as the desired acceleration \ddot{y}_d at zero time and the final time t_f , the following conditions must be satisfied:

$$\tilde{\tilde{y}}_d(0) = \ddot{y}_d(0), \quad \tilde{\tilde{y}}_d(t_f) = \ddot{y}_d(t_f) \quad (3-31)$$

The complete answer of X_I'' for Eq. (3-30) is given in Eq. (3-27), where $(X_I'')_c$ is given in Eq. (3-28), and $(X_I'')_p$ for the redefined acceleration $\tilde{\tilde{y}}_d$, is:

$$(X_I'')_p = \sum_{j=1}^r \frac{bc_j}{m_j - a} e^{m_j t} \quad (3-32)$$

Thus by selecting $m_j < 0$ and $m_j \neq a$, $(X_I'')_p$ is bounded. To have a bounded solution for X_I'' , $(X_I'')_c$ must then be zero, which means that $s = 0$. Therefore, assuming that the m_j in Eq. (3-29) are known, the unknowns c_j are chosen to make $s = 0$. A method for the selection of m_j is given in Section 3.6.

To have a unique solution for c_j , the number of the conditions, Eqs. (3-26) and (3-31), have to be the same as the number of the unknowns c_j . Therefore, for $r = 3$ to force $s = 0$ the $c_j, j = 1 \dots 3$ is calculated as:

$$\bar{\mathbf{c}}_k = \mathbf{Z}_k^{-1} (\mathbf{C}_T)_k \quad (3-33)$$

$$\mathbf{Z}_k = \begin{bmatrix} \frac{b}{m_1 - a} & \frac{b}{m_2 - a} & \frac{b}{m_3 - a} \\ 1 & 1 & 1 \\ e^{m_1 t_f} & e^{m_2 t_f} & e^{m_3 t_f} \end{bmatrix}, \bar{\mathbf{c}}_k = \begin{bmatrix} c_1 \\ c_2 \\ c_3 \end{bmatrix}, (\mathbf{C}_T)_k = \begin{bmatrix} X_0 \\ \ddot{y}_d(0) \\ \ddot{y}_d(t_f) \end{bmatrix} \quad (3-34)$$

After finding $c_j (j = 1 \dots 3)$ for the given $m_j (j = 1 \dots 3)$ from Eq. (3-33), $\tilde{\tilde{y}}_d$ is known as given in Eq. (3-29). In addition by integrating $\tilde{\tilde{y}}_d$ with respect to time for the given initial conditions, $\tilde{\tilde{y}}_d$ and \tilde{y}_d are also known. As well, $X_I'' = (X_I'')_p$, as given in Eq. (3-32), is bounded.

Remark 3.1: The smaller the error between $\tilde{\tilde{y}}_d$ and \ddot{y}_d , the closer will be $\tilde{\tilde{y}}_d$ to \dot{y}_d and \tilde{y}_d to y_d . To make $\tilde{\tilde{y}}_d$ closer to \ddot{y}_d , one can set the conditions that the time derivatives of the redefined acceleration $\tilde{\tilde{y}}_d$, up to the order h where $h \leq w$, be equal to the original desired acceleration \ddot{y}_d , at zero and t_f . This is in addition to the settings given in Eq. (3-31) and assuming that the desired acceleration is continuous up to the order w ; that is, $\ddot{y}_d \in C^w$. It is to be noted that, for the addition of these conditions, r in the above example has to be increased from 3 to $2h+3$ (see Section 3.6).

Remark 3.2: For the redefinition of the desired trajectory, the orthogonality of the employed functions, which are stable exponential functions, is not necessary. The orthogonality of two functions $f(x)$ and $g(x)$ over the range (a,b) with respect to the weight function $w(x)$ is defined as $O(f,g) = \int_a^b f(x).g(x).w(x)dx = 0$. Generally for the redefinition of a function, orthogonality of the contributing function is not a concern. As another example, in the finite element method, the solution of a differential equation is approximated (redefined) by shape functions, which are not orthogonal; for instance, the shape functions of the beam element, which is used in the structural analysis with bending, are cubic polynomials that are not orthogonal to each other; see Appendix 3.II for more details.

3.5. Piece-wise trajectory inversion by output redefinition

As explained in Section 4 to calculate the required torque through the end-effector inversion, a bounded response from the internal dynamics, Eq. (3-21), has to be obtained. Since the input to the internal dynamics is the acceleration of the end-effector trajectory (See Eq. (3-21) or (3-22)), the desired acceleration \ddot{y}_d is redefined to find a bounded response from the internal dynamics. Furthermore, by dividing the acceleration into several segments the accuracy of the redefinition of the desired trajectory is increased. For the piece-wise trajectory inversion the following steps have to be taken.

1- Divide the desired acceleration \ddot{y}_d , into several consecutive segments such that:

$$(\ddot{y}_d)_k = \ddot{y}_d, \quad t_{ik} \leq t \leq t_{fk}, \quad k = 1..v \quad (3-35)$$

where v is the number of the segments, t_{ik} and t_{fk} are the initial and final times of the k th segment and $(\ddot{y}_d)_k$ is in the k th segment. Note that $t_{i1} = t_i$ and $t_{fv} = t_f$ are the initial and the final maneuver times, respectively.

2- In the k th segment, redefine the desired acceleration $(\ddot{y}_d)_k$ by the SSEF:

$$(\tilde{\ddot{y}}_d)_k = \sum_{j=0}^r c_{jk} e^{m_{jk}t}, \quad m_{jk} < 0 \quad (3-36)$$

The selection of m_{jk} and r are explained in detail in Section 3.6.

3- Find the contribution of each exponential function, c_{jk} , for the k th segment such that the following three conditions are met:

3-1- Assuming that the original desired acceleration is continuous up to order w ; that is, $\ddot{y}_d \in C^w$, the values of the redefined acceleration and its derivatives up to order h , where $h \leq w$, at the beginning and end of each segment are equal to values of the original desired acceleration, that is:(see remark 3.1)¹⁷:

$$\begin{aligned} (\tilde{\ddot{y}}_d)_k \Big|_{t_{ik}} &= (\ddot{y}_d)_k \Big|_{t_{ik}}, \dots, (\tilde{\ddot{y}}_d)_k^{(h)} \Big|_{t_{ik}} = (\ddot{y}_d)_k^{(h)} \Big|_{t_{ik}} \\ (\tilde{\ddot{y}}_d)_k \Big|_{t_{jk}} &= (\ddot{y}_d)_k \Big|_{t_{jk}}, \dots, (\tilde{\ddot{y}}_d)_k^{(h)} \Big|_{t_{jk}} = (\ddot{y}_d)_k^{(h)} \Big|_{t_{jk}} \end{aligned} \quad (3-37a)$$

3-2- The complementary part of the solution of Eq. (3-23) is zero.

This condition assures that a bounded solution for the unstable part of the internal dynamics, Eq. (3-23), exists.

3-3- The continuity of \mathbf{X}_I^u at the beginning of each segment is satisfied, which guarantees that \mathbf{X} and torque τ_I are continuous.

To have a continuous torque from Eq. (3-14) when \ddot{y}_d is replaced by $\tilde{\ddot{y}}_d$, and $\tilde{\ddot{y}}_d$ have to be continuous. From Eq. (3-37a), it can be seen that $\tilde{\ddot{y}}_d$ is continuous. Also, $\mathbf{X} = \mathbf{T}^{-1} [y_d \quad \dot{y}_d \quad \mathbf{X}_I^T]^T$ and $\mathbf{X}_I = \mathbf{G} [(\mathbf{X}_I^s)^T \quad (\mathbf{X}_I^u)^T]^T$. Thus, to have a continuous \mathbf{X} , \mathbf{X}_I has to be continuous. This means \mathbf{X}_I^u and \mathbf{X}_I^s must be continuous. Since \mathbf{X}_I^s , which is calculated by the causal integration of Eq. (3-24) is continuous, if \mathbf{X}_I^u is also continuous, then \mathbf{X} and consequently the corresponding torque are continuous. Thus, to have a continuous solution for \mathbf{X}_I^u

¹⁷-The first and second derivatives of y with respect to time are shown as \dot{y} , \ddot{y} and the higher ones by $\ddot{y}^{(h)} = d^h \ddot{y} / dt^h = d^{(h+2)} y / dt^{(h+2)}$

the final value of X_I'' at the k th segment is considered as the initial condition of X_I'' at the $k+1$ th segment.

4- After calculating \tilde{y}_d and the corresponding bounded X_I'' , find the corresponding X_I^s from Eq. (3-24).

Finally, having X_I'' and X_I^s for the redefined acceleration \tilde{y}_d , the bounded X_I , $\psi = [\tilde{y}_d \quad \dot{\tilde{y}}_d \quad X_I^T]^T$, and X (from Eq. (3-16)) can be calculated. Then, the required causal torque for \tilde{y}_d is obtained from Eq. (3-14).

It is to be noted that the causal integration of the inverse dynamic equations when y_d is replaced with \tilde{y}_d , will be carried on from t_i to t_f . That is, the inverse dynamic feedforward command in Fig. 3-1 is only active from t_i to t_f . After t_f , only the joint PD feedback control assuming $\theta_d(t) = y_d(t_f)/L$ and $\dot{\theta}_d(t) = 0$, is active (see the simulation and experimental study sections). Therefore, since the feedforward inverse dynamic signal will not be used after t_f , the stability of the inverse dynamic equation for $t > t_f$ is not a concern.

Remark 3.3: Besides the conditions imposed in Eq. (3-37a), which were discussed in Remark 3.1, to make \tilde{y}_d closer to y_d in the k th segment, the following conditions can also be imposed.

$$\begin{aligned} (\tilde{y}_d)_k|_{t_{ik}} &= (y_d)_k|_{t_{ik}}, (\tilde{y}_d)_k|_{t_{jk}} = (y_d)_k|_{t_{jk}} \\ (\tilde{y}_d)_k|_{t_{ik}} &= (\dot{y}_d)_k|_{t_{ik}}, (\tilde{y}_d)_k|_{t_{jk}} = (\dot{y}_d)_k|_{t_{jk}} \end{aligned} \quad (3-37b)$$

As a result the redefined velocity, \tilde{y}_d , and redefined displacement, \tilde{y}_d , will have the same values as the desired velocity, \dot{y}_d , and the desired displacement, y_d , at times t_{ik} and t_{jk} . The extension of the proposed method by adding conditions (37b) is under investigation [22] and its experimental verification is underway; the results will be reported in the near future. However, even after imposing the above conditions, the

desired and redefined trajectories are not exactly the same at all times during the maneuver. This is due to the fact that the method presented in this chapter is based on the redefinition of the desired trajectory. It has to be emphasized that the approximation is the key in performing the causal inversion for non-minimum phase systems with hyperbolic and non-hyperbolic internal dynamics; for example, several other approximations has also been used in the pervious approaches [9 p. 264, 13,23,24], which neglected a part of the internal dynamics, utilized the feedback of the internal dynamics states to stabilize the internal dynamics or used the reflected new end-effector displacement. Thus, there is always a difference between \tilde{y}_d and y_d . The closeness of the desired and redefined trajectories can be measured by an error index which, for example, can be the normalized maximum difference between these trajectories; that is, $\max(|\tilde{y}_d - y_d|) / \max(|y_d|)$. If this index is not small enough, the redefined trajectory can be modified to bring the error index to an acceptable range. This modification can be done by increasing the number of segments or changing the value of m_{jk} of the k th segment.

3.6. Selection of variables (m_{jk}, r) of the redefined output

If the exact model of the system without any perturbation was available, the introduced inversion method could be used to calculate the required causal torque on-line. However, in the presence of the uncertainty, the required torque is calculated off-line using the nominal dynamic model and a state feedback is added for the robustness, as shown in Fig. 1, similar to [12]. Therefore, the end-effector inversion technique introduced here using the piece-wise trajectory redefinition is done off-line with causal integration. As a result, the selection of m_{jk} for the redefinition of the desired trajectory should also be done off-line. This off-line approach is explained in the following.

After the selection of m_{jk} for the k th segment, (explained later in this section) c_{jk} are found by solving a set of linear algebraic equations (see example in Section 3.4 and Eq. (3-33)). To find a unique c_{jk} from the linear algebraic equations the number of

unknowns, $r \text{ in } (\ddot{y}_d)_k = \sum_{j=0}^r c_{jk} e^{m_{jk} t}$, must be equal to the number of the equations resulting from imposing the conditions 3-1, 3-2 and 3-3 discussed in Section 3.5. Therefore, the required number of the exponential functions for each segment is:

$$r = 2(h+1) + nu \quad (3-38)$$

Here $2(h+1)$ equations come from the condition 3-1, Eq. (3-37a), where h is the highest derivative of the redefined acceleration used in Eq. (3-37a). Also, nu equations are due to the continuity of X_I'' at the start of each segment where nu is the size of the vector X_I'' (condition 3-3). After determining the required number of the exponential functions from Eq. (3-38), the satisfaction of conditions 3-1 to 3-3 results in the relationship between c_{jk} and m_{jk} (see example in the previous Section and Eq. (3-33)). Therefore, c_{jk} is available in terms of m_{jk} ($\bar{c}_k = \mathbf{Z}_k^{-1}(\mathbf{C}_T)_k$) and, consequently, $(\ddot{y}_d)_k$ in each segment can be calculated in terms of m_{jk} . Thus, it is possible to find the best set of m_{jk} for each segment

by minimizing the cost function, $error(m_{jk}) = \int_{t_{ik}}^{t_{fk}} ((\ddot{y}_d)_k - (\ddot{y}_d)_k)^2 dt$. It is one of the

potential benefits of the redefinition of the output through exponential functions. However, to find m_{jk} from this optimization approach, a set of nonlinear algebraic equations has to be numerically solved, which requires a set of initial values (guesses) for the unknown variables. Not only solving this nonlinear optimization might not be easy, but also without a suitable set of initial conditions obtaining the solution is not computationally efficient. As a remedy, in the following, a more computationally effective method is introduced and used. It should be noted that this method is easier to implement and more time efficient compared to calculating m_{jk} by optimization. Also, this method provides reasonably acceptable m_{jk} and makes it possible to continue and explore the concept of piece-wise trajectory redefinition by SSEF which is the main focus of this paper.

Consider the exponential function:

$$y = ce^{mt} \quad m < 0 \quad (3-39)$$

which has to be calculated in the interval $t_i < t < t_f$. The decay of the exponential function, y in Eq. (3-39) at t_f with respect to its value at time t_i is:

$$C_{dec} = y(t_f) / y(t_i) = e^{mt_f} / e^{mt_i} \quad (3-40)$$

Assuming a value for the decay C_{dec} , in the specified time interval $(t_i < t < t_f)$, the corresponding m is obtained by combining Eqs. (3-39) and (3-40), which is:

$$m = \ln(C_{dec}) / (t_f - t_i) \quad (3-41)$$

Thus, if the fastest and slowest decays for the exponential functions used in the k th segment are assumed to be $(C_{dec}^f)_k$ and $(C_{dec}^s)_k$ respectively, the corresponding m from Eq. (3-41), are:

$$m_k^f = \ln(C_{dec}^f)_k / (t_{fk} - t_{ik}), \quad m_k^s = \ln(C_{dec}^s)_k / (t_{fk} - t_{ik}) \quad (3-42)$$

According to Eq. (3-36), the number of the m at each segment has to be the same as the number of the required exponential functions. Thus, having the required number of the exponential functions for the k th segment from Eq. (3-38), and the slowest and the fastest m after the selection of $(C_{dec}^f)_k$ and $(C_{dec}^s)_k$ from Eq. (3-42), the other m are chosen between m_k^f and m_k^s . To have the maximum difference between the m for the numerical stability of the solution of the linear equations (see matrix \mathbf{Z}_k in Eq. (3-33)), the other m are equally spaced between m_k^f and m_k^s . Therefore, the m for the k th segment are:

$$m_{jk} = m_k^s + \frac{m_k^f - m_k^s}{(r-1)}(j-1), \quad j = 1 \dots r \quad (3-43)$$

From Eqs. (3-42) and (3-43) it is clear that by selecting different pairs of $(C_{dec}^f)_k$ and $(C_{dec}^s)_k$ different values for m_{jk} can be obtained. Thus, the redefinition of the desired trajectory at each segment can be done in several different ways, which is a benefit of using the SSEF instead of the polynomial functions.

3.7. Simulation results

To show the effectiveness of the proposed method in the cases of linear nonminimum phase systems with non-hyperbolic, near non-hyperbolic and hyperbolic internal dynamics, the simulation results of three examples are presented. The first example is a nonminimum phase SFLM with a non-hyperbolic internal dynamics; that is, there are purely imaginary zeros for its transfer function (or equally there are purely imaginary eigenvalues for matrix \mathbf{A}_l in Eq. (3-21)). The second example is a nonminimum phase SFLM with a near non-hyperbolic system, which means that its transfer function has zeros that are close to the imaginary axis. The third example is a nonminimum phase SFLM with hyperbolic internal dynamics and therefore it does not have any purely imaginary zeros or zeros that are close to the imaginary axis. The third example is also the simulation results for the SFLM which is available in the robotics laboratory of the University of Saskatchewan and its results are compared against the experimental ones given in Section 3-8.

3.7.1. Example 1: A SFLM with non-hyperbolic internal dynamics

For the first example, a SFLM with the physical properties given in table 3-1 was considered. This SFLM had the same physical parameters as in [12]. Moreover, the flexibility of the link was modeled with the first two flexible modes. The zeros of the transfer function which are the eigenvalues of matrix \mathbf{A}_l in Eq. (3-21) were ± 61.25 and $\pm 54.34 i$.

Table 3-1: Example 1: physical properties of the SFLM

$L(m)$	$EI(N.m^2)$	$I_h(kg.m^2)$	$\rho(kg / m)$	$I_{ip}(kg.m^2)$	$m_{ip}(kg)$
1.005	47.25	1.800×10^{-3}	2.032	4.742×10^{-2}	6.790

Since the transfer function of the SFLM had purely imaginary zeros $\pm 54.34 i$, it has non-hyperbolic internal dynamic. Thus, the non-causal inversion introduced in [8,10,11] was not possible [13]. However, the method described here can handle purely imaginary zeros. It is worth noting that although the linear model of a SFLM considering

the end-effector displacement as the output and the base torque as the input does not have purely imaginary zeros [25], due to the truncation, non-collocation of the sensor and actuator and without material damping consideration, purely imaginary zeros are inescapable [26, p.73].

For comparison, the desired end-effector displacement for the first example, as shown in Fig. 3-3, is taken exactly from [12], although this is a relatively slow trajectory. For the second example the speed of the maneuver was almost twice that of the first example. Although, these two examples may not be the best representations for (*very*) flexible link manipulators, nonetheless they are flexible manipulators with unstable internal dynamics.

That trajectory was obtained, using a polynomial for the planned output and assuming the following initial and final conditions (details can be found in [12]):

$$\begin{cases} y(5.50) = 1.57(m), y(0) = \dot{y}(0) = \ddot{y}(0) = \ddot{y}^{(1)}(0) = \ddot{y}^{(2)}(0) = \ddot{y}^{(3)}(0) = 0.0 \\ \dot{y}(5.5) = \ddot{y}(5.5) = \ddot{y}^{(1)}(5.5) = \ddot{y}^{(2)}(5.5) = \ddot{y}^{(3)}(5.5) = 0.00 \end{cases} \quad (3-44)$$

where $\ddot{y}^{(h)} = d^h \ddot{y} / dt^h = d^{(h+2)} y / dt^{(h+2)}$. The reason for selecting this trajectory is for comparison as discussed in the following. In [12] the trajectory, as given in Fig. 3-3, was obtained by adopting a point-to-point maneuver. However, the problem here was to follow a desired trajectory as opposed to a point-to-point motion. Therefore, the trajectory given in [12], and also shown in Fig. 3-3, was assumed as the desired trajectory and the piece-wise causal inversion was used to follow this trajectory. Thus, the required causal torques have to be the same here and in [12]. By comparing the torque in Fig. 3-4 and that obtained in [12] it was seen that these torques are in fact the same. This comparison can serve as a check for the validity of our new method.

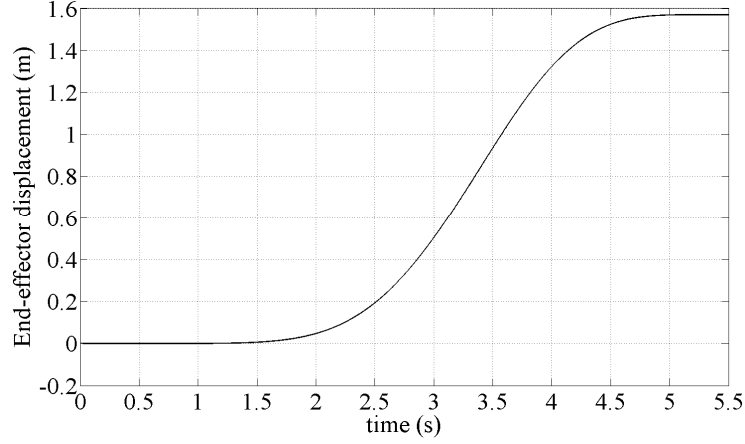


Fig. 3-3: Example 1, simulation, desired end-effector displacement

Since the input to the inverse equations was the second derivative of the desired end-effector displacement, Eqs. (3-14), (3-18) and (3-21), the acceleration of the end-effector was redefined by SSEF. Therefore, the desired end-effector acceleration, derived from the desired end-effector displacement, was divided into 5 equal segments which were:

$$0.00 \leq t \leq 1.1 \quad , \quad 1.1 \leq t \leq 2.2, \dots, \quad 4.4 \leq t \leq 5.5 \quad (3-45)$$

It was assumed that $h=2$ (see Eq. (3-37a) and remark 3.1 in Section 3.4). Moreover $nu=3$, where nu was the size of the vector X_l'' in Eq. (3-23). Therefore, the number of exponential functions for each segment was $r=9$ from Eq. (3-38). Also, the “ m ” for each segment were derived using Eqs. (3-42) and (3-43) and assuming:

$$(C_{dec}^f)_k = 0.0001 \quad (C_{dec}^s)_k = 1.000 \quad (3-46)$$

Due to the redefinition of the acceleration, the end-effector velocity at the end of the maneuver would not necessary be zero and the final position of the end-effector might be different from the desired one. The closer the redefined acceleration is to the desired acceleration, the smaller will be the difference. However, the addition of a joint PD controller to the nominal input torque, derived by piece-wise causal inversion, not only makes the closed loop control robust but also reduces these errors to zero and suppresses the link’s vibration [27]. Therefore, the input torque to the dynamic model was set to:

$$\tau = \tau_l + k_p(\theta_d - \theta) + k_D(\dot{\theta}_d - \dot{\theta}) \quad (3-47)$$

where τ_l was the piece-wise causal torque calculated from the inversion of the linear dynamic equation, of Eq. (3-8), k_p and k_D were the scalar gains, and θ_d and $\dot{\theta}_d$ were the redefined joint rotation and velocity, respectively. The torque obtained from Eq. (3-47) was applied to the linear dynamic model, Eq. (3-8). After 5.5 (s), the computed inverse dynamic torque, τ_l in Eq. (3-47), was set to zero. Thus for $t > 5.5$ (s) only the joint PD controller, assuming the desired joint rotation stayed constant at $y_d(t_f)/L = 1.56$ (rad), was active. The stability of the proposed controller is given in Appendix 3.III.

In Fig. 3-4, the simulation torque employing $k_p = 15$ and $k_D = 30$ is shown. These gains were obtained by trial and error observing the system's response (relatively fast settling time and small overshoot) and also noting that k_p and k_D had to be selected so that all the eigenvalues of matrix \mathbf{A}_E in Eq. (3- A20) in Appendix 3. III had negative real parts. For the initial estimate in the trial and error procedure, the gains k_p and k_D were selected based on the single rigid link counterpart of the SFLM as in [27]. By selecting the gains $k_p = 15$ and $k_D = 30$, the eigenvalues of \mathbf{A}_E in this example were $\{-573.2, -3.435 \pm 60.00i, -3.445 \pm 3.456i, -0.5858\}$. Since all the eigenvalues of matrix \mathbf{A}_E had negative real parts, the closed-loop system was stable and thus its response was guaranteed to be bounded (see the stability proof in Appendix 3. III).

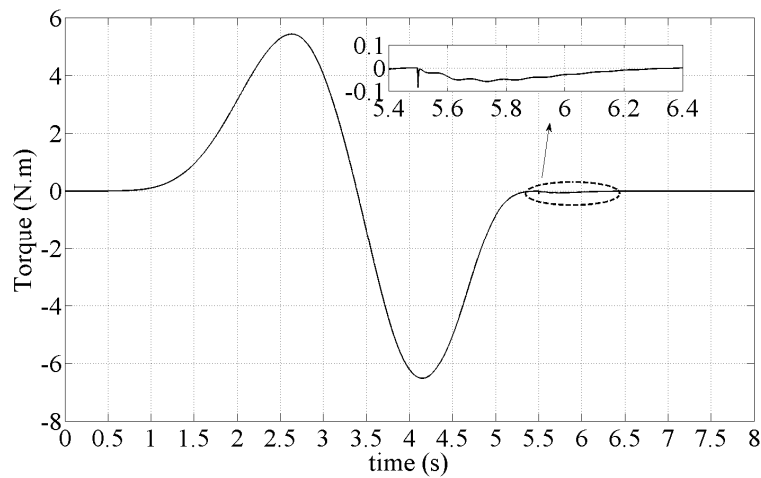


Fig. 3-4: Example 1, simulation, required base torque for causal end-effector trajectory inversion of the SFLM

The small value of the torque after 5.5 (s) was due to the joint PD controller. Moreover, it was observed that the torque was discontinuous at 5.5 (s) as expected. This was due to the fact that after 5.5 (s) the off-line inverse torque was set to zero and only the joint PD controller was active.

In Fig. 3-5, the desired and actual end-effector displacements are shown. In Fig. 3-6, the difference between the actual and desired end-effector displacements, $error = y_d - y$, is shown. As can be seen, after 5.5 (s), due to the PD controller, the actual displacement approached the desired displacement.

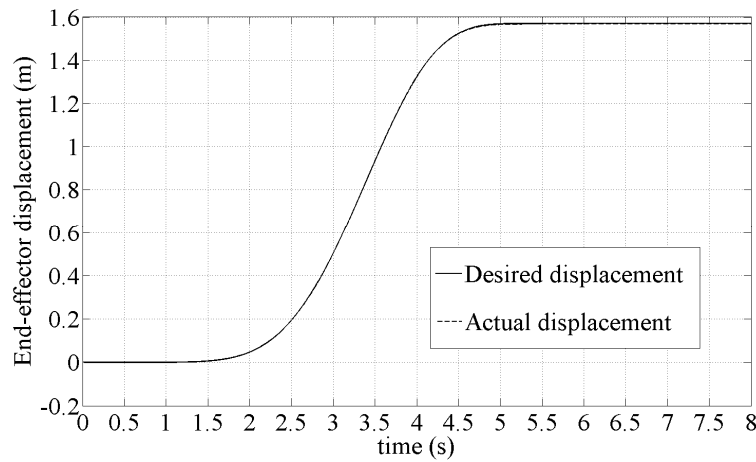


Fig. 3-5: Example 1, simulation, desired and actual end-effector displacements for the SFLM

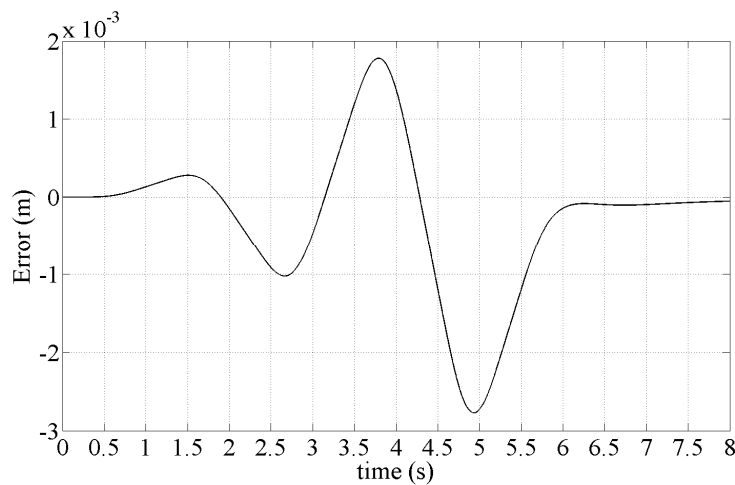


Fig. 3-6: Example 1, simulation, the difference between the actual and desired end-effector displacements of the SFLM which are shown in Fig. 3-5

Remark 3.4: To make the torque discontinuity at the end of the maneuver approach zero, the desired trajectory in the last segment can be redefined so that, at the end of the maneuver, t_f , not only the redefined displacement and its velocity have the same values as their desired ones, as explained in Remark 3.3, but also the link's deflection, due to the link flexibility, and its velocity set to be zero, that is $X_l(t_f) = 0$, where X_l is defined in Eq. (3-21). Therefore, after applying the torque obtained by the inversion process to the dynamic model, the manipulator comes to rest at the end of the maneuver, for a rest-to-rest motion, while the end-effector moves along a desired path. However, due to the existence of the unmodeled dynamic, even after applying such an inversion torque, the joint PD controller must be employed to suppress the link's vibration and reduce the steady tracking error to zero. This leads to a torque jump at the end of the maneuver. Nevertheless, the jump in the torque will be smaller compared to the case where the conditions $X_l(t_f) = 0$ and Eq. (3-37b) are not imposed on the redefined trajectory. The addition of these conditions to the method discussed in this chapter is under investigation [22] and the results will be available in the near future.

3.7.2. Example 2: A SFLM with near non-hyperbolic internal dynamics

The physical properties for the second example are given in Table 3-2. These properties were slightly different than those in Table 3-1. Moreover, to change the non-hyperbolic internal dynamics (purely imaginary zeros) into near a non-hyperbolic one (zeros which are close to imaginary axis) Rayleigh's material damping given in Eq. 3-9, was considered. The damping ratio of Rayleigh's material damping was set to $\eta = 0.02$, which corresponded to manipulators working in outer space [28]. The zeros of the transfer function were 77.58, -72.17, and $-1.31 \pm 52.20i$. Therefore there were no purely imaginary zeros, but, there were zeros ($-1.31 \pm 52.20i$) which were very closer to the imaginary axis than other two zeros (77.58 and -72.17).

Table 3-2. Example 2, physical properties of the SFLM

$L(m)$	$EI(N.m^2)$	$I_h(kg.m^2)$	$\rho(kg / m)$	$I_{tip}(kg.m^2)$	$m_{tip}(kg)$
1.000	47.00	1.800×10^{-3}	1.500	4.800×10^{-2}	7.000

The desired end-effector acceleration and the corresponding desired velocity and displacement, shown in Fig. 3-7, were considered. The desired end-effector acceleration was composed of several continuous third order polynomials, for time from 0 to 1, 1 to 3, and 3 to 4 (s). The average maneuver speed in this example was almost twice that of the first example. It is worth noting that by increasing the speed of maneuver, the link's lateral deflection will increase. However, if the link's lateral deflection is not small, then the nonlinear model of a SFLM has to be used. Therefore, there is a limitation for the speed of maneuver if the linear Euler-Bernoulli model of SFLM is to be used.

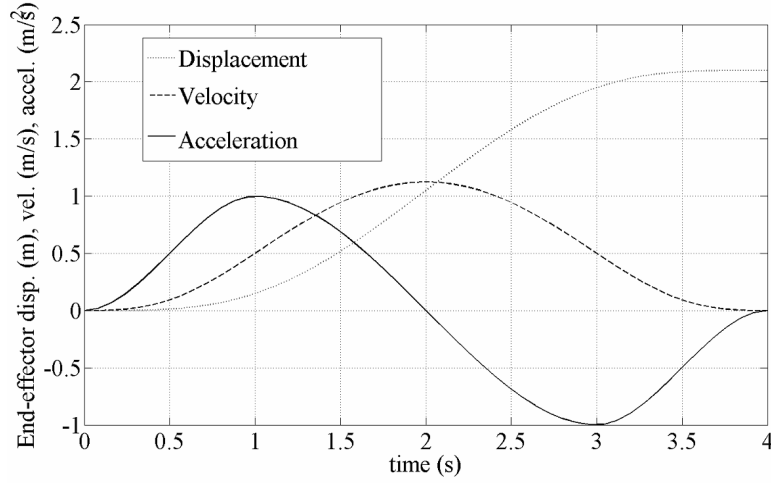


Fig. 3-7: Example 2, simulation, desired end-effector acceleration, velocity and displacement of the SFLM

For the stable inversion, the desired acceleration of the end-effector was divided into 8 equal segments which were:

$$0.0 \leq t \leq 0.5 \quad , \quad 0.5 \leq t \leq 1, \dots, \quad 3.5 \leq t \leq 4 \quad (3-48)$$

In addition, in each segment the desired acceleration was redefined by SSEF. The zeros of the transfer function which are the eigenvalues of the matrix \mathbf{A}_l in Eq. (3-21)

were $77.58, -72.17$, and $-1.31 \pm 52.20i$, as already mentioned. Due to the material damping consideration, there were no purely imaginary zeros [26 p. 73]. Also only one of the zeros had a positive real part, which was 77.58 ; that is, $nu=1$. Similar to Example 1, it was assumed that $h=2$. Therefore the required number of exponential functions in each segment was $r=7$ from Eq. (3-38). The “ m ” for each segment were found assuming:

$$(C_{dec}^f)_k = 0.0001 \quad (C_{dec}^s)_k = 1.000 \quad (3-49)$$

To investigate the response of the actual system, the evaluated torque from the inversion of the linear dynamic model with a joint PD controller, Eq. (3-47), was applied to the actual nonlinear model of the SFLM, Eq. (3-6), using $k_p = 15, k_D = 30$. These gains were found as explained in example 1. By using these gains the eigenvalues of the matrix \mathbf{A}_E in Eq. (3-A20) in Appendix 3.III were $\{-769.4, -4.904 \pm 61.99i, -3.447 \pm 3.460i, -0.5851\}$. Since all these eigenvalues of \mathbf{A}_E in this example had negative real parts, the closed-loop system was stable and thus its response was bounded as proved in Appendix 3.III. It is to be noted that in example 1, the torque was applied to the linear dynamic model presented in Eq. (3-8). The simulation torque is shown in Fig. 3-8. The off-line inverse torque was applied up to 4 (s). Due to the redefinition of the acceleration and also application of the torque evaluated from the inversion of the linear system to the nonlinear system, the actual values of the end-effector velocity and displacement at the end of the maneuver differed from the desired ones. However, as already stated in example 1, the application of a joint PD controller can reduce these errors and the vibration of the link to zero and also the small torque after $t_f = 4.0$ (s) from the PD controller was used to eliminate the tracking error. The desired joint rotation for $t > t_f$ stayed constant at $y_d(t_f)/L = 2.1$ (rad). Moreover in Fig. 3-8, as in Fig. 3-4, the torque had a small jump at $t_f = 4.0$ (s) for the same reason as explained in example one, (See remark 3.4).

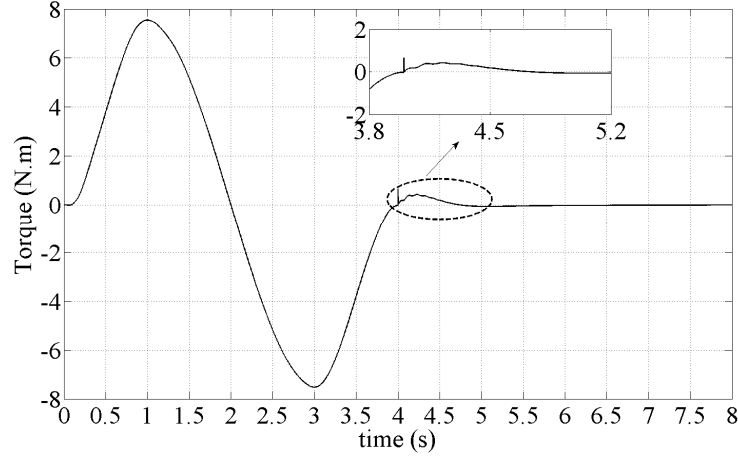


Fig. 3-8: Example 2, simulation, required base torque for causal end-effector trajectory tracking of the SFLM

The actual and desired end-effector displacements are shown in Fig. 3-9. Moreover, the difference between the actual and desired trajectories, $error = y_d - y$, is shown in Fig. 3-10. There are two reasons why the difference between the actual and desired trajectories in example 2, Fig. 3-10, is larger than the difference between the actual and desired trajectories in example 1, Fig. 3-6, as follows. First, the average speed of the maneuver for example 2 was approximately twice that for example 1. Second, in example 2 the inverse off-line computed torque obtained from linear model, Eq. (3-47), was applied to the nonlinear model, Eq. (3-6).

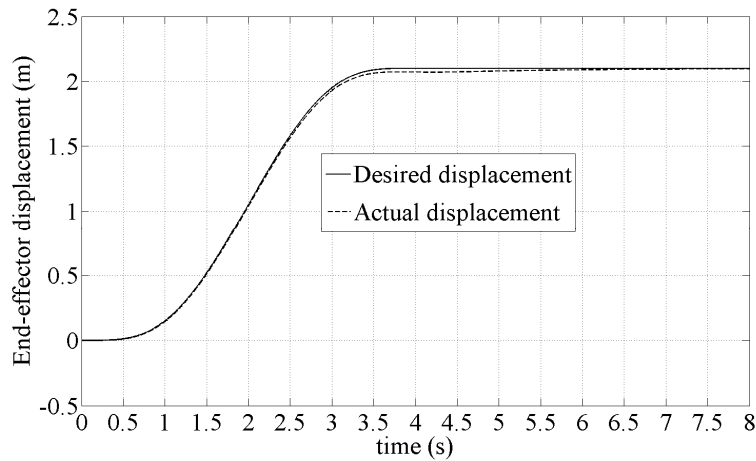


Fig. 3-9: Example 2, simulation, desired and actual end-effector displacements of the SFLM

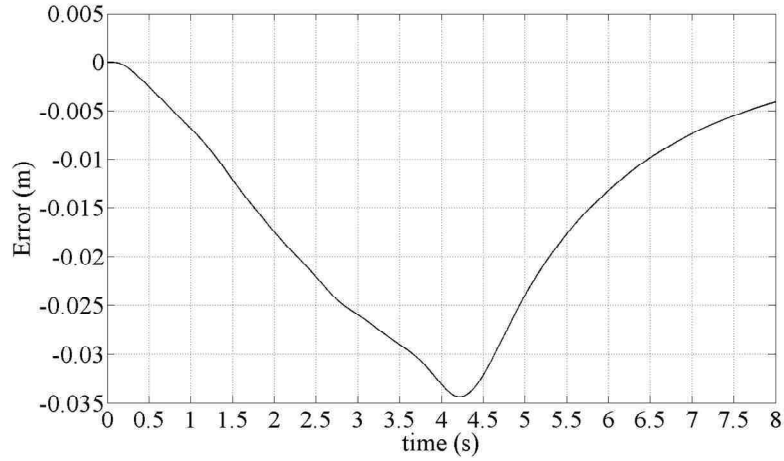


Fig. 3-10: Example 2, simulation, the difference between the actual and desired end-effector displacements of the SFLM which are shown in Fig. 3-9

The satisfactory results of the simulation with the nonlinear dynamic model confirm that the combination of the joint PD controller and the off-line inverse dynamic torque, computed from the linear model, can deal with the perturbation and uncertainty in this example.

3.7.3. Example 3: A SFLM with hyperbolic internal dynamics

For the third simulation example, the SFLM setup available in the robotics laboratory at the University of Saskatchewan (Robotics Lab of the U of S) was considered. This SFLM is shown in Fig. 3-11.

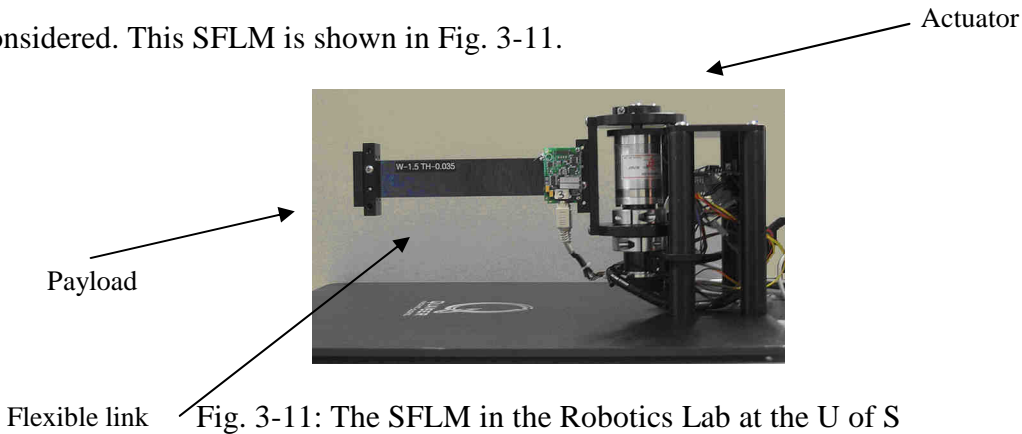


Fig. 3-11: The SFLM in the Robotics Lab at the U of S

The robot consisted of a DC driving via harmonic gearbox. The harmonic drive was a Precision Servo Actuator from Harmonic Drive Technologies. Specially, its model number was PSA-8-080. It offered zero backlash and used Maxon 118752 precision brush motor (20 watts). The flexible link of the SFLM in Fig. 3-11, was made of stainless

steel with a length of 0.2300 (m), a thickness of 8.890×10^{-4} (m) and a width of 0.0381(m). The mass moment of inertia of the hub was 0.0198 (kg.m^2), and the coefficient of viscous damping in the rotating joint was 0.3200 (N.m.s/rad). Moreover, the SFLM had a payload at the tip with the mass of 0.1690 (kg) and a mass moment of inertia of 2.570×10^{-5} (kg.m^2).

The link flexibility was modeled with one mode shape per link as will be explained later in this section. The time varying weight of this mode was measured with an stain gauge mounted on the base. The resolution of the end-effector measurement by using this strain gauge was 4.05×10^{-4} (m). The zeros of the corresponding transfer function considering the end-effector displacement as the output were at ± 212.0 . Thus, this SFLM was a nonminimum phase system with hyperbolic internal dynamics. It was nonminimum phase since it had a zero at +212.0 and it had hyperbolic internal dynamics since none of its zeros were on the imaginary axis or even close to it.

The link flexibility was modeled with one mode shape per link, since the maximum bandwidth of the actuator, in Fig. 3-11, was smaller than the second natural frequency. The maximum actuator bandwidth was 50 (Hz) while the natural frequency of the second mode was 54.25 (Hz). Therefore, the first mode of vibration was dominant and the contributions of the second and higher modes of vibration were minimal which justified modeling the link with only one mode. Moreover, generally, for a typical SFLM (or even multilink flexible manipulator) contributions of the higher modes of vibration are very small as also observed in the examples 1 and 2.

The desired end-effector acceleration, shown in Fig. 3-12, was considered to be composed of several third order polynomials, from 0 to 0.2, 0.2 to 0.4, and 0.4 to 0.6 (s). The corresponding desired velocity and displacement are presented in Fig. 3-13.

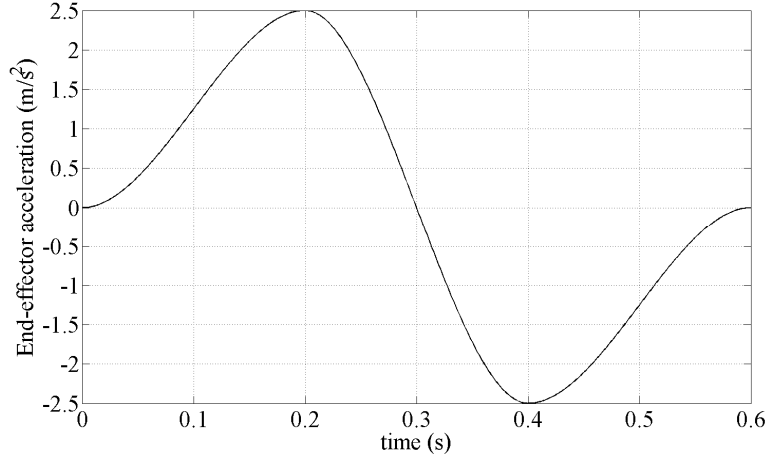


Fig. 3-12: Example 3, simulation, desired end-effector acceleration of the SFLM in the Robotics Lab at the U of S

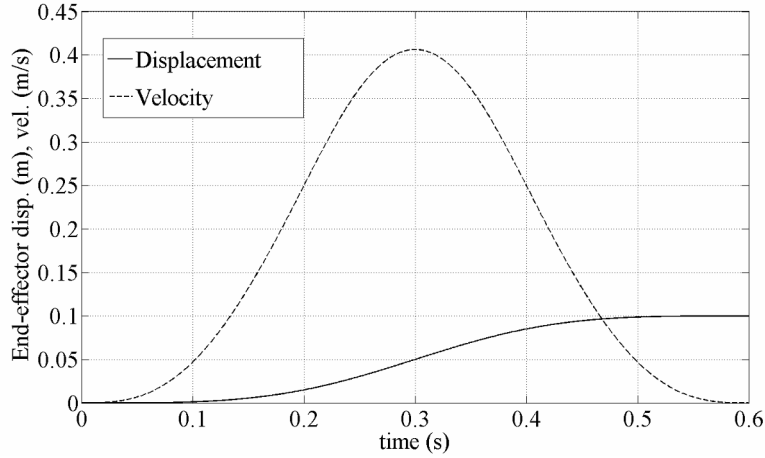


Fig. 3-13: Example 3, simulation, desired end-effector velocity and displacement of the SFLM in the Robotics Lab at the U of S

The desired end-effector acceleration was divided into 6 equal segments which were,

$$0.0 \leq t \leq 0.1 \quad , \quad 0.1 \leq t \leq 0.2, \dots, \quad 0.5 \leq t \leq 0.6 \quad (3-50)$$

Similar to the previous two simulation examples, $h=2$ was selected in Eq. (3-37a). Moreover, since there was only one unstable zero -212.0 , nu was equal to 1. Using Eq. (3-38), the required number of exponential functions for each segment was $r=7$. Also “ m ” for each segment was selected using Eqs. (3-42) and (3-43) and assuming $(C_{dec}^f)_k = 0.0100$ and $(C_{dec}^s)_k = 1.000$. As in examples 1 and 2, the off-line inverse torque was combined with the joint PD controller, Eq. (3-47), and after 0.6 (s)

only the joint PD controller with $\theta_d = y_d(t_f)/L$ and $\dot{\theta}_d = 0$ was active. The gains of the PD controller were $k_p=1.4$ and $k_D=0.40$. These values for the gains were again obtained by trial and error and observing the system's response as explained in the first example. For $k_p = 1.4$ and $k_D = 0.40$, the eigenvalues of \mathbf{A}_E in Eq. (3-A20) in Appendix III were $\{-23.86, -2.163, -4.971 \pm 30.86i\}$ which, since they all had negative real the closed-loop system was stable and consequently its response was assured to be bounded. To observe the response of the system under uncertainty, in the simulation the linear dynamic model of the SFLM given in Eq. (3-8) when the link flexibility was modeled with two mode shapes was used. The second mode shape was an uncertainty because the link flexibility, and consequently off-line inverse dynamic torque were obtained using only the first mode shape. In Fig. 3-14 the required base torque is shown. The reason that the shape of the torque in Fig. 3-14 was different than the torques in examples 1 and 2, Figs. 3-4 and 3-8 respectively, was due to the high value of the joint viscous friction in this example. Moreover, the discontinuity of the torque at $t_f = 0.6$ (s) was expected since, for $t > t_f$, the off-line computed torque was set to be zero and only the joint PD controller was active, as in the previous examples. However, in this example due to the larger error at t_f between the desired and actual displacements, than the error in the previous two examples, the jump in the torque, as shown in Fig. 3-14, was larger than the jump in the torques in Figs. 3-4 and 3-8 (see remark 3.4).

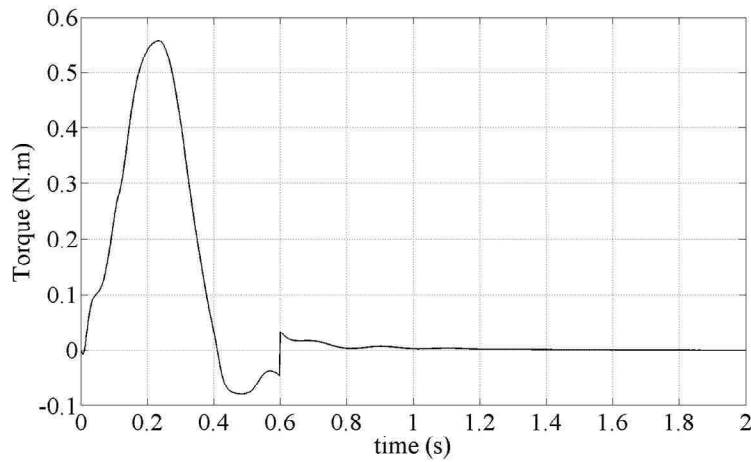


Fig. 3-14: Example 3, simulation, required base torque for causal end-effector trajectory tracking of the SFLM in the Robotics Lab at the U of S

The desired and actual end-effector displacements for the SFLM are presented in Fig. 3-15. Moreover, the difference between the desired and actual end-effector displacement $error = y_d - y$ is given in Fig. 3-16. From Figs. 3-15 and 3-16, it is clear that eventually the joint PD controller eliminates the steady end-effector trajectory tracking error, which is consistent with the result of [27].

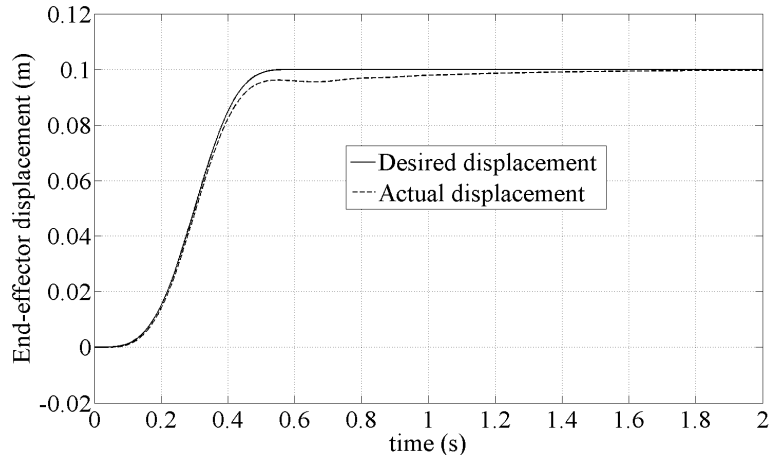


Fig. 3-15: Example 3, simulation, desired and actual end-effector displacements for the SFLM in the Robotics Lab at the U of S

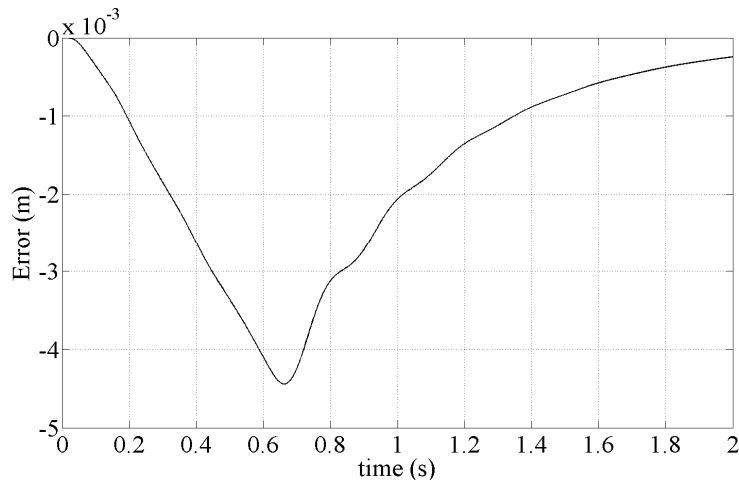


Fig. 3-16: Example 3, simulation, the difference between the actual and desired end-effector displacements of the SFLM in the Robotics Lab at the U of S which are shown in Fig. 3-15

3.8. Experimental results

To show the feasibility of the introduced technique, in this section the results of an experimental study are presented. The SFLM in the robotics laboratory at the University of Saskatchewan, shown in Fig. 3-11, was used for this experimental verification. It is to be noted that in example 3, the simulation result for this SFLM was given, while in this section the experimental results will be presented.

3.8.1. Example 4: End-effector trajectory tracking of an experimental SFLM

The physical parameters of the SFLM are given in example 3. The link flexibility is modeled using one mode shape due to the reason explained in example 3. The time varying weight of this mode was measured using a strain gage located at the clamped-base. The desired end-effector acceleration, velocity and displacement were the same as those used in example 3, which were shown in Figs 3-12 and 3-13, respectively.

Besides the physical parameters given in example 3, there was a high rotational dry friction in the experimental setup due to the employed harmonic drive. This friction is referred to as joint dry friction in the following and might be modeled approximately, for instance, by the model available in [29]. The existence of this joint dry friction, which is hard to model exactly, deteriorates the performance of the model-based controllers [30]. In this chapter, like in [31,32], to compensate for the friction, the average value of the joint dry friction was measured and added to the control torque in Eq. (3-47). Moreover, since the selected desired displacement was unidirectional, the dynamic effect of friction was easier to model [31]. That is because the manipulator does not change its direction.

The average value of the joint dry friction was obtained experimentally by applying a step input torque to the motor and recording the joint angular velocity versus time (velocity profile). Repeating this experiment gave different velocity profiles for different values of the step input torques. Since the closed-form function of the velocity profile for a step input torque is known, by using a curve fitting scheme the average value of the joint dry friction was obtained. This average value was 0.45 (N.m) which was added to the torque given in Eq. (3-47) and applied to the experimental setup. The gains of the joint PD controller in Eq. (3-47) were set $k_p = 1.4$ and $k_d = 0.40$. As in the previous

examples, after $t_f = 0.6$ (s) only the joint PD controller was active. Moreover, for the joint PD controller, for $t > t_f$, $\theta_d = y_d(t_f)/L$ (rad) and $\dot{\theta}_d = 0$ were utilized. The results of this experimental study are reported in Appendix 3.IV. From the reported results in Appendix 3.IV it is clear that a steady trajectory tracking error existed of about 0.01 (m). That is, the joint PD controller by itself could not eliminate the steady trajectory tracking error, contrary to simulation examples 1, 2 and 3 where the joint PD controller reduced the steady tracking error to zero. Moreover, it was clear that after $t_f = 0.6$ (s), the actuator applied a constant torque. This torque was due to the existence of the steady tracking error and application of the joint PD controller. Since the value of the constant torque was less than the value of the joint dry friction, it could not rotate the hub and reduce the steady tracking error to zero. By increasing the gains of the PD controller, the constant value of the torque would increase and allow overcoming the joint dry friction. But, implementing a joint PD controller in the presence of friction will eventually lead to a steady tracking error, where for higher PD gains the error becomes smaller [33]. As a side effect, selecting larger gains for a PD controller increases the sensitivity of the controller to noise and leads to torque saturation. Moreover, although applying a PID (proportional-derivative-integral) controller instead of PD controller for $t > t_f$ might be a solution for the reduction of the steady state error to zero; the combination of the PID controller and joint dry friction results in hunting limited cycles [33,34]. Finally, adding the calculated average value of the joint dry friction to the PD controller did not appear to be a solution. This is due to the fact that the successful reduction of the error by the PD controller to zero would occur [27] if the exact model of the joint dry friction, and not an average value, was used for compensation.

In the following section, a new controller is introduced to compensate for the joint dry friction. The utilization of this new controller does not indicate inefficiency of the new causal inversion end-effector controller introduced here. However, since the causal end-effector inversion is a model based controller and joint friction is not exactly known, a different controller is necessary to reduce the error to zero at the end of maneuver.

Introducing a new controller

As a remedy, to reduce the steady trajectory tracking error to zero, in the following a new two stage controller is proposed at the expense of torque discontinuity. Based on this proposed controller for the first stage up to $t_f = 0.6$ (s), a constant torque of 0.45 (N.m) was added to that given is Eq. (3-47) and applied to the SFLM (like before). For the second stage, for $t > t_f$, the pulse width control (PWC) [35,36] was used to reduced the steady state error of the hub to zero. According to the PWC, to reduce the steady trajectory tracking error to zero, the following steps have to be taken in each iteration j [35]:

- 1- $j = 0$
- 2- Measure the current hub position error $v_j = \theta_d - \theta$ where $\theta_d = y_d(t_f)/L$ and θ is the actual hub rotation.

- 3- Calculate the width $u_j = k\sqrt{v_j} \text{sgn}(v_j)$ of the pulse torque τ_{lm} , as shown in

Fig. 3-17, where¹⁸ $k = \sqrt{\frac{2\tau_a(I_h + I_{tip} + m_{tip}L^2 + \rho L^3/3)}{\tau_{lm}(\tau_{lm} - \tau_a)}}$, $\tau_a < \tau_{lm}$, τ_a is the

average value of the joint dry friction and parameters I_h , I_{tip} , m_{tip} , ρ and L are defined in Section 3.2 after Eq. (3-4c). If u_j is positive (or negative) the pulse torque will be in the Z_{Inertial} (or $-Z_{\text{Inertial}}$) direction where $Z_{\text{Inertial}} = X_{\text{Inertial}} \times Y_{\text{Inertial}}$ and X_{Inertial} and Y_{Inertial} are shown in Fig. 3-2 in Section 3.2.

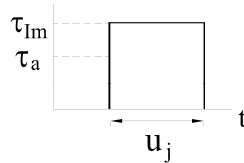


Fig. 3-17: Schematic of the j th iteration of the PWC

¹⁸ The effect of viscous damping was not considered in calculating k . This is based on the assumption that the duration of the pulse is short, so the velocity remains small and the linear damping is negligible compared to dry friction [36].

- 4- Apply the torque τ_{lm} with the duration obtained in step 3 to the SFLM
- 5- Wait so that the hub comes to rest
- 6- if $v^j \neq 0$ then $j = j+1$ and go to step 3, otherwise stop.

The schematic of the proposed two-stage controller is shown in Fig. 3-18. The stability of the first stage of this controller is similar to the stability analysis of the “joint PD controller plus the off-line computed inverse torque” given in Appendix 3.III. Moreover, the stability of the PWC, which is the second stage of this controller, is available in [35]. Therefore, the closed loop controller given in Fig. 3-18 is stable.

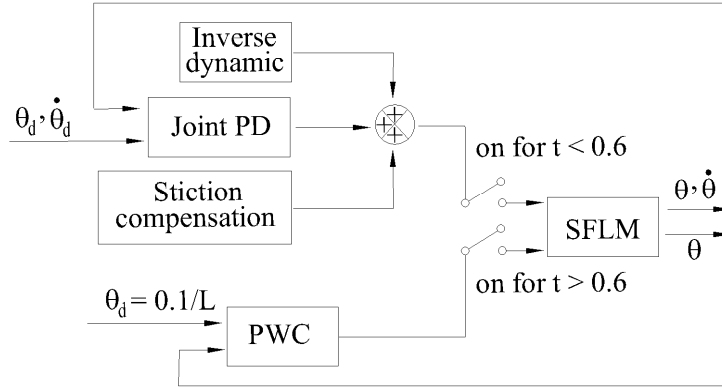


Fig. 3-18: Example 4, experimental, schematic of the two-stage controller used to eliminate the steady trajectory tracking error

The torque applied to the experimental SFLM using this two-stage controller is presented in Fig. 3-19. For the calculation of the duration of the PWC, which is u_j in step 3 above, $\tau_{lm} = 0.46$ (N.m) was selected. From Fig. 3-19, it can be seen that only one PWC after $t_f = 0.6$ (s) was required to reduce the error close to zero.

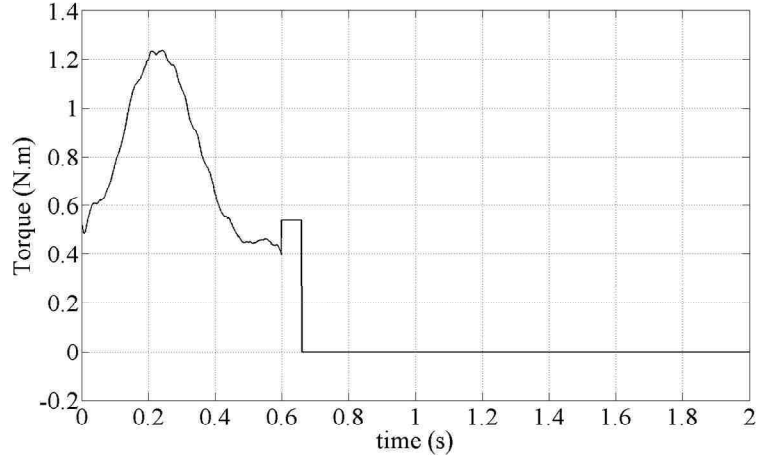


Fig. 3-19: Example 4, experimental, required base torque for causal end-effector trajectory tracking of the SFLM in the Robotics Lab at the U of S using the two-stage controller given in Fig. 3-18

The actual and desired displacements and their differences $error = y_d - y$ using the controller presented in Fig. 3-18 are shown in Figs. 3-20 and 3-21.

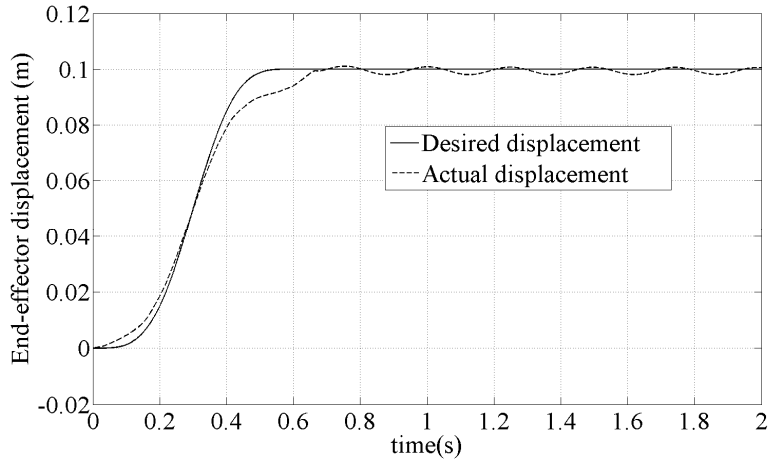


Fig. 3-20: Example 4, experimental, desired and actual end-effector displacements for the SFLM in the Robotics Lab at the U of S using the two-stage controller given in Fig. 3-18

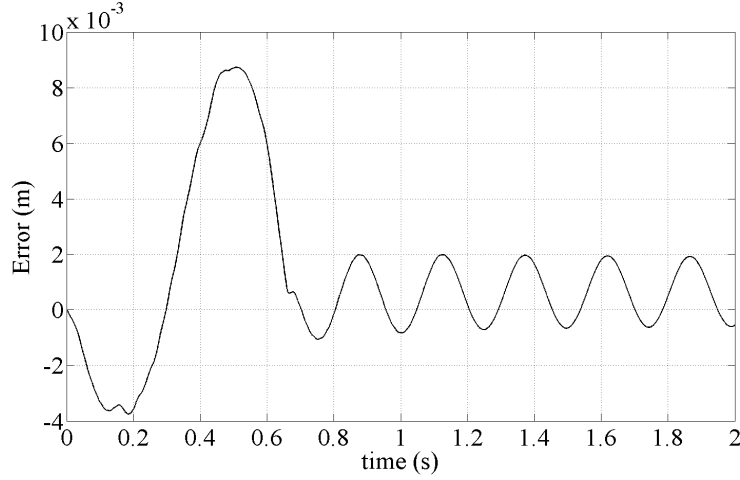


Fig. 3-21: Example 4, experimental, the difference between the actual and desired end-effector trajectories of the SFLM in the Robotics Lab at the U of S using the two-stage controller which are shown in Fig. 3-20

Comparing Figs. 3-20 and 3-21, with the end-effector displacement and error given in Appendix 3.IV, Figs. 3-24 and 3-25, which are the experimental results without PWC, showed that the steady tracking error was reduced essentially due to the PWC. That is, the steady state trajectory tracking error was reduced from about $0.010(m)$ to about $0.001(m)$.

Figs. 3-20 and 3-21 show that there existed a slowly vanishing vibration of the manipulator. When the hub reached $0.1/L(\text{rad})$ if the link vibration was suppressed, the steady end-effector trajectory tracking vanished. The joint PD controller was able to suppress the link's vibration [27] when there was no joint dry friction. However in the presence of the joint dry friction, the internal material damping was the only source of the suppression of the link's vibration. While relying on the link's material damping for eliminating the vibration is not always satisfactory, the available experimental SFLM has this limitation. The application of a piezoelectric actuator to overcome this drawback is among the possible solutions which are currently under study [37].

Finally, the difference between the actual and desired displacements in example 3, which is the simulation, is smaller compared with experimental example 4, even for $t < 0.6(s)$. The main reason for this difference was the joint dry friction, which was the drawback of the harmonic drive used in the experimental setup at the expense of no

backlash. In the experimental study, to compensate for this joint dry friction a constant torque was added to the controller torque. Moreover, in addition to the existence of the joint dry friction as a source for such a difference, the encoder and strain gauge noise [38], and the contribution of higher frequency modes contributed to this variation. It is to be noted that the controller proposed here, a combination of the joint PD with the inverse dynamic torque, was a model based controller. Therefore, the existence of unavoidable small differences between the real system physical parameters and the derived model deteriorated the performance of the controller, despite the fact that the controller was still stable.

3.9. Conclusions

A novel causal end-effector trajectory inversion of a Single Flexible Link Manipulator (SFLM) by means of output redefinition has been introduced. The desired trajectory is divided into a finite number of segments and in each segment is redefined so that a bounded causal continuous inversion torque can be found. The redefinition of the desired trajectory employed summation of stable exponential functions which led to a family of possible solutions. Thus, by minimizing the error between the desired trajectory and the redefined trajectory, the best member of the family could be found.

Although the available non-causal end-effector inversion technique did not tolerate existence of purely imaginary zeros for the transfer function between end-effector displacement and applied torque, the proposed method in this chapter is still valid even in the presence of purely imaginary zeros. The off-line computed inverse dynamic torque was combined with a joint PD controller and the stability of the proposed controller against the unmodeled dynamic was investigated. The joint PD controller suppressed the link's vibration at the end of the motion and was also robust against unmodeled dynamic due to its model independent nature. The simulation results for SFLMs with hyperbolic, non-hyperbolic and near non-hyperbolic internal dynamics, which is without purely imaginary zeros, with purely imaginary zeros and zeros which are close to imaginary axis respectively, were included. The experimental results showed the feasibility of the introduced method. In the experimental study, due to the existence of the joint dry friction, a new two-stage controller was used to reduce the trajectory

tracking error close to zero. While the method was studied here for the inversion of a SFLM, its extension to the causal inversion of linear single-input single-output, non-minimum phase systems with hyperbolic or non-hyperbolic internal dynamics is straight forward.

3.10.Nomenclature

a : A positive constant number

b : A constant number

c_{jk} : Coefficient of the j th exponential function used to redefine the desired trajectory in the k th segment

h : The highest derivative of the redefined acceleration that has to be the same as its corresponding from the desired acceleration

k_p : Scalar gain

k_D : Scalar gain

m_{jk} : Exponent of the j th exponential function used to redefine the desired trajectory in the k th segment

m_{tip} : Mass of the end-effector

n : Number of the assumed mode shapes

nu : Size of the vector \mathbf{X}_I^u

p_j : the j th coefficient of the polynomial y_p

\mathbf{q} : A vector composed of the degree of freedoms

r : Required number of the exponential functions for each segment

r_w : Relative degree

t_i : Initial manoeuvre time

t_f : Final manoeuvre time

t_{ik} : Initial time of the k th segment

t_{fk} : Final times of the k th segment

u_j : Width of the pulse torque τ_{lm}

y : End-effector displacement

y_d : Desired end-effector displacement

\tilde{y}_d : Redefinition of the desired end-effector displacement with the summation of the exponential functions

y_p : Redefinition of the desired end-effector displacement with the polynomial functions

$(\ddot{y}_d)_k$: Desired end-effector acceleration in the k th segment

\mathbf{A} : State matrix when the dynamic model is expressed in the state-space form

\mathbf{A}_ψ : State matrix when \mathbf{X} is transformed into ψ

\mathbf{A}_I : State matrix of the internal dynamic

\mathbf{A}_I^- : A diagonal matrix with the diagonal elements that are the eigenvalues of \mathbf{A}_I with negative real parts

\mathbf{A}_I^+ : A diagonal matrix with the diagonal elements that are the eigenvalues of \mathbf{A}_I with positive real parts

\mathbf{B} : Input matrix when the dynamic model is expressed in the state-space form

\mathbf{B}_ψ : Input matrix when \mathbf{X} is transformed into ψ

\mathbf{B}_I : Input matrix of the internal dynamic

\mathbf{B}_I^s : Input matrix which corresponds to \mathbf{A}_I^-

\mathbf{B}_I^u : Input matrix which corresponds to \mathbf{A}_I^+

C_{dec} : Decay of the exponential function

$(C_{dec}^f)_k$: The fastest decays for the exponential functions used in the k th

$(C_{dec}^s)_k$: The slowest decays for the exponential functions used in the k th

C : Output matrix when the dynamic model is expressed in the state-space form and the end-effector displacement is the output

C_{cc} : Matrix representing the Coriolis force and the component of the centrifugal force in the lateral direction

$$D := [L \quad \phi_1(L) \quad \dots \quad \phi_n(L)]$$

E : Young's modules

F : Force vector

G : Matrix with columns which are the eigenvectors of the matrix A_l

H : Mapping matrix between F and τ

I_h : Mass moment of inertia of the hub

I_{tip} : Mass moment of inertia of the end-effector

I : Second moment of cross section area

K_B : Stiffness matrix

$$K_{ct} := [k_p \quad 0 \quad 0 \quad k_D \quad 0 \quad 0]$$

K_p : Matrix gain

K_D : Matrix gain

L : Length of the link

M : Mass matrix

T_M : Total kinetic energy of the manipulator

T_l : Kinetic energy of the flexible link

T_h : Kinetic energy of the hub

T_{tip} : Kinetic energy of the end-effector

\mathbf{T} : Transformation matrix between \mathbf{X} and $\boldsymbol{\psi}$

U_M : Strain energy due to the link's flexibility

V_{fp} : Lyapunov candidate function selected for the stability analysis of the first stage of the proposed controller

V_{sp} : Lyapunov candidate function selected for the stability analysis of the second stage of the proposed controller

$(X_I'')_p$: The particular part of X_I''

$(X_I'')_c$: The complementary part of X_I''

\mathbf{X}_I'' : Stable part of \mathbf{X}_I

\mathbf{X}_I^s : Unstable part of \mathbf{X}_I

\mathbf{X}_I : State vector of the internal dynamics

\mathbf{X} : State vector when the dynamic model is expressed in the state-space

β_1, β_2 : Positive scalars

ξ : Spatial deflection of the flexible link

ϕ_j : The j th spatial pre-defined shape functions

λ_j : The j th time varying weight functions

ρ : Mass per unit length of the flexible link

θ : Rotation of the hub

τ : Actuator torque

η : Damping ratio of the fundamental vibration mode shape

ω : Natural frequency of the fundamental vibration mode shape

ψ : The vector obtained after transforming \mathbf{X} by \mathbf{T}

ν : Number of the segments

τ_l : The torque obtained after end-effector inversion of the linear dynamic model

τ_a : Average value of the joint dry friction

τ_{lm} : Value of the pulse torque

\mathcal{A} : Deviation of the linear mode from nonlinear model and non-modeled dynamics

$\mathbf{\Pi}$: A positive definite matrix obtained from the Lyapunov equation

$\mathbf{\Gamma}$: A positive definite matrix

3.11.Appendices

Appendix 3.I: The elements of the matrices in the nonlinear and linear dynamic equation

The nonlinear dynamic equation of a single flexible link manipulator, Eq. (3-6), is:

$$\mathbf{M}(\lambda)\ddot{\mathbf{q}} + \mathbf{C}_{cc}(\dot{\theta}, \lambda, \dot{\lambda})\dot{\mathbf{q}} + \mathbf{K}_B\mathbf{q} = \mathbf{H}\boldsymbol{\tau} \quad (3-A1)$$

or:

$$\begin{bmatrix} M_{11} & \dots & M_{1n+1} \\ \vdots & \ddots & \vdots \\ M_{n+11} & \dots & M_{n+1n+1} \end{bmatrix} \begin{bmatrix} \ddot{\theta} \\ \vdots \\ \ddot{\lambda}_n \end{bmatrix} + \begin{bmatrix} (C_{cc})_{11} & \dots & (C_{cc})_{1n+1} \\ \vdots & \ddots & \vdots \\ (C_{cc})_{n+11} & \dots & (C_{cc})_{n+1n+1} \end{bmatrix} \begin{bmatrix} \dot{\theta} \\ \vdots \\ \dot{\lambda}_n \end{bmatrix} + \begin{bmatrix} K_{11} & \dots & K_{1n+1} \\ \vdots & \ddots & \vdots \\ K_{n+11} & \dots & K_{n+1n+1} \end{bmatrix} \begin{bmatrix} \theta \\ \vdots \\ \lambda_n \end{bmatrix} = \begin{bmatrix} 1 \\ \vdots \\ 0 \end{bmatrix} \boldsymbol{\tau} \quad (3-A2)$$

where $(\Phi_{i,j} = \int_0^L \phi_j \phi_i d\gamma, \Phi_{i,\gamma} = \int_0^L \gamma \phi_i d\gamma, \phi'_i = \frac{\partial \phi_i(\gamma)}{\partial \gamma}, \phi''_i = \frac{\partial^2 \phi_i(\gamma)}{\partial \gamma^2})$

$$M_{11} = (\rho L^3 / 3) + \rho \left(\sum_{i=1}^n \sum_{j=1}^n \lambda_i \lambda_j \Phi_{i,j} \right) + I_h + I_{tip} + m_{tip} L^2 + m_{tip} \left(\sum_{i=1}^n \sum_{j=1}^n (\phi_i(L) \phi_j(L) \lambda_i \lambda_j) \right) \quad (3-A3)$$

$$M_{li} = M_{il} = \rho \Phi_{i-1,\gamma} + m_{tip} L \phi_{i-1}(L) + I_{tip} \phi'_{i-1}(L) \quad i = 2..n+1 \quad (3-A4)$$

$$M_{ij} = M_{ji} = \rho \Phi_{i-1,i-1} + m_{tip} \phi_{i-1}(L) \phi_{j-1}(L) + I_{tip} \phi'_{i-1}(L) \phi'_{j-1}(L) \quad i, j = 2..n+1 \quad (3-A5)$$

$$(C_{cc})_{11} = \rho \left(\sum_{i=1}^n \sum_{j=1}^n \dot{\lambda}_i \lambda_j \Phi_{i,j} \right) + m_{tip} \left(\sum_{i=1}^n \sum_{j=1}^n (\phi_i(L) \phi_j(L) \dot{\lambda}_i \lambda_j) \right) \quad (3-A6)$$

$$(C_{cc})_{1i} = -(C_{cc})_{i1} = \rho \dot{\theta} \left(\sum_{j=1}^n \lambda_j \Phi_{(i-1),j} \right) + m_{tip} \dot{\theta} \left(\sum_{j=1}^n \lambda_j \phi_{(i-1)}(L) \phi_j(L) \right) \quad i = 2..n+1 \quad (3-A7)$$

$$(C_{cc})_{ij} = (C_{cc})_{ji} = 0, \quad i, j \neq 1 \quad (3-A8)$$

$$\mathbf{K}_B = \begin{cases} K_{ij} & i = 2..n+1, \quad j = 2..n+1 \\ 0 & i = 1 \text{ or } j = 1 \end{cases} \quad (3-A9)$$

$$K_{ij} = EI \int_0^L \phi_i'' \phi_j'' d\gamma \quad (3-A10)$$

In the linear dynamic $\mathbf{C}_{cc}(\dot{\theta}, \dot{\lambda}, \dot{\lambda})$ does not exist and the elements for the mass matrix are:

$$M_{11} = (\rho L^3 / 3) + I_h + I_{tip} + m_{tip} L^2 \quad (3-A11)$$

$$M_{1i} = M_{i1} = \rho \Phi_{i-1,x} + m_{tip} L \phi_{i-1}(L) + I_{tip} \phi'_{i-1}(L) \quad i = 2..n+1 \quad (3-A12)$$

$$M_{ij} = M_{ji} = \rho \Phi_{i-1,i-1} + m_{tip} \phi_{i-1}(L) \phi_{j-1}(L) + I_{tip} \phi'_{i-1}(L) \phi'_{j-1}(L) \quad i, j = 2..n+1 \quad (3-A13)$$

Moreover, the stiffness matrix is as in (3-A9) and (3-A10)

Appendix 3.II: Checking the orthogonality of the shape function of beam element

The shape functions for the beam element are cubic polynomials [39, p. 242] as:

$$\begin{aligned} N_1 &= \frac{1}{4}(1-\eta)^2(2+\eta), \quad N_2 = \frac{L_2}{2} \left[\frac{1}{4}(1-\eta)^2(1+\eta) \right] \\ N_3 &= \frac{1}{4}(1+\eta)^2(2-\eta), \quad N_4 = \frac{L_2}{2} \left[\frac{1}{4}(1+\eta)^2(-1+\eta) \right] \end{aligned} \quad (3-A14)$$

where L_e is the length of the beam element and η is the linear distance measured from the center of the master beam element, which is changing from -1 to 1. These shape functions are shown in Fig. 3-22.

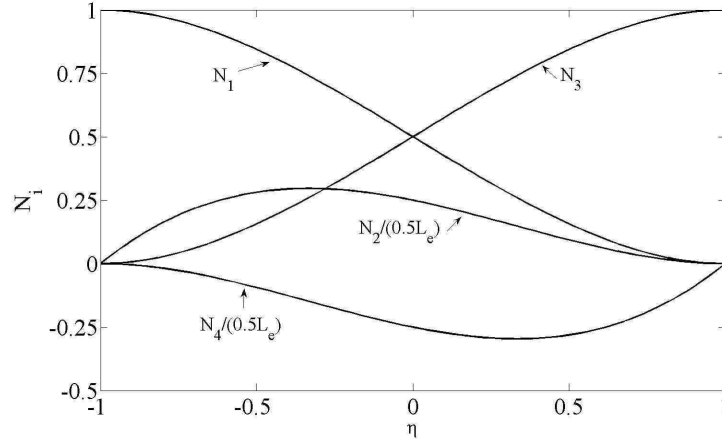


Fig. 3-22: Graph of the shape functions of the beam element

If the above shape functions with the weight function to be 1 were orthogonal to each

other, $O(N_i, N_j) = \int_a^b N_i(\eta) \cdot N_j(\eta) d\eta$ was equal to zero for $i \neq j, i = 1 \dots 4, j = 1 \dots 4$.

However, calculation of $O(N_i, N_j)$ for $i \neq j, i = 1 \dots 4, j = 1 \dots 4$ shows that:

$$\begin{aligned}
 O(N_1, N_2) &= O(N_2, N_1) = 0.105L_e \neq 0, & O(N_1, N_3) &= O(N_3, N_1) = 0.257 \neq 0 \\
 O(N_1, N_4) &= O(N_4, N_1) = -0.062L_e \neq 0, & O(N_2, N_3) &= O(N_3, N_2) = 0.062L_e \neq 0 \\
 O(N_2, N_4) &= O(N_4, N_2) = -0.014L_e^2 \neq 0, & O(N_3, N_4) &= O(N_4, N_3) = -0.105L_e \neq 0
 \end{aligned}
 \tag{3-A15}$$

Therefore the shape functions used to redefine the displacement along a beam element are not orthogonal.

Appendix 3.III: Stability proof

The proposed controller had two stages. In the first stage for $t < t_f$, a joint PD controller which is added to the off-line computed inverse dynamic torque was utilized. In the second stage for $t > t_f$, only the joint PD controller assuming constant $\theta_d = y(t_f)/L$, and $\dot{\theta}_d = \ddot{\theta}_d = 0$, was active. For the stability analysis, it will be first proven that the first stage controller, a joint PD controller plus the off-line computed inverse torque, leads to a trajectory tracking error dynamic which is stable. Then, it will be established that the

second stage controller, the joint PD controller, suppresses the vibration of the link and eliminates the steady tracking errors.

Proof of the Lyapunov stability of the joint PD controller plus the off-line computed inverse torque for $t < t_f$

The dynamic model of a SFLM in the state space form is:

$$\dot{\mathbf{X}} = \mathbf{A}\mathbf{X} + \mathbf{B}\boldsymbol{\tau} + \mathbf{A} \quad (3-A16)$$

where \mathbf{A} , \mathbf{B} and \mathbf{X} are defined in Eq. (3-12), $\boldsymbol{\tau}$ is the actuator torque, and \mathbf{A} represents the deviation of the linear mode from the nonlinear model and unmodeled dynamics. Moreover, according to the end-effector inversion procedure the off-line computed inverse torque $\boldsymbol{\tau}_l$ satisfies:

$$\dot{\mathbf{X}}_d = \mathbf{A}\mathbf{X}_d + \mathbf{B}\boldsymbol{\tau}_l \quad (3-A17)$$

where \mathbf{X}_d are the states corresponds to $\tilde{\mathbf{y}}_d$ which are calculated during the inversion procedure and

$$\tilde{\mathbf{y}}_d = \mathbf{C}\mathbf{X}_d \quad (3-A18)$$

where \mathbf{C} is defined in Eq. (3-12). The torque given in Eq. (3-47), which is the off-line computed inverse torque with the joint PD controller, can be written as:

$$\boldsymbol{\tau} = \boldsymbol{\tau}_l + \mathbf{K}_{ct}\boldsymbol{\Delta} \quad (3-A19)$$

where $\mathbf{K}_{ct} = [k_p \ 0 \ 0 \ k_D \ 0 \ 0]$ and $\boldsymbol{\Delta} = \mathbf{X}_d - \mathbf{X}$. By replacing $\boldsymbol{\tau}$ from Eq. (3-A19) into Eq. (3-A16) and utilizing Eq. (3-A17), the error dynamic is:

$$\dot{\boldsymbol{\Delta}} = \mathbf{A}_E\boldsymbol{\Delta} - \mathbf{A} \quad (3-A20)$$

where $\mathbf{A}_E = \mathbf{A} - \mathbf{B}\mathbf{K}_{ct}$.

Theorem: If:

- 1- The gains k_p and k_D are selected so that the matrix \mathbf{A}_E is Hurwitz

- 2- The unmodeled dynamic and the deviation of linear model from nonlinear model satisfy $\beta_1 < \mu_{\min}(\mathbf{\Pi})/(2\|\mathbf{\Gamma}\|)$ where $\mu_{\min}(\mathbf{\Pi})$ represents the minimum eigenvalue of $\mathbf{\Pi}$ defined in Eq. (3-A21) and positive scalar β_1 is defined in Eq. (3-A25)

then the error dynamic state Δ is globally bounded.

Proof: Since \mathbf{A}_E is a Hurwitz matrix, there exists a symmetric positive definite matrix $\mathbf{\Gamma}$ which satisfies the following Lyapunov equation:

$$\mathbf{A}_E^T \mathbf{\Gamma} + \mathbf{\Gamma} \mathbf{A}_E = -\mathbf{\Pi} \quad (3-A21)$$

where $\mathbf{\Pi}$ is a positive definite matrix. Choosing the Lyapunov candidate function:

$$V_{fp} = \Delta^T \mathbf{\Gamma} \Delta \quad (3-A22)$$

and taking its time derivative along the trajectories of Eq. (3-A20) yields:

$$\dot{V}_{fp} = -\Delta^T \mathbf{\Pi} \Delta - 2\Delta^T \mathbf{\Gamma} \mathbf{A} \quad (3-A23)$$

From Eq. (3-A23), it is concluded that:

$$\dot{V}_{fp} < -\mu_{\min}(\mathbf{\Pi})\|\Delta\|^2 + 2\|\Delta\|\|\mathbf{\Gamma}\|\|\mathbf{A}\| \quad (3-A24)$$

where $\mu_{\min}(\mathbf{\Pi})$ represents the minimum eigenvalue of $\mathbf{\Pi}$. Moreover, it is assumed that on a bounded region around origin, $\|\mathbf{A}\|$ is:

$$\|\mathbf{A}\| < \beta_1 \|\Delta\| + \beta_2 \quad (3-A25)$$

where β_1 and β_2 are positive scalars. Combining Eqs. (3-A24) and (3-A25) leads to:

$$\dot{V}_{fp} < -(\mu_{\min}(\mathbf{\Pi}) - 2\|\mathbf{\Gamma}\|\beta_1)\|\Delta\|^2 + 2\beta_2\|\mathbf{\Gamma}\|\|\Delta\|$$

Since $\beta_1 < \mu_{\min}(\mathbf{\Pi})/(2\|\mathbf{\Gamma}\|)$, the state error Δ is globally bounded [17 p. 22] and the closed loop system is stable.

Proof of the suppression of the link's vibration and vanishing of the steady tracking error by utilizing joint PD controller for $t > t_f$

The nonlinear dynamic model of SFLM as given in Eq. (3-6) is:

$$\mathbf{M}(\lambda)\ddot{\mathbf{q}} + \mathbf{C}_{cc}(\dot{\theta}, \lambda, \dot{\lambda})\dot{\mathbf{q}} + \mathbf{K}_B\mathbf{q} = \mathbf{H}\tau \quad (3-A26)$$

where the elements of $\mathbf{M}(\lambda)$, $\mathbf{C}_{cc}(\dot{\theta}, \lambda, \dot{\lambda})$, \mathbf{K}_B and \mathbf{H} are defined in Appendix 3.I. Moreover τ is the actuator torque. If the joint PD controller is only active, the actuator torque, as in Eq. (3-47), is:

$$\tau = k_p(\theta_d - \theta) + k_D(\dot{\theta}_d - \dot{\theta}) \quad (3-A27)$$

or

$$\tau = -\mathbf{K}_P\mathbf{q}_e - \mathbf{K}_D\dot{\mathbf{q}}_e \quad (3-A28)$$

where

$$\mathbf{K}_P = [k_p \quad 0_{1 \times n}] \quad (3-A29)$$

$$\mathbf{K}_D = [k_D \quad 0_{1 \times n}] \quad (3-A30)$$

$$\mathbf{q}_e = [\theta - \theta_d \quad \lambda_1 \quad \dots \quad \lambda_n] \quad (3-A31)$$

Theorem: The joint PD controller given in Eq. (3-A28) asymptotically stabilized a SFLM with the nonlinear dynamic model given in Eq. (3-A26)

Proof: Applying the torque given in Eq. (3-A28) to the nonlinear dynamic model given in Eq. (3-A26) leads to:

$$\mathbf{M}(\lambda)\ddot{\mathbf{q}}_e + (\mathbf{C}_{cc}(\dot{\theta}, \lambda, \dot{\lambda}) + \mathbf{H}\mathbf{K}_D)\dot{\mathbf{q}}_e + (\mathbf{K}_B + \mathbf{H}\mathbf{K}_P)\mathbf{q}_e = 0 \quad (3-A32)$$

It is to be noted that in deriving Eq. (3-A32), it was assumed that $\dot{\theta}_d = \ddot{\theta}_d = 0$. The assumption that $\dot{\theta}_d = \ddot{\theta}_d = 0$ is the consequence of the fact that θ_d is constant for $t > t_f$. For the stability analysis, the Lyapunov candidate function is selected to be:

$$V_{sp} = 1/2\dot{\mathbf{q}}_e^T \mathbf{M}(\lambda)\dot{\mathbf{q}}_e + 1/2\mathbf{q}_e^T (\mathbf{K}_B + \mathbf{H}\mathbf{K}_P)\mathbf{q}_e \quad (3-A33)$$

where $\mathbf{M}(\lambda)$ and $\mathbf{K}_B + \mathbf{H}\mathbf{K}_P$ matrices are positive definite matrices. Taking the derivative of V_{sp} , given in Eq. (3-A33), with respect to time along the trajectories of Eq. (3-A32) and using the fact that $\dot{\mathbf{q}}_e^T (-\mathbf{C}_{cc}(\dot{\theta}, \lambda, \dot{\lambda}) + 1/2\dot{\mathbf{M}})\dot{\mathbf{q}}_e = 0$ [40] yields:

$$\dot{V}_{sp} = -k_D(\dot{\theta}_d - \dot{\theta})^2 \quad (3-A34)$$

which shows that \dot{V}_{sp} is a negative semi-definite scalar. However, by adopting the LaSalle's theorem [9], the asymptotic stability of the closed-loop system can easily be concluded [27, p. 210]. It is worth noting that the proposed PD controller in Eq. (3-A28) is robust against the unmodeled dynamics because this controller is not model-dependent. Therefore, the stability proof given here will stand as long as the dynamic model of the real system can be expressed as Eq. (3-A26).

Appendix 3.IV: The experimental result without the PWC controller

In Fig. 3-23, the applied torque to the experimental SFLM is shown. This torque was the off-line inverse dynamic torque plus the joint PD controller and the PWC was not used. The actual end-effector displacement and the desired end-effector displacement are shown in Fig. 3-24. Moreover, the difference between the actual and desired end-effector trajectories $error = y_d - y$ is presented in Fig. 3-25.

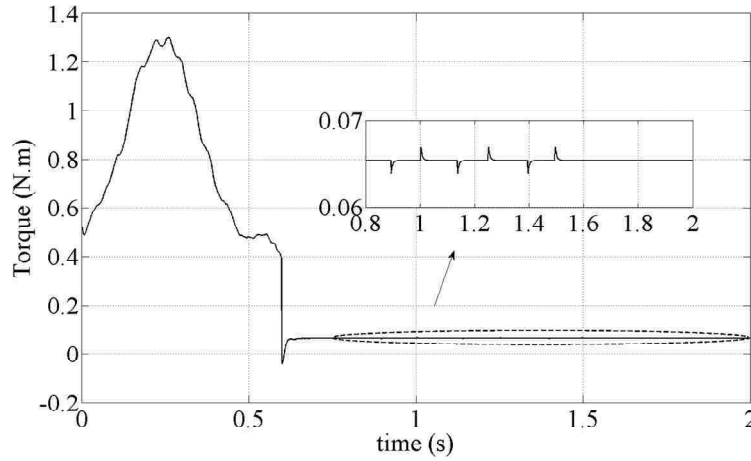


Fig. 3-23: Experimental, required base torque for causal end-effector trajectory tracking of the SFLM in the Robotics Lab at the U of S without PWC

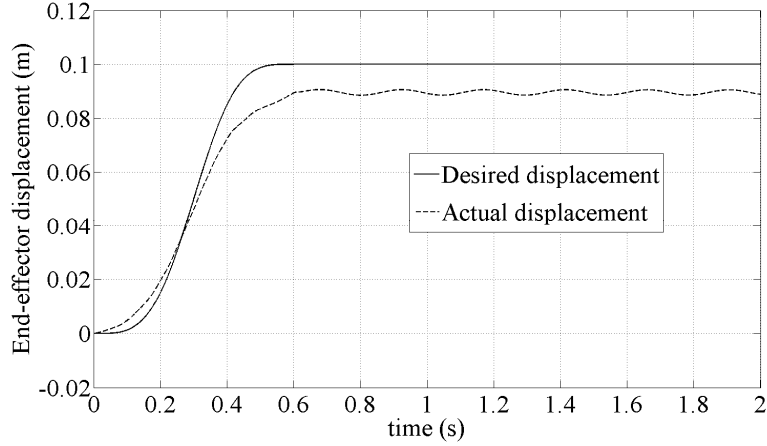


Fig. 3-24: Experimental, desired and actual end-effector displacements for the SFLM in the Robotics Lab at the U of S without PWC

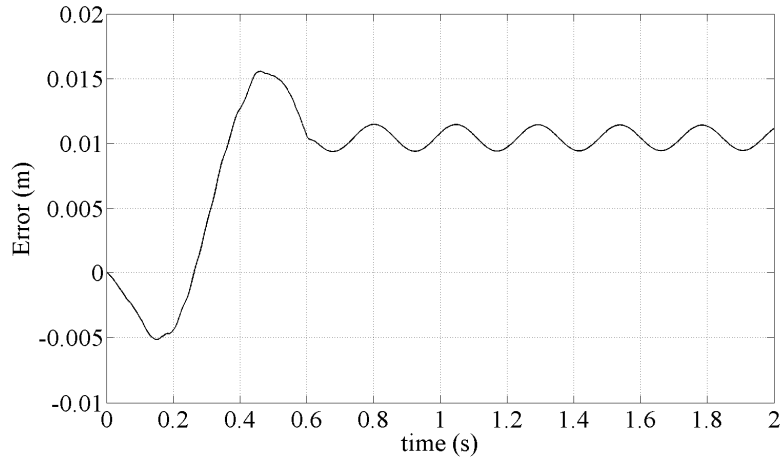


Fig. 3-25: Experimental, the difference between the actual and desired end-effector displacement of the SFLM in the Robotics Lab at the U of S which are shown in Fig. 3-24

3.12. References

1. T. Komatsu, and V. J. Modi, Precise Trajectory Control of a Redundant Flexible Manipulator on a Space Platform, *Advanced Robotics*, 17 (8), pp. 821-836 (2003).
2. D. Wang, and M. Vidyasagar, Transfer Function for a Single Flexible Link, Proceedings of the IEEE International Conference on Robotics Automation, Arizona, USA, 2, pp. 1042-1047, (1989).

3. V. A. Spector, and H. Flashner, Modeling and Design Implications of Noncollocated Control in Flexible Systems, *Journal of Dynamic Systems, Measurement and Control*, 112 (2), pp. 186-193, (1990).
4. J. H. Park, and H. Asada, Dynamic Analysis of Noncollocated Flexible Arms and Design of Torque Transmission Mechanisms, *Journal of Dynamic Systems, Measurement and Control*, 116 (2), pp. 201-207, (1994).
5. W. M. Gevarter, Basic Relations for Control of Flexible Vehicles, *AIAA Journal*, 8 (2), pp. 666-672, (1979).
6. A. Isidori, and C. Byrnes, Output Regulation of Nonlinear System, *IEEE Transactions on Automation and Control*, 35 (2), pp. 131-140, (1990).
7. A. De Luca, L. Lanari, and G. Ulivi, Tip Trajectory Tracking in Flexible Arms: Comparison of Approaches Based on Regulation Theory, *Lecture Notes in Control and Information Sciences*, 162, pp. 190-206, (1991).
8. S. Devasia, D. Chen, and B. Paden, Nonlinear Inversion-Based Output Tracking, *IEEE Transactions on Automatic Control*, 41 (7), pp. 930-942, (1996).
9. J. J. Slotine, and W. Li, *Applied Nonlinear Control*, Prentice Hall, NJ, USA, (1991).
10. E. Bayo, A Finite-Element Approach to Control the End-Point Motion of a Single Link Flexible Robot, *Journal of Robotic Systems*, 4 (1), pp. 63-75, (1989).
11. D. S. Kwon, and W. J. Book, Time-Domain Inverse Dynamic Tracking Control of a Single-Link Flexible Manipulator, *Journal of Dynamic Systems, Measurement and Control*, 116 (2), pp. 193-200, (1994).
12. M. Bensoussan, and G. LeVey, Stable Inversion of SISO Nonminimum Phase Systems through Output Planning: An Experimental Application to the One-Link Flexible Manipulator, *IEEE Transactions on Control Systems Technology*, 11 (4), pp. 588- 597, (2003).
13. S. Devasia, Approximated Stable Inversion for Nonlinear System with Nonhyperbolic Internal Dynamics, *IEEE Transactions on Automatic Control*, 44 (7), pp. 1419-1425, (1999).

14. M. Vakil, R. Fotouhi, and P. N. Nikiforuk, Causal Inversion of a Single-Link Flexible Link Manipulator via Output Planning, Proceedings of the IEEE International Conference on Mechatronics and Automation, Ontario, Canada, pp. 376-381, 2005.
15. K. H. Low, and M. Vidyasagar, Lagrangian Formulation of the Dynamic Model for Flexible Manipulator System, Journal of Dynamic Systems, Measurement and Control, 110 (2), pp. 175-181, (1988).
16. X. Zhang, W. Xu, S. S. Nair, and V. Cellabonia, PDE Modeling and Control of a Flexible Two-Link Manipulator, IEEE Transactions on Control System Technology, 13(2), pp. 301-312, (2005).
17. Y. F. Wang, and Y. Gao, Advanced Studies of Flexible Robotic Manipulators: Modeling, Design, Control and Application, World Scientific, NJ, USA, (2003).
18. W. J. Book, Recursive Lagrangian Dynamic of Flexible Manipulator Arms, International Journal of Robotics Research, 3 (3), pp. 87-101, (1984).
19. M. Vakil, R. Fotouhi, P. N. Nikiforuk, and H. Salmasi, A constrained Lagrange formulation of multi-link planar flexible manipulator, Journal of Vibration and Acoustics, Accepted, (2008).
20. F. Bellezza, L. Lanari, and G. Ulivi, Exact Modelling of the Flexible Slewing Link. Proceedings of the IEEE International Conference on Robotics and Automation, Ohio, USA, pp. 734-739, (1990).
21. J. S. Prezemienecki, Theory of Matrix Structural Analysis, McGraw-Hill, New York, USA, (1967).
22. M. Vakil, R. Fotouhi, P. N. Nikiforuk, End-Effector Trajectory Inversion of a Single Flexible Link Manipulator With Non-Zero Initial States, 16th IASTED International conference on Applied Simulation and Modeling, Palma de Mallorca, Spain, pp. 485-490, (2007).
23. X. Wang, and D. Chen, Output Tracking of a One-Link Flexible Manipulator via Causal Inversion, IEEE Transactions on Control Systems Technology, 14 (1), pp. 141-148, (2006).

24. M. Moallem, R. V. Patel, and K. Khorasani, An Inverse Dynamics Control Strategy for Tip Position Tracking of Flexible Multi-Link Manipulators, *Journal of Robotic Systems*, 14 (9), pp. 649-658, (1997).
25. M. Vakil, R. Fotouhi, and P. N. Nikiforuk, On the Zeros of a Single Flexible Link Manipulator, *Proceedings of the 17th IASTED Conference on Modeling and Simulation*, Montreal, Quebec, Canada, pp. 20-25, (2006).
26. A. R. Fraser, and R. W. Daniel, *Perturbation Techniques for Flexible Manipulators*, Kluwer Academic Publishers, Boston, USA, (1991).
27. A. S. Yigit, On the Stability of PD Control for a Two-Link Flexible Manipulator, *Journal of Dynamic Systems, Measurement and Control*, 116 (2), pp.208-215, (1994).
28. T. A. Alberts, H. Xia, and Y. Chen, Dynamic Analysis to Evaluate Viscoelastic Passive Damping Augmentation for the Space Shuttle Remote Manipulator System, *Advances in Dynamic and Control of Flexible Spacecraft and Spaced-based Manipulators*, 20, pp. 35-41, (1990).
29. C. C. de Wit, H. Olsson, K. J. Astrom, and P. Lischinsky, A New Model for Control of System with Friction, *IEEE Transactions on Automatic Control*, 40 (3), pp. 419-425, (1995).
30. B. Armstrong-Helouvry, *Control of Machines with Friction*, Kluwer, MA, USA, (1993).
31. P. S. Gandhi, and F. H. Chorbil, Closed Loop Compensation of Kinematic Error in Harmonic Drives for Precision Control Application, *IEEE Transactions on Control Systems Technology*, 10 (6), pp. 759-768, (2002).
32. D. Isobe, A unified Solution Scheme for Inverse Dynamics, *Advanced Robotics*, 18 (9), pp. 859-880, (2004).
33. R. H. A. Hensen, M. J. G. van de Molengraft, and M. Steinbuch, Friction Induced Hunting Limit Cycles: A Comparison Between the LuGre and Switch Friction Model, *Automatica*, 39, pp. 2131-2137, (2003).

34. B. Armstrong-Helouvry, and B. Amin, PID Control in the Presence of Static Friction: Exact and Describing Function Analysis, *Proceeding of American Control Conference*, pp. 597-601, (1994).
35. D. B. Rathbun, M. C. Berg, and K. W. Buffinton, Pulse Width Control for Positioning of Structurally Flexible Systems Subjected to Stiction and Coulomb Friction, *Journal of Dynamic Systems, Measurement and Control*, 126 (1), pp. 126-138, (2004).
36. S. Yang, and M. Tomizuka, Adaptive Pulse Width Control for Precise Positioning Under the Influence of Stiction and Coulomb Friction, *Journal of Dynamic Systems, Measurement and Control*, 110, pp. 186-193, (1988).
37. H. Salmasi, R. Fotouhi, and P. N. Nikiforuk, Active Vibration Suppression of a Flexible Link Manipulator Using Piezoelectric Actuator, *Computer Aided Optimum Design in Engineering, WIT Press*, pp. 199-208, (2007).
38. C. P. Tan, and M. K. Habib, The Development of Fault-Tolerant Control Approach and its Implementation on a Flexible arm robot, *Advanced Robotics*, 21 (8), pp. 887-904, (2007).
39. T. R. Chandrupatla, and A. D. Belegundu, *Introduction to finite element in engineering*, Prentice Hall, New Jersey, USA, (2002).
40. M. A. Arteage, On the properties of a Dynamic Model of Flexible Robot Manipulators, *Journal of Dynamic Systems, Measurement and Control*, 120 (1), pp. 8-14, (1998)

Chapter 4. End-effector trajectory tracking of a flexible link manipulator using integral manifold concept

Abstract:

A new controller for the end-effector trajectory tracking of a single flexible link manipulator is introduced. The linear dynamic model of the single flexible link manipulator is expressed in the singularly perturbed form. To reduce the end-effector trajectory tracking error, a corrective torque is added to the computed torque command of the rigid link counterpart of the single flexible link manipulator. The corrective torque is derived based on the concept of the integral manifold of the singularly perturbed differential equations. This corrective torque is of order ε^2 where $\varepsilon = 1/(2\pi f)$ and f is the fundamental natural frequency of the single flexible link manipulator. The implementation of the introduced technique does not require the full-state measurements since, by designing an observer the time derivative of the link's lateral deflection is estimated. The stability proof of the new controller, which is based on Lyapunov criterion, is presented. The results of the simulation and experimental studies which show the feasibility of the new approach are included. Making the error of the end-effector trajectory tracking smaller by using a new computationally cost effective controller, which was verified by simulation and experimental results, and reducing the numbers of state-measurements are the main contributions of this work.

Keywords: Flexible link manipulator, vibration control, trajectory tracking, Integral manifold, Singular perturbation

4.1. Introduction

Light-weight manipulators, usually called flexible link manipulators (FLM), are the next generation of the industrial manipulators provided that the challenges encountered during their dynamic modeling and control are addressed effectively. Since, for many industrial applications the time history of the end-effector's movement is given, end-effector trajectory tracking (EETT) of the FLM is of great importance and it has been studied for many years [1-9]. The challenging aspects of EETT of FLM are due to the facts that they are underactuated [10] and have non-minimum phase characteristics [11].

Since the FLM have a link rotations (slow subsystem) and the links' vibrations (fast subsystem), its dynamic model can be expressed in the singularly perturbed form

[1]. Consequently, the control strategies developed for singularly perturbed systems can be adopted for their EETT [12]. In this chapter, based on the concept of the integral manifold of the singularly perturbed differential equations [13,14], a new controller for the EETT of a single flexible link manipulator (SFLM) is proposed. By utilizing the concept of the integral manifold, a corrective torque is added to the computed torque command (CTC) of the rigid link counterpart of the SFLM [15 p. 135] so that the EETT error decreases. This corrective torque is of order ε^2 where $\varepsilon = 1/(2\pi f)$ and f is the fundamental natural frequency of the SFLM.

The implementation of the controller introduced here does not require the direct measurement of the full-state; since by an observer the time derivative of the link's lateral deflection is estimated. It is worth noting that the measurement of the time derivative of the link's lateral deflection is difficult, if not impossible, in practice. The fact that the new controller does not require this measurement makes it feasible.

The stability of the new proposed controller is proven using the Lyapunov criterion. The effectiveness and feasibility of the new controller is shown through several simulation and experimental studies.

The main contribution of this paper is in utilizing the concept of the integral manifold of singularly perturbed systems for the EETT. Although this concept is well-documented, there are very few reports of it being used for the EETT of FLM with experimental verification. Moreover, compared to the few available EETT controllers derived based on the concept of the integral manifold, such as [16], the method presented here is the most computationally efficient one due to the fewest corrective torques that have to be added to the CTC for the EETT reduction. Finally, the proper use of several mass matrix properties, introduced in Section 4.2, which facilitates the derivation of the corrective torque and ease the implementation of the controller, is another contribution of this work. Without the proper use of these properties the calculation of the controller command was very difficult.

$$r = \theta + \varphi = \theta + \xi(L, t) / L = \theta + \left(\sum_{i=1}^n \lambda_i \phi_i(L) \right) / L = \theta + W\lambda \quad (4-4)$$

where $W = [\phi_1(L)/L \quad \dots \quad \phi_n(L)/L]$ and L is the length of the single flexible link manipulator.

Properties of the mass matrix

The mass matrix, M in Eqs. (4-2) and (4-3), has specific properties which are used in deriving the controller in Section 4.4. These properties are as follows.

If $M^{-1} = \begin{bmatrix} (M_{\theta\theta})_{1 \times 1} & (M_{\theta\lambda})_{1 \times n} \\ (M_{\theta\lambda}^T)_{n \times 1} & (M_{\lambda\lambda})_{n \times n} \end{bmatrix}^{-1} = \begin{bmatrix} (J_{\theta\theta})_{1 \times 1} & (J_{\theta\lambda})_{1 \times n} \\ (J_{\theta\lambda}^T)_{n \times 1} & (J_{\lambda\lambda})_{n \times n} \end{bmatrix} = J$, then the following equalities between the components of M and J exist:

$$M_{\theta\lambda} M_{\lambda\lambda}^{-1} = -J_{\theta\theta}^{-1} J_{\theta\lambda} \quad (4-5a) \quad M_{\theta\lambda}^T M_{\theta\theta}^{-1} = -J_{\lambda\lambda}^{-1} J_{\theta\lambda}^T \quad (4-5b)$$

$$M_{\theta\theta} = J_{\theta\theta}^{-1} + M_{\theta\lambda} M_{\lambda\lambda}^{-1} M_{\theta\lambda}^T \quad (4-5c) \quad M_{\theta\theta}^{-1} = J_{\theta\theta} - J_{\theta\lambda} J_{\lambda\lambda}^{-1} J_{\theta\lambda}^T \quad (4-5d)$$

$$J_{\lambda\lambda} = M_{\lambda\lambda}^{-1} + J_{\theta\lambda}^T J_{\theta\theta}^{-1} J_{\theta\lambda} \quad (4-5e) \quad J_{\lambda\lambda}^{-1} = M_{\lambda\lambda} - M_{\theta\lambda}^T M_{\theta\theta}^{-1} M_{\theta\lambda} \quad (4-5f)$$

Proof: See Appendix

4.3. Singularly perturbed form and integral manifold concept

To express the dynamic model of a SFLM, Eq. (4-2), in the singularly perturbed form, the following new states are introduced:

$$x_1 = \theta \quad x_2 = \dot{\theta} \quad (4-6a)$$

$$z_1 = \lambda / \varepsilon^2 \quad z_2 = \dot{\lambda} / \varepsilon, \quad (4-6b)$$

where $x = [x_1 \quad x_2]^T$ and $z = [z_1^T \quad z_2^T]^T$ represent the vectors composed of the states of the slow and fast subsystems respectively, and $\varepsilon = 1/2\pi f$ where f is the fundamental natural frequency of the SFLM [16]. Using the new states defined in Eqs. (4-6a) and (4-6b), the dynamic model of a SFLM is:

$$\dot{x} = \begin{bmatrix} \dot{x}_1 \\ \dot{x}_2 \end{bmatrix} = \begin{bmatrix} x_2 \\ J_{\theta\theta} \tau - K_2 z_1 \end{bmatrix} \quad (4-7a)$$

$$\mathcal{E} \dot{z} = \mathcal{E} \begin{bmatrix} \dot{z}_1 \\ \dot{z}_2 \end{bmatrix} = \begin{bmatrix} z_2 \\ J_{\theta\lambda}^T \tau - K_1 z_1 \end{bmatrix} \quad (4-7b)$$

where $K_1 = J_{\lambda\lambda} K_{\lambda\lambda} / (2\pi f)^2$ and $K_2 = J_{\theta\lambda} K_{\lambda\lambda} / (2\pi f)^2$. Moreover, the end-effector's (angular) position as given in Eq. (4-4) is:

$$r = x_1 + \mathcal{E}^2 W z_1 \quad (4-8)$$

For Eqs. (4-7a) and (4-7b) with a given actuator torque, τ , the manifold defined by:

$$h^e(x_1, x_2, \tau, \mathcal{E}) = \begin{bmatrix} h_1^e(x_1, x_2, \tau, \mathcal{E}) \\ h_2^e(x_1, x_2, \tau, \mathcal{E}) \end{bmatrix} \quad (4-9)$$

is called the integral (invariant) manifold if ¹⁹:

$$z(t^*, \mathcal{E}) = h^e(x_1(t^*, \mathcal{E}), x_2(t^*, \mathcal{E}), \tau(t^*, \mathcal{E})) \Rightarrow z(t, \mathcal{E}) = h^e(x_1(t, \mathcal{E}), x_2(t, \mathcal{E}), \tau(t, \mathcal{E})) \quad \forall t > t^* \quad (4-10)$$

By definition, the integral manifold, Eq. (4-9), has to satisfy the following equations which are called the integral manifold conditions [12-14]:

$$\begin{cases} \mathcal{E} \dot{h}_1^e = h_2^e \\ \mathcal{E} \dot{h}_2^e = J_{\theta\lambda}^T \tau - K_1 h_1^e \end{cases} \quad (4-11)$$

To have an approximate solution for Eq. (4-11) up to $O(\mathcal{E}^{p+1})$, where p can be any positive integer, h^e and τ are expressed by series expansion in terms of \mathcal{E} that is :

$$\begin{aligned} h_i &= \left(\sum_{j=0}^p \mathcal{E}^j h_{ij} \right) + O(\mathcal{E}^{p+1}) \quad i = 1, 2 \\ \tau_s &= \left(\sum_{j=0}^p \mathcal{E}^j \tau_j \right) + O(\mathcal{E}^{p+1}) \end{aligned} \quad (4-12)$$

¹⁹ The superscript “e” emphasizes that h^e is the exact solution of the integral manifold.

The approximation of h_i^e ($i = 1, 2$) up to $O(\varepsilon^{p+1})$ is called h_i ($i = 1, 2$). Moreover, τ_s is the component of τ restricted (corresponded) to the approximate solution of the manifold up to $O(\varepsilon^{p+1})$. Substituting Eq. (4-12) into Eq. (4-11) and equating the terms which have the same power of ε , h_{ij} and τ_j will be obtained iteratively.

According to Eq. (4-6b), $\lambda = \varepsilon^2 z_1$. Thus for p less than 2, the flexible variables λ will not be observed in the end-effector's (angular) position given in Eq. (4-8), as also discussed in [16]. Furthermore, increasing p to more than 2 will increase the control effort and the linear modeling of the SFLM will not be valid (see simulation examples in [16]). Thus, in this article it is assumed that $p=2$. As a result Eq. (4-12) is:

$$h_i = h_{i0} + \varepsilon h_{i1} + \varepsilon^2 h_{i2} + O(\varepsilon^3) \quad i = 1, 2 \quad (4-13a)$$

$$\tau_s = \tau_0 + \varepsilon \tau_1 + \varepsilon^2 \tau_2 + O(\varepsilon^3) \quad (4-13b)$$

Substituting Eqs. (4-13a) and (4-13b) in Eq. (4-11) and equating the terms having the same power of ε , h_{ij} ($i = 1, 2, j = 0 \dots 2$) in terms of τ_i ($i = 0 \dots 2$) are:

$$h_{10} = K_1^{-1} J_{\theta\lambda}^T \tau_0 \quad (4-14a) \quad h_{11} = K_1^{-1} J_{\theta\lambda}^T \tau_1 \quad (4-14b)$$

$$h_{12} = K_1^{-1} (J_{\theta\lambda}^T \tau_2 - \dot{h}_{21}) \quad (4-14c) \quad h_{20} = 0 \quad (4-14d)$$

$$h_{21} = \dot{h}_{10} \quad (4-14e) \quad h_{22} = \dot{h}_{11} \quad (4-14f)$$

4.4. Controller design

Assuming that z is restricted to its integral manifold h , and by utilizing the approximate solution of the integral manifold up to $O(\varepsilon^3)$ given in Eqs. (4-13a) and (4-13b), Eq. (4-7a) is:

$$\dot{x} = \begin{bmatrix} \dot{x}_1 \\ \dot{x}_2 \end{bmatrix} = \begin{bmatrix} x_2 \\ J_{\theta\theta} (\tau_0 + \varepsilon \tau_1 + \varepsilon^2 \tau_2) - K_2 (h_{10} + \varepsilon h_{11} + \varepsilon^2 h_{12}) \end{bmatrix} \quad (4-15)$$

Employing the definition of h_{ij} ($i = 1, 2, j = 0 \dots 2$) provided in Eqs. (4-14a) to (4-14f) changes Eq. (4-15) into:

$$\dot{x} = \begin{bmatrix} \dot{x}_1 \\ \dot{x}_2 \end{bmatrix} = \begin{bmatrix} x_2 \\ (J_{\theta\theta} - K_2 K_1^{-1} J_{\theta\lambda}^T) \tau_0 + \varepsilon (J_{\theta\theta} - K_2 K_1^{-1} J_{\theta\lambda}^T) \tau_1 + \\ \varepsilon^2 ((J_{\theta\theta} - K_2 K_1^{-1} J_{\theta\lambda}^T) \tau_2 + K_2 K_1 \dot{h}_{21}) \end{bmatrix} \quad (4-16)$$

By recalling that $K_1 = J_{\lambda\lambda} K_{\lambda\lambda} / (2\pi f)^2$ and $K_2 = J_{\theta\lambda} K_{\lambda\lambda} / (2\pi f)^2$, using Eq. (4-14e), and utilizing the mass matrix properties given in Eqs. (4-5b) and (4-5d), Eq. (4-16) becomes:

$$\dot{x} = \begin{bmatrix} \dot{x}_1 \\ \dot{x}_2 \end{bmatrix} = \begin{bmatrix} x_2 \\ M_{\theta\theta}^{-1} (\tau_0 + \varepsilon \tau_1 + \varepsilon^2 (\tau_2 - M_{\theta\lambda} \ddot{h}_{10})) \end{bmatrix} \quad (4-17)$$

Moreover, using Eqs. (4-8) and (4-13a) and ignoring terms of order higher than ε^2 , the end-effector's (angular) position r shown in Fig. 4-1 is:

$$r = x_1 + \varepsilon^2 W h_{10} \quad (4-18)$$

where W is defined after Eq. (4-4). It is worth noting that the concise Eq. (4-17) would not have been derived if the properties of the mass matrix, given in Section 4.2, had not been introduced and used.

The subsystem described by Eq. (4-17) is called the second order corrected slow subsystem. Also the output defined in Eq. (4-18) is referred to as the output restricted to the second order manifold. This definition is due to the fact that the approximation of the integral manifold up to $O(\varepsilon^3)$ is used to obtain Eqs. (4-17) and (4-18). The objective is to design τ_0, τ_1 and τ_2 so that the output, r given in Eq. (4-18), follows a given desired trajectory, r_d .

Lemma: If the desired trajectory is $r_d \in C^4$, that is the desired trajectory and its time derivatives up to the fourth order are continuous and bounded, and K_d and K_p are positive constants, then:

$$\tau_0 = M_{\theta\theta} (\ddot{r}_d - K_d \dot{e} - K_p e) \quad (4-19)$$

$$\tau_1 = 0 \quad (4-20)$$

$$\tau_2 = M_{\theta\lambda} \ddot{h}_{10} + M_{\theta\theta} V \quad (4-21)$$

where

$$V = -W\ddot{h}_{10} - K_d W\dot{h}_{10} - K_p Wh_{10} \quad (4-22)$$

$$e = x_1 - r_d \quad (4-23)$$

make r , the output of the system restricted to the second order manifold as given in Eq. (4-18), asymptotically track r_d .

Proof: From Eq. (4-18):

$$r = x_1 + \varepsilon^2 Wh_{10} \quad (4-24)$$

Taking the derivatives of Eq. (4-24) with respect to time and using Eq. (4-17), results in:

$$\dot{r} = x_2 + \varepsilon^2 W\dot{h}_{10} \quad (4-25)$$

$$\ddot{r} = M_{\theta\theta}^{-1}(\tau_0 + \varepsilon\tau_1 + \varepsilon^2(\tau_2 - M_{\theta\lambda}\ddot{h}_{10})) + \varepsilon^2 W\ddot{h}_{10} \quad (4-26)$$

By using Eqs. (4-19) to (4-21) for τ_0, τ_1 and τ_2 and Eq. (4-22) for V , Eq. (4-26) becomes:

$$\ddot{r} = \ddot{r}_d - K_d (\overbrace{x_2 + \varepsilon^2 W\dot{h}_{10}}^{\dot{r}} - \dot{r}_d) - K_p (\overbrace{x_1 + \varepsilon^2 Wh_{10}}^r - r_d) \quad (4-27)$$

or

$$(\ddot{r}_s - \ddot{r}_d) + K_d (\dot{r}_s - \dot{r}_d) + K_p (r_s - r_d) = 0 \quad (4-28)$$

Therefore, based on the assumption that K_d and K_p are positive constants, the error dynamic of r , Eq. (4-28), is asymptotically stable. The assumption that $r_d \in C^4$, makes the control signal continuous and bounded. This is due to the fact that the calculation of τ_2 , given in Eq. (4-21), requires the evaluation of \ddot{h}_{10} and from Eqs. (4-14a) and (4-19) the calculation of h_{10} requires \ddot{r}_d , and thus the calculation of τ_2 needs the fourth derivative of r_d (QED)

According to the Lemma, if the output is restricted to the second order manifold, then r , given in Eq. (4-18), tracks the desired trajectory r_d by applying the torque $\tau_0 + \varepsilon^2 \tau_2$. Recalling that $M_{\theta\theta}$ is the mass matrix of the rigid link counterpart of the

SFLM, τ_0 given in Eq. (4-19) corresponds to the CTC of the rigid counterpart of the SFLM [15 p. 135]. Thus, to reduce the EETT error of a SFLM, the corrective torque $\varepsilon^2 \tau_2$ has to be added to τ_0 .

The fact that the fast variable, z , is restricted to its integral manifold is a key assumption in the Lemma. Therefore, to guarantee that the differences between z and its approximate manifold up to $O(\varepsilon^3)$ become essentially small, the fast component of the controller, τ_f , is designed as follows. For this purpose, the difference between z and its approximate manifold up to $O(\varepsilon^3)$, is defined here by $\hat{z} = [\hat{z}_1^T \quad \hat{z}_2^T]^T$ which is:

$$\begin{cases} \hat{z}_1 = z_1 - (h_{10} + \varepsilon h_{11} + \varepsilon^2 h_{12}) \\ \hat{z}_2 = z_2 - (h_{20} + \varepsilon h_{21} + \varepsilon^2 h_{22}) \end{cases} \quad (4-29)$$

Taking the derivative of Eq. (4-29) with respect to time, replacing \dot{z}_1 and \dot{z}_2 by their equivalences from Eq. (4-7b), substituting the control torque by $\tau = \tau_0 + \varepsilon^2 \tau_2 + \tau_f$, utilizing the expressions given for h_{ij} ($i=1,2, j=0\dots 2$) in Eqs. (4-14a) to (4-14f), and neglecting higher order terms of $O(\varepsilon^3)$, the dynamics of \hat{z} is found to be:

$$\varepsilon \dot{\hat{z}} = A_z \hat{z} + B_z \tau_f \quad (4-30)$$

where

$$A_z = \begin{bmatrix} 0 & I \\ -K_1 & 0 \end{bmatrix} \quad B_z = \begin{bmatrix} 0 \\ J_{\theta\lambda}^T \end{bmatrix} \quad \hat{z} = [\hat{z}_1^T \quad \hat{z}_2^T]^T \quad (4-31)$$

and K_1 and $J_{\theta\lambda}^T$ are defined in Eq. (4-7b). Moreover, I is the identity matrix. Considering Eq. (4-30), the full-state control command $\tau_f = -K_{cz} \hat{z}$ makes the dynamics of \hat{z} asymptotically stable, provided K_{cz} is selected so that $A_z - B_z K_{cz}$ is a Hurwitz matrix. However, for implementation of the full-state feedback controller $\tau_f = -K_{cz} \hat{z}$, the calculation of \hat{z} and thus the measurement of $z = [z_1^T \quad z_2^T]^T$ is required. From Eq. (4-6b), the measurement of z requires that the variables λ and $\dot{\lambda}$ are available. Although λ can be measured, for example with strain gauges, $\dot{\lambda}$ is not easily measurable. To

alleviate this problem, an observer-based controller for Eq. (4-30) is designed, assuming \hat{z}_1 as the output which is available if λ can be measured. That is, by assuming the following output for the system given in Eq. (4-30):

$$y = C_z \hat{z} \quad C_z = \begin{bmatrix} I_{n \times n} & 0_{n \times n} \end{bmatrix} \quad (4-32)$$

an observer-based controller is designed. This controller is:

$$\tau_f = -K_{cz} \tilde{z} \quad (4-33)$$

where \tilde{z} , the estimate of \hat{z} , is calculated from the following observer equation:

$$\varepsilon \dot{\tilde{z}} = (A_z - B_z K_{cz} - K_{oz} C) \tilde{z} + K_{oz} y \quad (4-34)$$

and K_{oz} , the observer gain matrix, has to be selected so that $A_z - K_{oz} C$ is a Hurwitz matrix.

Remark 1: According to Eqs. (4-21) and (4-22), evaluation of τ_2 requires calculation of h_{10} , \dot{h}_{10} , and \ddot{h}_{10} which are obtained as follows. By combining Eqs. (4-14a) and (4-19), h_{10} is:

$$h_{10} = (2\pi f)^2 K_{\lambda\lambda}^{-1} J_{\lambda\lambda}^{-1} J_{\theta\lambda}^T M_{\theta\theta} (\ddot{r}_d - K_d \dot{e} - K_p e) \quad (4-35)$$

Using Eq. (4-5b), Eq. (4-35) is:

$$h_{10} = -(2\pi f)^2 K_{\lambda\lambda}^{-1} M_{\theta\lambda}^T (\ddot{r}_d - K_d \dot{e} - K_p e) \quad (4-36)$$

Thus h_{10} is obtained in terms of $e = \theta - r_d$ and $\dot{e} = \dot{\theta} - \dot{r}_d$. Moreover, from Eq. (4-36), \dot{h}_{10} is:

$$\dot{h}_{10} = -(2\pi f)^2 K_{\lambda\lambda}^{-1} M_{\theta\lambda}^T (\ddot{r}_d - K_d \ddot{e} - K_p \dot{e}) \quad (4-37)$$

Since h_{10} is the integral manifold when $\varepsilon = 0$, the error dynamic on this *rigid manifold*, is $\ddot{e} + K_d \dot{e} + K_p e = 0$ [13 p. 147, 18 p. 297]. Thus, $\ddot{e} = -K_d \dot{e} - K_p e$. Substituting this into Eq. (4-37), \dot{h}_{10} is:

$$\dot{h}_{10} = -(2\pi f)^2 K_{\lambda\lambda}^{-1} M_{\theta\lambda}^T (\ddot{r}_d + K_d (K_d \dot{e} + K_p e) - K_p \dot{e}) \quad (4-38)$$

Hence, \dot{h}_{10} can also be evaluated in terms of the available signals, $e = \theta - r_d$ and $\dot{e} = \dot{\theta} - \dot{r}_d$. The same procedure can be employed for the evaluation of \ddot{h}_{10} .

Remark 2: To implement the observer-based controller, \hat{z}_1 should be available. From Eq. (4-29) to have \hat{z}_1 , the values of z_1 and $h_{10} + \varepsilon h_{11} + \varepsilon^2 h_{12}$ should be calculated. According to Eq. (4-6b) the value of z_1 is available since λ is measured. Moreover, h_{10} is given in Eq. (4-36). Also, combination of Eqs. (4-14b) and (4-20) results in $h_{11} = 0$. Thus to have \hat{z}_1 , only h_{12} is required which is calculated as follows. From Eq. (4-14c), h_{12} is:

$$h_{12} = (2\pi f)^2 K_{\lambda\lambda}^{-1} J_{\lambda\lambda}^{-1} (J_{\theta\lambda}^T \tau_2 - \ddot{h}_{10}) = (2\pi f)^2 K_{\lambda\lambda}^{-1} (J_{\lambda\lambda}^{-1} J_{\theta\lambda}^T \tau_2 - J_{\lambda\lambda}^{-1} \ddot{h}_{10}) \quad (4-39)$$

Combining Eq. (4-5b) and Eq. (4-39) results in:

$$h_{12} = (2\pi f)^2 K_{\lambda\lambda}^{-1} (-M_{\theta\lambda}^T M_{\theta\theta}^{-1} \tau_2 - J_{\lambda\lambda}^{-1} \ddot{h}_{10}) \quad (4-40)$$

and utilizing τ_2 provided in Eq. (4-21) leads to:

$$h_{12} = (2\pi f)^2 K_{\lambda\lambda}^{-1} (-(J_{\lambda\lambda}^{-1} + M_{\theta\lambda}^T M_{\theta\theta}^{-1} M_{\theta\lambda}) \ddot{h}_{10} - M_{\theta\lambda}^T V). \quad (4-41)$$

Finally using Eq. (4-5f) h_{12} given in Eq. (4-41) changes to:

$$h_{12} = -(2\pi f)^2 K_{\lambda\lambda}^{-1} (M_{\lambda\lambda} \ddot{h}_{10} + M_{\theta\lambda}^T V). \quad (4-42)$$

It is worth emphasizing that the use of the mass matrix properties given in Section 4.2 shortens the expressions of h_{10} , \dot{h}_{10} , \ddot{h}_{10} and h_{11} and h_{12} and makes the required computational effort minimum.

4.5. Stability analysis

In this section, the controller proposed in this chapter is summarized in the following theorem. Also, its stability analysis, which is similar to those explained in [8,16] and is based on the Lyapunov criterion, is presented as the proof of the proposed theorem.

Theorem: For a SFLM with the dynamic model given in Eqs. (4-7a) and (4-7b), applying the torque $\tau = \tau_0 + \varepsilon^2 \tau_2 + \tau_f$, where τ_0 , τ_2 , and τ_f are given in Eqs. (4-19), (4-21) and (4-33) respectively, makes z , given in Eqs. (4-6b), restricted to its second order integral manifold. Moreover, on this manifold the output given in Eq. (4-4) tracks the desired trajectory r_d provided that:

- 1: The gains K_d and K_p are positive constants,
- 2: The gains K_{cz} and K_{oz} are selected so that the matrices $A_z - B_z K_{cz}$ and $A_z - K_{oz} C_z$ are Hurwitz,
- 3: The condition $\mu_{\min}(S_\eta) \mu_{\min}(S_r) > \ell_1^2$ is satisfied, where S_η , S_r and ℓ_1 are defined in Eqs. (4-49), (4-50) and (4-53) respectively, and $\mu_{\min}(Q)$ is the minimum eigenvalue of matrix Q ; and
- 4: The desired trajectory $r_d \in C^4$, that is the desired trajectory and its derivative up to the fourth order are continuous and bounded.

Proof: The schematic of the closed loop system is shown in Fig. 4-2.

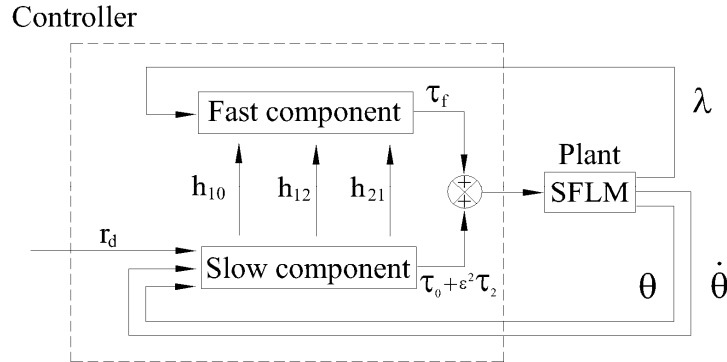


Fig. 4-2: Schematic of the closed-loop control system utilizing the concept of the integral manifold

By applying the torque $\tau = \tau_0 + \varepsilon^2 \tau_2 + \tau_f$ to a SFLM and after algebraic manipulation and neglecting term of order higher than ε^2 , the error dynamic becomes:

$$\varepsilon \dot{\eta} = A_\eta \eta \quad (4-43)$$

$$\dot{e}_r = A_r e_r + B_r \eta \quad (4-44)$$

where

$$\eta = \begin{bmatrix} \hat{z}^T & e_o^T \end{bmatrix}^T \quad e_o = \hat{z} - \tilde{z} \quad e_r = [r - r_d \quad \dot{r} - \dot{r}_d]^T \quad (4-45)$$

$$A_\eta = \begin{bmatrix} A_z - B_z K_{cz} & B_z K_{cz} \\ 0 & A_z - K_{oz} C_z \end{bmatrix} \quad A_r = \begin{bmatrix} 0 & 1 \\ -K_p & -K_d \end{bmatrix} \quad B_r = \begin{bmatrix} 0 & 0 \\ (B_r)_1 & (B_r)_2 \end{bmatrix} \quad (4-46)$$

$$(B_r)_1 = [(K_p w)/(2\pi f)^2 - K_2 \quad (K_d w)/(2\pi f) - w K_1] - (J_{\theta\theta} + w J_{\theta\lambda}^T) K_{cz} \quad (4-47)$$

$$(B_r)_2 = J_{\theta\theta} K_{cz} + w J_{\theta\lambda}^T K_{cz} \quad (4-48)$$

Since K_d and K_p are positive constants, A_r in Eq. (4-46) is Hurwitz. Moreover, according to the observer-based controller design procedure $(A_z - B_z K_{cz})$ and $(A_z - K_{oz} C_z)$ are Hurwitz, and so is A_η in Eq. (4-46). Therefore, since A_r and A_η are Hurwitz, there exist symmetric positive definite matrices P_η and P_r that satisfy the following Lyapunov equations:

$$A_\eta^T P_\eta + P_\eta A_\eta = -S_\eta \quad (4-49)$$

$$A_r^T P_r + P_r A_r = -S_r \quad (4-50)$$

where S_η and S_r are symmetric positive definite matrices. For the stability analysis, the Lyapunov candidate function is selected as:

$$V_L = \varepsilon \eta^T P_\eta \eta + e_r^T P_r e_r \quad (4-51)$$

Taking the time derivative of V_L along the trajectories of Eqs. (4-43) and (4-44) and using Eqs. (4-49) and (4-50), yields:

$$\dot{V}_L = -\eta^T S_\eta \eta - e_r^T S_r e_r + 2\eta^T B_r^T P_r e_r \quad (4-52)$$

Since B_r and P_r are constant matrices:

$$\|\eta^T B_r^T P_r e_r\| < \ell_1 \|\eta\| \|e_r\| \quad (4-53)$$

Using Eq. (4-53) and defining the symbol $\mu_{\min}(Q)$ as the minimum eigenvalues of a matrix Q , \dot{V}_L is:

$$\dot{V}_L < -\begin{bmatrix} \|\eta\| & \|e_r\| \end{bmatrix} \Omega \begin{bmatrix} \|\eta\| \\ \|e_r\| \end{bmatrix} \quad (4-54)$$

where:

$$\Omega = \begin{bmatrix} \mu_{\min}(S_\eta) & -\ell_1 \\ -\ell_1 & \mu_{\min}(S_r) \end{bmatrix} \quad (4-55)$$

Therefore, provided that

$$\mu_{\min}(S_\eta)\mu_{\min}(S_r) > \ell_1^2 \quad (4-56)$$

the matrix Ω defined in Eq. (4-55) will be positive definite and consequently the closed-loop control system is Lyapunov stable since $\dot{V}_L < 0$. The fact that $r_d \in C^4$, makes the control signals continuous and bounded, see the proof of the Lemma given in Section 4.4; otherwise, the tracking error will be unsatisfactory and large.

4.6. Simulation results

The SFLM shown in Fig. 4-1 with the physical properties given in Table 4-1 was considered. Here, L is the length of the link, EI is the link rigidity, I_h is the mass moment of inertia of the hub with respect to its center of mass, ρ is the mass per unit length, and I_{tip} and m_{tip} are the mass and the mass moment of inertia of the payload with respect to the payload center, respectively.

Table 4-1. Physical properties of the SFLM used for simulation study

$L(m)$	$EI(N.m^2)$	$I_h(kg.m^2)$	$\rho(kg / m)$	$I_{tip}(kg.m^2)$	$m_{tip}(kg)$
1.000	45.00	1.800×10^{-3}	2.000	4.800×10^{-2}	4.000

The flexibility of the link was modeled with two assumed mode shapes; that is, $n = 2$ in Eq. (4-1). The desired trajectory was selected for the end-effector's (angular) position r , which is shown in Fig. 4-1. This trajectory was chosen as the ninth order polynomial satisfying:

$$r_d(0) = 0 \quad d^i r_d / dt^i \Big|_{t=0} = 0 \quad i = 1,..4 \quad (4-57)$$

$$r_d(t_f) = \theta_f \quad d^i r_d / dt^i \Big|_{t_f} = 0 \quad i = 1,..4 \quad (4-58)$$

and it was kept constant at $r_d = \theta_f \text{ rad}$ for $t > t_f$. The simulation studies for the seventh and fifth order polynomials were also successfully conducted which their results are not reported here for brevity. For the seventh order polynomial, in addition to $r_d(0) = 0$ and $r_d(t_f) = \theta_f$, it was assumed that the velocity, acceleration and jerk of desired trajectory at time zero and t_f were all zero. To derive the fifth order polynomial, in addition to $r_d(0) = 0$ and $r_d(t_f) = \theta_f$, the conditions that the velocity and acceleration were zero at the initial and final instant of maneuver were imposed. Both the fifth and seventh order polynomials were kept constant at $r_d = r_f$ for $t > t_f$ similar to the ninth order polynomial.

Example one:

For the first simulation study, the angular position of $\theta_f = 1.570 \text{ rad}$ in Eq. (4-58) at the end of the maneuver time $t_f = 3.000 \text{ sec}$ was selected. This desired trajectory is shown in Fig. 4-3.

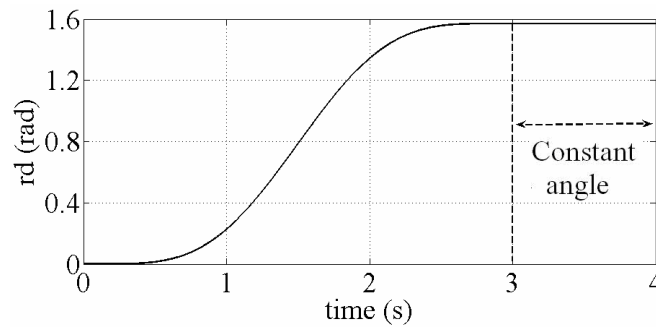


Fig. 4-3: Simulation, example 1, desired trajectory of the SFLM

The new controller proposed here for the SFLM was referred to as “*integral manifold controller*”. This controller, which was based on the integral manifold concept, added a corrective torque to the CTC of the rigid link counterpart of the SFLM. It should be noted that the controller without the corrective term was a combination of the CTC for a rigid link manipulator and state-feedback for suppressing the vibration [1] which was derived based on the singular perturbation model of the SFLM. The result of this controller was referred here to as the “*rigid link controller*”. To illustrate the superiority of the new controller introduced here, the results of the integral manifold controller were compared with the rigid link controller since both of these controllers were obtained according to the singular perturbation model of the SFLM.

For the slow component of the controller, it was assumed that $K_d = 1.000$ and $K_p = 0.2500$ in Eq. (4-19). Moreover, if $\mu(Q)$ represents the eigenvalues of the matrix Q , the eigenvalues of matrices $A_z - B_z K_{cz}$ and $A_z - K_{oc} C_z$, which were related to the fast component of the controller, were set to be $\mu(A_z - B_z K_{cz}) = \{-0.1000 \pm 1.000i, -0.1000 \pm 2.660i\}$ and $\mu(A_z - K_{oc} C_z) = \{-0.2000 \pm 2.000i, -0.2000 \pm 5.320i\}$. It is worth noting that $\mu(A_z - B_z K_{cz})$ and $\mu(A_z - K_{oc} C_z)$ have to be chosen so that the observer acts faster than the controller. That is, the real parts of $\mu(A_z - K_{oc} C_z)$ are farther from the origin than the real parts of $\mu(A_z - B_z K_{cz})$.

The trajectory tracking errors, $error = r - r_d$, employing the integral manifold controller and rigid link controller, are shown in Figs. 4-4 and 4-5, respectively. By comparing Fig. 4-4 with Fig. 4-5 the superiority of the new controller proposed here in reducing the EETT error over the rigid link controller is evident. The maximum absolute value of the EETT error for the integral manifold controller was $2.680 \times 10^{-4} \text{ rad}$ while it was much larger for the rigid link controller as $210.0 \times 10^{-4} \text{ rad}$.

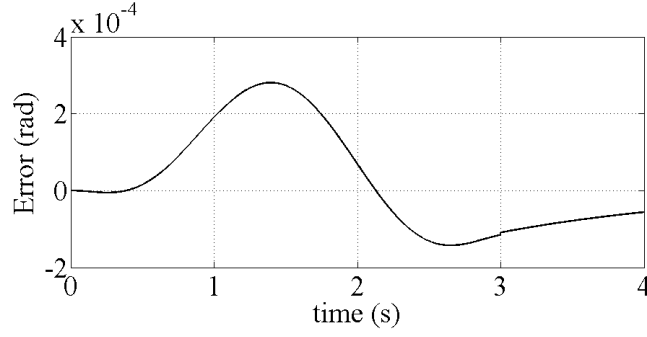


Fig. 4-4: Simulation, example 1, tracking error of r , integral manifold controller

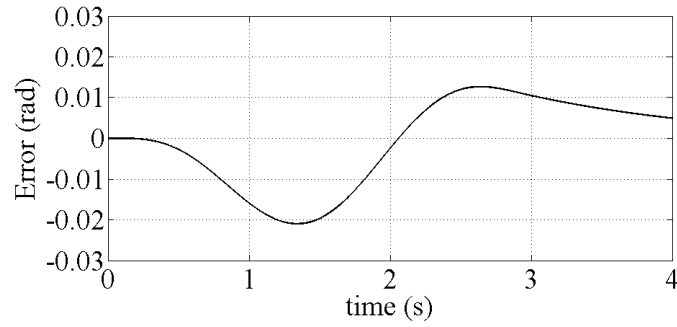


Fig. 4-5: Simulation, example 1, tracking error of r , rigid link controller

Example 2:

For the second simulation example, the final maneuver time t_f was set to 1.500 *sec* and the angular position was $\theta_f = 1.570$ *rad* in Eq. (4-58). Therefore, the average desired maneuver speed in the second example was twice the average desired maneuver speed in the first example. The desired trajectory for example 2 is shown in Fig. 4-6.

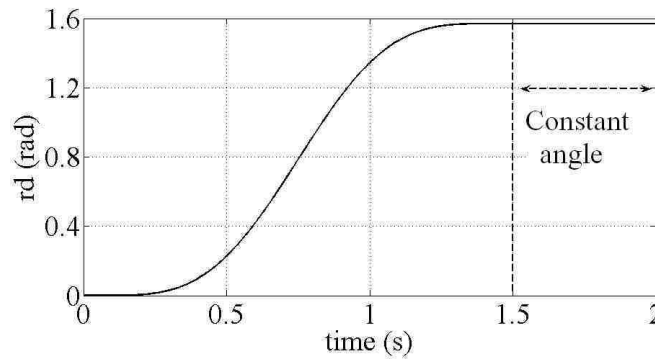


Fig. 4-6: Simulation, example 2, desired trajectory of the SFLM

The gains K_p , K_d , K_{cz} , and K_{oc} were the same as those selected in example 1. The end-effector trajectory tracking errors, $error = r - r_d$, after utilizing the integral manifold controller and rigid link controller are shown in Figs. 4-7 and 4-8, respectively.

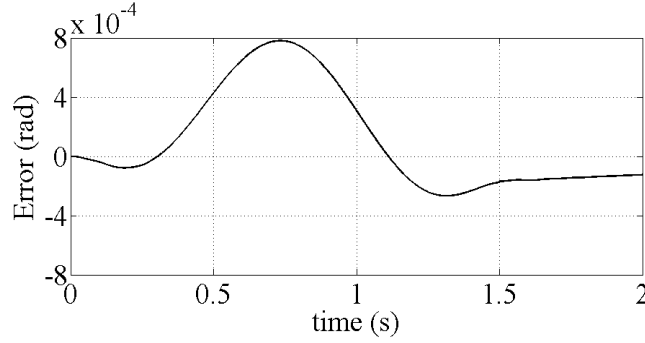


Fig. 4-7: Simulation, example 2, tracking error of r , integral manifold controller

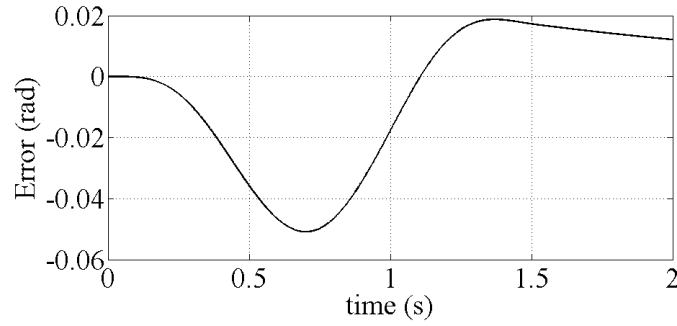


Fig. 4-8: Simulation, example 2, tracking error of r , rigid link controller

From Figs. 4-7 and 4-8, it was observed that the maximum tracking error of the integral manifold controller was $8.000 \times 10^{-4} \text{ rad}$ which was much smaller than $510.0 \times 10^{-4} \text{ rad}$ of the rigid link controller. This result showed the superiority of the new proposed controller here. Moreover, by comparing Fig. 4-4 with Fig. 4-7 and Fig. 4-5 with Fig. 4-8, it was seen that by increasing the speed of maneuver, the trajectory tracking error was increased. For the integral manifold controller, by doubling the average speed of maneuver, the maximum trajectory tracking error was increased from $2.680 \times 10^{-4} \text{ rad}$ to $8.000 \times 10^{-4} \text{ rad}$; for the rigid link controller this increase was from 0.0210 rad to 0.0510 rad . Therefore, as expected, the faster the maneuver, the higher the tracking error.

4.7. Experimental results

The SFLM that was used for the experimental study consisted of a DC motor, encoder, strain gage, data acquisition board, universal power module and flexible link with a hub. The DC motor was a Micro Mo Coreless DC motor which had high efficiency with low motor's inductance. The motor connection was a 4-pin DIN connector configured to be driven by a Quanser universal power module. The encoder was a US digital optical kit encoder having high resolution, 4096 counts in quadrature. The encoder sent a digital signal. The data acquisition board and the control software are provided by the Quanser Company. There was no payload at the tip of the manipulator. The flexible link, which was made of stainless steel, had a length of 0.4300 m , a thickness of $0.8200 \times 10^{-3}\text{ m}$ and a width of $20.74 \times 10^{-3}\text{ m}$. The hub mass moment of inertia with respect to its center of mass was approximately $6.500 \times 10^{-3}\text{ kg.m}^2$. The flexibility of the link was modeled with one mode shape and its time varying weight function was measured using a strain gauge mounted at the base. The strain gauge was calibrated to give 0.75 (volt) (approximately) for an inch deflection of the tip. The strain gauge measurement range was from -5 (volt) to 5 (volt). The experimental setup is shown in Fig. 4-9.

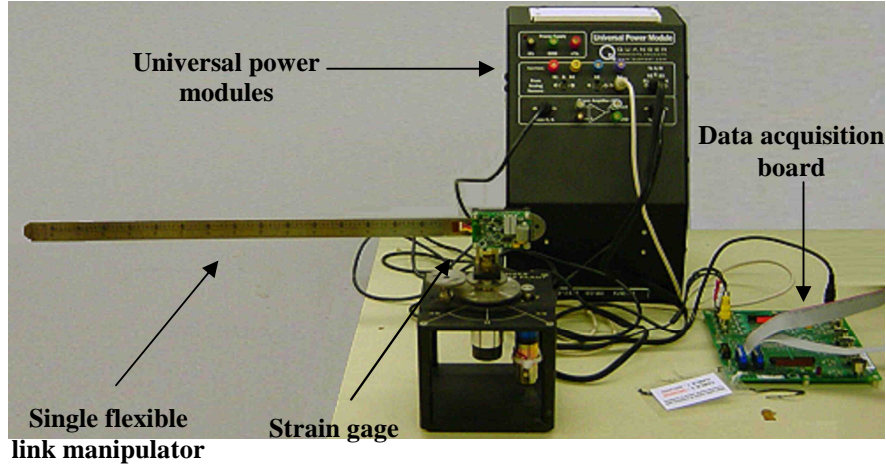


Fig. 4-9: The setup of SFLM used for experimental study

In the experimental setup, the control command was voltage. The relation between the applied voltage and the torque was $\tau = av_{\text{volt}} - b\dot{\theta}$ where constants a and b were approximately 0.1440 N.m/volt and 0.1050 N.m.s/rad , respectively. For the experimental

studies, the torque $\tau = av_{volt} - b\dot{\theta}$ was used in Eqs. (4-7a) and (4-7b). Pursuing the same approach as that given in the controller design section of this chapter, the control voltages $(v_{volt})_s$ and $(v_{volt})_f$, which corresponded to τ_s and τ_f respectively, were obtained.

Example 1:

For the first experiment verification, the desired trajectory was obtained using, $t_f = 1.000 \text{ sec}$, $\theta_f = 0.7800 \text{ rad}$ in Eq. (4-58). This desired trajectory is shown in Fig. 4-10.

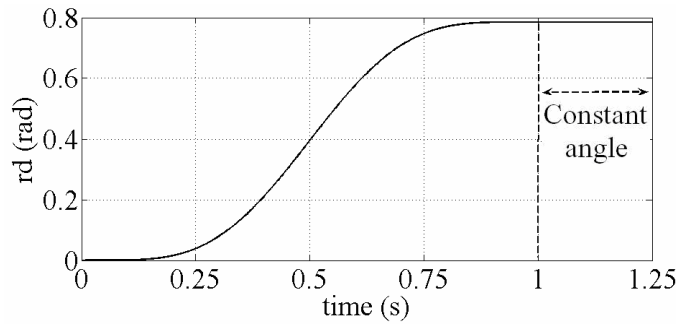


Fig. 4-10: Experiment, example 1, desired trajectory of the SFLM

For the controller implementation, it was assumed that $K_d = 4.000$, $K_p = 2.000$, $\mu(A_z - B_z K_{cz}) = \{-0.9700, -0.0230\}$ and $\mu(A_z - K_{oc} C_z) = \{-1.180, -0.8100\}$ where $\mu(Q)$ represents the eigenvalues of matrix Q . The trajectory tracking errors employing the integral manifold controller and rigid link controller are shown in Figs. 4-11 and 4-12, respectively.

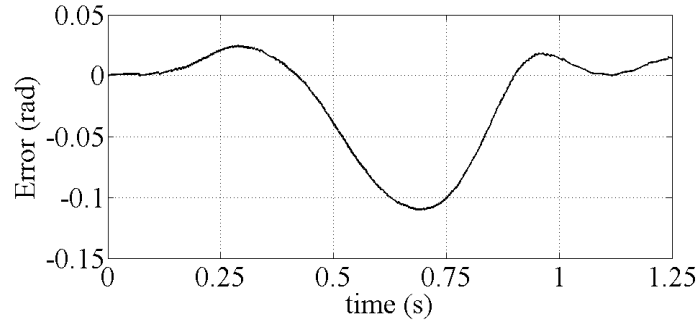


Fig. 4-11: Experiment, example 1, tracking error of r , integral manifold controller

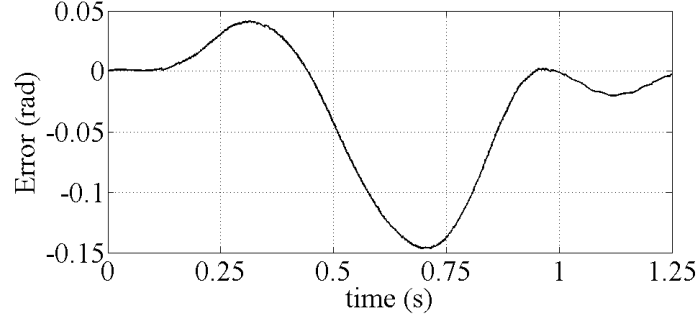


Fig. 4-12: Experiment, example 1, tracking error of r , rigid link controller

Although, the experimental results were not as good as the simulation results as far as the overall improvement of EETT error was concerned, they verified the effectiveness of the integral manifold controller over the rigid link controller²⁰. For the former, the maximum absolute values of the tracking error was 0.1160 rad , while for the latter it was bigger as 0.1460 rad , respectively. Therefore, after applying integral manifold controller, the maximum trajectory tracking error was about 1.26 times smaller.

The reasons that large differences between the EETT errors of the integral manifold and rigid link controllers were observed in the simulation section, while they were not observed in this experiment, might be attributed to the following : nonlinear friction, effects due to the movement of the strain gage cable, controller delay, modeling imperfection, not having proper values for the hub's mass moment of inertia, approximate values of a and b in $\tau = av_{volt} - b\dot{\theta}$, existence of backlash, the contribution of higher frequencies, and strain gauge error reading. Among the above sources of error, the movement of the cables and un-modeled nonlinear friction made major contributions. It is worthy to note that the integral manifold controller and rigid link controller are model based controllers. Therefore, the performance of the controller depends on how accurately the derived dynamic model represents the real physical system. Non-modeled dynamics, such as cable movement and nonlinear friction, or uncertainty in the physical system parameters, deteriorate the controller's performance. To recover the performance of the controller in the presence of the parameters' uncertainty, adaptive controllers may

²⁰ Note that the physical parameters in the simulation and experimental studies are different,. Therefore only the overall efficiency improvement can be compared with each other in the simulation and experimental studies and not the numerical values.

be implemented, such as the one used in [19] for flexible joint manipulators; this is the subject of the authors' future studies.

Example 2:

For the second experiment, the desired trajectory is shown in Fig. 4-13, which was obtained assuming $t_f = 0.5000 \text{ sec}$, $\theta_f = 0.7800 \text{ rad}$ and Eq. (4-58). The desired average maneuver speed in this experiment was twice of the first experiment.

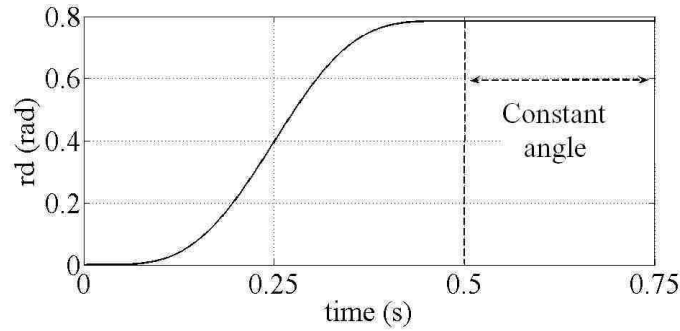


Fig. 4-13: Experiment, example2, desired trajectory of the SFLM

The controller gains for this experiment were selected as in the first experiment. The trajectory tracking errors employing the integral manifold controller and the rigid link controller are shown in Figs. 4-14 and 4-15, respectively. Although, as in the previous experiment, the results of this experiment are not as good as the simulation, they illustrate that the tracking error of the integral manifold controller is smaller than the rigid link controller. In this experiment, it was observed that, because of the corrective torque, the maximum tracking error was reduced from 0.5070 rad to 0.2790 rad . That is, the trajectory tracking error of the integral manifold controller was about 1.8 times smaller compared with the rigid link controller.

Comparing the results of this section with those of previous section showed that faster maneuver speed leads to higher trajectory tracking error, which was also observed in the simulation studies. In the experimental verification, by doubling the average speed of maneuver, the trajectory tracking error of the integral manifold controller was increased from 0.1160 rad to 0.2790 rad while for the rigid link controller it was increased from 0.1460 rad to 0.5070 rad .

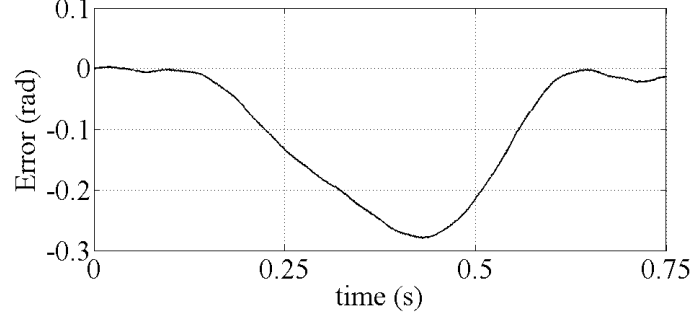


Fig. 4-14: Experiment, example 2, tracking error of r , integral manifold controller

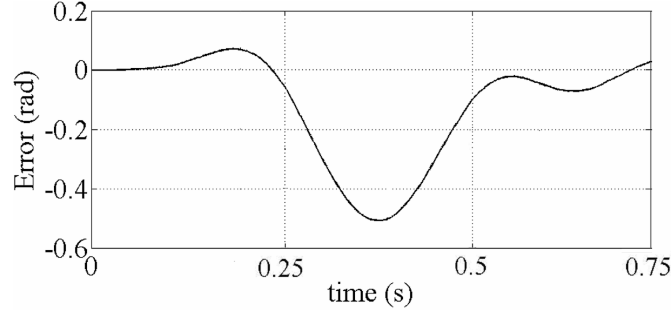


Fig. 4-15: Experiment, example 2, tracking error of r , rigid link controller

4.8. Conclusions

A new controller for the end-effector trajectory tracking of a single flexible link manipulator (SFLM) was presented. Based on the concept of the integral manifold of the singularly perturbed differential equations, a corrective term was added to the computed torque command of the rigid link counterpart of the SFLM, which was of order ε^2 where ε was the singular perturbation parameter. This scalar value, ε , was a function of the fundamental natural frequency of the manipulator and a measure of the flexibility of the link.

The implementation of the new controller did not require the measurement of the time derivative of the link's lateral deflection. This was achieved by designing an observer to estimate the time derivative of the link's lateral deflection. Practically, direct measurement of this time derivative is very difficult, if not impossible. Consequently, this feature made the introduced controller a novel and practical one.

Several simulation and experimental studies, which were conducted on SFLMs proved the effectiveness and feasibility of the proposed controller. That is the end-

effector trajectory tracking error was reduced in both the simulation and experimental studies. These studies were carried out for different desired maneuver speeds and it was observed that the faster the maneuver the higher the EETT error.

Since the proposed method here is model-based, a small difference between the derived dynamic model and the experimental setup deteriorates the expected performance of the controller. A possible remedy to recover the performance of the controller, even in the presence of these differences, is to use the adaptive control technique which can be the subject of future research.

4.9. Nomenclature

e : difference between the joint rotation and desired trajectory

$e_r = [r - r_d \quad \dot{r} - \dot{r}_d]^T$: Vector composed of the states of the error dynamics

f : Fundamental natural frequency

h^e : Integral (invariant) manifold

h : Approximation of h^e

h_i : The i th element of vector h

h_{ij} : Coefficient of ε^j in h_i

n : Number of the assumed mode shapes

r : End-effector's (angular) position

r_d : Desired trajectory

t_f : Final maneuver time

$x = [x_1, x_2]^T$: Vector composed of the states of the slow subsystem

$z = [z_1^T, z_2^T]^T$: Vector composed of the states of the fast subsystem

\hat{z} : Difference between z and its approximate manifold

\tilde{z} : Estimate of \hat{z} obtained from observer

A_z : State matrix of the fast subsystem

B_z : Input matrix of the fast subsystem

C_z : Output matrix of the fast subsystem

H : Matrix which corresponds τ to the generalized coordinates

I : Identity matrix

J : Inverse of the mass matrix

$J_{\theta\theta}, J_{\theta\lambda}, J_{\lambda\lambda}$: Component of matrix J

K_B : Stiffness matrix

$K_{\lambda\lambda}$: Matrix composed of the nonzero elements of K_B

$K_1 : J_{\lambda\lambda} K_{\lambda\lambda} / (2\pi f)^2$

$K_2 : J_{\theta\lambda} K_{\lambda\lambda} / (2\pi f)^2$

K_p, K_D : Positive constants

K_{cz}, K_{oz} : Controller and observer gains of the observer-based controller of fast subsystem

L : Length of the single flexible link manipulator

M : Mass matrix

$M_{\theta\theta}, M_{\theta\lambda}, M_{\lambda\lambda}$: Components of matrix M

P_η, P_r : Symmetric positive definite matrices

S_η, S_r : Symmetric positive definite matrices

V_L : Lyapunov candidate function

$W = [\phi_1(L)/L \quad \dots \quad \phi_n(L)/L]$:

$X = [\theta \quad \lambda^T]^T$: Matrix composed of the generalized coordinates

θ : Rotation of the hub

θ_f : Desired hub rotation at t_f

λ_i : i th flexible variable, time varying weight function of ϕ_i

ϕ_i : i th assumed mode shape

ε : Singular perturbation parameter

ξ : Link's lateral deflection of a SFLM

τ : Actuator torque

τ_j : Coefficient of ε^j in τ_s

τ_s : Component of τ restricted (corresponds) to the approximate solution of the manifold, slow component of the controller

τ_f : Fast component of the controller

$\mu_{\min}(Q)$: Minimum eigenvalue of Q

4.10. Appendix

Since the proofs for all of the equalities given in Eqs. (4-14a) to (4-14f) are similar, in this section, only the proofs for the following two equalities are provided.

$$M_{\theta\lambda} M_{\lambda\lambda}^{-1} = -J_{\theta\theta}^{-1} J_{\theta\lambda} \quad (4-A1)$$

$$M_{\theta\theta} = J_{\theta\theta}^{-1} + M_{\theta\lambda} M_{\lambda\lambda}^{-1} M_{\theta\lambda}^T \quad (4-A2)$$

where

$$M = \begin{bmatrix} (M_{\theta\theta})_{1 \times 1} & (M_{\theta\lambda})_{1 \times n} \\ (M_{\theta\lambda}^T)_{n \times 1} & (M_{\lambda\lambda})_{n \times n} \end{bmatrix}$$

$$M^{-1} = \begin{bmatrix} (M_{\theta\theta})_{1 \times 1} & (M_{\theta\lambda})_{1 \times n} \\ (M_{\theta\lambda}^T)_{n \times 1} & (M_{\lambda\lambda})_{n \times n} \end{bmatrix}^{-1} = \begin{bmatrix} (J_{\theta\theta})_{1 \times 1} & (J_{\theta\lambda})_{1 \times n} \\ (J_{\theta\lambda}^T)_{n \times 1} & (J_{\lambda\lambda})_{n \times n} \end{bmatrix} = J \quad (4-A3)$$

According the Eq. (4-A3), since J is the inverse of the mass matrix M , it is concluded that:

$$M^{-1}M = JM = I. \quad (4-A4)$$

Therefore from Eq. (4-A4):

$$\begin{bmatrix} J_{\theta\theta}M_{\theta\theta} + J_{\theta\lambda}M_{\theta\lambda}^T & J_{\theta\theta}M_{\theta\lambda} + J_{\theta\lambda}M_{\lambda\lambda} \\ J_{\theta\lambda}^TM_{\theta\theta} + J_{\lambda\lambda}M_{\theta\lambda}^T & J_{\theta\lambda}^TM_{\theta\lambda} + J_{\lambda\lambda}M_{\lambda\lambda} \end{bmatrix} = I_{(n+1) \times (n+1)} = \begin{bmatrix} I_{1 \times 1} & 0_{1 \times n} \\ 0_{n \times 1} & I_{n \times n} \end{bmatrix} \quad (4-A5)$$

Equating the elements of the first row of the Eq. (4-A5):

$$J_{\theta\theta}M_{\theta\theta} + J_{\theta\lambda}M_{\theta\lambda}^T = I_{1 \times 1} \quad (4-A6)$$

and

$$J_{\theta\theta}M_{\theta\lambda} + J_{\theta\lambda}M_{\lambda\lambda} = 0_{1 \times n} \quad (4-A7)$$

From Eq. (4-A7):

$$J_{\theta\theta}M_{\theta\lambda} + J_{\theta\lambda}M_{\lambda\lambda} = 0_{1 \times n} \Rightarrow J_{\theta\theta}M_{\theta\lambda} = -J_{\theta\lambda}M_{\lambda\lambda} \quad (4-A8)$$

Pre-multiplying both sides of Eq. (4-A8) with $J_{\theta\theta}^{-1}$ and post-multiplying it with $M_{\lambda\lambda}^{-1}$ result in:

$$M_{\theta\lambda}M_{\lambda\lambda}^{-1} = -J_{\theta\theta}^{-1}J_{\theta\lambda} \quad (4-A9)$$

and the property given in Eq. (4-A1) is proved.

From Eq. (4-A6):

$$J_{\theta\theta}M_{\theta\theta} + J_{\theta\lambda}M_{\theta\lambda}^T = I_{1 \times 1} \Rightarrow M_{\theta\theta} + J_{\theta\theta}^{-1}J_{\theta\lambda}M_{\theta\lambda}^T = J_{\theta\theta}^{-1} \quad (4-A10)$$

Substituting Eq. (4-A9), into Eq. (4-A10), leads to:

$$M_{\theta\theta} = J_{\theta\theta}^{-1} + M_{\theta\lambda}M_{\lambda\lambda}^{-1}M_{\theta\lambda}^T \quad (4-A11)$$

which is the property given in Eq. (4-A2).

4.11.Reference

1. B. Siciliano, and W. J. Book, A singular perturbation approach for control of a lightweight flexible manipulators. *International Journal of Robotics Research* 7 (4) (1988) 79-90.

2. E. Bayo, A Finite-element approach to control the end-point motion of a single link flexible robot. *Journal of Robotic Systems* 4 (1) (1989) 63-75.
3. A. De Luca, L. Lanari, and G. Ulivi, Tip trajectory tracking in flexible arms: comparison of approaches based on regulation theory. *Lecture Notes in Control and Information Sciences* 162 (1991) 190-206.
4. D. S. Kwon, and W. J. Book, Time-domain inverse dynamic tracking control of a single-link flexible manipulator. *Journal of Dynamic Systems, Measurement and Control* 116 (2) (1994) 193-200.
5. F. Y. Wang, and Y. Gao, *Advanced Studies of Flexible Robotic Manipulators: Modeling, Design, Control and Applications*, Series in Intelligent Control and Intelligent Automation, 4, Word Scientific, New Jersey, USA, 2003.
6. X. Wang, and D. Chen, Output tracking control of a one-link flexible manipulator via causal inversion. *IEEE Transactions of Control Systems Technology* 14 (1) (2006) 141-148.
7. M. Vakil, R. Fotouhi, and P. N. Nikiforuk, Piece-wise causal inversion by output redefinition for a flexible link manipulator. *Journal of Advanced Robotics* (2007) Submitted.
8. M. Vakil, R. Fotouhi, and P. N. Nikiforuk, Application of the integral manifold concept for the end-effector trajectory tracking of a flexible link manipulator, *Proceeding of American Control Conference*, New York, USA, July 11-13 2007, 741-747.
9. M. Vakil, Dynamic modeling and control of flexible link manipulators, *Ph.D thesis*, 2008, University of Saskatchewan, Saskatoon, Canada.
10. W. K. Spong, The swing up control problem for the acrobot. *IEEE Control Systems Magazine* 15 (1) (1995) pp. 49-55.
11. M. Bensman, and G. Le Vey, Stable inversion of SISO nonminimum phase linear system through output planning: an experimental application to the one-link flexible manipulator. *IEEE Transactions on Control System Technology* 11 (4) (2003) 588-597.

12. P. V. Kokotovic, H. K. Khalil, and J. O'Reilly, *Singular Perturbation Methods in Control: Analysis and Design*, Academic, New York, USA, 1999.
13. F. Ghorbel, and M. W. Spong, Integral manifold of singularly perturbed systems with application to rigid-link flexible-joint multibody system. *International Journal of Non-linear Mechanics* 35 (2000) 133-155.
14. V. A. Sobolev, Integral manifolds and decomposition of singularly perturbed systems. *Systems and Control Letters* 5 (1984) 169-179.
15. H. Asada, and J. J. E. Slotine, *Robot Analysis and Control*, John Wiley and Sons, New York, USA, 1986.
16. K. Hashtudi Zaad, and K. Khorasani, Control of non-minimum phase singularly perturbed system with application to flexible-link manipulators. *International Journal of Control* 63 (4) (1996) 679-701.
17. W. J. Book, Recursive Lagrangian dynamics of flexible manipulator arm. *International Journal of Robotics Research* 3 (3) (1984) 87-101.
18. M. W. Spong, K. Khorasani, and P. V. Kokotovic, An integral manifold approach for the feedback control of flexible joint robots. *IEEE Transactions on Robotics and Automation* 3 (4) (1987) 291-300.
19. Y. R. Hu, and G. Vukovich, Position and force control of flexible joint robots during constrained motion tasks. *Mechanism and Machine Theory* 36 (2001) 853-871.

Chapter 5. End-effector trajectory tracking for a class of flexible link manipulators

Abstract:

A new controller for the end-effector trajectory tracking (EETT) of a class of planar flexible link manipulators which consists of a chain of rigid links with the flexible end-link (CRFE) is introduced. The dynamic model of the CRFE is expressed in the standard singularly perturbed form that is decomposed into slow and fast subsystems. The states of the slow subsystem are the rotations of the joints and their time derivative, while the states of the fast subsystem are flexible variables which model the lateral deflection of the end-link and their time derivative.

For the slow subsystem, a corrective torque is added to the computed torque command (CTC) of the rigid link counterpart of the CRFE to reduce the EETT error. The corrective torque is derived based on the concept of the integral manifold of the singularly perturbed differential equations. It is shown that this corrective term is of order ε^2 where $\varepsilon = 1/(2\pi f)$ and f is the smallest non-zero natural frequency of the CRFE in the specified workspace of the manipulator.

To stabilize the fast subsystem, an observer-based controller is designed according to the gain-scheduling technique. Due to the application of the observer-based controller there is no need for the measurement of the time derivative of the flexible link's lateral deflection, which is difficult in practice, if not impossible.

To facilitate the derivation and implementation of the controller introduced here, several properties of the matrices in the dynamic model of the CRFE are described and used. The stability of this new controller is proved using the Lyapunov criterion. The effectiveness and feasibility of the new controller are shown by simulation and experimental studies.

The main contribution of this work is in introducing a new EETT controller, derived based on the singular perturbation model, which (1) - adds only one corrective term to the CTC, (2) - does not require the time derivative of the flexible link's lateral deflection for implementation, (3)- the calculation effort is minimized due to the use of several properties of the matrices in the dynamic model of the CREF , and (4) - is experimentally verified on the a nonlinear system.

Key words: Flexible multi-link manipulator, end-effector trajectory tracking, integral manifold concept, singularly perturbed differential equation

5.1. Introduction

Flexible link manipulators (FLM) are underactuated systems [1]; that is, they have more degrees-of-freedom than the number of actuators. Moreover, considering the end-effector displacement as the output, FLM are nonminimum phase systems [2], which means their end-effector inverse dynamic calculation results in a noncausal input torque²¹. These limitations of the FLM have made their end-effector trajectory tracking (EETT) a challenging subject which has been studied for years. Although, there are many controllers for the EETT of FLM, the controllers developed based on singularly perturbed systems [3] are promising candidates for the EETT of the FLM, which is the main motive of the new controller reported here. This is due to the fact that the dynamic response of a FLM is similar to that of a singularly perturbed system which has slow and fast subsystems. For the FLM, the states of the slow subsystem are the rotations of the joints and their time derivative, while the states of the fast subsystems are the flexible variables, which model the lateral deflections of the links, and their time derivative [4]; $\lambda_i, (i = 1 \dots n)$ in Eq. (5-1) are referred to here as flexible variables. In this chapter, after expressing the dynamic model of the FLM in the singularly perturbed form [4], a new EETT controller based on the concept of the integral manifold of the singularly perturbed differential equations [5, 6,7] is proposed. Since the integral manifold concept is utilized, the effect of flexible motion is also included in the EETT. Thus, this controller results in an essential improvement in reducing EETT error compared to controllers derived based on the singular perturbation approach which neglect the influence of the flexible motion. The controller introduced here is applicable to a class of planar FLM which consists of a chain of rigid links with a flexible end-link (CRFE) [12]; the CRFE is defined in Section 5.2. It is worth noting that this controller is an extension of the controller proposed by the authors in [7] which is for the EETT of a linear single flexible link manipulator.

²¹ A noncausal signal at any time depends on the values of the states before and after that time.

To reduce the EETT error, the new controller requires a corrective torque in addition to the computed torque command (CTC) of the rigid link counterpart of the CRFE, see [8] for the CTC. It was shown in this chapter that this corrective torque is of order ε^2 where $\varepsilon = 1/(2\pi f)$ and f is the smallest non-zero natural frequency of the CRFE in the specified workspace of the manipulator. To prove that the new controller adds a corrective torque to a CTC and also to derive its expression, several properties of the matrices associated with the dynamic modeling of a CRFE are introduced and used. These properties also facilitate the implementation of the new proposed controller.

The application of the new controller does not require the measurement of the time derivative of the flexible variables (time derivative of the flexible link's lateral deflection), which are cumbersome if not impossible in practice. This is due to the use of an observer-based controller to stabilize the fast subsystem, which is designed based on the gain-scheduling procedure [9]. The operating points for the gain scheduling are the joints' rotations, which are easy to measure. This ease in measurement is achieved due to the re-arrangement of the state and input matrices in the fast subsystem, detailed in Section 5.4. This rearrangement reduces the computational effort of the gain scheduling procedure considerably.

The main contribution of this paper is in utilizing the concept of the integral manifold of the singularly perturbed differential equations to design a controller for the EETT of a FLM which has nonlinear dynamics. Although the concept of the integral manifold is well-documented, to the best of authors' knowledge, there are very few reports of it being used for the EETT of nonlinear models of FLM [11]. Moreover, compared to the few available EETT controllers derived based on this concept, the novelties of the controller presented here are:

- It is computationally efficient since (1)- it only requires one corrective torque in addition to the CTC; (2)- the derivation of the control command is simplified by the use of properties of the matrices in the dynamic model; (3)- the operating point for the gain scheduling method, which is used for the calculation of the stabilizing controller of the fast subsystem, are the least possible one.

- It is feasible and practical since (1)- it is experimentally verified on a nonlinear model of a CRFE (2)- its implementation does not require measuring the time derivative of the flexible link's lateral deflection; thus, it is practical.

The rest of the present chapter is organized as follows. In Section 5.2, the CRFE is introduced and its dynamic model, including the properties of the associated matrices, as well as the control output variable, is given. The singular perturbed model of the CRFE and the controller design with its stability proof using the Lyapunov criterion are explained in Sections 5.3 and 5.4, respectively. The simulation study and experimental verification are presented in Sections 5.5 and 5.6, respectively, and the conclusions drawn from the research are given in Section 5.7.

5.2. A class of FLM with a chain of rigid links and the flexible end-link

A class of FLM consisting of a chain of rigid links with the flexible end-link (CRFE) will now be considered. A planar FLM falls into the category of CRFE if the following conditions are met:

- 1:** All the links except the last one are rigid. Moreover, the links are serially connected to each other through the revolute joints.
- 2:** The deflection of the flexible link is small; thus quadratic terms of λ_i^2 ($i = 1, \dots, n$) may be neglected in the kinetic energy expression; λ_i ($i = 1, \dots, n$) is defined in Eq. (5-1). However, the terms $\dot{\lambda}_i^2$ and $\lambda_i \dot{\lambda}_j$ ($i, j = 1 \dots n$) are considered in the kinetic energy derivation.
- 3:** The end-link has a constant density and cross section. Furthermore, the flexible end-link complies with the Euler- Bernoulli beam theory.
- 4:** All the revolute joints are active, which means there is an actuator for each revolute joint.

As an example, a schematic of a CRFE with two links is shown in Fig. 5-1 where the first link of length L_1 is rigid while the second link with the unstretched length L_2 is flexible.

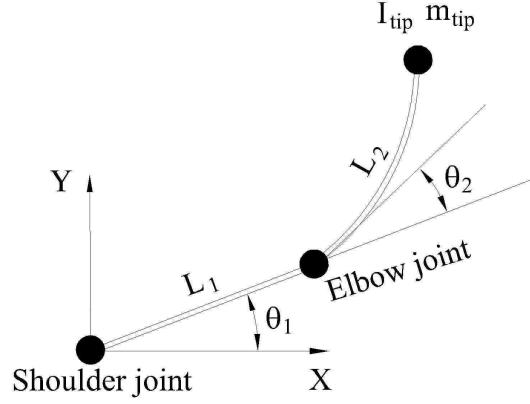


Fig. 5-1: Schematic of a CRFE with two links

5.2.1. Dynamic model of the CRFE

In deriving the dynamic model of the CRFE, the assumed mode method (AMM) [13,14] approximation is adopted to express the lateral deflection of the flexible link. Based on the AMM this deflection, $\xi(\gamma, t)$ shown in Fig. 5-2, is:

$$\xi(\gamma, t) = \sum_{i=1}^n \phi_i(\gamma) \lambda_i(t) \quad (5-1)$$

where $\phi_i(\gamma)$ is the i th spatial assumed mode shape out of n mode shapes, and $\lambda_i(t)$ is its time varying weight function, which is also referred to as a flexible variable. The generalized coordinates of the CRFE, adopting AMM to model the flexibility, will be finite and are:

$$q^T = [\theta_1 \quad \theta_2 \quad \dots \quad \theta_a \quad \lambda_1 \quad \lambda_2 \quad \dots \quad \lambda_n] \quad (5-2)$$

where $\theta_i (i = 1 \dots a)$ is the relative rotation of the i th revolute joint with respect to the $(i-1)$ th joint, a is the number of links, and $\lambda_i (i = 1 \dots n)$ is the i th flexible variable. Since the generalized coordinates of the CRFE are finite, based on the Hamiltonian principle, each generalized coordinate has to satisfy the following Lagrange equation:

$$\frac{d}{dt} \left(\frac{\partial T_{CRFE}}{\partial \dot{q}_i} \right) - \frac{\partial T_{CRFE}}{\partial q_i} + \frac{\partial U_{CRFE}}{\partial q_i} = Q_i \quad (5-3)$$

where, T_{CRFE} is the kinetic energy of the CRFE, U_{CRFE} is the combination of the potential energy of the CRFE due to the gravity and its strain energy due to the link's flexibility, q_i is the i th element of the vector q in Eq. (5-2), and Q_i is the generalized force corresponding to q_i .

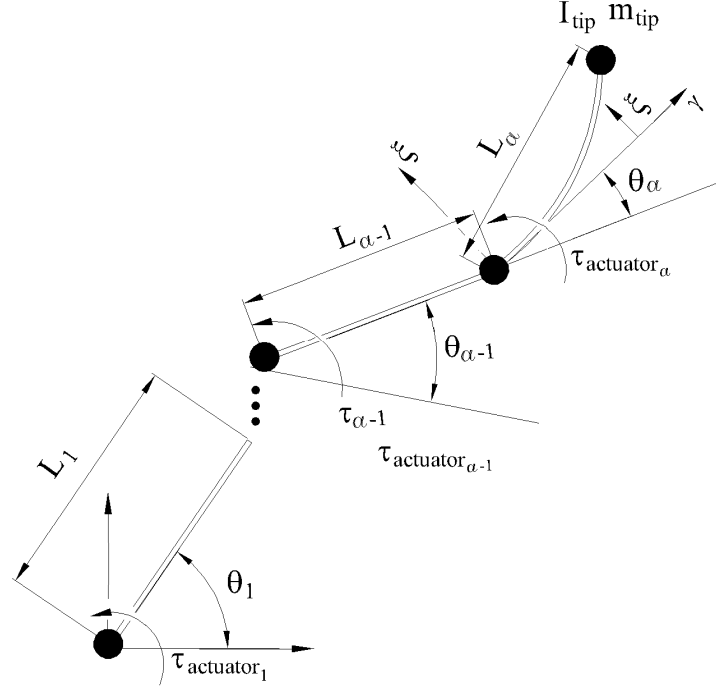


Fig. 5-2: A general CRFE with a link

Using Eq. (5-3), the dynamic equation of a CRFE is:

$$M(q)\ddot{q} + (C(q, \dot{q}) + C_D)\dot{q} + Kq + G(q) = B\tau \quad (5-4)$$

where $M(q)$ is the mass matrix, $C(q, \dot{q})$ is the matrix representing the Coriolis and centrifugal forces, C_D represents the joints' viscous damping²², K is the stiffness matrix, $G(q)$ is the gravity matrix, and B is the matrix which relates the vector of the input torques, $\tau^T = [\tau_{actuator_1} \quad \tau_{actuator_2} \quad \dots \quad \tau_{actuator_a}]$, to their corresponding generalized coordinates.

²² The internal material damping of the flexible link is neglected because of its small values [16]. It is to be noted that existence of the inherent damping facilitates the stability of the proposed controller here as discussed in [17, p. 316] for the flexible joint manipulator. Thus, the stability of the controller developed by neglecting the material damping, guarantee its successful implementation even in the presence of the link's damping.

The matrices in the dynamic model given in Eq. (5-4) have several properties that will be used in the next section for the controller design. To explain these properties, Eq. (5-4) is re-written as:

$$\begin{bmatrix} M_{\theta\theta} & M_{\theta\lambda} \\ M_{\theta\lambda}^T & M_{\lambda\lambda} \end{bmatrix} \begin{bmatrix} \ddot{q}_\theta \\ \ddot{q}_\lambda \end{bmatrix} + \begin{bmatrix} (C_D)_{\theta\theta} & 0 \\ 0 & 0 \end{bmatrix} \begin{bmatrix} \dot{q}_\theta \\ \dot{q}_\lambda \end{bmatrix} + \begin{bmatrix} F_\theta \\ F_\lambda \end{bmatrix} + \begin{bmatrix} 0 & 0 \\ 0 & K_{\lambda\lambda} \end{bmatrix} \begin{bmatrix} q_\theta \\ q_\lambda \end{bmatrix} = \begin{bmatrix} \tau \\ 0 \end{bmatrix} \quad (5-5)$$

where

$$q^T = [q_\theta^T \quad q_\lambda^T] \quad (5-6a) \quad q_\theta^T = [\theta_1 \quad \theta_2 \quad \dots \quad \theta_a] \quad (5-6b)$$

$$q_\lambda^T = [\lambda_1 \quad \lambda_2 \quad \dots \quad \lambda_n] \quad (5-6c) \quad [F_\theta^T \quad F_\lambda^T]^T = C(q, \dot{q})\dot{q} + G(q) \quad (5-6d)$$

$$\begin{bmatrix} M_{\theta\theta} & M_{\theta\lambda} \\ M_{\theta\lambda}^T & M_{\lambda\lambda} \end{bmatrix} = M(q) \quad (5-6e) \quad \begin{bmatrix} (C_D)_{\theta\theta} & 0 \\ 0 & 0 \end{bmatrix} = C_D \quad (5-6f)$$

$$\begin{bmatrix} 0 & 0 \\ 0 & K_{\lambda\lambda} \end{bmatrix} = K \quad (5-6g) \quad \begin{bmatrix} \tau \\ 0 \end{bmatrix} = B\tau \quad (5-6f)$$

$(C_D)_{\theta\theta}$ is a diagonal matrix composed of the coefficients of the viscous damping of the actuators, and θ_i ($i = 1, \dots, a$) and λ_i ($i = 1, \dots, n$) are defined in Eq. (5-2). The reasons for the assumptions that the mass matrix, M , is a function of only q_θ and F_λ is a function of only q_θ and \dot{q}_θ , as seen from Eq. (5-5), are explained in Section 5.2.2.

5.2.2. Properties of the matrices in the dynamic model of the CRFE

Property 1- The stiffness matrix, $K_{\lambda\lambda}$ given in Eq. (5-5), is constant, symmetric and positive definite.

Proof: Since, in deriving the strain energy of the flexible link, the geometric nonlinear terms for a beam in bending [15, p. 388] and axial deformation are neglected, $K_{\lambda\lambda}$ will be a constant matrix. Moreover $K_{\lambda\lambda}$ is symmetric and positive definite as proved in [18].

Property 2- Vector F_λ in Eq. (5-5), is independent of q_λ and \dot{q}_λ , thus it can be written as $F_\lambda(q_\theta, \dot{q}_\theta)$.

Proof: Matrix $C(q, \dot{q})$ and $G(q)$ in Eq. (5-4) can be partitioned as:

$$C(q, \dot{q}) = \begin{bmatrix} C_{\theta\theta} & C_{\theta\lambda} \\ C_{\lambda\theta} & C_{\lambda\lambda} \end{bmatrix} \quad G(q) = \begin{bmatrix} G_\theta \\ G_\lambda \end{bmatrix} \quad (5-7)$$

Based on Eq. (5-7) and considering Eqs. (5-6a) and (5-6d), F_λ is:

$$F_\lambda = C_{\lambda\theta} \dot{q}_\theta + C_{\lambda\lambda} \dot{q}_\lambda + G_\lambda \quad (5-8)$$

Since $C_{\lambda\theta}$ is independent of q_λ and \dot{q}_λ , $C_{\lambda\lambda} = 0_{n \times n}$ (properties 8 and 9 in [12]) and G_λ is independent of q_λ (property 11 in [12]), F_λ in Eq. (5-8) is independent of q_λ and \dot{q}_λ .

Property 3- If the inverse of the mass matrix in Eq. (5-5) is defined as:

$$\begin{bmatrix} (M_{\theta\theta})_{a \times a} & (M_{\theta\lambda})_{a \times n} \\ (M_{\theta\lambda}^T)_{n \times a} & (M_{\lambda\lambda})_{n \times n} \end{bmatrix}^{-1} = M^{-1} = J = \begin{bmatrix} (J_{\theta\theta})_{a \times a} & (J_{\theta\lambda})_{a \times n} \\ (J_{\theta\lambda}^T)_{n \times a} & (J_{\lambda\lambda})_{n \times n} \end{bmatrix} \quad (5-9)$$

then the following equalities between the components of M and J exist:

$$M_{\theta\lambda} M_{\lambda\lambda}^{-1} = -J_{\theta\theta}^{-1} J_{\theta\lambda} \quad (5-10a) \quad M_{\theta\lambda}^T M_{\theta\theta}^{-1} = -J_{\lambda\lambda}^{-1} J_{\theta\lambda}^T \quad (5-10b)$$

$$M_{\theta\theta} = J_{\theta\theta}^{-1} + M_{\theta\lambda} M_{\lambda\lambda}^{-1} M_{\theta\lambda}^T \quad (5-10c) \quad M_{\theta\theta}^{-1} = J_{\theta\theta} - J_{\theta\lambda} J_{\lambda\lambda}^{-1} J_{\theta\lambda}^T \quad (5-10d)$$

$$J_{\lambda\lambda} = M_{\lambda\lambda}^{-1} + J_{\theta\lambda}^T J_{\theta\theta}^{-1} J_{\theta\lambda} \quad (5-10e) \quad J_{\lambda\lambda}^{-1} = M_{\lambda\lambda} - M_{\theta\lambda}^T M_{\theta\theta}^{-1} M_{\theta\lambda} \quad (5-10f)$$

Proof: These properties are found after equating the corresponding terms from both sides of the equality $MJ = I$, where I is the identity matrix. Details can be found in Section 4.10.

Property 4: $M(q)$, the mass matrix in Eq. (5-4), is independent of q_λ and it can be thus

written as a function of only q_θ .

Proof: This is due to the assumption 2 in Section 5.2; see properties 5, 6, and 7 in [12]. Moreover, this can also be concluded from matrices in Appendix 2.I and noting that $(M_L)_3$ and $(M_L)_4$ are negligible.

Property 5: Matrix J , which is the inverse of the mass matrix $M(q_\theta)$, is independent of q_λ . Thus it can be written as $J(q_\theta)$

Proof: According to property 4, $M(q_\theta)$ is independent of q_λ , and therefore its inverse J is also independent of q_λ .

Property 6- The derivative $\partial F_\theta(q_\theta, q_\lambda)/\partial q_\lambda|_{q_\lambda=\dot{q}_\lambda=0}$ is a function of q_θ only.

From Eq. (5-7) and considering Eqs. (5-6a) and (5-6d), F_θ is:

$$F_\theta = C_{\theta\theta}\dot{q}_\theta + C_{\theta\lambda}\dot{q}_\lambda + G_\theta \quad (5-11)$$

The element of the matrix $C(q, \dot{q})$ given in Eq. (5-7) can be obtained from the element of the mass matrix using the Christoffel symbol as follows:

$$C(i, j) = \sum_{k=1}^s c_{i,jk} \dot{q}_k$$

$$c_{i,jk} = \frac{1}{2} \left(\frac{\partial M(i, j)}{\partial q_k} + \frac{\partial M(i, k)}{\partial q_j} - \frac{\partial M(j, k)}{\partial q_i} \right) \quad (5-12)$$

where s is number of the components of vector q , $c_{i,jk}$ is the Christoffel symbol and $M(i, j)$ is the i th row and j th column component of the mass matrix. Due to the fact that the mass matrix is independent of q_λ , property 4, and by using the Christoffel symbol in Eq. (5-12), the matrices $C_{\theta\theta}$ and $C_{\theta\lambda}$ in Eq. (5-11) do not depend on q_λ . Thus:

$$\left. \frac{\partial F_\theta(q_\theta, q_\lambda)}{\partial q_\lambda} \right|_{q_\lambda=\dot{q}_\lambda=0} = \left. \frac{\partial G_\theta}{\partial q_\lambda} \right|_{q_\lambda=\dot{q}_\lambda=0} \quad (5-13)$$

Moreover, G_θ is a linear function in terms of q_λ with the coefficients that are functions of q_θ (Appendix III in [14] or Appendix 2.I). Thus $\partial F_\theta(q_\theta, q_\lambda)/\partial q_\lambda|_{q_\lambda=\dot{q}_\lambda=0}$ will only be a function of q_θ .

5.2.3. The control variable of the CRFE

To consider the link flexibility of a CRFE in the EETT, the modified joint rotation for the a th link, $\tilde{\theta}_a$ shown in Fig. 5-3, is:

$$\tilde{\theta}_a = \theta_a + \frac{\xi(L_a, t)}{L_a} = \theta_a + wq_\lambda \quad (5-14)$$

where

$$w = \frac{1}{L_a} [\phi_1(L_a) \quad \phi_2(L_a) \quad \dots \quad \phi_n(L_a)] \quad (5-15)$$

and L_a is the unstretched length of the end-link.

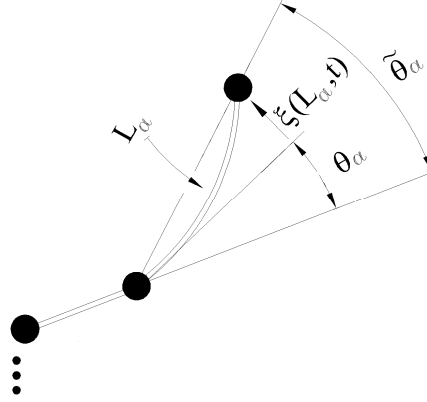


Fig. 5-3: The schematic of modified joint rotation, $\tilde{\theta}_a$, of the end-link

Using the modified joint rotation for the end-link, the control variable, r , for the CRFE is:

$$r^T = [\theta_1 \quad \theta_2 \quad \dots \quad \theta_{a-1} \quad \tilde{\theta}_a] \quad (5-16)$$

where $\theta_i (i = 1 \dots a - 1)$ are the joint rotations of the rigid links. Eq. (5-16) can also be rewritten as:

$$r = q_\theta + Wq_\lambda \quad (5-17)$$

where $W^T = [0_{n \times (a-1)} \quad w^T]$.

The output in Eq. (5-17) can be used for the precise EETT of the CRFE. As an example, the EETT of the manipulator shown in Fig. 5-1 can be converted to the trajectory tracking of its corresponding control variable defined in Eq. (5-17).

5.3. Singularly perturbed model of the CRFE and the integral manifold concept

Since the dynamic response of the CRFE is composed of slow joints' rotations and relatively fast link's vibration, this dynamic model can be represented into the singularly perturbed form. To express the dynamic model of a CRFE, in the singularly perturbed form, the following new states are defined [4]:

$$x_1 = q_\theta, \quad x_2 = \dot{q}_\theta \quad (5-18a)$$

$$z_1 = \frac{q_\lambda}{\varepsilon^2}, \quad z_2 = \frac{\dot{q}_\lambda}{\varepsilon} \quad (5-18b)$$

where the state vector of the slow subsystem $x^T = [x_1^T \quad x_2^T]$ are composed of the joints' rotations, x_1 , and their time derivative, x_2 , while the states vector of the fast subsystem $z^T = [z_1^T \quad z_2^T]$ are composed of flexible variables, z_1 , and their time derivative z_2 . Moreover, ε is the singular perturbation parameter which is [11]:

$$\varepsilon^{-1} = \sqrt{\mu_{\min}(J_{\lambda\lambda}(q_\theta)K_{\lambda\lambda})} \quad (5-19)$$

where $\mu_{\min}(J_{\lambda\lambda}K_{\lambda\lambda})$ is the minimum eigenvalue of the matrix $J_{\lambda\lambda}K_{\lambda\lambda}$. Since the matrix $J_{\lambda\lambda}(q_\theta)$ depends on q_θ , for the calculation of ε in Eq. (5-19) the minimum eigenvalue of $J_{\lambda\lambda}K_{\lambda\lambda}$, among all specified values of q_θ , should be selected. Physically, ε corresponds to the inverse of the smallest natural frequency of the CRFE over the specified range of q_θ . This is due to the fact that the eigenvalues of $J_{\lambda\lambda}K_{\lambda\lambda}$ are the square of the natural frequencies of the CRFE. Using the new states defined in Eqs. (5-18a) and (5-18b), the dynamic model of a CRFE, given in Eq. (5-5), becomes:

$$\begin{bmatrix} \dot{x}_1 \\ \dot{x}_2 \end{bmatrix} = \begin{bmatrix} x_2 \\ J_{\theta\theta}\tau - J_{\theta\theta}[F_\theta + (C_D)_{\theta\theta}x_2] - J_{\theta\lambda}F_\lambda - \frac{J_{\theta\lambda}K_{\lambda\lambda}}{\mu_{\min}(J_{\lambda\lambda}K_{\lambda\lambda})}z_1 \end{bmatrix} \quad (5-20a)$$

$$\varepsilon \begin{bmatrix} \dot{z}_1 \\ \dot{z}_2 \end{bmatrix} = \begin{bmatrix} z_2 \\ J_{\theta\lambda}^T\tau - J_{\theta\lambda}^T[F_\theta + (C_D)_{\theta\theta}x_2] - J_{\lambda\lambda}F_\lambda - \frac{J_{\lambda\lambda}K_{\lambda\lambda}}{\mu_{\min}(J_{\lambda\lambda}K_{\lambda\lambda})}z_1 \end{bmatrix} \quad (5-20b)$$

and, the control variable defined in Eq. (5-17) is:

$$r = x_1 + \varepsilon^2 W z_1 \quad (5-21)$$

For Eqs. (5-20a) and (5-20b) with a given actuator torque, τ , the manifold defined by:

$$h^e(x_1^e, x_2^e, \tau, \varepsilon) = \begin{bmatrix} h_1^e(x_1^e, x_2^e, \tau, \varepsilon) \\ h_2^e(x_1^e, x_2^e, \tau, \varepsilon) \end{bmatrix} \quad (5-22)$$

is called the integral (invariant) manifold if ²³ :

$$z(t^*, \varepsilon) = h^e(x_1^e(t^*, \varepsilon), x_2^e(t^*, \varepsilon), \tau(t^*), \varepsilon) \Rightarrow z(t, \varepsilon) = h^e(x_1^e(t, \varepsilon), x_2^e(t, \varepsilon), \tau(t), \varepsilon) \quad \forall t > t^* \quad (5-23)$$

That is if z , which represents link's lateral deflection and its derivatives, reach to h^e at t^* it stays on h^e thereafter. Consequently, when the fast variables, $z^T = [z_1^T \ z_2^T]$, are restricted to the integral manifold defined in Eq. (5-22), the $(r+n)$ second order governing equations in Eq. (5-5) are reduced to n second order differential equations which is called the *corrected slow subsystem*. As a result, the original underactuated CRFE system with $(r+n)$ degrees-of-freedom and n actuators, is converted to an approximate fully actuated control system, which has n degrees-of-freedom.

According to the definition of the integral manifold, h^e has to satisfy the following so called integral manifold conditions [3,5,6,7,10,11] which obtains by substituting h^e in Eq. (5-20b):

$$\varepsilon \begin{bmatrix} \dot{h}_1^e \\ \dot{h}_2^e \end{bmatrix} = \begin{bmatrix} h_2^e \\ J_{\theta\lambda}^T \tau - J_{\theta\lambda}^T [F_\theta + (C_D)_{\theta\theta} x_2^e] - J_{\lambda\lambda} F_\lambda - \frac{J_{\lambda\lambda} K_{\lambda\lambda}}{\mu_{\min}(J_{\lambda\lambda} K_{\lambda\lambda})} h_1^e \end{bmatrix} \quad (5-24)$$

The possibility of finding an exact algebraic solution for the integral manifold is hindered by the fact that Eq. (5-24) is a nonholonomic constraint. However, an approximation of the integral manifold can be obtained by the power series expansions of h_1^e, h_2^e and τ around $\varepsilon = 0$. For this purpose, h_1^e, h_2^e and τ are expressed as:

²³ The superscript “e” emphasizes that h^e is the exact solution of the integral manifold. Moreover, when z is restricted to its exact integral manifold h^e , the corresponding x from Eq. (20a) is called x^e .

$$h_1^e \approx h_1 = h_{10} + \varepsilon h_{11} + \varepsilon^2 h_{12} + \dots = \sum_{j=0}^p \varepsilon^j h_{1j} \quad (5-25a)$$

$$h_2^e \approx h_2 = h_{20} + \varepsilon h_{21} + \varepsilon^2 h_{22} + \dots = \sum_{j=0}^p \varepsilon^j h_{2j} \quad (5-25b)$$

$$\tau \approx \tau_s = \tau_0 + \varepsilon \tau_1 + \varepsilon^2 \tau_2 + \dots = \sum_{j=0}^p \varepsilon^j \tau_j \quad (5-25c)$$

where h_1 and h_2 are the approximations of h_1^e and h_2^e , respectively, and τ_s is the torque corresponding to the approximate solution of the integral manifold. By substituting Eqs. (5-25a) to (5-25c) into Eq. (5-24) and equating the terms having the same power of ε , the expressions of h_{ij} ($i = 1, 2$, $j = 1, 0, \dots, p$) are found iteratively in terms of τ_j ($j = 0, 1, \dots, p$). That is, the flexible link's lateral deflection and its derivatives can be found in terms of the input torque and joints' rotations and their derivatives.

For these calculations, $p = 2$ is selected in the rest of this chapter. The manifold obtained by assuming $p = 2$ in Eqs. (5-25a) to (5-25c), is called the *second order integral manifold*. To obtain the second order integral manifold, terms of order ε^p , where $p > 2$, are considered negligible and, consequently are omitted from the expressions. The reasons for the selection of $p = 2$ and the iterative calculation of h_{ij} and τ_j will now be discussed.

According to Eq. (5-18b), $q_\lambda = \varepsilon^2 z_1$. Therefore, for $p < 2$ the flexible variable q_λ will not be observed in the control variable r [11]. Moreover, for $p > 2$, the control effort will increase and the higher vibration modes will be excited [10]. Therefore, $p = 2$ is optimal and the expressions of h_1, h_2 and τ_s are:

$$h_1 = h_{10} + \varepsilon h_{11} + \varepsilon^2 h_{12} \quad (5-26a)$$

$$h_2 = h_{20} + \varepsilon h_{21} + \varepsilon^2 h_{22} \quad (5-26b)$$

$$\tau_s = \tau_0 + \varepsilon \tau_1 + \varepsilon^2 \tau_2 \quad (5-26c)$$

Substituting Eqs. (5-26a) to (5-26c), in Eq. (5-24) leads to:

$$\varepsilon \begin{bmatrix} \dot{h}_{10} + \varepsilon \dot{h}_{11} + \varepsilon^2 \dot{h}_{12} \\ \dot{h}_{20} + \varepsilon \dot{h}_{21} + \varepsilon^2 \dot{h}_{22} \end{bmatrix} = \begin{bmatrix} h_{20} + \varepsilon h_{21} + \varepsilon^2 h_{22} \\ J_{\theta\lambda}^T(\tau_0 + \varepsilon\tau_1 + \varepsilon^2\tau_2) - J_{\theta\lambda}^T[F_\theta + (C_D)_{\theta\theta}x_2] - J_{\lambda\lambda}F_\lambda - \\ + \frac{J_{\lambda\lambda}K_{\lambda\lambda}}{\mu_{\min}(J_{\lambda\lambda}K_{\lambda\lambda})}(h_{10} + \varepsilon h_{11} + \varepsilon^2 h_{12}) \end{bmatrix} \quad (5-27)$$

where x_1 and x_2 are the approximations of x_1^e and x_2^e respectively. Due to the properties of the dynamic model of CRFE, explained in Section 5.2.2, only $F_\theta(x_1, x_2, \varepsilon^2 h_1, \varepsilon h_2)$ in Eq. (5-27) is a function of ε . To iteratively find h_{ij} in terms of τ_j , and based on the assumption that ε is small, the series expansion of F_θ around $\varepsilon = 0$ is used. This series expansion around $\varepsilon = 0$ is:

$$F_\theta = (F_\theta)_0 + \varepsilon(F_\theta)_1 + \frac{1}{2}\varepsilon^2(F_\theta)_2 + \dots \quad (5-28)$$

where $(F_\theta)_i = d^i F_\theta / d\varepsilon^i \big|_{\varepsilon=0}$ and $(F_\theta)_0 = (F_\theta) \big|_{\varepsilon=0}$; the expressions of $(F_\theta)_1$ and $(F_\theta)_2$ are

available in Appendix 5.I. Replacing F_θ in Eq. (5-27) by its series expansion given in Eq. (5-28), and considering only the first three terms of the series expansion in Eq. (5-28) yields:

$$\varepsilon \begin{bmatrix} \dot{h}_{10} + \varepsilon \dot{h}_{11} + \varepsilon^2 \dot{h}_{12} \\ \dot{h}_{20} + \varepsilon \dot{h}_{21} + \varepsilon^2 \dot{h}_{22} \end{bmatrix} = \begin{bmatrix} h_{20} + \varepsilon h_{21} + \varepsilon^2 h_{22} \\ J_{\theta\lambda}^T(\tau_0 + \varepsilon\tau_1 + \varepsilon^2\tau_2) - J_{\theta\lambda}^T[(F_\theta)_0 + \varepsilon(F_\theta)_1 + \frac{1}{2}\varepsilon^2(F_\theta)_2 + (C_D)_{\theta\theta}x_2] - \\ J_{\lambda\lambda}F_\lambda - \frac{J_{\lambda\lambda}K_{\lambda\lambda}}{\mu_{\min}(J_{\lambda\lambda}K_{\lambda\lambda})}(h_{10} + \varepsilon h_{11} + \varepsilon^2 h_{12}) \end{bmatrix} \quad (5-29)$$

By equating the terms in Eq. (5-29) which have the same power of ε , the expression of h_{ij} in terms of τ_j are:

$$h_{10} = \left(\frac{J_{\lambda\lambda}K_{\lambda\lambda}}{\mu_{\min}(J_{\lambda\lambda}K_{\lambda\lambda})} \right)^{-1} [J_{\theta\lambda}^T(\tau_0 - (F_\theta)_0 - (C_D)_{\theta\theta}x_2) - J_{\lambda\lambda}F_\lambda] \quad (5-30a)$$

$$h_{20} = 0 \quad (5-30b)$$

$$h_{11} = \left(\frac{J_{\lambda\lambda}K_{\lambda\lambda}}{\mu_{\min}(J_{\lambda\lambda}K_{\lambda\lambda})} \right)^{-1} [J_{\theta\lambda}^T(\tau_1 - (F_\theta)_1) - \dot{h}_{20}] \quad (5-30c)$$

$$h_{21} = \dot{h}_{10} \quad (5-30d)$$

$$h_{12} = \left(\frac{J_{\lambda\lambda} K_{\lambda\lambda}}{\mu_{\min}(J_{\lambda\lambda} K_{\lambda\lambda})} \right)^{-1} [J_{\theta\lambda}^T (\tau_2 - \frac{1}{2} (F_\theta)_2) - \dot{h}_{21}] \quad (5-30e)$$

$$h_{22} = \dot{h}_{11} \quad (5-30f)$$

5.4. Controller design

Assuming that z_1 is restricted to its integral manifold h_1 , given in Eq. (5-26a), and by utilizing the expressions of h_1 and τ provided in Eqs. (5-26a) and (5-26c) respectively, Eq. (5-20a) becomes:

$$\begin{bmatrix} \dot{x}_1 \\ \dot{x}_2 \end{bmatrix} = \begin{bmatrix} x_2 \\ J_{\theta\theta}(\tau_0 + \varepsilon\tau_1 + \varepsilon^2\tau_2) - J_{\theta\theta}(F_\theta + (C_D)_{\theta\theta}x_2) - J_{\theta\lambda}F_\lambda - \frac{J_{\theta\lambda}K_{\lambda\lambda}}{\mu_{\min}(J_{\lambda\lambda}K_{\lambda\lambda})}(h_{10} + \varepsilon h_{11} + \varepsilon^2 h_{12}) \end{bmatrix} \quad (5-31)$$

which is the *second order corrected slow subsystem*. Moreover, the control variable, r defined in Eq. (5-21), after neglecting terms of order ε^p where $p > 2$ is:

$$r = x_1 + \varepsilon^2 W h_{10} \quad (5-32)$$

Substituting F_θ with its series expansion, given in Eq. (5-28), changes Eq. (5-31) to:

$$\begin{bmatrix} \dot{x}_1 \\ \dot{x}_2 \end{bmatrix} = \begin{bmatrix} x_2 \\ J_{\theta\theta}(\tau_0 + \varepsilon\tau_1 + \varepsilon^2\tau_2) - J_{\theta\theta}[(F_\theta)_0 + \varepsilon(F_\theta)_1 + \frac{1}{2}\varepsilon^2(F_\theta)_2 + (C_D)_{\theta\theta}x_1] - \\ + J_{\theta\lambda}F_\lambda - \frac{J_{\theta\lambda}K_{\lambda\lambda}}{\mu_{\min}(J_{\lambda\lambda}K_{\lambda\lambda})}(h_{10} + \varepsilon h_{11} + \varepsilon^2 h_{12}) \end{bmatrix} \quad (5-33)$$

After grouping the terms in Eq. (5-33) that have the same order of ε , the second order corrected slow subsystem is:

$$\begin{bmatrix} \dot{x}_1 \\ \dot{x}_2 \end{bmatrix} = \begin{bmatrix} x_2 \\ J_{\theta\theta}(\tau_0 - (F_\theta)_0 - (C_D)_{\theta\theta}x_2) - J_{\theta\lambda}F_\lambda - \frac{J_{\theta\lambda}K_{\lambda\lambda}}{\mu_{\min}(J_{\lambda\lambda}K_{\lambda\lambda})}h_{10} + \varepsilon[J_{\theta\theta}(\tau_1 - (F_\theta)_1) - \\ + \frac{J_{\theta\lambda}K_{\lambda\lambda}}{\mu_{\min}(J_{\lambda\lambda}K_{\lambda\lambda})}h_{11}] + \varepsilon^2[J_{\theta\theta}(\tau_2 - \frac{1}{2}(F_\theta)_2) - \frac{J_{\theta\lambda}K_{\lambda\lambda}}{\mu_{\min}(J_{\lambda\lambda}K_{\lambda\lambda})}h_{12}] \end{bmatrix} \quad (5-34)$$

Replacing $h_{ij}(i = 1,2 \ i = 0,1,2)$ in Eq. (5-34) with their equivalences provided in Eqs. (5-30a) to (5-30f) leads to the fact that the second order corrected slow subsystem has $\tau_j, j = 0,1,2$ as the control inputs. These control inputs are designed in Lemma 2 so that the output in Eq. (5-32) tracks a desired trajectory. Before obtaining τ_j , it is shown in Lemma 1 that, by the utilization of the mass matrix property, which are given in property 3 at Section 5.2.2, Eq. (5-34) will be shorter after replacing h_{ij} with their equivalences provided in Eqs. (5-30a) to (5-30f), without omitting any details. Therefore, the complicated mathematical equation will be simplified and the selection of the control inputs will be much easier.

Lemma 1: By the use of the expressions given in Eqs. (5-30a) to (5-30f) for $h_{ij}(i = 1,2 \ j = 0,1,2)$ and also the properties of the mass matrix given in Eqs. (5-10b) and (5-10d), Eq. (5-34) changes to:

$$\begin{bmatrix} \dot{x}_1 \\ \dot{x}_2 \end{bmatrix} = \begin{bmatrix} x_2 \\ M_{\theta\theta}^{-1}(\tau_0 - (F_\theta)_0 - (C_D)_{\theta\theta}x_2) + \varepsilon(M_{\theta\theta}^{-1}(\tau_1 - (F_\theta)_1) + \varepsilon^2(M_{\theta\theta}^{-1}(\tau_2 - \frac{1}{2}(F_\theta)_2 - M_{\theta\lambda}\ddot{h}_1)) \end{bmatrix} \quad (5-35)$$

Proof: See Appendix 5.II

Lemma 2: For the second order corrected slow subsystem given in Eq. (5-35) selecting

$$\tau_0 = M_{\theta\theta}[\ddot{r}_d - K_D(x_2 - \dot{r}_d) - K_P(x_1 - r_d)] + (F_\theta)_0 + (C_D)_{\theta\theta}x_2 \quad (5-36)$$

$$\tau_1 = 0 \quad (5-37)$$

$$\tau_2 = \frac{1}{2}(F_\theta)_2 + M_{\theta\lambda}\ddot{h}_1 + M_{\theta\theta}V \quad (5-38)$$

where

$$V = -(W\ddot{h}_{10} + K_D W\dot{h}_{10} + K_P W h_{10}) \quad (5-39)$$

makes the output r given in Eq. (5-32) asymptotically track the desired trajectory r_d provided that:

- 1- The gain matrices K_P and K_D are positive definite;

2- The desired trajectory is $r_d \in C^4$; that is, its time derivatives up to the fourth order are continuous and bounded.

Proof:

From Appendix 5.I and on the second order integral manifold, defined in Section 5.3, $(F_\theta)_1 = \frac{\partial F_\theta}{\partial \dot{q}_\lambda} \Big|_{q_\lambda = \dot{q}_\lambda = 0} z_2 \Big|_{\varepsilon=0} = \frac{\partial F_\theta}{\partial \dot{q}_\lambda} \Big|_{q_\lambda = \dot{q}_\lambda = 0} h_{20}$. Also, from Eqs. (5-26b) and (5-30b), it is concluded that $h_{20} = 0$ and therefore $(F_\theta)_1 = 0$. Replacing τ_0, τ_1 and τ_2 from Eqs. (5-36) to (5-38) into Eq. (5-35) and knowing that $(F_\theta)_1 = 0$ yields:

$$\begin{bmatrix} \dot{x}_1 \\ \dot{x}_2 \end{bmatrix} = \begin{bmatrix} x_2 \\ \ddot{r}_d - K_D(x_2 - \dot{r}_d) - K_P(x_1 - r_d) + \varepsilon^2 V \end{bmatrix} \quad (5-40)$$

Moreover, by taking time derivatives of Eq. (5-32) and employing the fact that $\dot{x}_1 = x_2$, then:

$$\dot{r} = \dot{x}_1 + \varepsilon^2 W \dot{h}_{10} = x_2 + \varepsilon^2 W \dot{h}_{10} \quad (5-41)$$

and

$$\ddot{r} = \dot{x}_2 + \varepsilon^2 W \ddot{h}_{10} \quad (5-42)$$

Replacing \dot{x}_2 from Eq. (5-40) into Eq. (5-42) and using the definition of V given in Eq. (5-39) results in:

$$\ddot{r} = \ddot{r}_d - K_D(x_2 + \varepsilon^2 W \dot{h}_{10} - \dot{r}_d) - K_P(x_1 + \varepsilon^2 W h_{10} - r_d) \quad (5-43)$$

Finally using Eqs. (5-32) and (5-41) for r and \dot{r} , respectively, Eq. (5-43) becomes:

$$(\ddot{r} - \ddot{r}_d) + K_D(\dot{r} - \dot{r}_d) + K_P(r - r_d) = 0 \quad (5-44)$$

Since the matrices K_D and K_P are positive definite, from Eq. (5-44) r asymptotically tracks r_d . From Eqs. (5-30a), (5-36) and (5-38), it is clear that calculation of τ_2 requires the fourth derivative of r_d . Therefore, the condition $r_d \in C^4$ makes the control torque bounded and continuous (**QDE**).

As given in Eq. (5-36), τ_0 is the CTC [8] for the rigid link counterpart of CRFE [4]. Therefore, based on Lemma 2, only the corrective torque $\varepsilon^2 \tau_2$ has to be added to the CTC of the rigid link counterpart of the CRFE for the EETT.

Remark 1: From Eq. (5-39), the implementation of the introduced controller requires the calculation of h_{10} , \dot{h}_{10} and \ddot{h}_{10} . By substituting τ_0 from Eq. (5-36) into Eq. (5-30a) and using the property given in Eq. (5-10b), h_{10} is:

$$h_{10} = -\mu_{\min}(J_{\lambda\lambda}K_{\lambda\lambda})K_{\lambda\lambda}^{-1}(M_{\theta\lambda}^T[\ddot{r}_d - K_D(x_2 - \dot{r}_d) - K_P(x_1 - r_d)] + F_\lambda) \quad (5-45)$$

and its time derivative is:

$$\begin{aligned} \dot{h}_{10} = & -\mu_{\min}(J_{\lambda\lambda}K_{\lambda\lambda})K_{\lambda\lambda}^{-1}(\dot{M}_{\theta\lambda}^T[\ddot{r}_d - K_D(x_2 - \dot{r}_d) - K_P(x_1 - r_d)] + \dot{F}_\lambda + \\ & M_{\theta\lambda}^T(\ddot{r}_d - K_D(\dot{x}_2 - \ddot{r}_d) - K_P(\dot{x}_1 - \dot{r}_d))) \end{aligned} \quad (5-46)$$

Since h_{10} is the integral manifold of the CRFE when $\varepsilon = 0$, on this so called *rigid manifold* [6p. 147, 20p. 297] $(\dot{x}_2 - \ddot{r}_d)$ is:

$$(\dot{x}_2 - \ddot{r}_d) = -K_D(x_2 - \dot{r}_d) - K_P(x_1 - r_d) \quad (5-47)$$

Therefore, by substituting $(\dot{x}_2 - \ddot{r}_d)$ from Eq. (5-47) in Eq. (5-46), \dot{h}_{10} can be calculated in terms of the available signals x_1 and x_2 where $x_1 = q_\theta$ and $x_2 = \dot{q}_\theta$. The calculation of \ddot{h}_{10} is similar to \dot{h}_{10} and is not discussed in this article for brevity.

The restriction of the fast variables $z^T = [z_1^T \quad z_2^T]$ to their manifold is the key assumption in deriving the control torques given in Eqs. (5-36) to (5-38). This assumption means that the link's lateral deflection and its derivative can be obtained in terms of the joints' rotations and their time derivative and input torque; and consequently, the underactuated system, CRFE, changes to an approximately fully actuated one. To ensure that this assumption is satisfied, the fast component of the controller, τ_f , is chosen in the following way. The deviation $\hat{z}^T = [\hat{z}_1^T \quad \hat{z}_2^T]$ of the state of the fast subsystem from their integral manifolds is:

$$\hat{z}_1 = z_1 - (h_{10} + \varepsilon h_{11} + \varepsilon^2 h_{12}). \quad (5-48a)$$

$$\hat{z}_2 = z_2 - (h_{20} + \varepsilon h_{21} + \varepsilon^2 h_{22}). \quad (5-48b)$$

Taking time derivative from Eqs. (5-48a) and (5-48b), using Eq. (5-20b) for \dot{z} , replacing τ with $\tau_f + \tau_0 + \varepsilon^2 \tau_2$ where τ_0 and τ_2 are defined in Eqs. (5-36) and (5-38) respectively, utilizing $h_{ij} (i=1,2 \ j=0,1,2)$ defined in Eqs. (5-30a) to (5-30f), and neglecting terms of order ε^p where $p > 2$ results in:

$$\varepsilon \dot{\hat{z}} = A_{z1} \hat{z} + B_{z1} \tau_f + N_{z1} \quad (5-49)$$

where

$$A_{z1} = \begin{bmatrix} 0 \\ -\frac{J_{\lambda\lambda} K_{\lambda\lambda}}{\mu_{\min}(J_{\lambda\lambda} K_{\lambda\lambda})} - \varepsilon^2 J_{\theta\lambda}^T \frac{\partial F_\theta}{\partial q_\lambda} & -\varepsilon J_{\theta\lambda}^T \frac{\partial F_\theta}{\partial \dot{q}_\lambda} \end{bmatrix}_{q_\lambda=\dot{q}_\lambda=0} \quad B_{z1} = \begin{bmatrix} 0 \\ J_{\theta\lambda}^T \end{bmatrix} \quad (5-50a)$$

$$N_{z1} = \begin{bmatrix} 0 \\ \frac{1}{2} \varepsilon^2 J_{\theta\lambda}^T \frac{\partial^2 F_\theta}{\partial \dot{q}_\lambda^2} (\hat{z}_2)^2 \end{bmatrix}_{q_\lambda=\dot{q}_\lambda=0} \quad (5-50b)$$

and I is the identity matrix. Detailed investigation shows that $\partial^2 F_\theta / \partial \dot{q}_\lambda^2 \Big|_{q_\lambda=\dot{q}_\lambda=0} = 0$ for the CRFE and consequently $N_{z1} = 0$. Thus, Eq. (5-49) will represent a linear dynamic equation for \hat{z} with time varying coefficients A_{z1} and B_{z1} . To stabilize \hat{z} with the dynamics given in Eq. (5-49), the full-state feedback controller $\tau_f = -K_{cz} \hat{z}$ can be used provided that $A_{z1} - B_{z1} K_{cz}$ is a Hurwitz matrix. Since the matrices A_{z1} and B_{z1} are functions of the slow variables x_1 and x_2 , the gain scheduling procedure [9] has been employed for the calculation of K_{cz} . Based on the gain scheduling procedure, in the range of variation of x_1 and x_2 several operating points like $v_i = (x_1, x_2)_i$ are selected, where i is varied to cover all the possible values of x_1 and x_2 . At each operating point $v_i = (x_1, x_2)_i$, the controller gain $(K_{cz})_{v_i}$ is calculated so that $A_{z1} - B_{z1} (K_{cz})_{v_i}$ is a Hurwitz matrix; between operating points the controller gain is linearly interpolated. The higher the number of the elements of v_i , the more complicated will be the linear interpolation in the gain

scheduling procedure and the higher the computational cost. To decrease the number of elements of v_i and ,thus, to ease the linear interpolation, Eq. (5-49) is re-written as:

$$\varepsilon \dot{\hat{z}} = A_{z2} \hat{z} + B_{z2} \tau_f + N_{z2} \quad (5-51)$$

where

$$A_{z2} = \begin{bmatrix} 0 & I \\ -\frac{J_{\lambda\lambda} K_{\lambda\lambda}}{\mu_{\min}(J_{\lambda\lambda} K_{\lambda\lambda})} - \varepsilon^2 J_{\theta\lambda}^T \frac{\partial F_{\theta}}{\partial q_{\lambda}} & 0 \end{bmatrix}_{q_{\lambda}=\dot{q}_{\lambda}=0} \quad B_{z2} = \begin{bmatrix} 0 \\ J_{\theta\lambda}^T \end{bmatrix} \quad (5-52a)$$

$$N_{z2} = \begin{bmatrix} 0 \\ -\varepsilon J_{\theta\lambda}^T \frac{\partial F_{\theta}}{\partial \dot{q}_{\lambda}} \hat{z}_2 \end{bmatrix}_{q_{\lambda}=\dot{q}_{\lambda}=0} \quad (5-52b)$$

Considering properties 1, 5 and 6 in Section 5.2.2, A_{z2} and B_{z2} in Eq. (5-51) are functions of x_1 (compare it with A_{z1} and B_{z1} in Eq. (5-49) which were functions of x_1 and x_2). Thus, the operating points for Eq. (5-51) in the gain scheduling procedure will be $v_i = (x_1)_i$ which have fewer elements than $v_i = (x_1, x_2)_i$ of Eq. (5-49). It is to be noted that for a bounded x_1 and x_2 , since $\|N_{z2}\| < \ell_1 \|\hat{z}\|$, where $\|N_{z2}\|$ is the Euclidean norm of N_{z2} in Eq. (5-51) and ℓ_1 is a constant scalar, it is possible to select the gain $(K_{cz})_{v_i}$ so that the full-state feedback $\tau_f = -(K_{cz})_{v_i} \hat{z}$ stabilizes Eq. (5-51) at $v_i = (x_1)_i$ (see, page 161 in [21] and the stability proof in Appendix 5.III).

Applying the torque $\tau_f = -K_{cz} \hat{z}$ to stabilize Eq. (5-51), requires the calculations of \hat{z}_1 and \hat{z}_2 , and thus measurements of z_1 and z_2 . From Eq. (5-18b) to measure z_1 and z_2 , the variables q_{λ} and \dot{q}_{λ} have to be available. Although q_{λ} can be directly measured, e.g. with strain gauge, the direct measurement of \dot{q}_{λ} is difficult if not impossible. To overcome this problem, an observer-based controller for Eq. (5-51) assuming \hat{z}_1 as the output, which is available by measuring q_{λ} , is proposed. That, is the output for Eq. (5-51) is assumed to be:

$$y = C_z \hat{z} \quad C_z = \begin{bmatrix} I_{n \times n} & 0_{n \times n} \end{bmatrix} \quad (5-53)$$

and τ_f is selected as:

$$\tau_f = -K_{cz}\tilde{z} \quad (5-54)$$

where \tilde{z} , the estimate of \hat{z} , is calculated from:

$$\mathcal{E}\dot{\tilde{z}} = (A_{z2} - B_{z2}K_{cz} - K_{oz}C_z)\tilde{z} + K_{oz}y \quad (5-55)$$

and K_{oz} is chosen so that $A_{z2} - K_{oz}C_z$ is a Hurwitz matrix.

Remark 2: To calculate \hat{z}_1 for the implementation of observer-based controller, h_{10} , h_{11} and h_{12} are required (see Eq. (5-48a) and note the z_1 is already measured). Parameter h_{10} is given in Eq. (5-45). From Eq. (5-30c) since $\tau_1 = 0$, $(F_\theta)_1 = 0$, and $h_{20} = 0$, then $h_{11} = 0$. Moreover:

$$h_{12} = -\mu_{\min}(J_{\lambda\lambda}K_{\lambda\lambda})K_{\lambda\lambda}^{-1}(M_{\theta\lambda}^T V + M_{\lambda\lambda}\ddot{h}_{10}) \quad (5-56)$$

where V is given in Eq. (5-39). The expression, given in Eq. (5-56) for h_{12} , can be obtained by replacing τ_2 from Eq. (5-38) and h_{21} from Eq. (5-30d) into Eq. (5-30e) and using the properties of the mass matrix given in Eqs. (5-10a) and (5-10f).

Theorem: For a CRFE with the dynamic model given in Eqs. (5-20a) and (5-20b), applying the torque $\tau_0 + \mathcal{E}^2\tau_2 + \tau_f$ where τ_0 , τ_2 and τ_f are defined in Eqs. (5-36), (5-38) and (5-54) respectively, makes the fast variables $z^T = [z_1^T \quad z_1^T]$, defined in Eq. (5-18b), restricted to its second order integral manifold defined in Eqs. (5-26a) to (5-26b), and on this manifold the output r , given in Eq. (5-17), track the desired trajectory r_d provided that:

- 1- The gain matrices K_p and K_D are selected to be positive definite;
- 2- The gain matrices K_{cz} and K_{oz} are selected so that $A_{z2} - B_{z2}K_{cz}$ and $A_{z2} - K_{oz}C_z$ are Hurwitz matrices, where A_{z2} , B_{z2} and C_z are given in Eqs. (5-52a) and (5-53) respectively;

3- The condition $\mu_{\min}(S_{\eta})\mu_{\min}(S_r) > \ell_2^2$ is satisfied, where S_{η}, S_r and ℓ_2 are defined in Eqs. (5-A31), (5-A32) and (5-A34) in Appendix 5.III, and $\mu_{\min}(Q)$ is the minimum eigenvalue of the matrix Q ; and

4- The desired trajectory and its time derivatives up to the fourth order are continuous and bounded, $r_d \in C^4$.

Proof: The proof of this theorem, which is based on the Lyapunov criterion and is similar to those in [7,11], is given in Appendix 5.III.

5.5. Simulation results

In this section the results of simulation study for a manipulator called rigid shoulder-link flexible elbow-link manipulator, with the schematic shown in Fig. 5-1 are presented. The first and second joints of this manipulator were called shoulder and elbow joints, respectively. Moreover, the actuators located on the shoulder and elbow joints were referred to as shoulder and elbow actuators, respectively. The physical parameters of the rigid shoulder-link flexible elbow-link manipulator used for the simulation studies are given in Table 1. The flexibility of the second link was modeled using two mode shapes, which were adopted from [14]. Moreover, it was assumed that the manipulator was operated in the horizontal plane and, consequently, there was no force of gravity involved. The desired trajectories were selected for the elements of the vector $r^T = [r_1 \ r_2] = [\theta_1 \ \tilde{\theta}_2]$ where θ_1 was the rotation of the first link (rigid shoulder-link), and $\tilde{\theta}_2$ which was the modified joint rotation for the flexible elbow-link, defined in Eq. (5-14). The desired trajectories r_{d1} and r_{d2} were selected to be the ninth order polynomials and satisfying conditions:

$$r_{dj}(0) = 0 \quad \left. \frac{d^i r_{dj}}{dt^i} \right|_{t=0} = 0 \quad i = 1, \dots, 4 \quad j = 1, 2 \quad (5-57)$$

$$r_{dj}(t_{ff}) = \theta_{ff} \quad \left. \frac{d^i r_{dj}}{dt^i} \right|_{t_{ff}} = 0 \quad i = 1, \dots, 4 \quad j = 1, 2 \quad (5-58)$$

These trajectories were kept constant at $r_{dj} = \theta_{ff}(\text{rad})$ for $t > t_{ff}$, where θ_{ff} were the desired final positions of r_{dj} at times t_{ff} ($j = 1, 2$), respectively. The simulation studies for the

seventh and fifth order polynomials were also successfully conducted which their results are not reported here for briefness. For the seventh order polynomial, in addition to $r_d(0) = 0$ and $r_d(t_f) = \theta_f$, it was assumed that the velocity, acceleration and jerk of desired trajectory at time zero and t_f were all zero. To derive the fifth order polynomial, in addition to $r_d(0) = 0$ and $r_d(t_f) = \theta_f$, the conditions that the velocity and acceleration were zero at the initial and final instant of maneuver were imposed. Both the fifth and seventh order polynomials were kept constant at $r_d = r_f$ for $t > t_f$ similar to the ninth order polynomial.

Table 1: Physical parameters of the rigid shoulder-link flexible elbow-link manipulator

Physical parameters	values
L_1 (Length of the rigid shoulder-link)	0.250 (m)
m_1 (Mass of the rigid shoulder-link)	0.585 (kg)
I_1 (Mass moment of inertia of the rigid shoulder-link)	3.04×10^{-3} (kg.m ²)
I_{h1} (Mass moment of inertia of the shoulder actuator)	2.00×10^{-3} (kg.m ²)
L_2 (Length of the flexible elbow-link)	1.00 (m)
ρ_2 (Mass per unit length of the flexible elbow-link)	0.468 (kg/m)
EI (Rigidity of the flexible elbow-link)	4.00 (N.m ²)
m_{h2} (Mass of the elbow actuator)	0.250(kg)
I_{h2} (Mass moment of inertia of the elbow actuator)	2.00×10^{-3} (kg.m ²)
m_{tip} (End-effector mass)	0.700 (kg)
I_{tip} (End-effector mass moment of inertia)	zero (kg.m ²)

For the simulation study, reported here, the desired trajectories r_{d1} and r_{d2} were obtained by selecting $\theta_{f1} = -\theta_{f2} = 0.785(\text{rad})(= 45.0^\circ)$ and $t_{f1} = t_{f2} = 3.00(\text{s})$ in Eqs. (5-57) and (5-58) and; these trajectories are shown in Fig. 5-4.

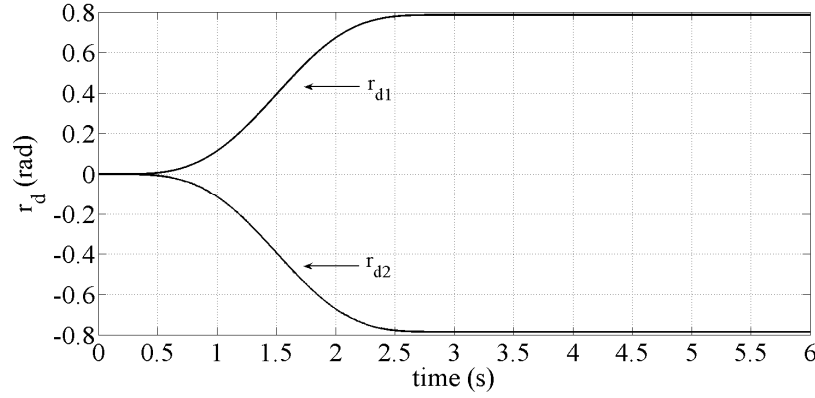


Fig. 5-4: Simulation, example 1, Desired trajectories r_{d1} and r_{d2}

To implement the controller, gains $K_p = 0.360I$ and $K_D = 1.20I$ in τ_0 , τ_2 and V were selected, where I is the identity matrix and the expressions of τ_0 , τ_2 and V were given in Eqs. (5-36), (5-38) and (5-39), respectively. For the design of the observer-based controller, the gain scheduling procedure, explained in Section 5.4, was employed. The matrices A_{z2} and B_{z2} which were used in design of the controller and observer gains, K_{cz} and K_{oz} , were functions of θ_2 . Thus, the operating points were $\vartheta_i = (\theta_2)_i$. Since the values of $r_{d2} = \tilde{\theta}_{d2}$ varied from zero to $-45.0^\circ (-0.785(\text{rad}))$, it was assumed that the possible range of the variation of θ_2 was from 12.0° to -57.0° . That is, $\min(r_{d2}) - \delta r_{d2} < \theta_2 < \max(r_{d2}) + \delta r_{d2}$ in which $\delta r_{d2} = 12.0^\circ$. Therefore, the selected range of variation of θ_2 was 12.0° wider from both sides compared to the range of the variation of r_{d2} . As a result, when in the simulation the value of θ_2 passed the limits of r_{d2} , the gains K_{cz} and K_{oz} could still be calculated. This range of θ_2 , from 12.0° to -57.0° , was divided into 23 equal segments and the operating points were selected as $\vartheta_i = (\theta_2)_i = 12 - 3(i - 1), (i = 1, \dots, 24)$. Then, the gains K_{cz} and K_{oz} were selected so that, $\mu(A_{z2} - B_{z2}K_{cz}) = \{-0.5 \pm 2.0j, -0.4 \pm 1.0j\}$ and $\mu(A_{z2} - C_zK_{oz}) = \{-1.0 \pm 4.0j, -0.8$

$\pm 2.0j\}$ at each operating point, where $\mu(Q)$ represent the eigenvalues of the matrix Q . Finally, the controller and observer gains were linearly interpolated between the operating points. In the design of the controller gain K_{cz} , it was considered that the elbow actuator was active and the shoulder actuator was deactive. This could be justified by the fact that the model accessibility of the second link vibration from the first link actuator was small.

The new controller proposed in this article is refereed to as “*integral manifold controller*” which adds a corrective term to the computed torque command (CTC) of the rigid link counterpart of the CRFE. The controller without the corrective term is the CTC of the rigid link manipulator plus a state-feedback controller for the vibration suppression similar to the one developed in [4], which is refereed to here as the “*rigid link controller*”. To observe the effectiveness of adding the corrective torque, the results of the integral manifold controller were compared with the rigid link controller. The trajectory tracking errors for r_1 and r_2 , measured by $error_1 = r_1 - r_{d1}$ and $error_2 = r_2 - r_{d2}$, after applying the integral manifold controller are given in Figs. 5-5 and 5-6, respectively. Moreover, the trajectory tracking errors for r_1 and r_2 , employing the rigid link controller, are shown in Figs. 5-7 and 5-8, respectively.

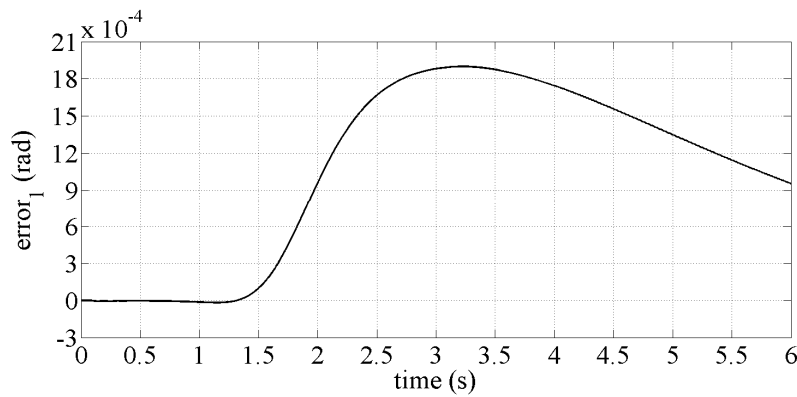


Fig. 5-5: Simulation, trajectory tracking error of r_1 , integral manifold controller

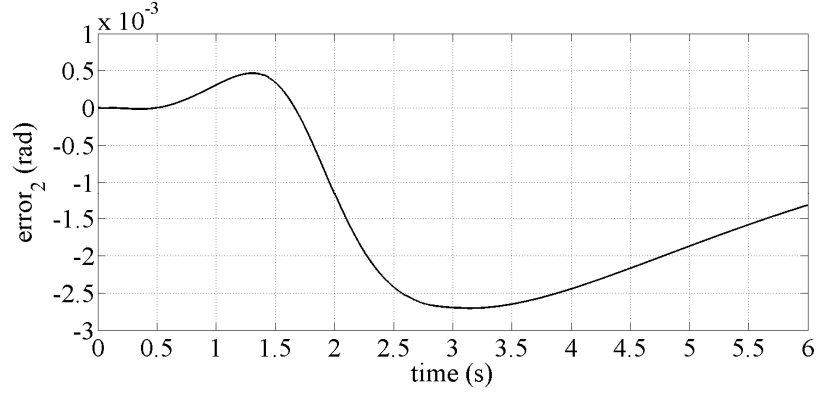


Fig. 5-6: Simulation, trajectory tracking error of r_2 , integral manifold controller

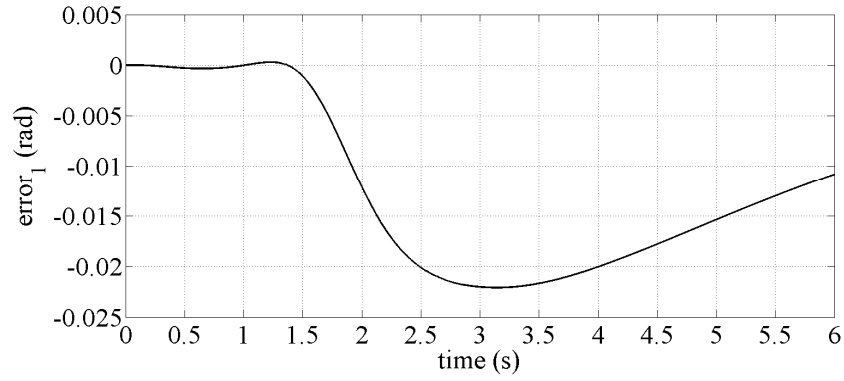


Fig. 5-7: Simulation, trajectory tracking error of r_1 , rigid link controller

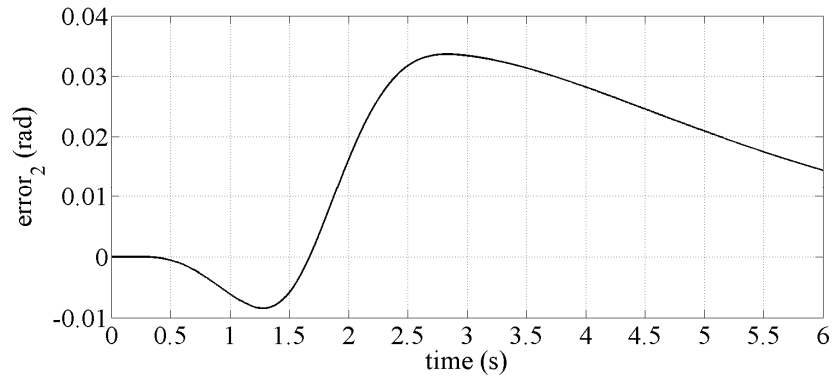


Fig. 5-8: Simulation, trajectory tracking error of r_2 , rigid link controller

By comparing Figs. 5-5 and 5-6 with Figs. 5-7 and 5-8, respectively, it is clear that the new integral manifold controller resulted in the trajectory tracking errors which were considerably smaller than those of the rigid link controller. The absolute maximum value of the $error_1$ and $error_2$ after the integral manifold controller were 0.0019 (rad)

and 0.0027 (*rad*) while for the rigid link controller they were larger, being 0.0221 (*rad*) and 0.0336 (*rad*), respectively. That is, the maximum tracking errors for the integral manifold controller were about twelve times smaller than those of the rigid link controller. Besides comparing the maximum absolute values of the errors, in the following a normalized index which was defined over the entire manoeuvre time was introduced and used. This index, which signified the overall tracking error reduction, was called the normalized mean square error (NMSE), and was defined as:

$$NMSE = \sqrt{\frac{1}{t_m} \int_0^{t_m} (error_1^2 + error_2^2) dt} \quad (5-59)$$

where

$$error_1 = r_1 - r_{d1}, \quad error_2 = r_2 - r_{d2} \quad (5-60)$$

and t_m is the total time of the simulation or experiment. Using Eqs. (5-59) and (5-60), the NMSE for the integral manifold controller was 0.0022 (*rad*) while for the rigid link controller it was 0.0264 (*rad*), which clearly indicated the effectiveness of addition of the new controller introduced here in reducing the overall tracking error. Finally, the end-effector paths, which are shown in Fig. 5-9, illustrated the reduction in the end-effector path tracking error due to the use of the integral manifold controller instead of the rigid link controller. In Fig. 5-9 the integral manifold controller path and desired path can hardly be distinguished, while the difference between the rigid link controller path and the desired path is apparent. For the integral manifold controller, the absolute maximum difference of the desired path and actual path was $5.979 \times 10^{-4} (m)$ while for the rigid link controller this difference was $91.00 \times 10^{-4} (m)$.

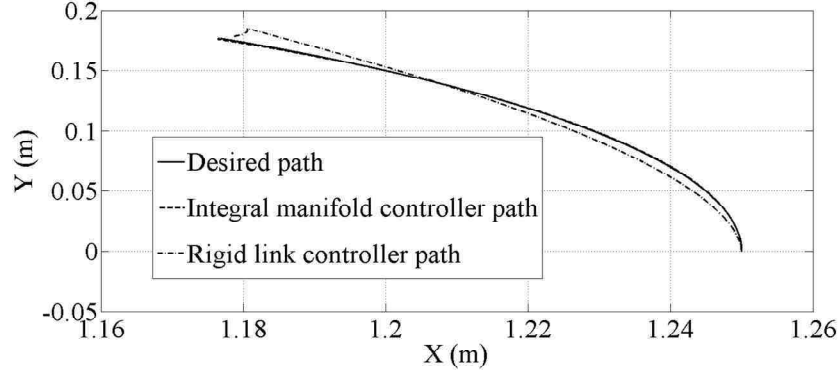


Fig. 5-9: Simulation, Actual paths after applying the integral manifold and rigid link controllers as well as the desired path

More simulation studies were performed on the manipulator used in this section but with different average speeds for r_{d1} and r_{d2} than those of the simulation presented here. The results of these simulations were not reported here. The conclusion after these simulations was the same as the one reached after the above simulation; that is, the integral manifold controller reduced the EETT error considerably. Moreover, these simulations showed that by increasing the average speeds of r_{d1} and r_{d2} , the maximum absolute value of the tracking errors were increased, as expected, which means the faster the maneuver, the greater the EETT error.

5.6. Experimental results

In this section the results of an experimental study carried out using the rigid shoulder-link flexible elbow-link manipulator, shown in Fig. 5-10, which is available in the robotic laboratory of the University of Saskatchewan, are presented. This manipulator has two DC motors which, by the means of harmonic gearboxes, drive the links. Both motors have quadrature optical encoders which have 1024 lines per revolution and are from Harmonic Drive technologies. The model number for the first one is PSA-14-100 and it uses Maxon 273759 precision brush (90 Watts). The model number of the second harmonic drive is PSA-8-080 and utilized the Maxon 118752 precision brush motor (20 Watts). The physical parameters of this manipulator are as follows. The length of the rigid shoulder-link is 0.3500 (m). The mass moment of inertia of the rigid shoulder-link with respect to the shoulder joint including the shoulder actuator, its hub and mounting

bracket is $0.2800 \text{ (kg.m}^2\text{)}$. The flexible elbow-link is made of stainless steel with a length of 0.2300 (m) , a thickness of $8.890 \times 10^{-4} \text{ (m)}$ and a height of 0.0381 (m) . The mass moment of inertia of the actuator on the elbow joint, its hub and mounting bracket is $0.0198 \text{ (kg.m}^2\text{)}$. Finally, the mass and mass moment of inertia of the end-effector are 0.1649 (kg) and $2.570 \times 10^{-5} \text{ (kg.m}^2\text{)}$, respectively²⁴.

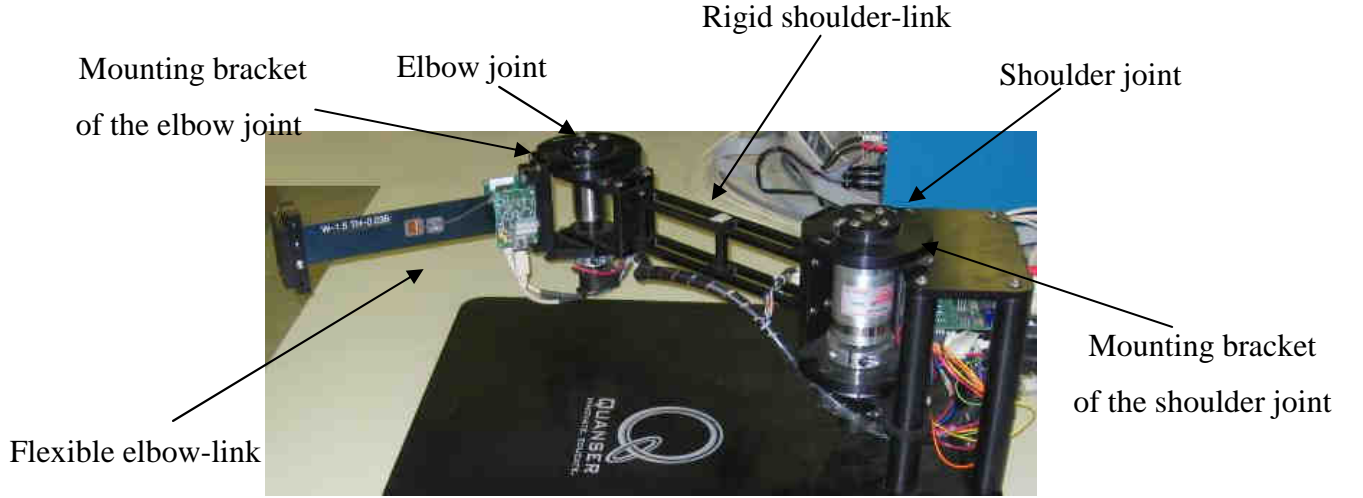


Fig. 5-10: Rigid shoulder-link flexible elbow-link manipulator in the robotics laboratory of the University of Saskatchewan used for experimental verification

In addition to the above physical parameters, due to the application of harmonic gearbox, there is rotational friction in each joint, which was referred to as joint friction (torque) in the rest of this chapter. The mostly used available model of this joint friction is a nonlinear dynamic equation in which the joint rotational velocity is the input [22]. As explained in [23], this modeling reveals that there are two different frictional regions namely pre-sliding region and sliding region. In the pre-sliding region the friction is a function of displacement, while in the sliding region the friction depends on the velocity [23]. In this article rather than using the nonlinear dynamic equation to model the friction of the harmonic gearboxes, it was assumed that the friction was only velocity dependent. That is, the friction in the sliding region was modeled and the pre-sliding friction was not. Although neglecting the pre-sliding friction resulted in an approximate friction model, it lead to a computationally simpler model which was easier and less costly to implement.

²⁴ The physical parameters of the manipulator used in the simulation and experimental studies are not the same.

This was due to the fact that instead of having a model composed of differential equations, the friction was represented by an algebraic equation, Eq. (5-61). Therefore, in this study the joint friction $\tau_{friction}$ was assumed to be as [22]:

$$\tau_{friction} = (\tau_c + (\tau_{st} - \tau_c)e^{-(\dot{\theta}/v_s)^2}) \text{sgn}(\dot{\theta}) + \sigma_v \dot{\theta} \quad (5-61)$$

where the terms $\sigma_v \dot{\theta}$ and $(\tau_c + (\tau_{st} - \tau_c)e^{-(\dot{\theta}/v_s)^2}) \text{sgn}(\dot{\theta})$ were called the viscous and dry friction torques, respectively. Moreover τ_c, τ_{st}, v_s and σ_v were the coulomb friction, static friction, Stribeck velocity constant, and the viscous damping coefficient, respectively, and $\text{sgn}(\dot{\theta})$:

$$\text{sgn}(\dot{\theta}) = \begin{cases} 1 & \text{for } \dot{\theta} > 0 \\ 0 & \text{for } \dot{\theta} = 0 \\ -1 & \text{for } \dot{\theta} < 0 \end{cases} \quad (5-62)$$

The friction model presented in Eq. (5-61) is known as the *LuGre* model. To calculate the τ_c, τ_{st}, v_s and σ_v for the shoulder and elbow joints, a constant velocity experiment [24] was performed for each joint as follows. First, the average value of the friction torque $\tau_{friction}$ was experimentally determined for different constant values of $\dot{\theta}$. Then having the corresponding $\tau_{friction}$ for each constant $\dot{\theta}$, a least square curve fitting scheme was used to find τ_c, τ_{st}, v_s and σ_v , which were the contributing parameters in Eq. (5-61). For the curve fitting scheme the MATLAB command “*lsqcurvefit*” was used. The values of the identified parameters τ_c, τ_{st}, v_s and σ_v for the elbow and shoulder joint frictions are presented in Table 2.

Table 2: Identified parameters of the LuGre friction model, Eq. (5-61), for the shoulder and elbow joints, Positive: Clockwise, Negative: Counter clockwise

Joint	Velocity	τ_c	τ_{st}	v_s	σ_v
Shoulder	Positive	1.788 N.m	2.580 N.m	0.0065 s^{-1}	$2.855 \text{ N.m.s.rad}^{-1}$
	Negative	-1.963 N.m	-2.889 N.m	0.0071 s^{-1}	$2.827 \text{ N.m.s.rad}^{-1}$
Elbow	Positive	0.3753 N.m	0.2041 N.m	0.1935 s^{-1}	$0.6239 \text{ N.m.s.rad}^{-1}$
	Negative	-0.4947 N.m	-0.2012 N.m	0.2055 s^{-1}	$0.4999 \text{ N.m.s.rad}^{-1}$

Since the control strategy developed in Section 5.4 was based on the model which had joint viscous friction, $\sigma_v \dot{\theta}$, and not joint dry friction, $(\tau_c + (\tau_{st} - \tau_c)e^{(-\dot{\theta}/v_s)^2}) \text{sgn}(\dot{\theta})$, to compensate for the joint dry friction, the torque $(\tau_c + (\tau_{st} - \tau_c)e^{(-\dot{\theta}/v_s)^2}) \text{sgn}(\dot{\theta})$ was added to the control command. The schematic of the control diagram of the experimental setup is shown in Fig. 5-11. The parameters τ_c , τ_{st} , v_s , and σ_v , given in table 2, were used for the calculation of the joint dry friction, $\tau_{friction}$. The acronyms “RSFEM” and “CC” in Fig. 5-11 were used for the rigid-shoulder link flexible-elbow link manipulator and control command, respectively. It is to be noted that the addition of the joint dry friction to the control signal to counterbalance the effect of the friction which is not included in the mathematical model of the system, was also used in the experimental study of [23] and [25].

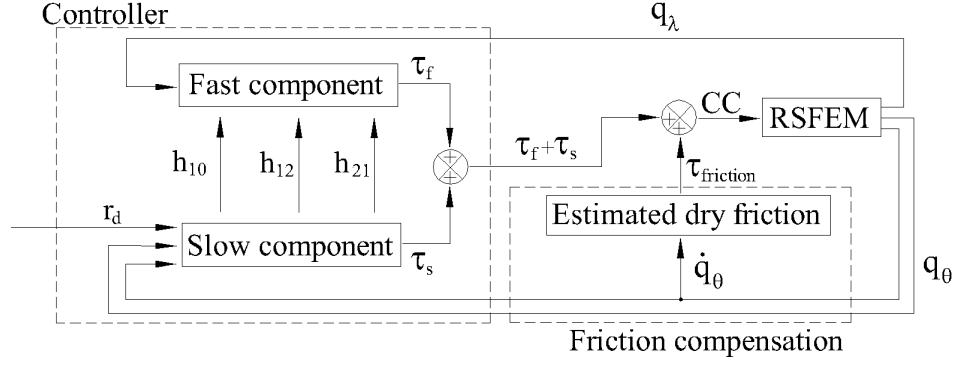


Fig. 5-11: Schematic of the control diagram employed in the experimental study

In the experimental study, the flexibility of the elbow-link was modeled using one mode shape and the time varying weight function of this mode, λ_1 in Eq. (5-1), was measured using a strain gauge mounted at the base of the link. Modeling the flexibility with one mode shape was reasonably accurate and justifiable due to the limited bandwidth of the actuators in the experimental setup as explained in the following. The natural frequency for the second mode of vibration for the experimental setup was 55 (Hz) while the maximum bandwidths for the actuators were 50 (Hz). Therefore the first mode of vibration was dominant and the contribution of higher modes of vibration was small and thus negligible. Moreover, in addition to the limited bandwidth of the actuator the first mode of vibration generally can predict the dynamic response quite well even for relatively large lateral deflection as explained in, which was also observed in simulation study presented in Section 5-5. The resolution of the end-effector measurement by using this strain gauge was theoretically 4.05×10^{-4} (m).

The desired trajectories r_{d1} and r_{d2} were selected using Eqs. (5-57) and (5-58) and assuming $\theta_{f1} = \theta_{f2} = 1.047$ (rad) and $t_{f1} = t_{f2} = 3.500$ (s). Since $\theta_{f1} = \theta_{f2}$ and $t_{f1} = t_{f2}$, then r_{d1} and r_{d2} were identical, as shown Fig. 5-12. Moreover, r_{d1} and r_{d2} were selected to be unidirectional, to reduce the possibility that $\text{sgn}(\dot{\theta})$ in the expression $(\tau_c + (\tau_{st} - \tau_c)e^{(-\dot{\theta}/v_s)^2})\text{sgn}(\dot{\theta})$ changed values during maneuver.

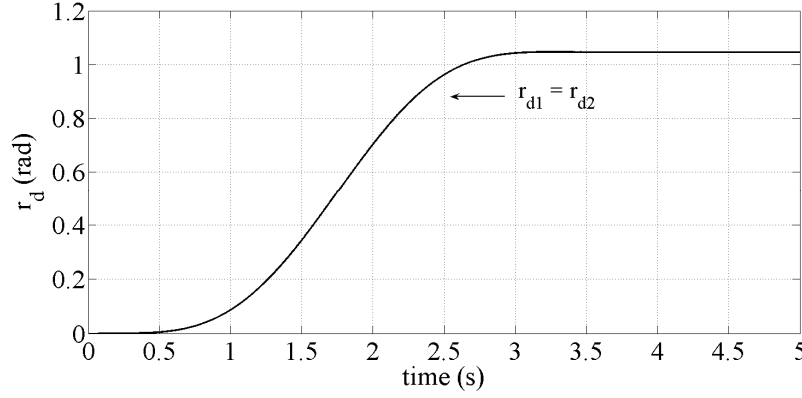


Fig. 5-12: Experiment, desired trajectories r_{d1} and r_{d2}

For the experimental implementation of the proposed controller, the gains $K_p = 20I$ and $K_D = 5I$ were used to calculate τ_0 and τ_2 in Eqs. (5-36) and (5-38), respectively and I is the identity matrix. Moreover, to obtain the fast component of the controller, τ_f , the gain scheduling procedure, discussed in Section 5.4, was utilized. The operating points for the gain scheduling were selected to be $\vartheta_i = (\theta_2)_i$ for the reason explained in the simulation section. Since $r_{d2} = \tilde{\theta}_{d2}$ changed from zero to 60.0° ($1.047(rad)$), it was assumed that θ_2 varied between -20.0° and 80.0° . That is, the possible range of variation for θ_2 was selected to be 20.0° wider from both sides compared to r_{d2} . As a result when the value of θ_2 passed the limits of r_{d2} during the experiment, the observer and controller gains for the calculation of τ_f could still be obtained and the algorithm could still be implemented. This range of θ_2 , from -20.0° to 80.0° , was divided into 10 equal segments with the operating point of $\vartheta_i = (\theta_2)_i = -20 + 10(i - 1)$, ($i = 1, \dots, 11$). Then at each operating point, K_{cz} and K_{oz} were selected so that $\mu(A_{z2} - B_{z2}K_{cz}) = \{-0.2 \pm 1.0j\}$ and $\mu(A_{z2} - C_zK_{oz}) = \{-0.4 \pm 2.0j\}$ where $\mu(Q)$ represents the eigenvalues of the matrix Q . Similar to the simulation study the fast controller in the experimental study was designed as if the elbow actuator was only active.

The trajectory tracking errors, $error_1 = r_1 - r_{d1}$ and $error_2 = r_2 - r_{d2}$, in the experimental study after applying the integral manifold controller are given in Figs. 5-13

and 5-14, respectively. To compare the effectiveness of the new controller in reducing the EETT, the trajectory tracking error adopting rigid link controller, are also presented in Figs. 5-15 and 5-16.

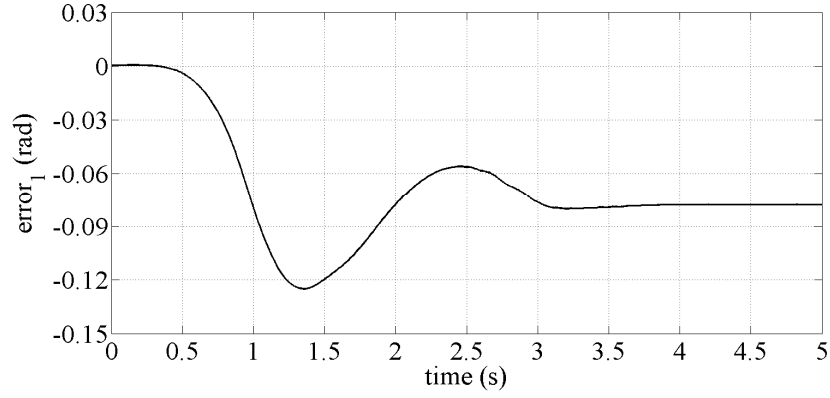


Fig. 5-13: Experiment, trajectory tracking error of r_1 , integral manifold controller

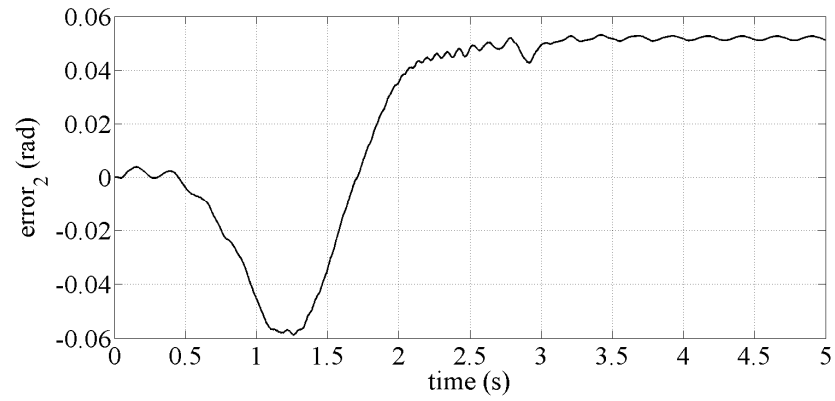


Fig. 5-14: Experiment, trajectory tracking error of r_2 , integral manifold controller

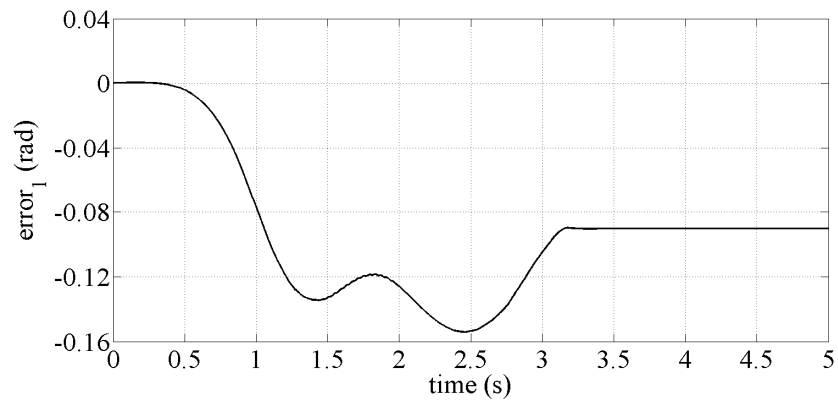


Fig. 5-15: Experiment, trajectory tracking error of r_1 , rigid link controller

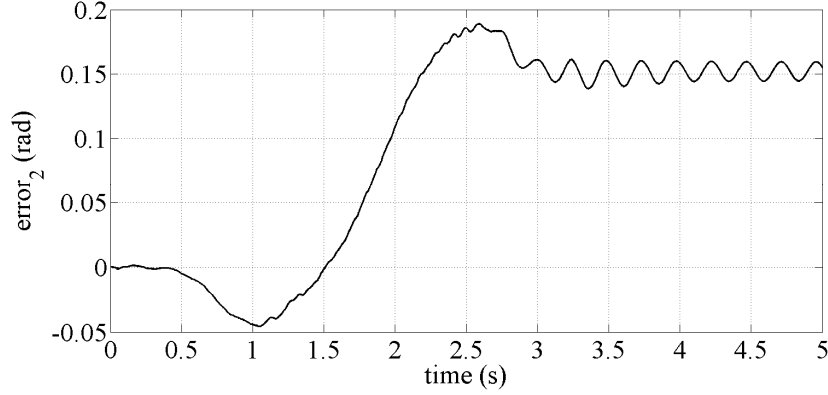


Fig. 5-16: Experiment, trajectory tracking error of r_2 , rigid link controller

From Figs. 5-13 to 5-16 it is observed that the tracking errors for the integral manifold controller were smaller than those of the rigid link controller. The maximum absolute value of the $error_1 = r_1 - r_{d1}$ and the $error_2 = r_2 - r_{d2}$ for the integral manifold controller were 0.1250 (rad) and 0.0588 (rad), respectively, while for the rigid link controller they were larger as 0.1541 (rad) and 0.1890 (rad), respectively. Also, the normalized mean square error (NMSE) from Eqs. (5-59) and (5-60) for the integral manifold controller was 0.0874 (rad) which was smaller than the 0.1599 (rad) of the rigid link controller. Finally, as shown in Fig. 5-17, the end-effector path of the experimental setup, indicated that the integral manifold controller was superior to the rigid link controller in reducing the tracking error.

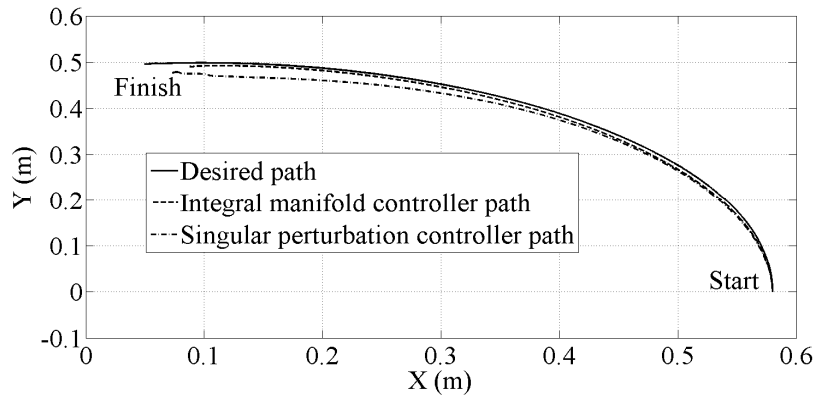


Fig. 5-17: Experiment, actual paths after applying the integral manifold and rigid link controllers

Although, compared to the results of the simulation study those of the experimental study appeared not to be as good as far as the overall improvement of EETT error was concerned;²⁵ they still, however, verified the advantage of the integral manifold controller over the rigid link controller. The main reason for the overall difference between the simulation and experimental results, was the high value of the dry frictions in the shoulder and elbow joints. Although, this friction was compensated by using the LuGre model, it has been argued in [23,26,27] that this model is not the most precise model for the friction. Moreover, the adopted model $(\tau_c + (\tau_{st} - \tau_c)e^{(-\dot{\theta}/v_s)^2})\text{sgn}(\dot{\theta})$ was only valid for the sliding region. Therefore, the friction in the pre-sliding region could not be compensated for. The pre-sliding friction was of importance at the beginning and end of the maneuver when the velocity was small. The steady tracking error at the end of the maneuver was due to the existence of the unmodeled pre-sliding friction which could not be compensated for by using the employed model. Furthermore, it had been observed that the parameters τ_c, τ_{st}, v_s and σ_v in Eq. (5-61) did not have a constant value and were functions of load, room temperature, room humidity and the starting position of the motion. In addition, τ_c, τ_{st}, v_s and σ_v of the elbow joint had been obtained in the absence of the flexible elbow-link for practical reasons. The flexible elbow-link had to be removed during the constant velocity experiment of the elbow joint since the slow damping vibration of the link was a substantial source of error for the experiment. Due to the load dependent nature of the friction, the flexible link removal could be a source of error in identifying the friction of the elbow joint. Finally, the noise in the sensors' readings and time delay could be among the other source of errors.

5.7. Conclusions

A class of flexible link manipulator consisting of a chain of rigid links with a flexible end-link (CRFE) have been considered. A new controller for the end-effector trajectory tracking (EETT) of the CRFE which utilized the concept of the integral manifold of the singularly perturbed differential equations was introduced. The dynamic

²⁵ Note that the physical parameters of the manipulators used in the simulation and experimental studies are different. Therefore, only the overall efficiency of reducing the tracking errors, not the numerical values, can be compared.

model of the CRFE was expressed into the standard singularly perturbed form where the joints' rotations and their time derivatives were the states of the slow subsystem while the states of the fast subsystem were the flexible variables, which model the link's lateral deflection, and their time derivative. Moreover, the singular perturbation parameter was selected as $\varepsilon = 1/(2\pi f)$ where f was the smallest non-zero natural frequency of the CRFE in the specified workspace of the manipulator

Compared to the few available EETT controller desired based on the singularly perturbed model of flexible link manipulators, the controller introduced here was new since (1) - it only required one corrective term of order ε^2 besides computed torque command of the rigid link counterpart of the CRFE, (2) - the derivation of the corrective torque and implementation of the controller was simplified by the use of the properties of the matrices associated with the dynamic model of CRFE, (3)- the calculation of the stabilizing torque for the fast subsystem did not require the time derivative of the flexible variables (time derivative of the link's lateral deflection) which was not easily available. Moreover, this stabilizing torque was obtained based on the gain scheduling procedure in which least possible interpolation effort is required.

The stability of the new controller was proven using the Lyapunov criterion. The effectiveness and feasibility of the new controller introduced here were shown by the simulation study and experimental verification. The simulation and experimental studies were carried on a two-link manipulator with the first link rigid and second link flexible. The improvement in reducing the EETT error, both in the simulation and experimental studies, justified the application of the proposed new controller.

Due to the model-based nature of the controller, the successful implementation of the controller requires accurate modeling of the apparatus. Therefore, unavoidable differences between the derived model and apparatus deteriorate the performance of the controller. To recover the performance of the controller the adaptive control strategy can be employed which is the subject of the future research.

5.8. Nomenclature

a : Number of links

A_{z1} : State matrix of the fast subsystem which represents the deviation of the z from h and is a function of x_1, x_2

A_{z2} : State matrix of the fast subsystem which represents the deviation of the z from h and is a function of x_1

B : Mapping matrix which relates the vector of input torques to their corresponding generalized coordinates

B_{z1} : Input matrix corresponds to A_{z1}

B_{z2} : Input matrix corresponds to A_{z2}

$c_{i,jk}$: Christoffel symbol

$C(q, \dot{q})$: The matrix which represents the Coriolis and centrifugal forces

C_D : Joints' viscous damping matrix

C_z : Output matrix

$\begin{bmatrix} F_\theta^T & F_\lambda^T \end{bmatrix}^T$: Vector composed of the summation of the Coriolis, centrifugal and gravity forces

$G(q)$: Gravity matrix

h^e : Integral (invariant) manifold

h : Approximation of h^e

h_i : The i th element of vector h

h_{ij} : Coefficient of ε^j in h_i

I : Identity matrix

I_{tip} : Mass moment of inertia of the end-effector

J : Inverse of the mass matrix $M(q)$

$J_{\theta\theta}, J_{\theta\lambda}, J_{\lambda\lambda}$: Components of the matrix J

K : Stiffness matrix

$K_{\lambda\lambda}$: Non-zero sub-matrix of K

$K_P, K_D, K_{c_z}, K_{o_z}$: Controller gains

$\ell_i, i = 1 \dots 6$: Positive constants

L_i : Length of the i th link

m_{tip} : Mass of the end-effector

$M(q)$: Mass matrix

$M_{\theta\theta}, M_{\theta\lambda}, M_{\lambda\lambda}$: Components of the mass matrix $M(q)$

n : Number of mode shapes used to model the flexibility of the link

q : Generalized coordinates of the CREF

q_θ : Part of the generalized coordinate q which is composed of $\theta_i, i = 1 \dots a$

q_λ : Part of the generalized coordinate q which is composed of $\lambda_i, i = 1 \dots n$

Q_i : Generalized force corresponding to q_i

r : Control variable for CREF

r_d : Desired trajectory for r

T_{CREF} : Kinetic energy of the CREF

U_{CREF} : Combination of the potential energy of the CREF due to the gravity and its strain energy due to the link's flexibility

$x^e = [(x_1^e)^T \quad (x_2^e)^T]^T$: States of slow subsystem when the states of the fast subsystem are restricted to their exact integral manifold h^e

$x = [x_1^T \quad x_2^T]^T$: Approximation of x^e when states of the fast subsystem are restricted to h

y : output of the fast subsystem

$z = \begin{bmatrix} z_1^T & z_2^T \end{bmatrix}^T$: States of the fast subsystem

\hat{z} : Deviation of the states of the fast subsystems from their integral manifolds

\tilde{z} : Estimate of \hat{z} which is obtained from observer

ξ : Deflection of the flexible link

ϕ_i : The i th spatial mode shape, assumed mode shape

λ_i : Time varying weight function of ϕ_i

θ_i : Relative rotation of the i th revolute joint with respect to the $(i-1)$ th revolute joint

$\tilde{\theta}_a$: Modified joint rotation for the flexible link

ε : Singular perturbation parameter

$\mu_{\min}(Q)$: Minimum eigenvalue of the matrix Q

$\tau_{friction}$: Joint friction torque

τ_c : Coulomb friction

τ_{st} : Static friction

$\tau_{actuator_i}$: The torque of the i th link's actuator

τ : Vector composed of the $\tau_{actuator_i}$

v_s : Stribeck velocity constant

σ_v : Viscous damping coefficient

τ_f : Fast component of the controller

v_i : The i th operating point in the gain scheduling procedure

$\|\psi\|$: Euclidean norm of ψ

5.9. Appendix

Appendix 5.I: Calculation of $(F_\theta)_1$ and $(F_\theta)_2$

From Eq. (5-18b):

$$q_\lambda = \varepsilon^2 z_1 \quad (5-A1)$$

$$\dot{q}_\lambda = \varepsilon z_2 \quad (5-A2)$$

Using the chain rule:

$$(F_\theta)_1 = \left. \frac{dF_\theta}{d\varepsilon} \right|_{\varepsilon=0} = \left. \frac{\partial F_\theta}{\partial q_\lambda} \right|_{q_\lambda=\dot{q}_\lambda=0} \left. \frac{\partial q_\lambda}{\partial \varepsilon} \right|_{\varepsilon=0} + \left. \frac{\partial F_\theta}{\partial \dot{q}_\lambda} \right|_{q_\lambda=\dot{q}_\lambda=0} \left. \frac{\partial \dot{q}_\lambda}{\partial \varepsilon} \right|_{\varepsilon=0} \quad (5-A3)$$

From Eqs. (5-A1) and (5-A2):

$$\left. \frac{\partial q_\lambda}{\partial \varepsilon} \right|_{\varepsilon=0} = 0 \quad (5-A4)$$

$$\left. \frac{\partial \dot{q}_\lambda}{\partial \varepsilon} \right|_{\varepsilon=0} = z_2|_{\varepsilon=0} \quad (5-A5)$$

Using Eqs. (5-A4) and (5-A5), $(F_\theta)_1$ from Eq. (5-A3) is:

$$(F_\theta)_1 = \left. \frac{\partial F_\theta}{\partial \dot{q}_\lambda} \right|_{q_\lambda=\dot{q}_\lambda=0} z_2|_{\varepsilon=0} \quad (5-A6)$$

By adopting the same technique used for the derivation of $(F_\theta)_1$, the expression for $(F_\theta)_2$ is:

$$(F_\theta)_2 = \left. \frac{\partial^2 F_\theta}{\partial \dot{q}_\lambda^2} \right|_{q_\lambda=\dot{q}_\lambda=0} (z_2|_{\varepsilon=0})^2 + 2 \left. \frac{\partial F_\theta}{\partial q_\lambda} \right|_{q_\lambda=\dot{q}_\lambda=0} z_1|_{\varepsilon=0} + \left. \frac{\partial F_\theta}{\partial \dot{q}_\lambda} \right|_{q_\lambda=\dot{q}_\lambda=0} \left. \frac{\partial z_2}{\partial \varepsilon} \right|_{\varepsilon=0} \quad (5-A7)$$

Appendix 5.II: Simplifying the expression of the corrected slow subsystem

The corrected slow subsystem given in Eq. (5-34) is:

$$\begin{bmatrix} \dot{x}_1 \\ \dot{x}_2 \end{bmatrix} = \begin{bmatrix} J_{\theta\theta}(\tau_0 - (F_\theta)_0 - (C_D)_{\theta\theta}x_2) - J_{\theta\lambda}F_\lambda - \frac{J_{\theta\lambda}K_{\lambda\lambda}}{\mu_{\min}(J_{\lambda\lambda}K_{\lambda\lambda})}h_{10} + \varepsilon[J_{\theta\theta}(\tau_1 - (F_\theta)_1) - \\ + \frac{J_{\theta\lambda}K_{\lambda\lambda}}{\mu_{\min}(J_{\lambda\lambda}K_{\lambda\lambda})}h_{11}] + \varepsilon^2[J_{\theta\theta}(\tau_2 - \frac{1}{2}(F_\theta)_2) - \frac{J_{\theta\lambda}K_{\lambda\lambda}}{\mu_{\min}(J_{\lambda\lambda}K_{\lambda\lambda})}h_{12}] \end{bmatrix} \quad (5-A8)$$

Eq. (5-A8) can be written as:

$$\begin{bmatrix} \dot{x}_1 \\ \dot{x}_2 \end{bmatrix} = \begin{bmatrix} x_2 \\ \bar{x}_{20} + \varepsilon \bar{x}_{21} + \varepsilon^2 \bar{x}_{22} \end{bmatrix} \quad (5-A9)$$

where:

$$\bar{x}_{20} = J_{\theta\theta}(\tau_0 - (F_\theta)_0 - (C_D)_{\theta\theta}x_2) - J_{\theta\lambda}F_\lambda - \frac{J_{\theta\lambda}K_{\lambda\lambda}}{\mu_{\min}(J_{\lambda\lambda}K_{\lambda\lambda})}h_{10} \quad (5-A10)$$

$$\bar{x}_{21} = J_{\theta\theta}(\tau_1 - (F_\theta)_1) - \frac{J_{\theta\lambda}K_{\lambda\lambda}}{\mu_{\min}(J_{\lambda\lambda}K_{\lambda\lambda})}h_{11} \quad (5-A11)$$

$$\bar{x}_{22} = J_{\theta\theta}(\tau_2 - \frac{1}{2}(F_\theta)_2) - \frac{J_{\theta\lambda}K_{\lambda\lambda}}{\mu_{\min}(J_{\lambda\lambda}K_{\lambda\lambda})}h_{12} \quad (5-A12)$$

In the following it will be proven that $\bar{x}_{20} = M_{\theta\theta}^{-1}(\tau_0 - (F_\theta)_0 - (C_D)_{\theta\theta}x_2)$, $\bar{x}_{21} = M_{\theta\theta}^{-1}(\tau_1 - (F_\theta)_1)$ and $\bar{x}_{22} = M_{\theta\theta}^{-1}((\tau_2 - \frac{1}{2}(F_\theta)_2) - M_{\theta\lambda}\ddot{h}_{10})$. Then by using these expressions for $\bar{x}_{20}, \bar{x}_{21}, \bar{x}_{22}$ the corrected slow subsystem will be shorter and thus easier to use.

Substituting h_{10} from Eq. (5-30a) in Eq. (5-A10) results in:

$$\bar{x}_{20} = J_{\theta\theta}(\tau_0 - (F_\theta)_0 - (C_D)_{\theta\theta}x_2) - J_{\theta\lambda}F_\lambda - J_{\theta\lambda}J_{\lambda\lambda}^{-1}(J_{\theta\lambda}^T(\tau_0 - (F_\theta)_0 - (C_D)_{\theta\theta}x_2) - J_{\lambda\lambda}F_\lambda) \quad (5-A13)$$

Regrouping the terms in Eq. (5-A13) leads to:

$$\bar{x}_{20} = (J_{\theta\theta} - J_{\theta\lambda}J_{\lambda\lambda}^{-1}J_{\theta\lambda}^T)(\tau_0 - (F_\theta)_0 - (C_D)_{\theta\theta}x_2) \quad (5-A14)$$

Using the equality $M_{\theta\theta}^{-1} = J_{\theta\theta} - J_{\theta\lambda} J_{\lambda\lambda}^{-1} J_{\theta\lambda}^T$ given in Eq. (5-10d), Eq. (5-A14) is changed to:

$$\bar{x}_{20} = M_{\theta\theta}^{-1}(\tau_0 - (F_\theta)_0 - (C_D)_{\theta\theta} x_2) \quad (5-A15)$$

Utilization of h_{11} given in Eq. (5-30c) in Eq. (5-A11) and knowing that $h_{20} = 0$, turns \bar{x}_{21} into:

$$\bar{x}_{21} = J_{\theta\theta}(\tau_1 - (F_\theta)_1) - J_{\theta\lambda} J_{\lambda\lambda}^{-1} (J_{\theta\lambda}^T(\tau_1 - (F_\theta)_1)) \quad (5-A16)$$

Using the equality $M_{\theta\theta}^{-1} = J_{\theta\theta} - J_{\theta\lambda} J_{\lambda\lambda}^{-1} J_{\theta\lambda}^T$ given in Eq. (5-10d), Eq. (5-A16) becomes:

$$\bar{x}_{21} = M_{\theta\theta}^{-1}(\tau_1 - (F_\theta)_1) \quad (5-A17)$$

Employing the expression of h_{12} given in Eq. (5-30e) in Eq. (5-A12) results in:

$$\bar{x}_{22} = J_{\theta\theta}(\tau_2 - \frac{1}{2}(F_\theta)_2) - J_{\theta\lambda} J_{\lambda\lambda}^{-1} (J_{\theta\lambda}^T(\tau_2 - \frac{1}{2}(F_\theta)_2) - \dot{h}_{21}) \quad (5-A18)$$

By rearrangement Eq. (5-A18), becomes:

$$\bar{x}_{22} = (J_{\theta\theta} - J_{\theta\lambda} J_{\lambda\lambda}^{-1} J_{\theta\lambda}^T)(\tau_2 - \frac{1}{2}(F_\theta)_2) + J_{\theta\lambda} J_{\lambda\lambda}^{-1} \dot{h}_{21} \quad (5-A19)$$

Using the equality $M_{\theta\theta}^{-1} = J_{\theta\theta} - J_{\theta\lambda} J_{\lambda\lambda}^{-1} J_{\theta\lambda}^T$ given in Eq. (5-10d), the expression $M_{\theta\lambda}^T M_{\theta\theta}^{-1} = -J_{\lambda\lambda}^{-1} J_{\theta\lambda}^T$ given in Eq. (5-10b) and knowing $\dot{h}_{21} = \ddot{h}_{10}$ from Eq. (5-30d), \bar{x}_{22} is:

$$\bar{x}_{22} = M_{\theta\theta}^{-1}((\tau_2 - \frac{1}{2}(F_\theta)_2) - M_{\theta\lambda} \ddot{h}_{10}) \quad (5-A20)$$

Replacing \bar{x}_{20} , \bar{x}_{21} , and \bar{x}_{22} in Eq. (5-A9) with their equivalence given in Eqs. (5-A15), (5-A17) and (5-A20) respectively, results in:

$$\begin{bmatrix} \dot{x}_1 \\ \dot{x}_2 \end{bmatrix} = \begin{bmatrix} x_2 \\ M_{\theta\theta}^{-1}(\tau_0 - (F_\theta)_0 - (C_D)_{\theta\theta} x_2) + \varepsilon(M_{\theta\theta}^{-1}(\tau_1 - (F_\theta)_1) + \varepsilon^2(M_{\theta\theta}^{-1}(\tau_2 - \frac{1}{2}(F_\theta)_2) - M_{\theta\lambda} \ddot{h}_{10})) \end{bmatrix} \quad (5-A21)$$

Therefore, by the use of Eqs. (5-30a) to (5-30f) for h_{ij} $i = 1, 2$ and $j = 0, 1, 2$, and also the properties of the mass matrix given in Section 5.2.2, Eq. (5-A8) was converted to Eq. (5-A21) as stated in Lemma 1.

Appendix 5.III: Stability analysis of the proposed theorem in Section 5.4

For the stability analysis the torque $\tau = \tau_0 + \varepsilon^2 \tau_2 + \tau_f$, where the expressions of τ_0 , τ_2 and τ_f are given in Eqs. (5-36), (5-38) and (5-54) respectively, is applied to the dynamic model given in Eqs. (5-20a) and (5-20b). After algebraic manipulation and neglecting the terms of order ε^3 and higher, the errors' dynamics are:

$$\dot{e}_r = A_r e_r + N_r \quad (5-A22)$$

$$\varepsilon \dot{\eta} = A_\eta \eta + N_\eta \quad (5-A23)$$

where:

$$e_r^T = [(r - r_d)^T \quad (\dot{r} - \dot{r}_d)^T], \quad \eta^T = [e_z^T \quad \hat{z}^T], \quad e_z = \hat{z} - \tilde{z} \quad (5-A24)$$

$$A_r = \begin{bmatrix} 0 & I \\ -K_p & -K_D \end{bmatrix}, \quad A_\eta = \begin{bmatrix} A_{z2} - K_{oz} C & 0 \\ B_{z2} K_{cz} & A_{z2} - B_{z2} K_{cz} \end{bmatrix} \quad (5-A25)$$

$$N_\eta = \begin{bmatrix} N_{z2} \\ N_{z2} \end{bmatrix}, \quad N_r = \begin{bmatrix} 0 \\ D_r \end{bmatrix} \quad (5-A26)$$

$$N_{z2} = \begin{bmatrix} 0 \\ -\varepsilon J_{\theta\lambda}^T \frac{\partial F_\theta}{\partial \dot{q}_\lambda} \Big|_{q_\lambda = \dot{q}_\lambda = 0} \hat{z}_2 \end{bmatrix} \quad (5-A27)$$

$$D_r = (WJ_{\theta\lambda}^T K_{cz} + J_{\theta\theta} K_{cz}) e_z + ([D_{r1} \quad D_{r2}] - WJ_{\theta\lambda}^T K_{cz} - J_{\theta\theta} K_{cz}) \hat{z} \quad (5-A28)$$

$$D_{r1} = \varepsilon^2 (K_p W - (WJ_{\theta\lambda}^T + J_{\theta\theta}) \frac{\partial F_\theta}{\partial q_\lambda} \Big|_{q_\lambda = \dot{q}_\lambda = 0}) - W \frac{J_{\lambda\lambda} K_{\lambda\lambda}}{\mu_{\min}(J_{\lambda\lambda} K_{\lambda\lambda})} - \frac{J_{\theta\lambda} K_{\lambda\lambda}}{\mu_{\min}(J_{\lambda\lambda} K_{\lambda\lambda})} \quad (5-A29)$$

$$D_{r2} = \varepsilon (K_D W - (WJ_{\theta\lambda}^T + J_{\theta\theta}) \frac{\partial F_\theta}{\partial \dot{q}_\lambda} \Big|_{q_\lambda = \dot{q}_\lambda = 0}) \quad (5-A30)$$

Since matrices K_p and K_D are positive definite, the matrix A_r in Eq. (5-A25) is Hurwitz. Moreover, according to the observer-based controller design procedure $A_{z2} - B_{z2}K_{cz}$ and $A_{z2} - K_{oz}C$ are Hurwitz matrices and so is the matrix A_η in Eq. (5-A25). Given that A_r and A_η are Hurwitz matrices, there exist symmetric positive definite matrices P_η and P_r that satisfy the following Lyapunov equations:

$$A_\eta^T P_\eta + P_\eta A_\eta = -S_\eta \quad (5-A31)$$

$$A_r^T P_r + P_r A_r = -S_r \quad (5-A32)$$

where S_η and S_r are symmetric positive definite matrices. For the stability analysis the Lyapunov candidate function is selected as:

$$V_{Lyp} = e_r^T P_r e_r + \varepsilon \eta^T P_\eta \eta \quad (5-A33)$$

Calculating the time derivative of the Lyapunov candidate function defined in Eq. (5-A33) along the trajectories of Eqs. (5-A22) and (5-A23) and using Eqs. (5-A31) and (5-A32) results in:

$$\dot{V}_{Lyp} = -e_r^T S_r e_r - \eta^T S_\eta \eta + 2N_r^T P_r e_r + 2N_\eta^T P_\eta \eta + \varepsilon \eta^T \dot{P}_\eta \eta \quad (5-A34)$$

On a bounded region around the origin of e_r and η , it is possible to assume [11,19]:

$$\|N_r^T P_r\| < (\ell_2 + \varepsilon \ell_3 + \varepsilon^2 \ell_4) \|\eta\| \quad (5-A35)$$

$$\|N_\eta^T P_\eta\| < \varepsilon \ell_5 \|\eta\| \quad (5-A36)$$

$$\|\dot{P}_\eta\| < \ell_6 \quad (5-A37)$$

where $\ell_2, \ell_3, \ell_4, \ell_5$ and ℓ_6 are positive constants. By using Eqs. (5-A35) to (5-A37) and defining the symbol $\mu_{\min}(Q)$ as the minimum eigenvalues of a matrix Q , \dot{V}_{Lyp} given in Eq. (5-A34) changes to:

$$\dot{V}_{Lyp} < -\begin{bmatrix} \|e_r\| & \|\eta\| \end{bmatrix} \Omega \begin{bmatrix} \|e_r\| \\ \|\eta\| \end{bmatrix} \quad (5-A38)$$

where

$$\Omega = \begin{bmatrix} \mu_{\min}(S_r) & -(\ell_2 + \varepsilon\ell_3 + \varepsilon^2\ell_4) \\ -(\ell_2 + \varepsilon\ell_3 + \varepsilon^2\ell_4) & \mu_{\min}(S_\eta) - \varepsilon\ell_6 - 2\varepsilon\ell_5 \end{bmatrix} \quad (5-A39)$$

As $\varepsilon \rightarrow 0$ and provided that $\mu_{\min}(S_\eta)\mu_{\min}(S_r) > \ell_2^2$, the matrix Ω defined in Eq. (5-A39) is positive definite. Thus, there exists ε_{\max} so that for all $0 < \varepsilon < \varepsilon_{\max}$, Ω is a positive definite matrix. As a result, assuming that $\varepsilon \in (0, \varepsilon_{\max})$ the trajectory tracking error with the dynamics given in Eqs. (5-A22) and (5-A23), is Lyapunov stable. By imposing the positive definite property on matrix Ω which is defined in Eq. (5-A39), ε_{\max} is:

$$\varepsilon_{\max} = \frac{\mu_{\min}(S_r)\mu_{\min}(S_\eta) - \ell_2^2}{(\ell_6 + 2\ell_5)\mu_{\min}(S_r) + 2\ell_2\ell_3} \quad (5-A40)$$

In deriving the expression for ε_{\max} , given in Eq. (5-A40), it is assumed that the terms of order ε^2 are negligible compared to the terms of order ε . The fact that $r_d \in C^4$, makes the control signals continuous and bounded. Otherwise, the tracking error will be unsatisfactory and large.

5.10. Reference

1. A. De Luca, S. Iannitti, R. Mattone, and G. Oriolo, "Control Problems in Underactuated Manipulators", *Proceeding of the IEEE/ASME International Conference on Advanced Intelligent Mechatronics*, Vol. 2, pp. 855-861, 2001.
2. M. Bensman, and G. Le Vey, "Stable Inversion of SISO Nonminimum Phase Linear System Through Output Planning: An Experimental Application to the One-Link Flexible Manipulator", *IEEE Transactions on Control System Technology*, Vol. 11, No. 4, pp. 588-597, 2003.
3. P. V. Kokotovic, H. K. Khalil, and J. O'Reilly, "*Singular Perturbation Methods in Control: Analysis and Design*", Academic, New York, USA, 1999.

4. B. Siciliano, J. V. R. Prasad, and A. J. Calise, "Output Feedback Two-Time Scale Control of Multi-link Flexible Arms", *Journal of Dynamics, Measurement and Control*, Vol. 114, pp. 70-77, 1992.
5. V. A. Sobolev, "Integral Manifolds and Decomposition of Singularly Perturbed Systems", *Systems and Control Letters*, Vol. 5, pp. 169-179, 1984.
6. F. Ghorbel, and M. W. Spong, "Integral Manifold of Singularly Perturbed Systems with Application to Rigid-Link Flexible-Joint Multibody System", *International Journal of Non-linear Mechanics*, Vol. 35, pp. 133-155, 2000.
7. M. Vakil, R. Fotouhi, R., and P. N. Nikiforuk, "Application of the Integral Manifold Concept for the End-effector Trajectory Tracking of a Flexible Link Manipulator", *American Control Conference*, July 11-13, New York, USA, pp. 741-747, 2007.
8. H. Asada, and J. J. E. Slotine, "*Robot Analysis and Control*", John Wiley and Sons, New York, USA, 1986.
9. S. M. Shahruz, and S. Behtash, "Design of Controllers for Linear Parameter-Varying System By Gain Scheduling Technique", *Journal of Mathematical Analysis and Application*, Vol. 168, pp. 195-217, 1992.
10. K. Hashtudi Zaad, and K. Khorasani, "Control of Non-minimum Phase Singularly Perturbed System with Application to Flexible-link Manipulators", *International Journal of Control*, Vol. 63, No. 4, pp. 679-701, 1996.
11. M. Moallem, K. Khorasani and R.V. Patel, "An Integral Manifold Approach for Tip Position Tracking of Flexible Multi-Link Manipulators," *IEEE Transactions on Robotics and Automation*, Vol. 13, No. 6, pp. 823-837, 1997.
12. P. Bigras, M. Saad, and J. O'shea, "Exponential Trajectory Tracking Control in the Workspace of a Class of Flexible Robots", *Journal of Robotic Systems*, Vol. 15, No. (9), pp. 487-504, 1998.
13. W. J. Book, "Recursive Lagrangian Dynamics of Flexible Manipulator Arms," *International Journal of Robotics Research*, Vol. 3, No. 3, pp. 87-101, 1984.

14. M. Vakil, R. Fotouhi and P. N. Nikiforuk, "A Constrained Lagrange formulation of multi-link planar flexible manipulator", Accepted for publication in the *Journal of Vibration and Acoustics*, 2007.
15. J. S., Prezemienecki, "*Theory of Matrix Structural Analysis*", McGraw-Hill, New York, USA, 1967.
16. A. T. Alberts, H. Xia, Y. Chen, "Dynamic Analysis to Evaluate Viscoelastic Passive Damping Augmentation for the Space Shuttle Remote Manipulator System" *Advances in Dynamic and Control of Flexible Spacecraft and Spaced-based Manipulators*, Vol. 20, pp. 35-41, 1990.
17. M. W. Spong, "Modeling and Control of Elastic Joint Manipulators", *Journal of Dynamic Systems, Measurement and Control*, Vol. 109, pp. 310-319, 1987.
18. M. A. Arteaga, "On the Properties of a Dynamic Model of Flexible Robot Manipulators", *Journal of Dynamic Systems, Measurement and Control*, Vol. 120, No. 1, pp. 8-14, 1998.
19. K. Khorasani, "Adaptive Control of Flexible-Joint Robots", *IEEE Transactions on Robotics and Automation*, Vol. 8, No. 2, pp. 250-267, 1992.
20. M. W. Spong, K. Khorasani, and P. V. Kokotovic, "An Integral Manifold Approach to the Feedback Control of Flexible Joint Robots", *IEEE Transactions on Robotics and Automation*, Vol. 3, No. 4, pp. 291-300, 1987.
21. H. K. Khalil, "*Nonlinear Systems*", Prentice Hall, New Jersey, USA, 2002.
22. C. C. de Wit, H. Olsson, K. J. Astrom, and P. Lischinsky, "A new model for control of systems with friction", *IEEE Transactions on Automatic Control*, Vol. 40. No. 3, pp. 419-425, 1995.
23. J. Swevers, F. Al-Bender, C. G. Ganseman, and T. Prajogo, "An integrated friction model structure with improved presliding behaviour for accurate friction compensation", *IEEE Transactions on Automatic Control*, Vol. 45, No. 4, pp. 675-686, 2000.

24. P. S. Gandhi, F. H. Ghorbel, and J. Dabney, “ Modeling, identification and compensation of friction in harmonic drives”, *IEEE Conference on Decision and Control*, December 10-13, Las Vegas, NV, USA, pp. 160-166, 2002.
25. P. S. Gandhi, and F. H. Chorbél, “Closed Loop Compensation of Kinematic Error in Harmonic Drives for Precision Control Application”, *IEEE Transactions on Control Systems Technology*, Vol. 10, No. 6, 759-768, 2002.
26. V. Lampaert, J. Swevers, and F. Al-Bendar, “ Modification of the Leuven integrated friction model structure”, *IEEE Transactions on Automatic Control*, Vol. 47, No. 4, pp. 683-687, 2002.
27. P. Dunpont, V. Hayward, F. Armstrong, and F. Altpeter, “Single state elastoplastic friction models”, *IEEE Transactions on Automatic Control*, Vol. 47, No. 5, pp. 787-792, 2002.

Chapter 6. Maneuver control of the multilink flexible manipulators

Abstract:

In this chapter a new controller for the end-effector trajectory tracking of multilink flexible manipulators (MLFM) is introduced. The new controller is derived utilizing the concept of the integral manifold of the singularly perturbed differential equations.

Based on the new controller, to reduce the end-effector trajectory tracking error, a corrective term of order ε^2 has to be added to the computed torque command (CTC) of the rigid link counterpart of the MLFM, where the parameter $\varepsilon = 1/2\pi f$ and f is the smallest non-zero natural frequency of the MLFM in the specified range of operation of the manipulator. The implementation of the new controller requires measurement of the links' rotations, their time derivative and the flexible variables which represent the links' lateral deflections, but not the measurement of the time derivative of the flexible variables (time derivative of links' lateral deflections) which may be practically impossible. This is achieved since the time derivative of the links' lateral deflections estimated using an observer which is designed based on the gain-scheduling technique. The stability of the proposed controller is proven using the Lyapunov criterion. Simulation results showed the effectiveness of the new controller.

One of the main contributions of this work is in the derivation of a new controller for the EETT of nonlinear MLFM, based on the integral manifold concept, which (1)- requires the fewest corrective terms in addition to the CTC and (2)- its calculation effort is minimized.

6.1. Introduction

The energy consumption and heavy mass of rigid link manipulators reduce their mobility and efficiency. As a remedy, the use of the slender links decreases the mass and increases the mobility of the manipulators. However, the slender links vibrate and bend during, at the end of and after the maneuver, and this behavior leads to limited performance. Thus, provided that the performance of the flexible (slender) link manipulators becomes reliable through the utilization of suitable controllers, the flexible link manipulators can be a promising substitute for the rigid link manipulators. Since in

most of the industrial application, like welding, the end-effector trajectory tracking (EETT) is of importance, the EETT of the multilink flexible manipulators (MLFM) has to be addressed properly if they want to be industrially implemented.

Here, a new EETT controller considering the full nonlinear dynamic model of the MLFM is introduced. The proposed controller is derived based on the singularly perturbed form of the MLFM. Although there are many control strategies for the flexible link manipulator, the techniques for the control of singularly perturbed systems [1], are potential candidates for the EETT of the MLFM. This is due to the fact that the dynamic model of the MLFM can be expressed in the singularly perturbed form [2], which composed of slow and fast subsystems. For a MLFM, the states of the slow subsystem are the links' rotations and their time derivative while the states of the fast subsystem are the relatively fast links' lateral deflections, modeled by parameters called flexible variables, and their time derivative. In this chapter, after expressing the dynamic model of MLFM into the singularly perturbed form, the concept of the integral manifold [3,4] is used to introduce a new EETT controller. Based on this concept a corrective term (torque) is added to the computed torque command (CTC) of the rigid link counterpart of the MLFM for the reduction of the EETT error, see [5] for the CTC. This corrective term is of order ε^2 , where $\varepsilon = 1/2\pi f$ and f is smallest non-zero natural frequency of the MLFM in the specified range of operation of the manipulator. To stabilize the subsystem which composed of the flexible variables and their time derivative (links' lateral deflections and their time derivative), an observer-based feedback controller according to the gain-scheduling technique is employed, see [6] for the gain-scheduling technique. Due to the use of the observer-based feedback controller, there was no need for the direct measurement of the time derivative of the flexible variable, which is hardly practical. It is worth noting that the operating points in the gain-scheduling procedure were the links' rotations, which can be easily measured.

The major contribution of this work is in utilizing the concept of the integral manifold of the singularly perturbed differential equations to design an EETT controller for the MLFM considering the full nonlinear dynamic model. To the authors' best knowledge, this concept has only been used so far for single flexible link manipulators

with linear models [7,8,10], two-link manipulators with one rigid link one flexible link [11], or the joint trajectory tracking of two-link manipulators with both links flexible [9,12], but not for their EETT. In contrast in this chapter, based on the concept of integral manifold, a new EETT controller for MLFM is introduced whose performance has been verified by simulation studies on a two-link manipulator with both links flexible and also is to be experimentally validated in a later research. Moreover, compared to the above developed methods based on this concept [7-12], the controller introduced here is the most computationally efficient one since only one corrective term was added to the CTC of the rigid link counterpart of the MLFM. Furthermore, another contribution of this work is the use of several properties of the mass matrix of MLFM in design of the controller. The importance of the use of these properties is in the ease of calculation and implementation of the controller proposed here. Without the proper use of these properties it may not be possible to use this controller for MLFM, e.g. two-link manipulators with both links flexible. It is worth noting that the new EETT controller proposed here is an extension of our previously introduced controllers for the single flexible link manipulators [13] and a class of flexible link manipulator composed of a chain of rigid links with a flexible end-link [14], which have been experimentally verified.

The rest of this chapter is organized as follows. In Section 6.2, the singularly perturbed dynamic model of the MLFM and the properties associated with its mass matrix as well as the integral manifold concept are discussed. In Section 6.3 the corrective term which has to be added to the CTC of the rigid link counterpart of the MLFM to reduce the EETT error, and the observer-based feedback controller, which stabilizes the subsystem composed of the links' lateral deflections and their time derivative, are designed. Moreover in Section 6.3, the stability of the proposed controller using the Lyapunov stability criterion is discussed. The simulation results for a flexible two-link manipulator with both links flexible, which showed the effectiveness of the introduced technique is presented in Section 6.4. Finally in Section 6.5 the conclusions drawn from the research are given.

6.2. Dynamic model of MLFM and the integral manifold concept

In this section first the dynamic model of MLFM and the properties of its mass matrix are presented. Then this dynamic model is presented into the singularly perturbed form and the integral manifold concept is detailed.

6.2.1. Dynamic model of MLFM

The dynamic model of a MLFM [15,16] with n links is:

$$M(q)\ddot{q} + F(q, \dot{q}) + Kq = B\tau \quad (6-1)$$

where $M(q)$ is the mass matrix, $F(q, \dot{q})$ represents the summation of the Coriolis, centrifugal, gravity and viscous damping forces, K is the stiffness matrix, q is the vector composed of the generalized coordinates of the MLFM, $\tau^T = [\tau_{1a} \quad \dots \quad \tau_{na}]$ where τ_{ia} is the torque of the i th link's actuator and B is a constant matrix which maps τ to their corresponding generalized coordinates. The vectors and matrices in Eq. (6-1) can be expanded as:

$$M = \begin{bmatrix} M_{\theta\theta}(\theta, \lambda) & M_{\theta\lambda}(\theta, \lambda) \\ M_{\theta\lambda}^T(\theta, \lambda) & M_{\lambda\lambda}(\theta, \lambda) \end{bmatrix}, q = \begin{bmatrix} \theta \\ \lambda \end{bmatrix}, F(q, \dot{q}) = \begin{bmatrix} F_{\theta}(\theta, \lambda, \dot{\theta}, \dot{\lambda}) \\ F_{\lambda}(\theta, \lambda, \dot{\theta}, \dot{\lambda}) \end{bmatrix}, K = \begin{bmatrix} 0 & 0 \\ 0 & K_{\lambda\lambda} \end{bmatrix}, B\tau = \begin{bmatrix} \tau \\ 0 \end{bmatrix}$$

$$\theta^T = [\theta_1 \quad \dots \quad \theta_n], \lambda^T = [\lambda_1^T \quad \dots \quad \lambda_n^T], \lambda_i^T = [\lambda_{i1} \quad \lambda_{i2} \quad \dots \quad \lambda_{im}] \quad (6-2)$$

where θ_i ($i = 1 \dots n$) is the rotation of the i th link, λ_i ($i = 1 \dots n$) is the vector composed of the flexible variables used to describe the lateral deflection of the i th link, λ_{ij} ($i = 1 \dots n, j = 1 \dots m$) is the time varying coefficient of the j th mode of the i th link and m is the number of the mode shapes used to describe the lateral deflection of the i th link. Although, the number of mode shapes used to model the flexibility of each link can be different, for the simplicity of notation it is assumed that this number, m , is the same for all the links.

Properties of the mass matrix of the MLFM

The components of the mass matrix in Eq. (6-2) have several properties that facilitate the derivation and implementation of the controller proposed here. These

properties are given in this section. If the inverse of the symmetric positive definite mass matrix²⁶ M is J , then:

$$\begin{bmatrix} M_{\theta\theta} & M_{\theta\lambda} \\ M_{\theta\lambda}^T & M_{\lambda\lambda} \end{bmatrix}^{-1} = M^{-1} = J = \begin{bmatrix} J_{\theta\theta} & J_{\theta\lambda} \\ J_{\theta\lambda}^T & J_{\lambda\lambda} \end{bmatrix} \quad (6-3)$$

and the following equalities between the components of M and J exist:

$$M_{\theta\lambda} M_{\lambda\lambda}^{-1} = -J_{\theta\theta}^{-1} J_{\theta\lambda} \quad (6-4a) \quad M_{\theta\lambda}^T M_{\theta\theta}^{-1} = -J_{\lambda\lambda}^{-1} J_{\theta\lambda}^T \quad (6-4b)$$

$$M_{\theta\theta} = J_{\theta\theta}^{-1} + M_{\theta\lambda} M_{\lambda\lambda}^{-1} M_{\theta\lambda}^T \quad (6-4c) \quad M_{\theta\theta}^{-1} = J_{\theta\theta} - J_{\theta\lambda} J_{\lambda\lambda}^{-1} J_{\theta\lambda}^T \quad (6-4d)$$

$$J_{\lambda\lambda} = M_{\lambda\lambda}^{-1} + J_{\theta\lambda}^T J_{\theta\theta}^{-1} J_{\theta\lambda} \quad (6-4e) \quad J_{\lambda\lambda}^{-1} = M_{\lambda\lambda} - M_{\theta\lambda}^T M_{\theta\theta}^{-1} M_{\theta\lambda} \quad (6-4f)$$

Proof: See Section 4.10

6.2.2. Singularly perturbed form and the integral manifold concept

Since the dynamic response of MLFM is composed of slow links' rotations upon which there are relatively fast links' vibrations, the dynamic model of MFLM can be expressed in the singularly perturbed form. For this purpose, the new states:

$$x_1 = \theta, \quad x_2 = \dot{\theta} \quad (6-5a)$$

$$z_1 = \frac{\lambda}{\varepsilon^2}, \quad z_2 = \frac{\dot{\lambda}}{\varepsilon} \quad (6-5b)$$

are defined where $x^T = [x_1^T \ x_2^T]$ and $z^T = [z_1^T \ z_2^T]$ are the vectors composed of the states of the slow and fast subsystems and the vectors θ and λ are defined in Eq. (6-2).

Moreover, ε is the singular perturbation parameter and is defined as:

$$\varepsilon^{-1} = \sqrt{\mu_{\min}((J_{\lambda\lambda})_0 K_{\lambda\lambda})} \quad (6-6)$$

where $(J_{\lambda\lambda})_0 = J_{\lambda\lambda}|_{\lambda=0}$ and $\mu_{\min}((J_{\lambda\lambda})_0 K_{\lambda\lambda})$ is the smallest eigenvalue of the matrix

²⁶ For brevity in the rest of this chapter the arguments of functions are dropped unless their appearance leads to further clarification.

$(J_{\lambda\lambda} K_{\lambda\lambda})$ when $\lambda=0$ and θ is varied in the specified range of operation of the manipulator [11,14]. Physically since the eigenvalues of $((J_{\lambda\lambda})_0 K_{\lambda\lambda})$ are the square of the natural frequencies of the linearized dynamic model of the MFLM, ε is equal to the inverse of the smallest natural frequency over the specified range of θ .

Using the new states defined in Eqs. (6-5a) and (6-5b), the dynamic model given in Eq. (6-1) with details in Eq. (6-2), is expressed in the singularly perturbed form as:

$$\begin{cases} \dot{x}_1 = x_2 \\ \dot{x}_2 = -J_{\theta\theta}F_\theta - J_{\theta\lambda}F_\lambda - \frac{J_{\theta\lambda}K_{\lambda\lambda}}{\mu_{\min}((J_{\lambda\lambda})_0 K_{\lambda\lambda})} z_1 + J_{\theta\theta}\tau \end{cases} \quad (6-7a)$$

$$\begin{cases} \varepsilon \dot{z}_1 = z_2 \\ \varepsilon \dot{z}_2 = -J_{\theta\lambda}^T F_\theta - J_{\lambda\lambda} F_\lambda - \frac{J_{\lambda\lambda} K_{\lambda\lambda}}{\mu_{\min}((J_{\lambda\lambda})_0 K_{\lambda\lambda})} z_1 + J_{\theta\lambda}^T \tau \end{cases} \quad (6-7b)$$

where Eqs. (6-7a) and (6-7b) represent the dynamics of the slow and fast subsystems, respectively. For the above dynamic model, the manifold defined by:

$$h^e(x_1^e, x_2^e, \tau, \varepsilon) = \begin{bmatrix} h_1^e(x_1^e, x_2^e, \tau, \varepsilon) \\ h_2^e(x_1^e, x_2^e, \tau, \varepsilon) \end{bmatrix} \quad (6-8)$$

is called the integral (invariant) manifold if ²⁷:

$$z(t^*, \varepsilon) = h^e(x_1^e(t^*, \varepsilon), x_2^e(t^*, \varepsilon), \tau(t^*), \varepsilon) \Rightarrow z(t, \varepsilon) = h^e(x_1^e(t, \varepsilon), x_2^e(t, \varepsilon), \tau(t), \varepsilon) \quad \forall t > t^* \quad (6-9)$$

That is, if the fast variable z (which represented the links' lateral deflections and their time derivative) reaches to the manifold h^e at time t^* , it stays on this manifold thereafter. To assure that the fast variable z will eventually restrict to its integral manifold, the fast component of the controller, τ_f , is designed in Section 6.3. The restriction of z to h^e means that the links' lateral deflections and their time derivative can be obtained in terms of the joints' rotations, their time derivative and input torques.

²⁷ The superscript “e” emphasizes that h^e is the exact solution of the integral manifold. Moreover, when z is restricted to its exact integral manifold h^e , the corresponding x from Eq. (7a) is called x^e .

According to the definition of the integral manifold, $(h^e)^T = [(h_1^e)^T \quad (h_2^e)^T]^T$ has to satisfy the following so called integral manifold condition, which obtains by substituting z in Eq. (6-7b) with h^e from Eq. (6-8) [3]:

$$\begin{cases} \varepsilon \dot{h}_1^e = h_2^e \\ \varepsilon \dot{h}_2^e = -J_{\theta\lambda}^T F_\theta - J_{\lambda\lambda} F_\lambda - \frac{J_{\lambda\lambda} K_{\lambda\lambda}}{\mu_{\min}((J_{\lambda\lambda})_0 K_{\lambda\lambda})} h_1^e + J_{\theta\lambda}^T \tau \end{cases} \quad (6-10)$$

Since the above constraints on h^e are nonholonomic, finding an algebraic expression for h^e from Eq. (6-10) is unattainable. However, it is possible to find an approximate solution by using the series expansions of h_1^e , h_2^e and τ around $\varepsilon = 0$. Therefore, based on the assumption that ε is small, h_1^e , h_2^e and τ are expanded as:

$$h_1^e \approx h_1 = \sum_{j=0}^p \varepsilon^j h_{1j} = h_{10} + \varepsilon h_{11} + \varepsilon^2 h_{12} + \dots \quad (6-11a)$$

$$h_2^e \approx h_2 = \sum_{j=0}^p \varepsilon^j h_{2j} = h_{20} + \varepsilon h_{21} + \varepsilon^2 h_{22} + \dots \quad (6-11b)$$

$$\tau \approx \tau_s = \sum_{j=0}^p \varepsilon^j \tau_j = \tau_0 + \varepsilon \tau_1 + \varepsilon^2 \tau_2 + \dots \quad (6-11c)$$

where h_1 and h_2 are the approximations of h_1^e and h_2^e and τ_s is the approximation of τ when the approximate solutions of h_1^e and h_2^e , that is h_1 and h_2 , are used. By substituting the expression of h_1, h_2 and τ_s , given in Eqs. (6-11a) to (6-11c), in Eq. (6-10) and equating the terms having the same power of ε , h_{ij} in terms of τ_j where $i = 1, 2$ and $j = 0, \dots, p$ will be found iteratively. To find h_{ij} and τ_j in this chapter, the series expansions, given in Eqs. (6-11a) to (6-11c), are truncated by assuming $p = 2$, similar to our pervious work [13,14]. This is due to the fact that if $p < 2$, then the contribution of the links' flexibility will not be observed in the end-effector displacement, while on the other hand for $p > 2$ the control effort will increase. Therefore $p = 2$ is the optimal value and with this selection, Eqs. (6-11a) to (6-11c) become:

$$h_1 = h_{10} + \varepsilon h_{11} + \varepsilon^2 h_{12} \quad (6-12a)$$

$$h_2 = h_{20} + \varepsilon h_{21} + \varepsilon^2 h_{22} \quad (6-12b)$$

$$\tau_s = \tau_0 + \varepsilon \tau_1 + \varepsilon^2 \tau_2 \quad (6-12c)$$

The manifold obtained by assuming $p = 2$ in Eqs. (6-11a) to (6-11c), is called the *second order integral manifold*. Substituting the h_1 , h_2 and τ_s from Eqs. (6-12a) to (6-12c) into Eq. (6-10) leads to:

$$\left\{ \begin{array}{l} \varepsilon(\dot{h}_{10} + \varepsilon \dot{h}_{11} + \varepsilon^2 \dot{h}_{12}) = h_{20} + \varepsilon h_{21} + \varepsilon^2 h_{22} \\ \varepsilon(\dot{h}_{20} + \varepsilon \dot{h}_{21} + \varepsilon^2 \dot{h}_{22}) = -J_{\theta\lambda}^T F_\theta - J_{\lambda\lambda} F_\lambda - \frac{J_{\lambda\lambda} K_{\lambda\lambda}}{\mu_{\min}((J_{\lambda\lambda})_0 K_{\lambda\lambda})} (h_{10} + \varepsilon h_{11} + \varepsilon^2 h_{12}) + \\ J_{\theta\lambda}^T (\tau_0 + \varepsilon \tau_1 + \varepsilon^2 \tau_2) \end{array} \right. \quad (6-13)$$

Since $J_{\theta\lambda}^T$, F_θ , F_λ , and $J_{\lambda\lambda}$ in Eq. (6-13) are functions of ε , to find h_{ij} and τ_j from this equation by iteratively equating the terms having the same power of ε , the series expansions of $J_{\theta\lambda}^T$, F_θ , F_λ , and $J_{\lambda\lambda}$ around $\varepsilon = 0$ is used. These series expansions of $J_{\theta\lambda}^T$, F_θ , F_λ , and $J_{\lambda\lambda}$ neglecting terms of order ε^p where $p > 2$ (for the same reason that in Eqs. (6-12a) to (6-12c) terms of order ε^p where $p > 2$ are neglected) are:

$$\begin{aligned} J_{\theta\lambda}^T &= (J_{\theta\lambda}^T)_0 + \varepsilon (J_{\theta\lambda}^T)_1 + \frac{1}{2} \varepsilon^2 (J_{\theta\lambda}^T)_2 & J_{\lambda\lambda} &= (J_{\lambda\lambda})_0 + \varepsilon (J_{\lambda\lambda})_1 + \frac{1}{2} \varepsilon^2 (J_{\lambda\lambda})_2 \\ F_\theta &= (F_\theta)_0 + \varepsilon (F_\theta)_1 + \frac{1}{2} \varepsilon^2 (F_\theta)_2 & F_\lambda &= (F_\lambda)_0 + \varepsilon (F_\lambda)_1 + \frac{1}{2} \varepsilon^2 (F_\lambda)_2 \end{aligned} \quad (6-14)$$

where for the arbitrary function $g(\varepsilon)$, $(g)_i = d^i g / d\varepsilon^i \Big|_{\varepsilon=0}$ and $(g)_0 = g(0)$. As an example the derivations of $(F_\theta)_1$ and $(F_\theta)_2$ are presented in Appendix I.

Substituting Eq. (6-14) into Eq. (6-13) and equating the terms having the same power of ε yields:

$$h_{10} = \left(\frac{(J_{\lambda\lambda})_0 K_{\lambda\lambda}}{\mu_{\min}((J_{\lambda\lambda})_0 K_{\lambda\lambda})} \right)^{-1} \left[(J_{\theta\lambda}^T)_0 \tau_0 - (J_{\theta\lambda}^T)_0 (F_\theta)_0 - (J_{\lambda\lambda})_0 (F_\lambda)_0 \right] \quad (6-15a)$$

$$h_{20} = 0 \quad (6-15b)$$

$$h_{11} = \left(\frac{(J_{\lambda\lambda})_0 K_{\lambda\lambda}}{\mu_{\min}((J_{\lambda\lambda})_0 K_{\lambda\lambda})} \right)^{-1} [(J_{\theta\lambda}^T)_0 \tau_1 - (J_{\theta\lambda}^T)_0 (F_\theta)_1 - (J_{\lambda\lambda})_0 (F_\lambda)_1] \quad (6-15c)$$

$$h_{21} = \dot{h}_{10} \quad (6-15d)$$

$$h_{12} = \left(\frac{(J_{\lambda\lambda})_0 K_{\lambda\lambda}}{\mu_{\min}((J_{\lambda\lambda})_0 K_{\lambda\lambda})} \right)^{-1} [(J_{\theta\lambda}^T)_0 \tau_2 + \frac{1}{2}(J_{\theta\lambda}^T)_2 \tau_0 - \frac{1}{2}(J_{\theta\lambda}^T)_0 (F_\theta)_2 - \frac{1}{2}(J_{\theta\lambda}^T)_2 (F_\theta)_0 - \frac{1}{2}(J_{\lambda\lambda})_0 (F_\lambda)_2 - \frac{1}{2}(J_{\lambda\lambda})_2 (F_\lambda)_0 - \frac{(J_{\lambda\lambda})_2 K_{\lambda\lambda} h_{10}}{2\mu_{\min}((J_{\lambda\lambda})_0 K_{\lambda\lambda})} - \dot{h}_{21}] \quad (6-15e)$$

$$h_{22} = \dot{h}_{11} \quad (6-15f)$$

The usage of obtaining the integral manifold concept, as has been done in this section, can be summarized as follows. The dynamic model of the MLFM presented in Eqs. (6-7a) and (6-7b) has $(n+nm)$ degrees-of-freedom while it has only n actuators, thus MLFM is an underactuated system (number of degrees-of-freedom is more the number of actuators). By using the integral manifold concept, an approximate solution for Eq. (6-7a) will be obtained. That is, if z is restricted to its integral manifold, the links' lateral deflections and their time derivative can be obtained in terms of the links' rotations, their time derivative and input torques (note that links' lateral deflections and their derivative on the integral manifold are represented by h_{ij} and see Eqs. (6-15a) to (6-15f)). Thus by using this concept changes the underactuated MLFM, appears to be a fully actuated one and its EETT can be accomplished.

6.3. End-effector trajectory tracking

In this Section it is proven that to reduce the EETT error of MLFM, a corrective term of order ε^2 has to be added to the computed torque command (CTC) of the rigid link counterpart of the MFLM. Since the addition of the corrective term to the CTC for the EETT error reduction is based on the assumption that z (the parameters represent links' lateral deflections and their time derivative) is restricted to its integral manifolds, a fast component of controller τ_f is also designed to assure the satisfaction of this assumption. The implementation of τ_f , which was initially a full-state feedback controller, needed the direct measurement of the time derivative of the flexible variables

(time derivative of λ defined in Eq. (6-2)), which made the implementation of the proposed controller almost impractical. However, this drawback has been removed by the design of an observer to estimate the time derivative of the flexible variables. That is, τ_f is an observer-based feedback controller. Finally the stability of the proposed controller is proven by the Lyapunov criterion.

The end-effector displacement of the MLFM can be described by:

$$r = \theta + W\lambda \quad (6-16)$$

where the components of the vector r represent the end-effector displacement, vectors θ and λ are defined after Eq. (6-2), and W is the matrix that relates the flexible variables, λ , to the end-effector displacement. As an example for the two-link-flexible manipulator shown in Fig. 6-1, $r^T = [r_1 \quad r_2]$. Details of Eq. (6-16) for the end-effector displacement of a two-flexible-link manipulator as well as the definition of its W are given in Appendix II.

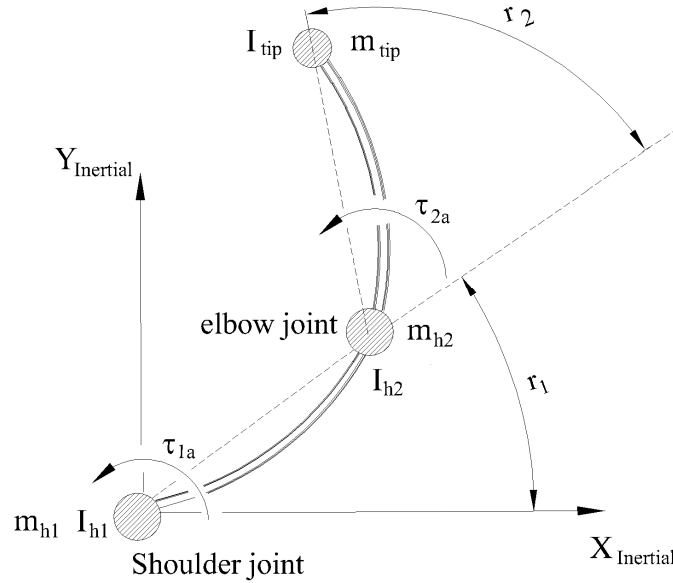


Fig. 6-1: Schematic of a two-flexible-link manipulator

After describing the end-effector displacement in terms of θ and λ , substitutions of θ and λ from Eqs. (6-5a) and (6-5b) into Eq. (6-16) result in:

$$r = x_1 + \varepsilon^2 W z_1 \quad (6-17)$$

Assuming that z is restricted to its integral manifold, z_1 in Eq. (6-17) is replaced with h_1 , as given in Eq. (6-12a). Thus:

$$r = x_1 + \varepsilon^2 W(h_{10} + \varepsilon h_{11} + \varepsilon^2 h_{12}) \quad (6-18)$$

Since terms of order ε^p where $p > 2$ are neglected in this chapter, (see Eqs. (6-12a) to (6-12c) and (6-14) for example), the end-effector displacement given in Eq. (6-18) is:

$$r = x_1 + \varepsilon^2 W h_{10} \quad (6-19)$$

In the following, the torques τ_0 , τ_1 and τ_2 will be selected so that the end-effector displacement, given in Eq. (6-19), tracks a desired trajectory, r_d .

Lemma 1: Selecting

$$\tau_0 = (M_{\theta\theta})_0 (\ddot{r}_d - K_D \dot{e} - K_P e) + (F_\theta)_0 \quad (6-20a)$$

$$\tau_1 = 0 \quad (6-20b)$$

$$\tau_2 = (M_{\theta\theta})_0 V + (M_{\theta\lambda})_0 \ddot{h}_{10} - (M_{\theta\theta})_0 d + \frac{1}{2} (F_\theta)_2 \quad (6-20c)$$

where

$$e = x_1 - r_d \quad (6-21a)$$

$$V = -(W \ddot{h}_{10} + K_D W \dot{h}_{10} + K_P W h_{10}) \quad (6-21b)$$

$$d = \left[(J_{\theta\theta})_2 - (J_{\theta\lambda})_0 (J_{\lambda\lambda})_0^{-1} (J_{\theta\lambda})_2^T \right] \left[\frac{1}{2} (\tau_0 - (F_\theta)_0) \right] - \left[(J_{\theta\lambda})_2 - (J_{\theta\lambda})_0 (J_{\lambda\lambda})_0^{-1} (J_{\lambda\lambda})_2^T \right] \left[\frac{1}{2} ((F_\lambda)_0 + \frac{K_{\lambda\lambda}}{\mu_{\min}((J_{\lambda\lambda})_0 K_{\lambda\lambda})} h_{10}) \right] \quad (6-21c)$$

makes the end-effector displacement given in Eq. (6-19) asymptotically track the desired trajectory, r_d , provided that:

- 1- The gain matrices K_P and K_D are positive definite;

2- $r_d \in C^4$, that is the desired trajectory and its time derivatives up to the fourth order are continuous and bounded.

Proof:

Replacing z_1, z_2 and τ in Eq. (6-7a) by h_1, h_2 and τ_s given in Eqs. (6-12a) to (6-12c) respectively, and also using the expression of h_{ij} given in Eqs. (6-15a) to (6-15f), yields:

$$\begin{cases} \dot{x}_1 = x_2 \\ \dot{x}_2 = (M_{\theta\theta})_0^{-1}[\tau_0 - (F_\theta)_0] + \varepsilon(M_{\theta\theta})_0^{-1}\tau_1 + \varepsilon^2[(M_{\theta\theta})_0^{-1}(\tau_2 - \frac{1}{2}(F_\theta)_2 - (M_{\theta z})_0\ddot{h}_{10}) + d] \end{cases} \quad (6-22)$$

where d is defined in Eq. (6-21c). Details of the derivation of Eq. (6-22) can be found in Appendix III. It is worth noting that without the use of the properties of the mass matrix introduced in Section 6.2.1, which is one of the contributions of this chapter, the concise derivation of Eq. (6-22) is not possible. This simplification makes the selection of the control inputs easier and less computationally costly.

Taking the first and second time derivatives from Eq. (6-19) and replacing \dot{x}_1 with x_2 results in:

$$\dot{r} = \dot{x}_1 + \varepsilon^2 W \dot{h}_{10} = x_2 + \varepsilon^2 W \dot{h}_{10} \quad (6-23a)$$

$$\ddot{r} = \dot{x}_2 + \varepsilon^2 W \ddot{h}_{10} \quad (6-23b)$$

By substituting \dot{x}_2 from Eq. (6-22) into Eq. (6-23b) and using torques τ_0 , τ_1 and τ_2 defined in Eqs. (6-20a) to (6-20c), \ddot{r} is:

$$\ddot{r} = \ddot{r}_d - K_D \dot{e} - K_P e + \varepsilon^2 (W \ddot{h}_{10} + V) \quad (6-24)$$

The utilization of e and V , which are given in Eqs. (6-21a) and (6-21b) respectively, changes Eq. (6-24) into:

$$(\ddot{r} - \ddot{r}_d) + K_D(x_2 + \varepsilon^2 W \dot{h}_{10} - \dot{r}_d) + K_P(x_1 + \varepsilon^2 W h_{10} - r_d) = 0 \quad (6-25)$$

Finally, considering Eqs. (6-19) and (6-23a) for r and \dot{r} , the error dynamics from Eq. (6-25) is:

$$(\ddot{r} - \ddot{r}_d) + K_D(\dot{r} - \dot{r}_d) + K_P(r - r_d) = 0 \quad (6-26)$$

which is asymptotically stable since K_P and K_D are positive definite matrices. The assumption that $r_d \in C^4$, makes the control command continuous and bounded. This is due to the fact that the calculation of τ_2 requires evaluation of \ddot{h}_{10} (Eq. (6-20c)), and computation of h_{10} by itself needs having τ_0 (Eq. (6-15a)) which depends on \ddot{r}_d (Eq. (6-20a)). Thus, calculation of τ_2 requires the fourth derivative of r_d , and the assumption that $r_d \in C^4$ makes τ_2 and τ_0 ; thus the control command, to be continuous and bounded.

QED

The expression given in Eq. (6-20a) for τ_0 is the CTC of the rigid link counterpart of the MLFM [2]. Therefore, based on Lemma 1, to reduce the EETT error only the corrective term $\varepsilon^2 \tau_2$, which is of order ε^2 , has to be added to the CTC of the rigid link counterpart of the MLFM.

Remark 6.1: To calculate h_{10} , which is required for the calculation of the corrective term, τ_0 from Eq. (6-20a) is substituted into Eq. (6-15a) and the property of the mass matrix given in Eq. (6-4b) is used which after some algebraic manipulations results in:

$$h_{10} = -\mu_{\min}(J_{\lambda\lambda}K_{\lambda\lambda})K_{\lambda\lambda}^{-1}((M_{\theta\lambda}^T)_0(\ddot{r}_d - K_D(x_2 - \dot{r}_d) - K_P(x_1 - r_d) + (F_\lambda)_0) \quad (6-27)$$

Moreover, by taking time derivatives from Eq. (6-27), the expressions of \dot{h}_{10} and \ddot{h}_{10} , which are required for the evaluation of V in Eq. (6-21b) can be obtained, employing the analysis similar to that in [4p. 147, 20 p. 297, 13,14]. Furthermore, to evaluate d in Eq. (6-21c), $(J_{\theta\theta})_2, (J_{\lambda\lambda})_2, (J_{\theta\lambda})_2$ and $(J_{\theta\lambda}^T)_2$ are required. Although these terms can be obtained from:

$$(J)_2 = d^2(M^{-1}(\varepsilon))/d\varepsilon^2 \Big|_{\varepsilon=0} \quad (6-28)$$

finding $(J)_2$ from Eq. (6-28) requires that the second derivative of $M^{-1}(\varepsilon)$ with respect to ε be calculated which is a complicated task and prone to error. In the following $(J)_2$, and consequently its components $(J_{\theta\theta})_2, (J_{\lambda\lambda})_2, (J_{\theta\lambda})_2$ and $(J_{\theta\lambda}^T)_2$, are obtained by a new method which does not need this derivative calculation. Since $J(\varepsilon)$ is the inverse of $M(\varepsilon)$:

$$M(\varepsilon)J(\varepsilon) = I \quad (6-29)$$

By substituting the series expansions of $M(\varepsilon)$ and $J(\varepsilon)$ around $\varepsilon = 0$ as:

$$M(\varepsilon) = (M)_0 + \varepsilon(M)_1 + \frac{1}{2}\varepsilon^2(M)_2 \quad J(\varepsilon) = (J)_0 + \varepsilon(J)_1 + \frac{1}{2}\varepsilon^2(J)_2 \quad (6-30)$$

into Eq. (6-29), equaling the terms having the same power of ε and knowing that $(M)_1 = (J)_1 = 0$:

$$(J)_2 = -(M)_0^{-1} M_2 (M)_0^{-1} \quad (6-31)$$

which contrary to Eq. (6-28) does not need the derivative calculation of $M^{-1}(\varepsilon)$ with respect to ε .

The key assumption in Lemma 1 is that the vectors z_1 and z_2 have to be respectively restricted to their second order integral manifold h_1 and h_2 given in Eqs. (6-12a) and (6-12b). To assure this key assumption is satisfied the fast component of the controller τ_f is designed as follows. The deviation of the vector of fast variables $z^T = [z_1^T \quad z_2^T]$ from their integral manifold $h^T = [h_1^T \quad h_2^T]$ is:

$$\hat{z} = \begin{bmatrix} \hat{z}_1 \\ \hat{z}_2 \end{bmatrix} = \begin{bmatrix} z_1 - h_1 \\ z_2 - h_2 \end{bmatrix} \quad (6-32)$$

Using Eqs. (6-12a) and (6-12b) for h_1 and h_2 , Eq. (6-32) changes to:

$$\hat{z} = \begin{bmatrix} \hat{z}_1 \\ \hat{z}_2 \end{bmatrix} = \begin{bmatrix} z_1 - (h_{10} + \varepsilon h_{11} + \varepsilon^2 h_{12}) \\ z_2 - (h_{20} + \varepsilon h_{21} + \varepsilon^2 h_{22}) \end{bmatrix} \quad (6-33)$$

Multiplying both sides of Eq. (6-33) with ε , taking time derivative from it, replacing $\varepsilon \dot{z}_1$ and $\varepsilon \dot{z}_2$ with their equivalences from Eq. (6-7b), substituting τ with $\tau_0 + \varepsilon^2 \tau_2 + \tau_f$, using Eqs. (6-15a) to (6-15f) for h_{ij} and Eqs. (6-20a) to (6-20c) for τ_0 and τ_2 , and neglecting the terms of order ε^p where $p > 2$, yields:

$$\varepsilon \dot{\hat{z}} = A_z \hat{z} + B_z \tau_f + \varepsilon N_{z1} + \varepsilon^2 N_{z2} \quad (6-34)$$

where

$$A_z = \begin{bmatrix} 0 & I \\ \frac{-(J_{\lambda\lambda})_0 K_{\lambda\lambda}}{\mu_{\min}((J_{\lambda\lambda})_0 K_{\lambda\lambda})} & 0 \end{bmatrix}, B_z = \begin{bmatrix} 0 \\ (J_{\theta\lambda}^T)_0 \end{bmatrix}, N_{z1} = \begin{bmatrix} 0 \\ O_{z1} \end{bmatrix}, N_{z2} = \begin{bmatrix} 0 \\ O_{z2} \end{bmatrix} \quad (6-35)$$

and the expressions of O_{z1} and O_{z2} are given in Appendix IV. In the absence of N_{z1} and N_{z2} in Eq. (6-34), the full-state feedback controller $\tau_f = -K_{cz} \hat{z}$ stabilizes the dynamic equation of \hat{z} provided that the gain K_{cz} is selected so that the matrix $A_z - B_z K_{cz}$ is Hurwitz. The stability of the dynamic equation of \hat{z} , Eq. (6-34), means that eventually the vectors z_1 and z_2 will get restricted to their second order integral manifold h_1 and h_2 . In the presence of N_{z1} and N_{z2} with the assumptions that $\|N_{z1}\| < \ell_1 \|\hat{z}\|$ and $\|N_{z2}\| < \ell_2 \|\hat{z}\|$, where $\|N_{z1}\|$ and $\|N_{z2}\|$ are the Euclidean norm of N_{z1} and N_{z2} and ℓ_1 and ℓ_2 are scalar constants, still the full-state feedback controller $\tau_f = -K_{cz} \hat{z}$ can stabilize the dynamic equation of \hat{z} [page 161 in 21]. However, this time there is another extra restriction on the gain K_{cz} besides the requirement to make the matrix $A_z - B_z K_{cz}$ Hurwitz. This extra restriction is explained in the stability proof, given in Appendix V, where the stability of the whole system with the control torque $\tau_0 + \varepsilon^2 \tau_2 + \tau_f$ is studied.

Since matrices A_z and B_z in Eq. (6-35) are functions of x_1 , the gain matrix K_{cz} is selected according to the gain-scheduling procedure [6]. Based on the gain-scheduling procedure, first in the possible range of the variation of x_1 , several operating points like $\nu_i = (x_1)_i$ are selected, where i is varied to cover all the possible x_1 . Then, at each

operating point the gain $(K_{cz})_{v_i}$ is designed so that the stability of the system at $v_i = (x_1)_i$ is guaranteed. Finally, the gain matrix is linearly interpolated between these operating points. After adopting the gain scheduling procedure, implementing the full-state feedback controller $\tau_f = -K_{cz} \hat{z}$ requires that \hat{z} be available, which from Eqs. (6-32) and (5b), need the measurement of λ and $\dot{\lambda}$. Although, the measurement of λ , which is required for the calculation z_1 and consequently \hat{z}_1 , is possible, for example by strain gauges, the measurement of $\dot{\lambda}$, which is needed for the evaluation of z_2 and consequently \hat{z}_2 , is not easy. As a remedy, to remove the need for measuring $\dot{\lambda}$ which was required by the full-state feedback controller, an observer-based feedback controller assuming z_1 as the output is employed to stabilize the dynamic equations of \hat{z} . That is the output for Eq. (6-34) is assumed to be:

$$y = C_z \hat{z} \quad C_z = \begin{bmatrix} I_{n \times n} & 0_{n \times n} \end{bmatrix} \quad (6-36)$$

which only requires the measurement of \hat{z}_1 , and τ_f is selected as:

$$\tau_f = -K_{cz} \tilde{z} \quad (6-37)$$

where \tilde{z} , the estimate of \hat{z} , is calculated from:

$$\mathcal{E} \dot{\tilde{z}} = (A_z - B_z K_{cz} - K_{oz} C_z) \tilde{z} + K_{oz} y \quad (6-38)$$

and the observer gain K_{oz} is selected so that $A_z - K_{oz} C_z$ is a Hurwitz matrix. The same gain scheduling procedure is used for the evaluation of K_{oz} as did for K_{cz} .

Remark 6.2: To implement the above observer-based controller \hat{z}_1 should be calculated, which according to Eq. (6-32) needs evaluation of h_{10}, h_{11} and h_{12} . The expression of h_{10} is given in Eq. (6-27). Combining Eq. (6-15c) with Eq. (6-20b) and considering the fact that $(F_\theta)_1 = (F_\lambda)_1 = 0$ (See Eq. (6-A22) in Appendix V), resulted in $h_{11} = 0$. Finally, the expression of h_{12} is given in Eq. (6-15e) where for its calculation, τ_0 and τ_2 are presented in Eqs. (6-20a) and (6-20c) respectively, $(F_\theta)_2$ and $(F_\lambda)_2$ can be obtained as explained in

Appendix I, and $(J_{\theta\lambda}^T)_2$ and $(J_{\lambda\lambda})_2$ can be computed according to Remark 6.1, Eq. (6-31).

Theorem: For the MLFM with the dynamic model given in Eqs. (6-7a) and (6-7b), applying the torque $\tau_0 + \varepsilon^2 \tau_2 + \tau_f$ where τ_0 , τ_2 , and τ_f are given in Eqs. (6-20a), (6-20c) and (6-37) respectively, restricts the fast variables z_1 and z_2 to their manifold defined in Eqs. (6-12a) and (6-12b), and makes the output r given in Eq. (6-16) track the desired trajectory r_d provided that:

- 1- The gain matrices K_p and K_D are positive definite;
- 2- The gain matrices K_{cz} and K_{oz} are such that $A_z - B_z K_{cz}$ and $A_z - K_{oz} C_z$ are Hurwitz, where A_z , B_z and C_z are given in Eqs. (6-35) and (6-36), respectively;
- 3- The condition $\mu_{\min}(S_\eta) \mu_{\min}(S_r) > \ell_3^2$ is satisfied, where S_η , S_r and ℓ_3 are defined in Eqs. (6-A38), (6-A39) and (6-A41) in Appendix V, respectively and symbol $\mu_{\min}(S)$ represents the minimum eigenvalue of the matrix S ; and
- 4- The $r_d \in C^4$, that is up to the fourth order derivative of the desired trajectory has to be continuous and bounded.

Proof: The proof of the stability which is based on the Lyapunov criterion is given in Appendix V.

6.4. Simulation Studies

In this section, the results of simulation studies for the two-flexible-link manipulator, shown in Fig. 6-1, are presented. The first and second links of this manipulator were the shoulder and elbow links, while their corresponding actuators were the shoulder and elbow actuators. It was assumed that the manipulator operated in the horizontal plane; therefore gravity was not a factor. Moreover, the flexibility of each link was modeled using one mode shape, similar to the previously reported simulation and experimental studies in [9,22,23].

The physical parameters of the two-flexible-link manipulator which are given in table 1 were the same as those in [16]. Here, L_1 and L_2 were the length of the shoulder and elbow links respectively, ρ_1 and ρ_2 were the mass per unit length for the shoulder and elbow links respectively, I_{h1} and I_{h2} were the shoulder and elbow actuators' mass moment of inertias respectively, m_{h1} and m_{h2} were the shoulder and elbow actuators' masses respectively, EI_1 and EI_2 were the rigidity of the shoulder and elbow links respectively, and m_{tip} and I_{tip} were the mass and mass moment of inertia of the end-effector payload, respectively.

Table 1: Physical parameters of a two-flexible-link manipulator

Physical Properties	Value	unit
L_1, L_2	0.5000	(m)
ρ_1, ρ_2	0.2000	(kg / m)
I_{h1}, I_{h2}	0.1000	($kg.m^2$)
m_{h1}, m_{h2}	1.000	(kg)
EI_1, EI_2	1.000	($N.m^2$)
m_{tip}	0.1000	(kg)
I_{tip}	0.0005	($kg.m^2$)

As in Eq. (6-16) the end-effector displacement can be represented by $r^T = [r_1 \ r_2]$, where r_1 and r_2 are shown in Fig. 6-1, and their relations to the links' rotations, θ , and flexible variables, λ , are given in Appendix II. The desired trajectories r_{d1} and r_{d2} , to be followed by r_1 and r_2 respectively, were selected to be the ninth order polynomial satisfying the following conditions:

$$r_{dj}(0) = 0 \quad \left. \frac{d^i r_{dj}}{dt^i} \right|_{t=0} = 0 \quad i = 1, \dots, 4 \quad j = 1, 2 \quad (6-39)$$

$$r_{dj}(t_{ff}) = \theta_{ff} \quad \left. \frac{d^i r_{dj}}{dt^i} \right|_{t_{ff}} = 0 \quad i = 1, \dots, 4 \quad j = 1, 2 \quad (6-40)$$

where θ_{ff} were the desired final values for r_{dj} at the final maneuver times t_{ff} ($j = 1, 2$), respectively. These trajectories were kept constant at θ_{ff} for $t > t_{ff}$.

The end-effector controller introduced in this chapter was referred to as the “integral manifold controller”, which added a corrective term to the CTC of the rigid link counterpart of the MFLM, as explained in Section 6.3. The controller without the corrective terms discussed in [2] and was called here as “rigid link controller”. To illustrate the reduction in the ETT error due to the new controller, the results using integral manifold controller were compared against those of the rigid link controller in the following studies.

4-1- Example 1: two-flexible-link manipulator, relatively slow speed maneuver

In the first simulation, the desired trajectories r_{d1} and r_{d2} were selected according to Eqs. (6-39) and (6-40) by using $t_{f1} = t_{f2} = 6(s)$, $\theta_{f1} = 60.0^\circ (1.047(rad))$ and $\theta_{f2} = 45.0^\circ (0.785(rad))$. These desired trajectories are shown in Fig. 6-2.

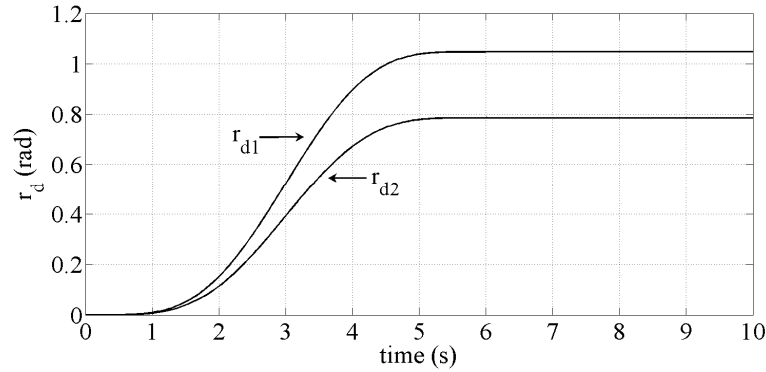


Fig. 6-2: Example 1, desired trajectories r_{d1} and r_{d2} for the two-flexible-link manipulator of Fig. 6-1

For the calculation of τ_0 and τ_2 , given in Eqs. (6-20a) and (6-20c), the gains $K_p = 0.16$ and $K_D = 0.80$ were selected. To calculate K_{cz} and K_{oz} of the fast component of the controller τ_f , the gain-scheduling technique, as discussed in Section

6.3, was used. Since, for the two-flexible-link manipulator of Fig. 6-1, the matrices A_z and B_z were functions of θ_2 , then the operating points in the gain-scheduling technique were $\nu_i = (\theta_2)_i$. Because $0^\circ < r_{d2} < 45^\circ$, the possible range of θ_2 was selected as $\min(r_{d2}) - \delta r_{d2} < \theta_2 < \max(r_{d2}) + \delta r_{d2}$, in which $\delta r_{d2} = 20.0^\circ$ was chosen, such that $-20.0^\circ < \theta_2 < 65.0^\circ$. That is the possible range of variation for θ_2 was selected to be 20.0° wider from both sides compared to r_{d2} . Therefore, when during the simulation the value of the θ_2 passed the limits of r_{d2} , the observer-based controller still worked. This range of θ_2 , $-20.0^\circ < \theta_2 < 65.0^\circ$, was divided into 13 equal segments and the operating points were $\nu_i = -20 + 5(i-1)$, $(i = 1, \dots, 14)$. The gain matrix K_{cz} at each operating point was obtained using the Linear-quadratic regulator, as in [2]. The gain K_{oz} was selected at each operating point such that $\mu(A_z - K_{oz}C_z) = 2\mu(A_z - B_zK_{cz})$, where the symbol $\mu(Q)$ represents the eigenvalues of matrix Q . That is the observer gain was selected so that the observer acted twice as fast as the controller. The commands “lqr” and “place” in MATLAB were respectively used for the calculation of K_{cz} and K_{oz} at each operating point.

The trajectory tracking errors, $error_1 = r_1 - r_{d1}$ and $error_2 = r_2 - r_{d2}$ respectively, for the integral manifold controller and rigid link controller are shown in Figs. 6-3 and 6-4. These figures clearly illustrate the superiority of the integral manifold controller compared to the rigid link controller in reducing the tracking errors. The maximum absolute values of $error_1$ and $error_2$ using the rigid link controller were 0.0261 (rad) and 0.0280(rad), respectively, while for the integral manifold controller they were much smaller; 0.0011(rad) and 0.0014(rad), respectively. That is, the new controller made the maximum of the $error_1$ and the $error_2$ about 24 and 20 times smaller, respectively. In addition to comparing the maximum absolute value of the errors, a normalized index, called the normalized mean square error (NMSE) was also introduced and used. This index, which signified the overall tracking error reductions over the entire maneuver time, was defined as:

$$NMSE = \sqrt{\frac{1}{t_m} \int_0^{t_m} (error_1^2 + error_2^2) dt} \quad (6-41)$$

where

$$error_1 = r_1 - r_{d1}, \quad error_2 = r_2 - r_{d2} \quad (6-42)$$

and t_m was the total time of the simulation. The NMSE for the rigid link controllers was $175.0 \times 10^{-4} (rad)$, while it was much smaller being $9.743 \times 10^{-4} (rad)$ for the integral manifold controller.

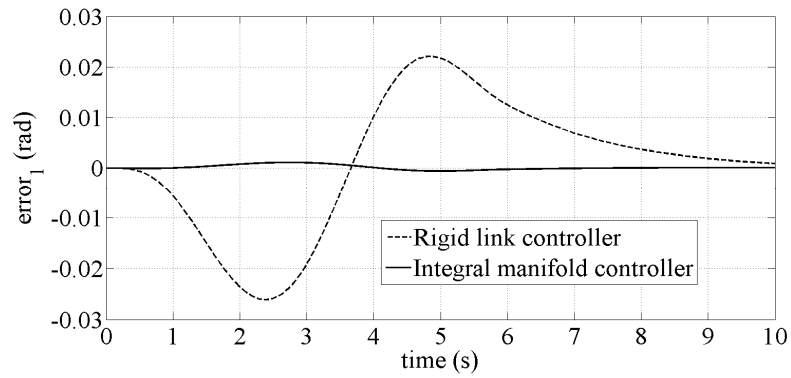


Fig. 6-3: Example 1, tracking error for r_1 , $error_1 = r_1 - r_{d1}$, using two controllers

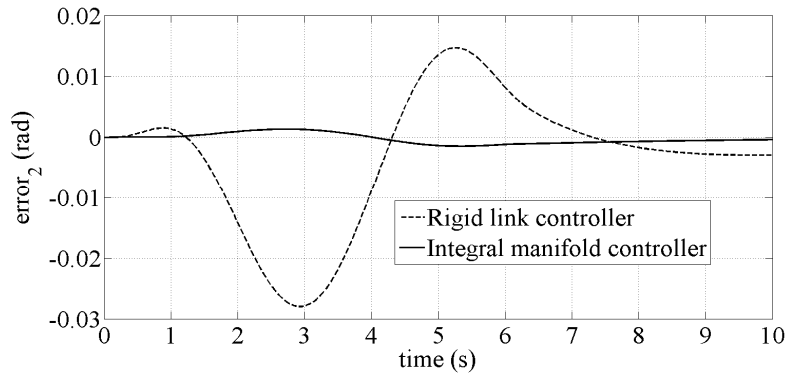


Fig. 6-4: Example 1, tracking error for r_2 , $error_2 = r_2 - r_{d2}$, using two controllers

Finally, the difference between the desired and the actual end-effector paths adopting the integral manifold and rigid link controllers are shown in Fig. 6-5. The acronym “DADP” in Fig. 6-5 was used for the difference between the actual and desired end-effector paths and was shown in Fig. 6-6. The improvement in reducing the EETT

error due to the new controller introduced in this chapter is evident from Fig. 6-5. The maximum difference between actual and desired end-effector paths for the integral manifold was $0.0018(m)$ which was about 21 times smaller compared to the $0.0380(m)$ of the rigid link controller.

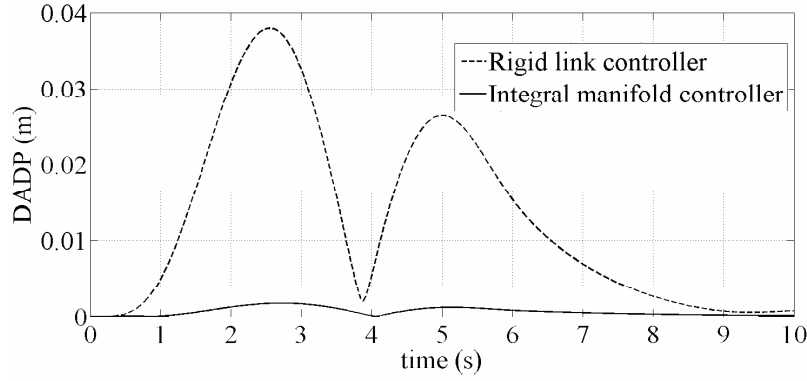


Fig. 6-5: Example 1, difference between the actual and desired end-effector paths (DADP)

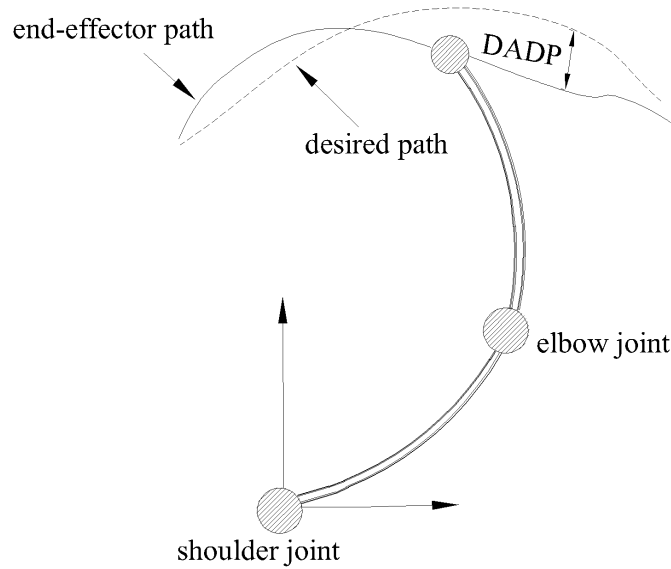


Fig. 6-6: Schematic of the DADP

4-2- Example 2: two-flexible-link manipulator, relatively fast speed maneuver

For the second simulation example, r_{d1} and r_{d2} were obtained assuming $t_{f1} = t_{f2} = 4(s)$, $\theta_{f1} = 60.0^\circ (1.047(rad))$ and $\theta_{f2} = 45.0^\circ (0.785(rad))$ in Eqs. (6-39) and (6-40). These desired trajectories are given in Fig. 6-7. The average speed of the desired trajectories in the second simulation was 1.5 faster compared to those of the first simulation.

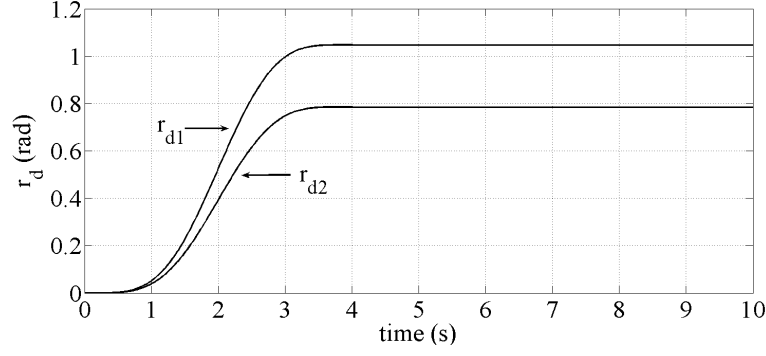


Fig. 6-7: Example 2, Desired trajectories r_{d1} and r_{d2} for the two-flexible-link manipulator of Fig. 6-1

For the implementation of the controller the same gains that were used in the first example were employed here as well. In Figs. 6-8 and 6-9, the tracking errors of r_1 and r_2 using the rigid link controller as well as the integral manifold controller are presented. The maximum absolute values of $error_1$ and $error_2$ for the rigid link controller were $0.0492(rad)$ and $0.0579(rad)$ respectively, while these errors using the integral manifold controller were only $error_1 = 0.0023(rad)$ and $error_2 = 0.0050(rad)$. That is, $error_1$ and $error_2$ of the new controller were respectively about 21 and 12 respectively smaller than those of the rigid link controller. Moreover, the small value of NMSE for the integral manifold controller, which was $0.0034(rad)$ compared with $0.0281(rad)$ of the rigid link controller is another evidence of the improvement due to the controller introduced in this chapter.

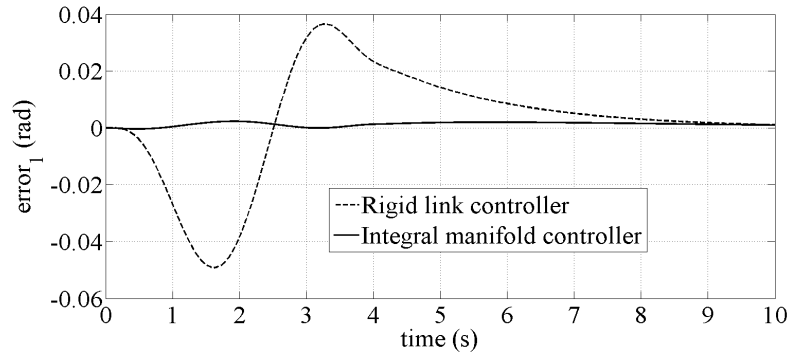


Fig. 6-8: Example 2, tracking error for r_1 , $error_1 = r_1 - r_{d1}$, using two controllers

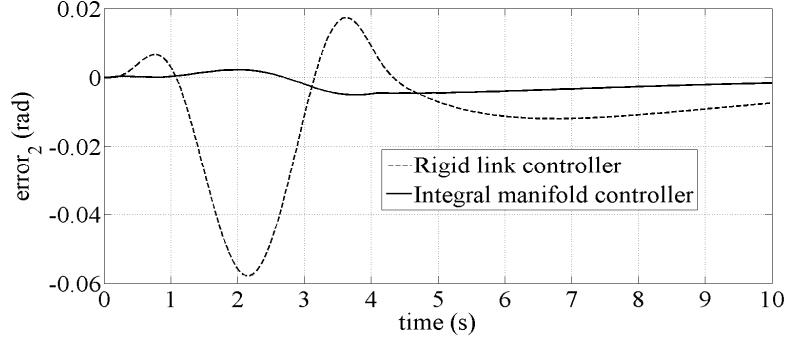


Fig. 6-9: Example 2, tracking error for r_2 , $error_1 = r_1 - r_{d1}$, using two controllers

Finally, the differences between the actual and desired paths utilizing the rigid link and integral manifold controller are shown in Fig. 6-10 (See Fig. 6-6 for the definition of DADP). The maximum difference between the desired and actual end-effector paths for the rigid link controller was $0.0699(m)$, while it was considerably smaller, $0.0034(m)$, for the integral manifold controller.

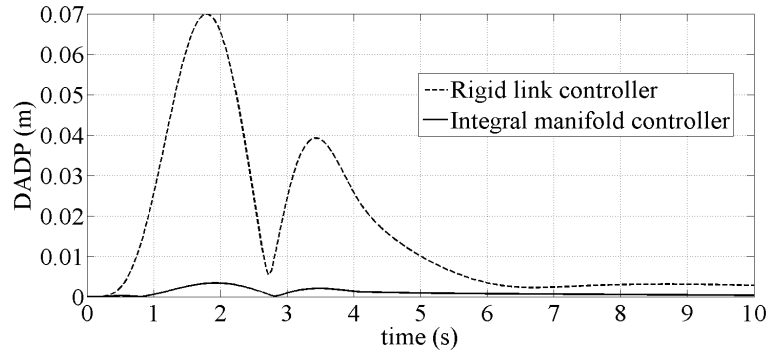


Fig. 6-10: Example 2, difference between the actual and desired end-effector paths (DADP)

Two other examples were also conducted on the same manipulator used here, but for different average speeds for the r_{d1} and r_{d2} . In these two tests, the values of θ_{f1} and θ_{f2} , as well as the controller gains, were the same as those used in the first and second simulations here. However in the third simulation (relatively very fast speed maneuver) $t_{f1} = t_{f2} = 3(s)$ and in the fourth simulation (relatively moderate speed maneuver) $t_{f1} = t_{f2} = 5(s)$. Details of the results of these two more simulations are not reported here for purpose of brevity; however a summary of the results for all four tests are given in table 2 and Figs. (6-11a) to (6-11d). The acronyms used in table 2 and Figs. (6-11a) to (6-11d) were (1)- RLC for the

rigid link controller, (2)- IMC for the integral manifold controller and (3)- $(DADP)_{\max}$ for the maximum difference between the actual and desired paths, respectively. From table 2 and Figs. (6-11a) to (6-11d) , it is obvious that the integral manifold controller has very small tracking errors compared with those of the rigid link controller independent of the average speed of the desired trajectories. Moreover, by decreasing the average speed of the desired trajectories, that is selecting a larger t_{f1} and t_{f1} , the $(error_1)_{\max}$, $(error_2)_{\max}$, NMSE and $(DADP)_{\max}$ were all decreased, as expected.

Table 2: Summary of simulation examples, $\theta_{f1} = 60^\circ$ and $\theta_{f2} = 45^\circ$

CASE	$t_{f1} = t_{f2}$ (s)	Controller	$(error_1)_{\max}$ (rad)	$(error_2)_{\max}$ (rad)	NMSE (rad)	$(DADP)_{\max}$ (m)
Very high speed (Example 3)	3	RLC	0.0770	0.0986	0.0410	0.1058
		IMC	0.0095	0.0159	0.0123	0.0056
High speed (Example 2)	4	RLC	0.0492	0.0579	0.0281	0.0699
		IMC	0.0023	0.0050	0.0034	0.0034
Moderate speed (Example 4)	5	RLC	0.0347	0.0387	0.0215	0.0501
		IMC	0.0015	0.0024	0.0015	0.0023
Low speed (Example 1)	6	RLC	0.0261	0.0280	0.0175	0.0380
		IMC	0.0011	0.0014	9.743×10^{-4}	0.0018

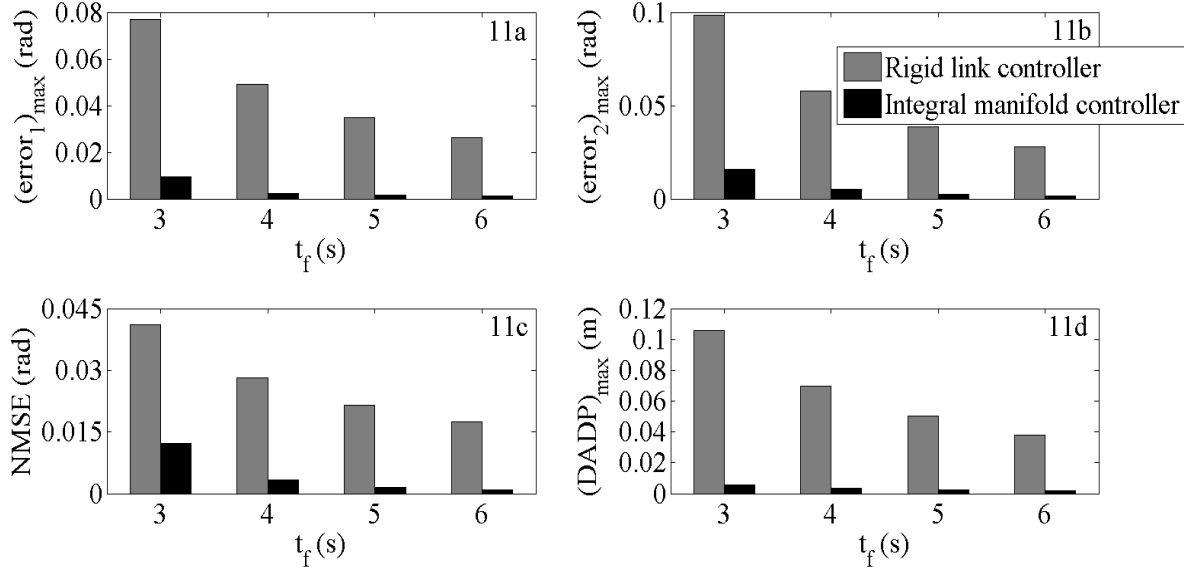


Fig. 6-11: summary of the examples for different desired maneuver time,

$$t_{f1} = t_{f2} = t_f$$

$$(error_1)_{\max}, (error_2)_{\max}, NMSE, (DADP)_{\max}$$

6.5. Conclusions

A new controller for the end-effector trajectory tracking (EETT) of general multi-link flexible manipulators (MLFM) based on the concept of the integral manifold of the singularly perturbed differential equations was introduced. The new controller added a corrective term to the computed torque command (CTC) of the rigid link counterpart of the MLFM for the reduction of the EETT error. This corrective torque was of second order of the parameter $\varepsilon = 1/2\pi f$, where f was the smallest non-zero natural frequency of the MLFM in the specified range of operation of the manipulator. The implementation of the new controller did not require measurement of the time derivative of the links' lateral deflections, measurements that are hardly practical. This is due to the use of an observer-based controller where the observer estimates the time derivative of the links' lateral deflections. The employed observer based-controller was designed using the gain-scheduling procedure. The stability of the new controller was proven by the Lyapunov stability criterion. To show the effectiveness of the new controller several simulation studies were carried out on a two-link manipulator with both links flexible. The average

speed of maneuver was varied in these examples from relatively low to high. In all these examples a great improvement was observed in reducing the EETT error, which justified the effectiveness of the new controller. Moreover, it was observed that, for the same controller gains, the EETT error was increased when the average maneuver speed was increased.

The main contribution of this work is in the introduction of a new EETT controller, designed based on the concept of integral manifold, which (1)- needs the fewest corrective terms in addition to the CTC of its rigid link counterpart, thus is computationally efficient (2)- its implementation did not require measurement of the time derivative of the flexible variables, thus is practical and (3)- calculation of its corresponding terms is simplified by introducing and using several mass matrix properties thus its calculation effort is minimized.

6.6. Nomenclature

A_z : State matrix of the fast subsystem which represents the deviation of the z from h

B_z : Input matrix of the fast subsystem which represents the deviation of the z from h

B : Constant matrix which maps vector τ to their corresponding generalized coordinates

C_z : Output matrix of the fast subsystem which represents the deviation of the z from h

EI_1, EI_2 : Rigidity of the shoulder and elbow links, respectively

F : Summation of the Coriolis, centrifugal, gravity and viscous damping forces

F_θ, F_λ : Components of the vector F

f : The smallest non-zero natural frequency of the MLFM in the specified range of the operation of the manipulator

h^e : Integral (invariant) manifold

h : Approximation of h^e

h_i : The i th element of vector h

h_{ij} : Coefficient of ε^j in h_i

I : Identity matrix

I_{tip} : Mass moment of inertia of the end-effector

J : Inverse of the mass matrix M

$J_{\theta\theta}, J_{\theta\lambda}, J_{\lambda\lambda}$: Components of the matrix J

K : Stiffness matrix

$K_{\lambda\lambda}$: Non-zero sub-matrix of K

K_P, K_D, K_{cz}, K_{oz} : Controller gains

L_1, L_2 : Length of the shoulder and elbow links

M : Mass matrix

$M_{\theta\theta}, M_{\theta\lambda}, M_{\lambda\lambda}$: Components of the mass matrix M

m : Number of mode shapes used to model the flexibility of the link

m_{h1}, m_{h2} :

m_{tip} : Mass of the end-effector

n : Number of links

q : Vector composed of generalized coordinates

r : End-effector displacement

W : Matrix that relates λ to the end-effector displacement

x : Vector composed of the states of the slow subsystem

z : Vector composed of the states of the fast subsystem

\hat{z} : Deviation of z from h

\tilde{z} : Estimate of \hat{z}

ε : Singular perturbation parameter

τ : Vector composed of τ_{ia}

τ_{ia} : torque of the i th link's actuator

τ_f : Fast component of the controller

θ_i : Relative rotation of the i th revolute joint with respect to the $(i-1)$ th revolute joint

θ : Vector composed of θ_i

λ : Vector composed of λ_i

λ_i : Vector composed of the flexible variable used to describe the lateral deflection of the i th link

λ_{ij} : time varying coefficient of the j th mode of the i th link

$(g)_i$: is equal to $d^i g / d\varepsilon^i \Big|_{\varepsilon=0}$ for arbitrary function $g(\varepsilon)$

ℓ_1, \dots, ℓ_8 : Positive constants

ρ_1, ρ_2 : Mass per unit length for the shoulder and elbow links, respectively

θ_{dj} : Desired final value for the r_{dj}

t_{ff} : Final maneuver time for the i th link

ν_i : the i th operating point the gain scheduling procedure

$\mu_{\min}(Q)$: Minimum eigenvalue of the matrix Q

6.7. Appendices

Appendix I: Sample calculation of the terms in the series expansion given in Eq. (6-14).

From Eq. (6-5b)

$$\lambda = \varepsilon^2 z_1 \quad \dot{\lambda} = \varepsilon z_2 \quad (6-A1)$$

Since F_θ is a function of λ and $\dot{\lambda}$, the expression for $(F_\theta)_1$ using the chain rule is :

$$(F_\theta)_1 = \left. \frac{dF_\theta}{d\varepsilon} \right|_{\varepsilon=0} = \left. \frac{\partial F_\theta}{\partial \lambda} \right|_{\lambda=\dot{\lambda}=0} \left. \frac{\partial \lambda}{\partial \varepsilon} \right|_{\varepsilon=0} + \left. \frac{\partial F_\theta}{\partial \dot{\lambda}} \right|_{\lambda=\dot{\lambda}=0} \left. \frac{\partial \dot{\lambda}}{\partial \varepsilon} \right|_{\varepsilon=0} \quad (6-A2)$$

Moreover, from Eq. (6-A1):

$$\left. \frac{\partial \lambda}{\partial \varepsilon} \right|_{\varepsilon=0} = 0 \quad \left. \frac{\partial \dot{\lambda}}{\partial \varepsilon} \right|_{\varepsilon=0} = z_2|_{\varepsilon=0} \quad (6-A3)$$

Using Eq. (6-A3), $(F_\theta)_1$ from Eq. (6-A2) is:

$$(F_\theta)_1 = \left. \frac{\partial F_\theta}{\partial \dot{\lambda}} \right|_{\lambda=\dot{\lambda}=0} z_2|_{\varepsilon=0} \quad (6-A4)$$

By adopting the same technique used for the derivation of $(F_\theta)_1$, the expression for $(F_\theta)_2$ is:

$$(F_\theta)_2 = \left. \frac{\partial^2 F_\theta}{\partial \dot{\lambda}^2} \right|_{\lambda=\dot{\lambda}=0} (z_2|_{\varepsilon=0})^2 + 2 \left. \frac{\partial F_\theta}{\partial \lambda} \right|_{\lambda=\dot{\lambda}=0} z_1|_{\varepsilon=0} + \left. \frac{\partial F_\theta}{\partial \dot{\lambda}} \right|_{\lambda=\dot{\lambda}=0} \left. \frac{\partial z_2}{\partial \varepsilon} \right|_{\varepsilon=0} \quad (6-A5)$$

Appendix II: Derivation of matrix W for a two-flexible-link manipulator

The schematic of a two-flexible-link manipulator, shown in Fig. 6-1, is presented in Fig. 6-12 with more details. The angular positions r_1 and r_2 , which represent the location of the end-effector, are respectively:

$$r_1 = \theta_1 + \varphi_1 \quad (6-A6)$$

$$r_2 = \theta_2 + \varphi_2 + \alpha \quad (6-A7)$$

where θ_1 is the angle between the $X_{Inertial}$ and γ_1 , θ_2 is the angle between γ_2 and the tangent to the shoulder link (first link) at the elbow joint, α is the angle between the line1 and tangent to the shoulder link at the elbow joint, φ_1 is the angle between the line1 and γ_1 , and φ_2 is the angle between the line2 and γ_2 . The angles θ_1 and θ_2 , represent rigid body rotation of the links, while φ_1 , φ_2 and α are due to the flexibility of the links.

$$W = \begin{bmatrix} W_{11} & W_{12} \\ W_{21} & W_{22} \end{bmatrix} \quad (6-A12)$$

and

$$\begin{aligned} W_{11} &= \frac{1}{L_1} [\phi_{11}(L_1) \quad \dots \quad \phi_{1m}(L_1)]_{1 \times m} & W_{12} &= [0 \quad \dots \quad 0]_{1 \times m} \\ W_{21} &= \frac{1}{L_1} [\phi_{11}(L_1) - \phi'_{11}(L_1)L_1 \quad \dots \quad \phi_{1m}(L_1) - \phi'_{1m}(L_1)L_1]_{1 \times m} \\ W_{22} &= \frac{1}{L_2} [\phi_{21}(L_2) \quad \dots \quad \phi_{2m}(L_2)]_{1 \times m} \end{aligned} \quad (6-A13)$$

Appendix III: Derivation of Eq. (6-22)

By replacing z_1 and τ in Eq. (6-7a) with $h_1 = \sum_{i=0}^2 \varepsilon^i h_{1i}$ and $\tau = \sum_{i=0}^2 \varepsilon^i \tau_i$ respectively and using the series expansions given in Eq. (6-14) for $J_{\theta\lambda}^T, J_{\lambda\lambda}, F_\theta$ and F_λ , the corrected second order slow subsystem is:

$$\begin{cases} \dot{x}_1 = x_2 \\ \dot{x}_2 = \Pi_0 + \varepsilon \Pi_1 + \varepsilon^2 \Pi_2 \end{cases} \quad (6-A14)$$

where

$$\Pi_0 = (J_{\theta\theta})_0 \tau_0 - (J_{\theta\theta})_0 (F_\theta)_0 - (J_{\theta\lambda})_0 (F_\lambda)_0 - \frac{(J_{\theta\lambda})_0 K_{\lambda\lambda}}{\mu_{\min}((J_{\lambda\lambda})_0 K_{\lambda\lambda})} h_{10} \quad (6-A15)$$

$$\Pi_1 = (J_{\theta\theta})_0 \tau_1 - (J_{\theta\theta})_0 (F_\theta)_1 - (J_{\theta\lambda})_0 (F_\lambda)_1 - \frac{(J_{\theta\lambda})_0 K_{\lambda\lambda}}{\mu_{\min}((J_{\lambda\lambda})_0 K_{\lambda\lambda})} h_{11} \quad (6-A16)$$

$$\begin{aligned} \Pi_2 &= (J_{\theta\theta})_0 \tau_2 + \frac{1}{2} (J_{\theta\theta})_2 \tau_0 - \frac{1}{2} (J_{\theta\theta})_0 (F_\theta)_2 - \frac{1}{2} (J_{\theta\theta})_2 (F_\theta)_0 - \frac{1}{2} (J_{\theta\lambda})_0 (F_\lambda)_2 - \\ &\quad \frac{1}{2} (J_{\theta\lambda})_2 (F_\lambda)_0 - \frac{(J_{\theta\lambda})_0 K_{\lambda\lambda}}{\mu_{\min}((J_{\lambda\lambda})_0 K_{\lambda\lambda})} h_{12} - \frac{(J_{\theta\lambda})_2 K_{\lambda\lambda}}{2\mu_{\min}((J_{\lambda\lambda})_0 K_{\lambda\lambda})} h_{10} \end{aligned} \quad (6-A17)$$

By using h_{10} from Eq. (6-15a) and after algebraic manipulation, Π_0 from Eq. (6-A15) is:

$$\Pi_0 = [(J_{\theta\theta})_0 - (J_{\theta\lambda})_0 (J_{\lambda\lambda})_0^{-1} (J_{\theta\lambda})_0^T] (\tau_0 - (F_\theta)_0) \quad (6-A18)$$

Employing the property of the mass matrix given in Eq. (6-4d), Eq. (6-A18) changes to:

$$\Pi_0 = (M_{\theta\theta})_0^{-1}(\tau_0 - (F_\theta)_0) \quad (6-A19)$$

Substituting h_{11} from Eq. (6-15b) into Eq. (6-A16) results in:

$$\Pi_1 = [(J_{\theta\theta})_0 - (J_{\theta\lambda})_0(J_{\lambda\lambda})_0^{-1}(J_{\theta\lambda}^T)_0](\tau_1 - (F_\theta)_1) \quad (6-A20)$$

Using Eq. (6-4d), which is a property of the mass matrix, Eq. (6-A20) is:

$$\Pi_1 = (M_{\theta\theta})_0^{-1}(\tau_1 - (F_\theta)_1) \quad (6-A21)$$

From Eq. (6-A4) in Appendix II $(F_\theta)_1 = \partial F_\theta / \partial \dot{\lambda} \Big|_{\lambda=\dot{\lambda}=0} z_2 \Big|_{\varepsilon=0}$ and since on the second order manifold $z_2 \Big|_{\varepsilon=0} = h_{20}$ then $(F_\theta)_1 = \partial F_\theta / \partial \dot{\lambda} \Big|_{\lambda=\dot{\lambda}=0} h_{20}$. However $h_{20} = 0$ (See Eq. (6-15b)) and thus:

$$(F_\theta)_1 = 0 \quad (6-A22)$$

and Eq. (6-A21) is:

$$\Pi_1 = (M_{\theta\theta})_0^{-1} \tau_1 \quad (6-A23)$$

The procedure for the derivation of Π_2 is similar to those detailed above to obtain Eqs. (6-A19) and (6-A23) for Π_0 and Π_2 . This procedure is briefly explained in the following with the details removed for the brevity. Substituting h_{12} from Eq. (6-15e) into Eq. (6-A17), replacing \dot{h}_{21} with \ddot{h}_{10} (See Eq. (6-15d)), using the properties of the mass matrix given in Eqs. (6-4b) and (6-4d) and after some algebraic manipulation, Π_2 is:

$$\Pi_2 = (M_{\theta\theta})_0^{-1}(\tau_2 - \frac{1}{2}(F_\theta)_2 - (M_{\theta\lambda})_0 \ddot{h}_{10}) + d \quad (6-A24)$$

where d is given in Eq. (6-21c). Finally, combining Eq. (6-A14) with Eqs. (6-A19), (6-A23) and (6-A24), the corrected slow subsystem given in Eq. (6-22) obtained.

Appendix IV: Expressions of O_{z1} and O_{z2} in Eq. (35)

The expressions of O_{z1} and O_{z2} are:

$$O_{z1} = (J_{\theta\lambda}^T)_0((F_\theta)_1 - (\hat{F}_\theta)_1) + (J_{\lambda\lambda})_0((F_\lambda)_1 - (\hat{F}_\lambda)_1) \quad (6-A25)$$

$$\begin{aligned} O_{z2} = & \frac{1}{2}[(J_{\theta\lambda}^T)_0((F_\theta)_2 - (\hat{F}_\theta)_2) + ((J_{\theta\lambda}^T)_2 - (\hat{J}_{\theta\lambda}^T)_2)((F_\theta)_0 - \tau_0) + (J_{\lambda\lambda})_0((F_\lambda)_2 - (\hat{F}_\lambda)_2) + \\ & ((J_{\lambda\lambda})_2 - (\hat{J}_{\lambda\lambda})_2)((F_\lambda)_0 + \frac{K_{\lambda\lambda} h_{10}}{\mu_{\min}((J_{\lambda\lambda})_0 K_{\lambda\lambda})}) - (\hat{J}_{\lambda\lambda})_2 \frac{K_{\lambda\lambda} \hat{z}_1}{\mu_{\min}((J_{\lambda\lambda})_0 K_{\lambda\lambda})} + (\hat{J}_{\theta\lambda})_2 \tau_f] \end{aligned} \quad (6-A26)$$

where $(F_\theta)_1, (F_\lambda)_1, (F_\lambda)_2, (F_\theta)_2, (J_{\theta\lambda}^T)_2$ and $(J_{\lambda\lambda})_2$ are evaluated when $z = h$, while $(\hat{F}_\theta)_1, (\hat{F}_\lambda)_1, (\hat{F}_\lambda)_2, (\hat{F}_\theta)_2, (\hat{J}_{\theta\lambda}^T)_2$ and $(\hat{J}_{\lambda\lambda})_2$ are evaluated when $z = \hat{z} + h$. By using the chain rule to calculate terms in Eqs. (6-A25) and (6-A26) which contain differentiation, (See Appendix I), N_{z1} and N_{z2} are respectively:

$$O_{z1} = -((J_{\theta\lambda}^T)_0 \frac{\partial F_\theta}{\partial \dot{\lambda}} \Big|_{\lambda=\dot{\lambda}=0} + (J_{\lambda\lambda})_0 \frac{\partial F_\lambda}{\partial \dot{\lambda}} \Big|_{\lambda=\dot{\lambda}=0}) \hat{z}_2 \quad (6-A27)$$

$$\begin{aligned} O_{z2} = & -\frac{1}{2}(J_{\theta\lambda}^T)_0 \left[\frac{\partial^2 F_\theta}{\partial \dot{\lambda}^2} \Big|_{\lambda=\dot{\lambda}=0} (\hat{z}_2)^2 + 2 \frac{\partial F_\theta}{\partial \dot{\lambda}} \Big|_{\lambda=\dot{\lambda}=0} \hat{z}_2 \right] - \frac{\partial J_{\theta\lambda}^T}{\partial \lambda} \Big|_{\lambda=0} \hat{z}_1 ((F_\theta)_0 - \tau_0) - \frac{\partial J_{\lambda\lambda}}{\partial \lambda} \Big|_{\lambda=0} \\ & \hat{z}_1 [(F_\lambda)_0 + \frac{K_{\lambda\lambda}}{\mu_{\min}((J_{\lambda\lambda})_0 K_{\lambda\lambda})} h_{10}] - \frac{\partial J_{\lambda\lambda}}{\partial \lambda} \Big|_{\lambda=0} \frac{(h_{10} + \hat{z}_1) K_{\lambda\lambda} \hat{z}_1}{\mu_{\min}((J_{\lambda\lambda})_0 K_{\lambda\lambda})} + \frac{\partial J_{\theta\lambda}^T}{\partial \lambda} \Big|_{\lambda=0} (\hat{z}_1 + h_{10}) \tau_f - \\ & \frac{1}{2}(J_{\lambda\lambda})_0 \left[\frac{\partial^2 F_\lambda}{\partial \dot{\lambda}^2} \Big|_{\lambda=\dot{\lambda}=0} (\hat{z}_2)^2 + 2 \frac{\partial F_\lambda}{\partial \dot{\lambda}} \Big|_{\lambda=\dot{\lambda}=0} \hat{z}_2 \right] \end{aligned} \quad (6-A28)$$

Appendix V: The stability proof of the proposed controller

After applying torque $\tau_0 + \varepsilon^2 \tau_2 + \tau_f$, where τ_0, τ_2 , and τ_f are given in Eqs. (6-20a), (6-20c) and (6-37) respectively, to the governing dynamic equations of MLFM, Eqs. (6-7a) and (6-7b), and neglecting the terms of order ε^p , $p > 2$, the errors' dynamics are:

$$\dot{e}_r = A_r e_r + N_r \quad (6-A29)$$

$$\varepsilon \dot{\eta} = A_\eta \eta + N_\eta \quad (6-A30)$$

where:

$$e_r^T = [(r - r_d)^T \quad (\dot{r} - \dot{r}_d)^T]^T, \quad \eta^T = [e_z^T \quad \hat{z}^T], \quad e_z = \hat{z} - \tilde{z} \quad (6-A31)$$

$$A_r = \begin{bmatrix} 0 & I \\ -K_p & -K_D \end{bmatrix}, \quad A_\eta = \begin{bmatrix} A_z - K_{\theta z} C_z & 0 \\ B_z K_{cz} & A_z - B_z K_{cz} \end{bmatrix} \quad (6-A32)$$

$$N_\eta = \begin{bmatrix} \varepsilon N_{z1} + \varepsilon^2 N_{z2} \\ \varepsilon N_{z1} + \varepsilon^2 N_{z2} \end{bmatrix}, \quad N_r = \begin{bmatrix} 0 \\ D_r \end{bmatrix} \quad (6-A33)$$

$$\begin{aligned} D_r = & -(W(J_{\theta\lambda}^T)_0 K_{cz} + (J_{\theta\theta})_0 K_{cz})(e_z - \hat{z}) + \left[\varepsilon^2 K_p W - \left(\frac{W(J_{\lambda\lambda})_0 + (J_{\theta\lambda})_0}{\mu_{\min}(J_{\lambda\lambda} K_{\lambda\lambda})} \right) K_{\lambda\lambda} \quad \varepsilon K_p W \right] \hat{z} + \\ & \varepsilon(D_{r3} + O_{z1}) + \varepsilon^2(D_{r4} + O_{z2}) \end{aligned}$$

(6-A34)

$$D_{r3} = -(J_{\theta\theta})_0(\hat{F}_\theta)_1 - (J_{\theta\lambda})_0(\hat{F}_\lambda)_1 \quad (6-A35)$$

$$\begin{aligned} D_{r4} = & \frac{1}{2}((\hat{J}_{\theta\theta})_2 - (J_{\theta\theta})_2)((\tau_0 - (F_\theta)_0) + \frac{1}{2}((J_{\theta\lambda})_2 - (\hat{J}_{\theta\theta})_2)((F_\lambda)_0 + \frac{K_{\lambda\lambda}h_{10}}{\mu_{\min}(J_{\lambda\lambda}K_{\lambda\lambda})}) + \\ & \frac{1}{2}(J_{\theta\theta})_0((F_\theta)_2 - (\hat{F}_\theta)_2) + \frac{1}{2}(J_{\theta\lambda})_0((F_\lambda)_2 - (\hat{F}_\lambda)_2) - \frac{1}{2}(\hat{J}_{\theta\theta})_2 K_{cz}(\hat{z} - e_z) - \frac{1}{2} \frac{(\hat{J}_{\theta\lambda})_2 K_{\lambda\lambda}}{\mu_{\min}(J_{\lambda\lambda}K_{\lambda\lambda})} \hat{z}_1 \end{aligned} \quad (6-A36)$$

Moreover N_{z1} and N_{z2} in Eq. (6-A34) are given in Eq. (6-35) in Section 3, $(J_{\theta\theta})_2, (J_{\theta\lambda})_2, (F_\lambda)_2$ and $(F_\theta)_2$ in Eq. (6-A36) are evaluated when $z = h$ and $(\hat{F}_\lambda)_1, (\hat{F}_\theta)_1, (\hat{J}_{\theta\theta})_2, (\hat{J}_{\theta\lambda})_2, (\hat{F}_\lambda)_2$ and $(\hat{F}_\theta)_2$ in Eqs. (6-A35) and (6-A36) are evaluated when $z = \hat{z} + h$. It is to be noted that $(\hat{F}_\lambda)_1, (\hat{F}_\theta)_1, (\hat{J}_{\theta\theta})_2, (\hat{J}_{\theta\lambda})_2, (\hat{F}_\lambda)_2, (\hat{F}_\theta)_2, (J_{\theta\theta})_2, (J_{\theta\lambda})_2, (F_\lambda)_2$ and $(F_\theta)_2$ in Eqs. (6-A35) and (6-A36) can be re-written in terms of \hat{z} and h by using the chain rule, similar to Appendix IV, which is not repeated here.

For the stability analysis of the error dynamics, the Lyapunov candidate function is selected as:

$$V_{Lyp} = e_r^T P_r e_r + \varepsilon \eta^T P_\eta \eta \quad (6-A37)$$

where P_r and P_η are symmetric positive definite matrices obtaining from the following Lyapunov equations, in which S_η and S_r are also symmetric positive definite matrices:

$$A_\eta^T P_\eta + P_\eta A_\eta = -S_\eta \quad (6-A38)$$

$$A_r^T P_r + P_r A_r = -S_r \quad (6-A39)$$

The existence of positive definite matrices P_r and P_η satisfying Eqs. (6-A38) and (6-A39) is due to the fact that A_r and A_η given in Eq. (6-A32) are Hurwitz, which is the consequence of having K_p and K_D positive definite and $A_z - K_{oz}C_z$ and $A_z - B_z K_{cz}$ Hurwitz.

Calculating the time derivative of V_{Lyp} along the trajectories of Eqs. (6-A29) and (6-A30) and using Eqs. (6-A38) and (6-A39) results in:

$$\dot{V}_{Lyp} = -e_r^T S_r e_r - \eta^T S_\eta \eta + 2N_r^T P_r e_r + 2N_\eta^T P_\eta \eta + \varepsilon \eta^T \dot{P}_\eta \eta \quad (6-A40)$$

On a bounded region around the origin of e_r and η , it is possible to assume [11,13,14]:

$$\|N_r^T P_r\| < (\ell_3 + \varepsilon \ell_4 + \varepsilon^2 \ell_5) \|\eta\| \quad (6-A41)$$

$$\|N_\eta^T P_\eta\| < (\varepsilon \ell_6 + \varepsilon^2 \ell_7) \|\eta\| \quad (6-A42)$$

$$\|\dot{P}_\eta\| < \ell_8 \quad (6-A43)$$

where the symbol $\|\psi\|$ is the Euclidean norm of the arbitrary matrix ψ and $\ell_3, \ell_4, \ell_5, \ell_6, \ell_7$ and ℓ_8 are positive constants. By employing Eqs. (6-A41) to (6-A43), \dot{V}_{Lyp} in Eq. (6-A40) is:

$$\dot{V}_{Lyp} < -\begin{bmatrix} \|e_r\| & \|\eta\| \end{bmatrix} \Omega \begin{bmatrix} \|e_r\| \\ \|\eta\| \end{bmatrix} \quad (6-A44)$$

where

$$\Omega = \begin{bmatrix} \mu_{\min}(S_r) & -(\ell_3 + \varepsilon \ell_4 + \varepsilon^2 \ell_5) \\ -(\ell_3 + \varepsilon \ell_4 + \varepsilon^2 \ell_5) & \mu_{\min}(S_\eta) - \varepsilon(2\ell_6 + \ell_8) - 2\varepsilon^2 \ell_7 \end{bmatrix} \quad (6-A45)$$

and the symbol $\mu_{\min}(S)$ represents the minimum eigenvalues of a matrix S . As $\varepsilon \rightarrow 0$ and provided that $\mu_{\min}(S_\eta) \mu_{\min}(S_r) > \ell_3^2$, the matrix Ω defined in Eq. (6-A45) is positive definite. Thus there exists ε_{\max} so that for all $0 < \varepsilon < \varepsilon_{\max}$, matrix Ω is positive definite and consequently, the error dynamics in Eqs. (6-A29) and (6-A30) is Lyapunov stable. The ε_{\max} , after imposing the positive definite property on Ω and considering only terms of order ε is:

$$\varepsilon_{\max} = \frac{\mu_{\min}(S_r) \mu_{\min}(S_\eta) - \ell_3^2}{(2\ell_6 + \ell_8) \mu_{\min}(S_r) + 2\ell_3 \ell_4} \quad (6-A46)$$

The fact that $r_d \in C^4$, makes the control signals continuous and bounded. Otherwise, the tracking error will be large and unsatisfactory.

6.8. References

1. P. V. Kokotovic, H. K. Khalil, and J. O'Reilly, "Singular Perturbation Methods in Control: Analysis and Design", Academic, New York, 1999.

2. B. Siciliano, J. V. R. Prasad, and A. J. Calise, 1992, "Output Feedback Two-Time Scale Control of Multi-link Flexible Arms", *Journal of Dynamics, Measurement and Control*, 114, pp. 70-77.
3. V. A. Sobolev, 1984, "Integral Manifolds and Decomposition of Singularly Perturbed Systems", *Systems and Control Letters*, 5, pp. 169-179.
4. F. Ghorbel, and M. W. Spong, 2000, "Integral Manifold of Singularly Perturbed Systems with Application to Rigid-Link Flexible-Joint Multibody System", *International Journal of Non-linear Mechanics*, 35, pp. 133-155.
5. H. Asada, and J. J. E. Slotine, 1986, "Robot Analysis and Control", John Wiley and Sons, New York, USA.
6. S. M. Shahruz, and S. Behtash, 1992, "Design of Controllers for Linear Parameter-Varying System By Gain Scheduling Technique", *Journal of Mathematical Analysis and Application*, 168, pp. 195-217.
7. B. Siciliano, W. J. Book, and G. De Maria, 1986, "An integral manifold approach to control of a one link flexible arm", *Proceeding of the IEEE conference on Decision of Control*, Athens, Greece, pp. 1131-1134.
8. F. Khorrami, and U. Ozguer, 1988, "Singular perturbation analysis of a distributed model of flexible manipulators", *Proceeding of the American control conference*, Atlanta, USA, pp. 1704-1709.
9. D. A. Schoenwald, and U. Ozguner, 1996, "Control of flexible manipulator via singular perturbation and distributed vibration damping", *Dynamics and Control*, 6 (1), pp. 5-32.
10. K. Hashtudi Zaad, and K. Khorasani, 1996, "Control of Non-minimum Phase Singularly Perturbed System with Application to Flexible-link Manipulators", *International Journal of Control*, 63(4), pp. 679-701.
11. M. Moallem, K. Khorasani and R.V. Patel, 1997, "An Integral Manifold Approach for Tip Position Tracking of Flexible Multi-Link Manipulators", *IEEE Transactions on Robotics and Automation*, 13 (6), pp. 823-837.
12. Y. Morita, H. Ukai, and H. Kando, 1997, "Robust trajectory tracking control of elastic robot manipulators," *Journal of Dynamics, Measurement and Control*, 119, pp. 727-735.

13. M. Vakil, R. Fotouhi, R., and P. N. Nikiforuk, 2007, "Application of the Integral Manifold Concept for the End-effector Trajectory Tracking of a Flexible Link Manipulator", Proceeding of the American control conference, New York, USA, pp. 741-747.
14. M. Vakil, R. Fotouhi, and P. N. Nikiforuk, 2008, "End-effector trajectory tracking for a class of flexible link manipulator", Accepted at the ASME 32nd Annual mechanisms and robotics conference, New York, USA.
15. M. Vakil, R. Fotouhi and P. N. Nikiforuk, 2007, "A Constrained Lagrange formulation of multi-link planar flexible manipulator", Accepted for publication at the Journal of Vibration and Acoustics.
16. A. De Luca, and B. Siciliano, 1991, "Closed-Form dynamic model of planar multilink lightweight robots", IEEE Transactions on Systems, Man and Cybernetics, 21 (4), pp. 826-839.
17. M. W. Spong, K. Khorasani, and P. V. Kokotovic, 1987, "An Integral Manifold Approach to the Feedback Control of Flexible Joint Robots", IEEE Transactions on Robotics and Automation, 3 (4), pp. 291-300.
18. H. K. Khalil, "*Nonlinear Systems*", Prentice Hall, New Jersey, USA, 2002.
19. M. Moallem, R. V. Patel, and K. Khorasani, 2001, "Nonlinear Tip-Position Control of a Flexible-Link Manipulator: Theory and Experiments", Automatica, 37, pp-1825-1834.
20. J. Cheong, W. K. Chung, and Y. Youm, 2004, "Inverse Kinematics of Multilink Flexible Robots for High-Speed Application", IEEE Transactions on Robotics and Automation, 20 (2), pp. 269-282.

Chapter 7. Closing

In this section the summary and conclusion of the thesis are presented. The contributions of the candidate's work are highlighted and the potential future extensions of the candidate's research are discussed.

7.1. Summary and Conclusion

The dynamic modeling and model-based end-effector trajectory tracking of flexible link manipulators have been addressed in this thesis.

In Chapter 2 the dynamic modeling of flexible link manipulators was discussed and simulation studies performed on a two-link flexible manipulator and compared with those of the full nonlinear finite element analysis. Also details of the matrices in the dynamic modeling of flexible link manipulator were provided. The introduced method in Chapter 2 reduced the computational complexity of the dynamic model derivation which was its advantages. This dynamic model was used in the rest of the chapters for the design of model-based end-effector trajectory tracking controllers.

In Chapter 3, a new end-effector inversion method for the linear model of a single flexible link manipulator was introduced and experimentally tested. This new end-effector inversion method redefined the desired end-effector trajectory so that the end-effector inversion was possible. For the purpose of output redefinition the summation of stable exponential function was used which lead to a family of possible solutions for the redefined trajectory. Therefore, the member of the family of the redefined trajectory, best member, which had the smallest difference with the desired trajectory, can be selected.

In Chapter 4 a new end-effector trajectory tracking controller for a single flexible link manipulator was introduced and experimentally verified. This new controller was based on the concept of the integral manifold of the singularly perturbed differential equations. Based on this concept, the link's lateral deflection and its time derivative was approximately represented in terms of the link's rotation, its time derivative and input torque. Consequently, the underactuated single flexible link manipulator approximately appeared to be a fully actuated system and its end-effector trajectory tracking was accomplished.

In Chapter 5, the new end-effector trajectory tracking control, which was introduced in Chapter 4 for a single flexible link manipulator, has been extended to a

class of flexible link manipulators composed of a chain of rigid link with the flexible end-link (CRFE) and experimentally verified. The extension of the controller, introduced in Chapter 4 for a linear system, to end-effector trajectory tracking of CRFE, with nonlinear dynamic model, increased its possibility of implementation to the multilink flexible manipulator.

In Chapter 6, the new end-effector trajectory tracking controller (introduced in Chapter 4 for a single flexible link manipulator and extended in Chapter 5 to a class of flexible link manipulators) was successfully extended to the multilink flexible manipulator and the simulation results for a two-link flexible manipulator has been presented. Simulation studies were performed for different maneuver speeds. It was observed that for the same controller gains the faster the maneuver, the greater will be the tracking error. This was also seen in the simulation studies and experimental verifications carried out in Chapters 4 and 5.

7.2. Contributions of the research:

The contributions of the candidate's research cover the objectives set out for his thesis. These objectives were:

1- Developing the dynamic model of FLM.

2- Developing controllers for the EETT of FLM and its feasibility study through the experimental verifications.

For this objective the following sub-objectives were defined and achieved:

2-1- Approximate end-effector inversion of a SFLM and experimental verification

2-2- EETT of a SFLM and experimental verification

2-3- EETT of a class of FLM which is composed of a chain of rigid links with the flexible end-link and experimental verification

2-4- EETT of the multilink flexible manipulator

Contribution 1 (objective 1) - A new method of obtaining a dynamic model of flexible link manipulators has been developed which combines the assumed mode shape method with the Lagrange equations. The novelty of this method is in deriving the dynamic model without calculating the lengthy Lagrangian function of the flexible link

manipulator and without evaluating its corresponding derivatives. Thus, the calculation effort of the new method is minimized. To verify this new method the result of the dynamic simulation for a two-link manipulator with both links flexible were compared with those obtained using full nonlinear finite element analysis from ANSYS. These comparisons showed sound agreement. This contribution was discussed in Chapter 2.

Contribution 2 (objective 2-1) - A new dynamic end-effector inversion technique for a single flexible link manipulator with a linear dynamic model has been developed. The novelty of this technique is in redefining the desired end-effector trajectory so that the dynamic end-effector inversion is achievable. For the redefinition of the desired trajectory the summation of the stable exponential functions was used. The experimental verification of the technique was performed on a single flexible link manipulator which is available in the robotic laboratory at the University of Saskatchewan. This contribution was detailed in Chapter 3 of this thesis.

Contribution 3 (objectives 2-2, 2-3, 2-4) – A new end-effector trajectory tracking controller for flexible link manipulators has been developed. This new end-effector trajectory tracking controller has been derived based on the concept of the integral manifold of the singularly perturbed differential equations. For this purpose, the singular perturbed form of the dynamic models of flexible link manipulators was used. The novelties of this controller compared to available controllers are:

- It is computationally efficient, since (1) - it only requires one corrective torque in addition to the computed torque command of the rigid link counterpart of the flexible link manipulator (2)- several properties of the matrices in the dynamic model of the flexible link manipulator were used, the derivation of the control command is simplified.
- It is feasible and practical, since (1) - it has been experimentally verified on a linear model of a single flexible link manipulator and a nonlinear model of a two-link manipulator with the first link rigid and second link flexible (2)- its implementation does not require measuring the time derivative of links' lateral deflections, which are not easily available.

This contribution resulted in three submitted journal papers which are Chapters 4, 5 and 6.

Contribution 4 - A new method for deriving the zeros of the transfer function of a single flexible link manipulator considering the end-effector displacement as the output without evaluating the transfer function has been introduced by the candidate. The possibility of removing the nonminimum phase characteristic of a single flexible link manipulator by the partial collocation of the sensor and actuator was studied by the candidate. For this purpose, a small actuator was placed on the end-effector of a single flexible link manipulator. This actuator applied a torque at the end-effector which was synchronized with the base actuator. The variation of the location of right-hand-side zeros due to the existence of the end-effector actuator was studied. It was observed that the partial collocation of the sensor and actuator for a single flexible link manipulator can not completely remove the right-hand-side zeros to the left-hand-side of the S-plane. That is, the partial collocation of the sensor and actuator can not change the nonminimum phase transfer function of a single flexible link manipulator into a minimum phase one. The publications from this contribution were the following conference papers

- **Vakil M.**, Fotouhi R., Nikiforuk P. N., “Zeros of the transfer function of a rigid-flexible manipulator”, *21st Canadian Congress on Applied Mechanics, Toronto, Canada (CD-Rom), June 3rd - 7th, 2007.*
- **Vakil M.**, Fotouhi R., Nikiforuk P. N., “On the zeros of the transfer function of a single flexible link manipulator”, *17th IASTED International Conference on Modeling and Simulation, Montreal, Quebec, Canada, pp. 20-25, May 24th - 26th 2006.*

7.3. Potential Future research

The extension of the research presented here can be from the theoretical and the experimental points of views. The possible future research directions are as follows:

- 1- The end-effector trajectory tracking derived based on the concept of the integral manifold of the singularly perturbed differential equations, discussed in Chapters 4, 5 and 6 is a model based controller. To account for the disturbances in the physical parameters of the system and improve the performance, the controller proposed here should be

adaptive. The possibility of combining adaptive control strategies with the new controller introduced here and its experimental verification can be an interesting research subject.

2- For the precise end-effector trajectory tracking the joints' flexibilities should also be considered in the dynamic model. In the controllers described in Chapters 3, 4, 5 and 6 the flexibility of joints were not considered in the dynamic model. The extension of the controller for the end-effector trajectory tracking of the flexible link manipulators with joints' flexibilities with experimental verification is another potential extension of the research presented here.

3- The dynamic end-effector inversion method, discussed in Chapter 3, used the summation of the exponential function for the redefinition of the desired end-effector. As a possible extension, the combination of the summation of stable exponential functions with the sinusoidal or polynomial functions can be used for the redefinition of the desired end-effector trajectory. Therefore, a wider family of answers for the redefined trajectory will be available which an advantage is for control engineers.